รายงานวิจัยฉบับสมบูรณ์

โครงการ แบบจำลองสำหรับปัญหาพื้นฐานทางกลศาสตร์วิศวกรรม โดยพิจารณาอิทธิพลในระดับนาโน

โดย ศ.ดร. ธีรพงศ์ เสนจันทร์ฒิไชย และคณะ

กรกฎาคม 2557

สัญญาเลขที่ BRG5480006

รายงานวิจัยฉบับสมบูรณ์

โครงการ แบบจำลองสำหรับปัญหาพื้นฐานทางกลศาสตร์วิศวกรรมโดยพิจารณาอิทธิพลในระดับนาโน

โดย ศ.ดร.ธีรพงศ์ เสนจันทร์ฒิไชย และ รศ.ดร. จรูญ รุ่งอมรรัตน์

ภาควิชาวิศวกรรมโยธา

คณะวิศวกรรมศาสตร์

จุฬาลงกรณ์มหาวิทยาลัย

สนับสนุนโดยสำนักงานกองทุนสนับสนุนการวิจัย

(ความเห็นในรายงานนี้เป็นของผู้วิจัย สกว. ไม่จำเป็นต้องเห็นด้วยเสมอไป)

ACKNOWLEDGEMENTS

The principal investigator and co-researcher gratefully acknowledge the financial support provided by the Thailand Research Fund (Grant No. BRG 5480006). They would also like to thank Professor Dr. Nimal Rajapakse, Dean of Faculty of Applied Science, Simon Fraser University, Canada; Professor Mark E. Mear, Department of Aerospace Engineering and Engineering Mechanics, University of Texas at Austin, USA; and Associate Professor Dr. Anil C. Wijeyewickrema, Department of Civil and Environmental Engineering, Tokyo Institute of Technology, Japan for their useful comments during the course of this investigation. In addition, thanks are conveyed to Dr. Pong-In Intarit, Mr. Bin Thai Nguyen, Ms. Yutiwadee Pinyochotiwong, and Ms. Porjan Tuttipongsawat for their assistance in the development of solution schemes and the preparation of this manuscript.

TEERAPONG SENJUNTICHAI
JAROON RUNGAMORNRAT

Department of Civil Engineering
Faculty of Engineering
Chulalongkorn University
July 2014

ABSTRACT

Project Code: BRG5480006

Project Title: Models for fundamental problems in engineering mechanics with consideration of nano-scale influence

Investigators: Teerapong Senjuntichai and Jaroon Rungamornrat, Department of Civil Engineering, Faculty of Engineering, Chulalongkorn University

Email Address: Teerapong.S@chula.ac.th and Jaroon.r@chula.ac.th

Project Period: 3 years

Abstract: In this research project, accurate and efficient techniques are developed for solving fundamental problems in solid mechanics with consideration of nano-scale influence. Three problems are considered in the present study, namely, elastic layer under surface loading, nano-indentation, and nano-sized cracks. The concept of surface elasticity, which has been widely employed in the investigation of nano-scale problems, is adopted to derive a suitable mathematical model capable of simulating the influence from surface energy that has been considered essential for nano-sized objects. In the present formulation, the classical theory of linear elasticity is utilized to establish the key governing equations of the bulk material whereas the well-known Gurtin-Murdoch surface elasticity model is employed to simulate responses of an infinitesimally thin layer of material adhered perfectly to the surface of the body. The governing equations for the surface and the bulk material are both formulated in an appropriate form for the solution sought, and properly coupled via appropriate interface conditions. Selected solution procedures are then implemented to efficiently and accurately determine solutions of the fully coupled governing equations. Once the proposed techniques are verified with available benchmark solutions, they are applied to investigate the size dependency of predicted solutions and nano-scale influence on the fundamental problems under consideration. Numerical results from an extensive parametric study confirm the fact that the presence of surface stresses is significant in the analysis of solid mechanics problems involving nano-scale influence and soft elastic materials where the surface energy effects are not negligible.

Keywords: cracks, nano-indentations, elastic layer, nano-scale influence, Gurtin-Murdoch, surface stresses, SGBEM, FEM

บทคัดย่อ

รหัสโครงการ: BRG5480006

ชื่อโครงการ: แบบจำลองสำหรับปัญหาพื้นฐานทางกลศาสตร์วิศวกรรมโดยพิจารณาอิทธิพลในระดับนาโน

ชื่อนักวิจัย: ศ.ดร. ธีรพงศ์ เสนจันทร์ฒิไชย และ รศ.ดร.จรูญ รุ่งอมรรัตน์ ภาควิชาวิศวกรรมโยธา คณะวิศวกรรมศาสตร์ จุฬาลงกรณ์มหาวิทยาลัย

อีเมล์: Teerapong.S@chula.ac.th และ Jaroon.r@chula.ac.th

ระยะเวลาโครงการ: 3 ปี

บทคัดย่อ: โครงการวิจัยนี้นำเสนอระเบียบวิธีที่มีประสิทธิภาพสำหรับการวิเคราะห์ปัญหาพื้นฐานทางกลศาสตร์ของแข็งที่พิจารณาผลกระทบในระดับนาโนได้แก่ ปัญหาแรงกระทำบนชั้นยืดหยุ่น ปัญหาการกดในระดับนาโน และปัญหารอยแตกร้าวขนาดนาโน หลักการของหน่วยแรงที่ผิวซึ่งนิยมใช้แพร่หลายในการศึกษาปัญหาในระดับนาโนถูกนำมาใช้ในการพัฒนาแบบจำลองทางคณิตศาสตร์ ทฤษฎีความยืดหยุ่นเชิงเส้นพื้นฐานถูกนำมาใช้ในการสร้างสมการกำกับของวัสดุบัลก์ โดยมีแผ่นผิวบางของวัสดุซึ่งถูกจำลองให้เป็นพื้นผิวที่มีความหนาเป็นศูนย์และยึดแน่นกับวัสดุบัลก์โดยพฤติกรรมถูกกำกับโดยความสัมพันธ์เชิงวัสดุของเกอร์ตินและเมอร์ดอค สมการกำกับของวัสดุบัลก์และพื้นผิวที่มีความหนาเป็นศูนย์ถูกสร้างขึ้นในรูปแบบที่เหมาะสมและพิจารณาความสัมพันธ์ระหว่างวัสดุทั้งสองบริเวณรอยต่อ ระเบียบวิธีต่างๆได้ถูกพัฒนาขึ้นในงานวิจัยนี้เพื่อแก้ปัญหาค่าขอบเขตของปัญหาพื้นฐานที่ทำการศึกษาอย่างมีประสิทธิภาพ หลังจากสอบเทียบกับผลเฉลยอ้างอิงแล้วระเบียบวิธีที่พัฒนาขึ้นถูกนำมาใช้ในการศึกษาพฤติกรรมที่ขึ้นอยู่กับขนาดของวัสดุและอิทธิพลของหน่วยแรงที่ผิวที่มีต่อหน่วยแรงและการเคลื่อนที่ในแต่ละปัญหา ผลการศึกษาแสดงให้เห็นว่าหน่วยแรงที่ผิวมีอิทธิพลสำคัญต่อพฤติกรรมเชิงกลของวัสดุในปัญหากลศาสตร์ของแข็งในระดับนาโนและวัสดุยืดหยุ่นอ่อน

คำสำคัญ: รอยร้าว, การกดระดับนาโน, ชั้นยืดหยุ่น, อิทธิพลระดับนาโน, เกอร์ติน-เมอร์ดอค, หน่วยแรงพื้นผิว, SGBEM, FEM

TABLE OF CONTENTS

LIST OF FIGURES

LIST OF TABLES

CHAPTER I

INTRODUCTION

1.1 Motivation and Significance

Nowadays, Nanotechnology has become one of the most interesting research areas in various fields such as biology, chemistry, physics, medicine and engineering. Although nanotechnology deals only with extremely tiny objects with their length scale of few nanometers (where one nanometer is approximately about 50,000 times smaller than the average of a human hair), its applications tend to be substantial. For instance, nano-crystals are examples of a new invention at a nano-scale level. Metal nano-crystals can be incorporated into car bumpers, making the parts stronger, or into aluminum, making it more durable. Other applications of the metal nano-crystals can be found in the production of bearings, new types of sensors and components for computers and electronic hardware. The nano-crystals of various metals have been shown to be 100 percent, 200 percent and even as much as 300 percent harder than the same materials in the bulk form. Since the wear resistance is often dictated by the hardness of a metal, parts made from the nano-crystals might last significantly longer than conventional parts. In a field of medicine and healthcare, ones apply the nanotechnology to produce a nano-particulate-based synthetic bone. It is well known that the human bone is made of a calcium and phosphate composite called hydroxyapatite. By manipulating the calcium and phosphate at a molecular level, ones can create a patented material that is identical in structure and composition to the natural bone. This novel synthetic bone can be used in areas where the natural bone is damaged or removed, such as in the treatment of fractures and soft tissue injuries. For public utilities, nano-filters are capable of filtering the smallest particles of impurities. Such performance results directly from the nano-sized alumina fiber attracting and retaining sub-micron and nano-sized particles. This disposable filter retains 99.9999 percentages of viruses at water flow rates several hundred times greater than virus-rated ultra-porous membranes. This product can be exploited to sterilize drinking water, allowing inhabitants in third-world countries to access the clean water. In a field of advanced materials, researches related to nano-science and nanotechnology such as nano-tubes, nano-wires, nano-composites and nano-films have grown rapidly and continuously. For examples, the carbon nano-tube, which was discovered by Iijima in 1991 (Iijima 1991, Iijima and Ichihashi 1993), has been known as an ideal material that possesses excellent mechanical properties. For instance, Young's modulus, tensile strengths and failure strains of a defect-free single-walled carbon nano-tube are up to 1 TPa, greater than 100 GPa and about 15-30%, respectively (Peng *et al.* 2008). All above excellent products come from advanced researches conducted at the nano-scale level. What we have seen is just the beginning of a revolution, caused by the ability to work on the same scale as nature. The nanotechnology is going to affect every aspect of our life. It will become the next industrial revolution (Ratner and Ratner 2003). The nanotechnology can be compared to a dawn of the digital revolution that totally changes the face of technology and human life. Unlike the internet, the nanotechnology can equally be applied to old things and processes. It is about creating entirely new materials, products, and systems as well as making existing products faster, stronger and better.

Due to enormous benefits that nanotechnology has brought out for the human, applications of nano-sized devices and nano-structured materials rapidly grow in various field.

The physical modeling and corresponding comprehensive analysis to gain an insight into the complex behavior of nano-sized devices and nano-structured materials become crucial aspects in the optimal design of nano-scale products. Besides the fundamental understanding of mechanical properties in the nano-scale level, failure/damage analysis and assessment has been found one of the essential steps that must be properly considered to ensure their safety and integrity in the design procedure.

In the past three decades, various techniques have been developed and used extensively to investigate the nano-mechanical properties and characteristics of nano-sized structures. Several experimental researches have been found in the literature; for instance, Wong et al. (1997) utilized an atomic-force microscopy to determine the mechanical properties of isolated silicon carbide (SiC) nano-rods (NRs) and multi-wall carbon nano-tubes (MWNTs), Mao et al. (2003) employed the atomic-force microscope to investigate the hardness of both ZnO and SnO_2 nano-belts, and Poncharal et al. (1999) statically and dynamically measured the bending modulus of carbon nano-tubes in a transmission electron microscope. In addition, some researchers attempted to use the experimental approaches to explore the behavior of nano-sized cracks (e.g., Karimi *et al.* 2002, Sumomogi *et al.* 2002, Sundararajan and Bhushan 2002, Chen *et al.* 2008, Peng *et al.* 2008, Zhao and Xing 2008, Qin *et al.* 2009, Zhao and Xing 2010, Yan *et al.* 2011). It is generally acknowledged that experimental methods yield results reflecting real behavior. However, it is still found highly dependent on experimental environments and, more importantly, expensive due to the requirement of sophisticated equipments and high-precision testing procedures. As a result, the mathematical simulations and modeling has become an attractive alternative and been widely used to develop fundamental understanding and further predict complex phenomena. In addition, once integrating essential features and properly calibrated with data from basic experiments, mathematical models are found capable of simulating responses under various conditions. Within the context of modeling nano-scale influence of solids, two predominant mathematical models, one known as the molecular or atomistic models and the other corresponding to the modified or enhanced continuum-based models, have been commonly employed in the literature. The molecular-based simulations have been verified to yield accurate prediction of responses of interest due to their effectiveness in detailing of bonds or atoms (e.g., Buehler *et al.* 2003, Zhang *et al.* 2005, Buehler and Gao 2006, Rafii-Tabar *et al.* 2006, Pugno *et al.* 2008, Huang *et al.* 2009, Masuda-Jindo *et al.* 2009, Phan and Tippur 2009, Adnan and Sun 2010), however, such simulations require enormous computational effort and resources to treat billions of atoms at a nano-scale. This therefore renders the discrete atomic-scale models impractical in various applications.

As a result, modified or enhanced continuum-based models have become an attractive alternative due to their advantages of saving computational resources. Unlike macro-structures, in the case of nano-sized objects (e.g., thin films, quantum dots, nano-wires, nano-tubes and nano-composites), the surface to volume ratio is much higher and, as a direct consequence, the surface free energy often plays a crucial role in the mechanical behavior (Yakobson 2003). Therefore, the classical theory of continuum-based mechanics commonly used in the modeling of macroscopic bodies cannot be directly applied to accurately treat the problem of nano-scale structures and nano-sized cracks. While a conventional theory of linear elasticity has been well established and employed in the modeling of linear elastic uncracked and cracked bodies, the enhancement of classical models to incorporate the nano-scale influence is essentially required.

Due to the rapid growth of interests and increasing applications of nano-technology, the investigation of mechanical behaviors and responses at a nano-scale level has gained significant

attention from many researchers and various sophisticated models have been proposed to study those phenomena. Problems of surface loadings and contacts, nano-indentations, nano-sized cracks are considered fundamental in nano-mechanics and have a wide range of applications including the investigation of mechanical properties such as hardness and elastic modulus. Work towards the modeling of near-surface fields under different surface loading conditions by using modified continuum-based models to characterize the surface energy effects has started gaining attention from several researchers in the past two decades since it offers computationally efficient techniques capable of reasonably predicting the behavior of materials at a nano-scale level. Similarly, nano-indentations have become a widely adopted technique to be used in the measurement of mechanical properties at the nano-scale. Unfortunately, the effect of surface elasticity during the indentation has been usually considered by experimental measurements and molecular dynamics/atomistic simulations which are generally very time-consuming and expensive. To minimize such limitations, modified continuum models accounted for the surface effects could be developed for nano-indentation problems, additionally, in order to clearly understand the nano-mechanical properties. It can be noted further that existing investigations using continuum-based theories to model defects/fractures at the nano-scale level have also been very limited. Most of them are restricted to situations where cracks can be treated either within the context of two-dimensional boundary value problems (e.g., Fu *et al.* 2008, Wang *et al.* 2008, Fang *et al.* 2009, Fu *et al.* 2010, Kim *et al.* 2010, Kim *et al.* 2011, Kim *et al.* 2011, Nan and Wang 2012, Kim *et al.* 2013, Nan and Wang 2013) or within the context of relatively simple three-dimensional problems (Intarit *et al.* 2012, Intarit 2013). However, bodies or components involved in practices are, in general, relatively complex in terms of geometries, loading conditions, and influences to be treated (e.g., surface free energy). Existing simplified mathematical models are therefore of limited capabilities and insufficient to be used in the prediction of responses in those practical cases. This, as a result, necessitates the development of a fully three-dimensional models supplemented by efficient and powerful numerical procedures.

1.2 Background and Review

In this section, an extensive literature survey including the existing work relevant to the current study and the sequence of historical background in this specific area is provided. In order to be systematic, results from such overview are separated into four parts regarding to their main focus. Firstly, the development of surface elasticity model is reviewed to observe how important of surface energy effects in the material characterization of nano-scale elements and soft elastic solids. Then, previous studies related to elastic media under surface loadings, indentation problems, and nano-sized cracks are summarized.

1.2.1 Surface elasticity models

Gibbs (1906), who originally formulated the most useful and powerful concepts in studying surface phenomena, defined the quantity γ to represent the excess free energy per unit area owing to the existence of a surface. Gibbs was the first who pointed out that, for solid-solid interfaces, there is another type of fundamental parameter called the surface stress that critically affects the behavior of surfaces, i.e. to elastically stretch a pre-existing surface. Simply saying that, to deform such a solid, excessive work is needed to stretch the surface in addition to straining the bulk. The larger partition of work done to surface, the more important the effect of surface stress (He and Lim, 2006). Comprehensive literature review on the surface energy effect and the Gibbsian formulation of the thermodynamics of surfaces can be found in general researches of

surface and interface stresses (Cammarata, 1994; Cammarata, 1997; Shuttleworth, 1950; Fischer et al., 2008). Especially, Cammarata (1994) gave an excellent explanation of the concept of the surface stress and also showed that the difference between the surface stress and the surface free energy γ is equal to the change in surface free energy per unit change in elastic strain of the surface. It should be noted that γ is a scalar quantity, while the surface stress is a second order tensor in the tangent plane of the surface and the strain normal to the surface is excluded.

A surface can be identified as a layer that an excess energy is attached and certain energy is usually termed as the surface energy γ (Fischer et al., 2008). Due to the different number of nearest neighbors between surface atoms and bulk atoms, it results in a corresponding redistribution of electronic charge and modifies layer spacing to be lesser at the surface, which deviates from the bulk value (Sander, 2003). As a result, the energy at a free surface will, in general, be different from that of the atoms in the bulk (Dingreville et al., 2005). The ratio of surface free energy γ (J/m^2) and Young's modulus E (J/m^3), γ/E, is an inevitable parameter of materials (Yakobson, 2003). For usual metallic materials, the ratio is normally less than one Angstrom. For some soft solids, such as polymer gels and biological materials, however, the surface energy (or surface stress) is a little less than that of a metal, but the elastic modulus can be nearly 7-8 orders smaller than that of conventional solids. Therefore, the corresponding intrinsic length scale of soft solids is much larger, implying that the surface energy can play an important role on the properties of the materials, and thus the properties become size-dependent (He and Lim, 2006). As a consequence, the effects of surface stress should be incorporated into classical continuum models in order to study the behavior of soft materials or to obtain the correct response for nanoscale problems.

Many authors have developed continuum models that include surface energy effects, and one of them is Gurtin-Murdoch model. Gurtin and Murdoch (1975, 1978), and Gurtin et al. (1998) proposed a mathematical framework to study the mechanical behavior of material surfaces through a continuum model with the surface stress. An elastic surface is assumed to be very thin and modeled as a mathematical layer of zero thickness bonded to the bulk without slipping. Also, the elastic moduli of the surface can be different from the bulk. For an isotropic elastic surface, a linearized surface stress-strain constitutive relation is given by

$$\sigma_{\beta\alpha}^{s} = \tau^{s}\delta_{\beta\alpha} + 2\left(\mu^{s} - \tau^{s}\right)\varepsilon_{\beta\alpha}^{s} + \left(\lambda^{s} + \tau^{s}\right)\varepsilon_{\gamma\gamma}^{s}\delta_{\beta\alpha} + \tau^{s}u_{\beta,\alpha}^{s} \tag{1.1}$$

where the subscript 's' denotes the quantities corresponding to the surface, μ^{s} and λ^{s} are surface Lamé constants and τ^{s} is the residual surface tension under unstrained conditions, which is a constant.

In order to verify Gurtin-Murdoch model, Miller and Shenoy (2000) employed such a model to describe the size dependence of the stiffness of plates, bars and beams under either uniaxial tension or bending. Their results were compared with direct atomistic simulations of nanoscale structures using the embedded atom method for face-centered cubic aluminum and the Stillinger–Weber model for silicon. By neglecting the error induced from the effects of corners present in the modeling of beams, excellent agreement between the simulations and the model is observed. Shenoy (2002) completed a framework derived earlier by Miller and Shenoy (2000) by adding the torsional rigidities of nanosized structural elements and applied to the case of nanoscale bars in torsion. The theoretical results were compared with direct atomistic simulations for the torsion of square bars of various metals and found in good agreement. It is noted that the difference in theoretical values and simulation results mainly came from the

assumption that the surface energy depends only on the surface strain; however, it should also depend on the surface curvature strain. Dingreville et al. (2005) derived analytical expressions for an elastic modulus tensor of nanosized structural elements accounted for surface energy effects and showed that the overall elastic properties of nanosized particles, wires and films are size-dependent. The effective Young's modulus of thin films of various thicknesses computed by using molecular static (MS) simulations and their proposed formulation are in excellent agreement. They also pointed out that results obtained from MS simulations were much more computationally intensive than the proposed formulation. This should confirm the benefit of employing such alternative continuum-based model to save the computational resources. Undoubtedly, Gurtin-Murdoch continuum model has been applied and widely used in nanoscale problems by several investigators, for example, to analyze the size dependent mechanical response of ultra-thin elastic films (He et al., 2004; Huang, 2008) and thin plates (Lu et al., 2006). Recently, such a model has been employed to study the problems of nanoscale inhomogeneities. For instance, Sharma and Wheeler (2007) and Sharma et al. (2003) reformulated the size dependent elastic field of spherical and ellipsoidal nano-inclusions by applying this model. Duan et al. (2005) presented the interior and exterior Eshelby tensors for a spherical inhomogeneity subjected to arbitrary uniform eigenstrain under the surface/interface effects. Tian and Rajapakse (2006, 2007) derived the solution for a nanoscale circular and elliptical inhomogeneity in an infinite matrix under remote loading based on the Gurtin-Murdoch model. Moreover, Zhao and Rajapakse (2009) presented the analytical solution of the plane and axisymmetric problems for an elastic layer of finite thickness subjected to surface loading by using Fourier and Hankel Transform techniques. Numerical results indicated that the surface effects show significant influence on the vertical surface displacement of a layer and such influence on the stress field in the case of horizontal point load is more significant than that in the case of vertical point load. Intarit et al. (2010) recently confirmed the significance of the surface stress on very near the surface of both shear and opening dislocations, and also on buried vertical and horizontal loads in an elastic half-plane. They also found that the stress field has an asymptotic solution with increasing the characteristic length parameter.

It is obviously seen from (1.1) that, to employ Gurtin-Murdoch continuum model, surface elastic properties (i.e. surface energy, surface stress, and surface elastic stiffness) must be known a priori. In addition, these particular quantities are also strongly influenced on the overall mechanical behavior in nanostructures. Thus, many approaches have been proposed, based either on experimental measurements or atomistic simulations, to determine such properties. Among various experimental techniques, Jing et al. (2006) measured the elastic properties of the nanowires by using contact atomic force microscopy (C-AFM) and found that the Young's modulus of the silver nanowire with consideration of the surface effect, surface modulus and surface stress are 56 GPa, 8.7 N/m, and 5.8 N/m respectively. Another method, rather computationally intensive, is atomistic simulations. Shenoy (2005) developed a fully nonlinear formulation of the surface elasticity and established a procedure for calculating surface elastic constants from atomistic simulations by adopting the embedded atom method. To reduce disadvantages of both experimental and atomistic approaches, Dingreville and Qu (2007) presented a semi-analytical method to compute a full set of data on surface elastic properties of crystalline materials. By applying this developed method, the surface elastic properties were formulated analytically and explicitly in terms of inter-atomic potentials, and a standard molecular simulation was used to obtain the relaxed positions of the atoms near the free surface in order to evaluate such analytical expressions.

1.2.2 Elastic layer under surface loadings

Problems of surface loadings and contacts are considered essential in nano-mechanics since they have a wide range of applications including the investigation of mechanical properties such as hardness and elastic modulus. Work towards the modeling of near-surface fields under different surface loading conditions by using enhanced continuum-based models to characterize the surface energy effects has started gaining attentions from various researchers in the past two decades since it offers computationally efficient techniques capable of reasonably predicting the behavior of materials at a nano-scale level.

For instance, Wang and Feng (2007) studied the responses of an elastic half-plane subjected to surface pressure by considering the influence of a constant residual surface tension but ignoring the surface elastic constants. Huang and Yu (2007) extended the work of Wang and Feng (2007) by incorporating the surface elastic constants. Recently, Zhao and Rajapakse (2009) studied the near-surface responses and size dependency of a two-dimensional and an axisymmetric three-dimensional infinite elastic layers under surface loads by using Fourier and Hankel integral transform techniques. It should be emphasized, however, that the Gurtin-Murdoch model used in their study was still incomplete since the out-of-plane contribution of the residual surface tension was ignored in their formulation. Intarit et al. (2010) studied the effect of surface stresses on the near-surface responses of semi-infinite dislocations and buried loads in an elastic half-plane. Again, the contribution of out-of-plane terms was still not considered. Most recently, Intarit et al. (2011) generalized the work of Intarit et al. (2010) by integrating the influence of the residual surface tension in addition to the surface elastic constants to model a two-dimensional elastic layer under buried loading conditions.

On the basis of an extensive literature survey, the study of near-surface responses of a three-dimensional elastic layer using a complete version of Gurtin-Murdoch model has not been well recognized. In particular, an analytical solution of a three-dimensional elastic layer subjected to arbitrary axisymmetric surface loads by incorporating both in-plane and out-of-plane contribution of surface stresses is still not available in the literature and is the main focus of the present study. Results from this fundamental problem should not only shed some light on the nano-scale influence but also be potentially useful in the investigation of more complex boundary value problems such as nano-indentations.

1.2.3 Nano-indentations

It is understood that indentation techniques have been widely used for measuring mechanical properties on nanoscale such as hardness and elastic modulus. For example, the use of nanoindentation to measure the mechanical properties of ceramics (Hainsworth and Page, 1994), metals (Armstrong et al., 1995; Beegan et al., 2007) and polymers (Yang and Li, 1995; Yang and Li, 1997). By using depth-sensing indentation tests with either spherical or conical indenters, Young's modulus can be calculated from the slope of the linear portion of the unloading curves in the load versus penetration depth while hardness can be calculated from data along the loading curves (Doerner and Nix, 1986; Oliver and Pharr, 1992).

Several authors have obtained the elastic solution of the indentation problems by using various mathematical methods. The classical problem of axisymmetric rigid punch indenting on an elastic half-space was first considered by Boussinesq (Boussinesq, 1885). According to the form of a solution, his numerical results were obtained only for a flat-ended cylindrical and a conical punch. Harding and Sneddon (1945) and Sneddon (1965) solved Boussinesq's problem

under a punch of arbitrary profile by applying Hankel integral transform techniques. Clements (1971) later determined the stress fields produced from the rigid indentation on an anisotropic half-space by employing the theory of anisotropic elasticity developed by Eshelby et al. (1953) and Stroh (1958). Since the smart materials have recently gained significant interest from several researchers in the field of mechanics, the classical theory of elasticity becomes an important tool in studying their behavior from indentation techniques. Chen (2000) generalized the potential theory to analyze the piezoelastic contact problem of a punch pressed against a piezoelectric half-space. Giannakopoulos and Parmaklis (2007) examined the quasistatic contact problem of a circular rigid punch on piezomagnetic materials and confirmed their theoretical results by conducting an experiment on Terfenol-D. In addition, an elastic behavior of a nonhomogeneous transversely isotropic half-space was studied by Chaudhuri and Ray (2003) under the action of a smooth rigid axisymmetric indenter.

The indentation problems associated with an elastic layer perfectly bonded to an elastic half-space were also investigated. Lebedev and Ufliand (1958) considered a problem of a flat-ended rigid cylindrical indenter on an elastic layer resting on a rigid foundation by using Papkovich-Neuber's representation for the displacement vector. After reducing mixed boundary conditions to a pair of integral equations, Fredholm integral equation was obtained and solved numerically. By taking the Hankel transform technique, Dhaliwal and Rau (1970) reduced the axisymmetric Boussinesq problem of an elastic layer lying over an elastic half-space under a rigid punch of arbitrary profile to a Fredholm integral equation but no numerical result was presented in their study. Subsequently, Rau and Dhaliwal (1972) developed a numerical technique to solve the integral equation proposed by Dhaliwal and Rau (1970) and obtained the complete elastic field. Yu et al. (1990) presented numerical results obtained from solving Fredholm integral equation of the second kind to demonstrate the effect of a substrate on the elastic properties of films and provided useful guidelines for the proper choice of an approximate layer thickness and substrate elastic properties to determine the elastic constants of the layer. Motivated by a recently developed multi-dimensional nanocontact system (Lucas et al., 2003), Gao et al. (2008) gave an analytical formulation by applying Green's function in Fourier space to predict the effective elastic modulus of film-on-substrate systems under normal and tangential contact. In addition, Yang (1998) studied the problem of impressing a rigid flat-ended cylindrical indenter onto an incompressible elastic film by following a standard procedure such that the Hankel transformation was applied to the mixed boundary conditions and the Fredholm integral equation of the second kind was subsequently solved numerically.

The surface stress effect on mechanical responses of nanoindentation was recently studied based on the Gurtin-Murdoch continuum model by several researchers. Zhao (2009) derived an analytical solution of a classical indentation problem in the presence of the surface energy effect. By applying Gurtin-Murdoch continuum model, he obtained a solution for elastic fields within the half-space caused by flat-ended cylindrical, conical and spherical rigid indenters. Although Gurtin-Murdoch continuum model used in his formulation is not complete (e.g. no out-of-plane term), obtained numerical solutions still showed a size-dependent behavior due to the presence of surface energy effect, i.e. when the contact area becomes smaller, the material behaves stiffer. In addition, it is remarked that atomistic simulations (Sinnott et al., 1997; Liu et al., 2007; Chen et al., 2008; Lu et al., 2009) can also be used to investigate the mechanism of an indentation process under different indenter shapes (i.e. spherical indenter and pyramidal indenter), sizes and indentation loads on the materials. In this approach, applied

molecular dynamics theory is employed to finally obtain the mechanical properties such as hardness and load-displacement curves.

As mentioned in the introduction and extensive review of existing works in this area, the influence of surface energy effects by using a complete set of Gurtin-Murdoch continuum model in order to capture the size-dependent behavior of nano-indention problems has not been investigated. This therefore requires profound exploration to further enhance the correct elastic fields accounted for surface effects.

1.2.4 Nano-sized cracks

Research focusing on the investigation of nano-sized defects and fractures has become of central interest in the past two decades. Basic approaches proposed in those investigations can be categorized into two groups, namely experimental methods and theoretical simulations. Some of previous studies in the first group can be briefly summarized as follows. Sumomogi *et al.* (2002) investigated both subsurface and surface cracks of single-crystal silicon by using a scanning force microscope (SFM) and a scanning laser microscope (SLM). Sundararajan and Bhushan (2002) evaluated the elastic modulus and bending strength, and estimated the fracture toughness of nanometer-scale fixed-end beam specimens made of single-crystal silicon and SiO_2 by using a quasi-static bending test technique, which was developed by using an atomic force microscope. Karimi *et al.* (2002) combined a depth sensing nano-indentation and a nano-scratch testing along with the atomic force microscopy and electron microscopy observations to study mechanical properties and fracture behavior of a number of TiAlN(Si, C) hard thin films. Chen *et al.* (2008) carried out an experiment of the composite to examine the local mechanical and fracture behavior of an EPON 862 based-epoxy with 12 nm (primary) and 100 nm (secondary) fumed silica particles by using the atomic force microscopy/digital image correlation (AFM/DIC) method. Peng *et al.* (2008) conducted an experiment by using an in-situ transmission electron microscopy (TEM) method. They employed a MEMS material testing system that allows accurate measurement of both load and displacement along with the TEM imaging to measure a single shell failure for multiwalled carbon nano-tubes that display the fracture strengths of about 100 GPa and also showed that fracture strains are very close to theoretical predictions. Zhao and Xing (2008, 2010) experimentally investigated a micro-crack in silicon by using high-resolution transmission electron microscopy (HRTEM) and a combination of geometric phase analysis (GPA), the numerical moiré method (NM) and the transmission electron microscopy (TEM). Qin *et al.* (2009) quantitatively investigated the effect of the density of nano-scale twin bundles on the tensile strength and fracture toughness. In their study, the fracture surface characteristics were elucidated by using scanning electron microscopy (SEM) and focused ion beam (FIB) microscopy analysis. The fracture toughness was measured by a conventional three-point bending test based on ASTM-E399. Most recently, Yan *et al.* (2011) experimentally investigated crack initiation and propagation along the Cu/Si interface in multilayered films (Si/Cu/SiN) with different thicknesses of the Cu layer (20 and 200 nm) by using a nano-cantilever and millimeter-sized four-point bending specimens. Those experiments demonstrated that the elastic modulus, bending strength, and fracture toughness were size-dependent at the nano-scale. Values of mechanical properties had a tendency to be higher when compared to those obtained from experiments of macro-scale structures. The experimental approaches offer results reflecting the actual responses or behaviors, they are, however, highly dependent on experimental settings and, generally, expensive due to the requirement of high precision testing devices and procedures.

Another alternative is based on the mathematical modeling and simulations. In this group, a set of governing physics and assumptions is chosen to construct a set of mathematical equations governing representative quantities of interest and a solution methodology is developed to obtain such representative solutions for describing the real behavior. The discrepancy between the real responses and the representative solutions depends primarily on the choice of governing physics and assumptions, and the accuracy of the solution strategy. Based on an extensive literature review, most of existing studies employed two different types of mathematical models, one employing discrete-based models whereas the other utilizing modified continuum-based models.

Within the context of modeling nano-sized cracks, several studies based on the discrete atomic-scale model have been recognized. For instance, Buehler *et al.* (2003), Zhang *et al.* (2005), Buehler and Gao (2006), Rafii-Tabar *et al.* (2006), Huang *et al.* (2009), Masuda-Jindo *et al.* (2009), Adnan and Sun (2010) and Sakib and Adnan (2012) investigated the crack by using molecular dynamics (MD) atomistic simulations. Phan and Tippur (2009) presented a numerical method to evaluate the quantized fracture mechanics (QFM) stress intensity factors (SIFs). Pugno *et al.* (2008) combined quantized fracture mechanics and molecular dynamics atomistic simulations to study atomistic fractures. While those proposed models have been verified to yield accurate prediction of responses of interest due to their effectiveness in detailing of bonds or atoms, such simulations require enormous computational effort and resources to treat billions of atoms at a nano-scale. This therefore renders the discrete atomic-scale models impractical in various applications.

Consequently, a group of approaches based upon continuum-based theories is considered attractive since it can substantially reduce both the computational cost and complexity of the governing physics. Work towards applying the surface elasticity model to simulate the nano-scale influence of nano-sized fracture problems has become a subject of numerous investigations. Based upon the investigation of an elliptical void, Wu (1999) argued that presence of the surface stresses can effectively reduce an applied stress-intensity factor to a lower effective stress-intensity factor. Wu and Wang (2000), (2001) proposed the method using a pair of point forces, one at each crack tip, a uniformly distributed compressive load on the convex side of the crack, and a uniformly distributed tensile load on the concave side to study the influence of surface stress on two-dimensional crack problems and pointed out that the singularity of the crack-tip stress fields becomes $1/r$ instead of being $1/\sqrt{r}$. Wang *et al.* (2007) explored the dependent relationship of crack-tip stresses on surface elastic parameters for both mode-I (opening mode) and mode-III (tearing mode) cracks based on the Gurtin Murdoch surface elasticity theory along with a local asymptotic approach. They found in their study, that the stress intensities in the vicinity of the crack tip are significantly affected by the surface energy when the curvature radius of a blunt crack front decreases to nanometers. Fu *et al.* (2008), (2010) incorporated the effect of surface elasticity into the finite element analysis (via ANSYS® and ABAQUS®) to study the influence of surface stresses on the mode-I (opening mode) and mode-II (sliding mode) crack tip fields. They found that when the curvature radius of the crack root decreases to micro-/nano-meters, the surface elasticity exhibits significant influence on stresses near the crack tip. Fang *et al.* (2009) investigated the influence of surface stresses on the dislocation emission from an elliptically blunt crack under mode-I and mode-II loading conditions and reported that the impact of the surface stresses on the critical stress intensity factors for dislocation emission becomes remarkable when the size of the blunted crack is very

small, typically of a nanometer scale. However, their results for stresses are valid only in the vicinity ahead the crack-tip of the blunt crack.

Use of a sharp crack-tip model has also been commonly employed in the modeling of nano-sized cracks. The fundamental problem of mode-I crack was elaborated by Oh *et al.* (2005) based upon an extension of continuum mechanics by incorporating effects of the nano-scale through the long-range intermolecular force obtained from atomistic simulations. They concluded that the fracture tip should be sharp rather than blunt and, unlike the classical case, there is no stress singularity at the fracture tip when considered at a nano-scale level. It is also important to remark that the surface energy is generally nonzero and a function of position on the fracture surface. Sendova and Walton (2010) examined mode-I crack in an infinite elastic medium using various models of surface energy effects (e.g., a model of constant surface tension and a model of curvature dependent surface tension). In their study, they proposed that the stress singularity at the crack tip was reduced to the logarithmic singularity in the case of the constant surface tension, whereas the finite stress at the crack tip was observed for the case of the curvature dependent surface tension. Kim *et al.* (2010) first examined a mode-III crack problem (i.e., anti-plane shear deformations of a linearly elastic solid) subjected to non-uniform surface tractions. Later, Kim *et al.* (2011) studied the plane deformations of a linearly elastic solid containing a crack under either mode-I or mode-II loading conditions. Kim *et al.* (2011) considered the contribution of the surface elasticity to the anti-plane deformations of a linearly elastic bi-material containing mode-III interface crack. For the above three studies, the continuum-based surface/interface model of Gurtin and Murdoch was employed in the formulation of the boundary value problem, and the complex variable techniques were applied in the solution procedure. They pointed out that the surface stresses result in elastic responses and corresponding stress fields being size-dependent and also argued that, in contrast to classical results from linear elastic fracture mechanics, their model yielded the finite stresses at the sharp crack-tips. Recently, Kim *et al.* (2013) examined the role of surface stresses on the singularity behavior of near-tip stress field. They showed that the necessary and sufficient conditions for bounded stresses at the crack tip cannot be satisfied with the first-order (curvature-independent) theory of surface effects, which leads, at most, to the reduction of the classical strong square-root singularity to the weaker logarithmic singularity. This finding agrees with the previous study of Sendova and Walton (2010) in the case of the constant surface tension. Nan and Wang (2012) considered the effect of the residual surface stress on the crack surface and obtained solutions of the crack opening displacement (COD) and the mode-I stress intensity factor (K_I). Their obtained results demonstrated that the influence of the surface stresses on the crack deformation and crack-tip field is prominent at the nano-scale. Moreover, the COD and K_I are influenced by the residual surface stress not only on the surface near the crack-tip region but also on the entire crack-face. Most recently, Nan and Wang (2013) investigated a problem of a nano-scale crack in piezoelectric nano-materials by considering the effect of the residual surface stress on the crack surface. They pointed out that the electromechanical coupling fracture behavior of the piezoelectric materials is influenced by the residual surface stress on the entire crack surface.

On the basis of an extensive literature survey, it can be said that work related to the modeling of defects/cracks at nano-scale level has been very limited. For most existing studies related to the analysis of nano-sized fractures, the corresponding boundary value problems were formulated within the context of two-dimensional settings, and most of them were solved by using analytical techniques such as complex variable techniques, complex potential method and Chebyshev polynomials technique. Due to limitations of both inherent simplified assumptions

and solution techniques, complex but more practical loading conditions and fracture geometries cannot readily be treated in those existing works. Recently, Intarit *et al.* (2012) and Intarit (2013) analytically investigated a nano-sized crack in a three-dimensional elastic media under a mode-I loading conditions. Although a complete Gurtin-Murdoch surface elasticity model was employed to model the effect of surface stresses, it was still limited to a crack of circular shape and axisymmetric loading conditions. However, bodies or components containing existing defects/flaws involved in practical applications are, in general, relatively complex in terms of geometries, loading conditions, and influences to be treated (e.g., surface free energy). The existing mathematical models are therefore of limited scope and insufficient for the prediction of responses in practical cases. This, as a result, necessitates the development of fully three-dimensional models, supplemented by efficient and powerful numerical procedures. This current gap of knowledge is to be fully investigated in the present study.

1.3 Objectives

The key objectives of the current investigation are

(1) to establish physically suitable, mathematical models for fundamental problems in solid mechanics with consideration of the nano-scale influence, and
(2) to develop analytical procedures for investigating various *basic* boundary value problems that are fundamental in the area of solid mechanics, and
(3) to establish the framework of powerful numerical procedures capable of solving a broader class of boundary value problems that are relatively complex and often encountered in engineering and industrial applications, and
(4) to fully investigate the size-dependent behavior and nano-scale influence on various fundamental problems in solid mechanics and also compare results from continuum-based simulations with existing molecular dynamics simulations and experimental measurements.

1.4 Scope of Work

Scope of the present study and assumptions relevant to the development are summarized as follows:

(1) the boundary value problem considered in this investigation is *linear* and governed by the theory of local linear elasticity;
(2) a body associated with the boundary value problem is three-dimensional with applications to infinite media, half-spaces, and thin layers;
(3) a body is assumed to be free of a body force;
(4) the influence of nano-scale in the local region near the boundary is modeled by properly incorporating the surface elasticity model (proposed by Gurtin and Murdoch (1975)) into classical continuum theory for solid mechanics;
(5) analytical and semi-analytical solutions are constructed for boundary value problems involving simple geometry, loading conditions and boundary conditions (e.g., surface axisymmetric loadings in half-space, surface axisymmetric loadings on elastic thin layer, and indentation problems with axisymmetric profiles, etc.); and
(6) a framework of numerical techniques (e.g., FEM, SGBEM, Coupling of FEM and SGBEM) capable of solving relatively complex boundary value problems induced by the presence of surface elasticity, embedded singularity such as cracks and

dislocations, complicated geometries, loadings and boundary conditions is developed. In-house computer codes using FORTRAN 90 are implemented to demonstrate accuracy and capabilities of the proposed technique.

1.5 Methodology

The present study consists of several main tasks with methodology, procedures, and involved fundamental theories for each task briefly summarized below.

(1) Extensive literature survey is first conducted in related fields such as surface elasticity, modeling of size-dependent behavior, and nano-scale influence in various fundamental problems (such as cracks, surface loadings, indentations, etc.). Next, the fundamental theories in linear elasticity and surface elasticity crucial for the current development along with the relevant solution techniques such as the Hankel integral transform, potential-theory-based methods, finite element methods, and boundary integral equation methods are reviewed. Finally, the scope of work and the problem statement is clearly defined.

(2) A domain decomposition technique is utilized to decompose the domain into two parts: a bulk material and a surface with zero thickness perfectly bonded to the bulk. The behavior of the surface is modeled by Gurtin-Murdoch surface elasticity model whereas that of the bulk material is governed by a classical theory of linear elasticity.

(3) For an elastic layer under axisymmetric loadings, the governing equation for the bulk material is expressed in terms of Love's strain potential whereas the governing equation of the surface is derived directly from the Gurtin-Murdoch surface elasticity model. A general solution for the bulk is derived by using Hankel integral transform and its inversions, and its final form is given in terms of arbitrary functions. The boundary conditions at the top and bottom surfaces of the bulk are enforced along with applying Hankel integral transform to determine all arbitrary functions. The elastic fields (i.e., displacement and stress fields) are expressed in terms of the Hankel integral inversion. An efficient numerical integration scheme is adopted to evaluate all involved integrals. Results of elastic fields for general axisymmetric loading conditions are then specialized to obtain results for the half-space and to construct fundamental solutions of a layer under special surface loading cases.

(4) For axisymmetric indentation problem, a corresponding mixed boundary value problem is formulated and reduced to a set of dual integral equations by using Hankel integral transform. Such dual integral equations are further reduced to a Fredholm integral equation of the second kind by using a procedure based on Sonine's integrals. Selected numerical techniques are adopted to solve the resulting Fredholm integral equation of the second kind. Once the solution of such governing equation is obtained, Hankel transform inversions are then employed to determine elastic fields and other interesting quantities such as contact pressure, indentation force, stresses, and displacements.

(5) For nano-sized crack problem, the governing equations of the bulk part are established in terms of weakly singular boundary integral equations following the work of Rungamornrat and Mear (2008a) whereas those for the surface is established in a form of weak statement using standard weight residual approach. The weak-form equation of the surface part is discretized into a set of linear algebraic equations using standard finite element procedure and a set of weakly singular integral equations are

discretized into a set of linear algebraic equations using weakly singular SGBEM similar to that employed by Rungamornrat and Mear (2008b). Continuity conditions between the surface part and the bulk material are utilized to obtain a fully coupled system of linear algebraic equations and it is then solved by a selected linear solver. All field quantities within the bulk material can be obtained from a set of boundary integral relations proposed by Rungamornrat and Mear (2008a). Extensive numerical experiments are conducted and results are compared with available benchmark solutions to validate the proposed numerical technique.

(6) Developed analytical and numerical techniques are employed to fully investigate the size-dependent behavior and nano-scale influence for various fundamental problems in solid mechanics such as nano-indentations, surface loadings on elastic half-space and thin layers, and nano-sized cracks.

1.6 Contribution

The present study offers a complete analytical solution of a three-dimensional, infinite elastic layer under the action of axisymmetric normal and tangential surface loading by taking surface energy effects into account. The integration of surface elasticity in the mathematical model provides an alternative, computationally cheap, continuum-based approach for investigating the influence of nano-scale on various responses of interest. As a result of using a *complete* Gurtin Murdoch constitutive relation for modeling the surface energy effects, proposed formulation can demonstrate the influence of the out-of-plane term resulting from residual surface tension on material stiffness. Furthermore, the solution of elastic fields are also specialized to construct fundamental solutions of a layer under a unit normal concentrated force, a unit normal ring force, and a unit tangential ring force. Such basic results constitute the essential basis for the development of boundary integral equations governing other related problems, e.g. nano-indentations.

The current investigation proposes an application of continuum-based concepts in the analysis of indentation problems for nano-scale structures and soft elastic solids by incorporating surface energy effects into a classical continuum model. With use of complete Gurtin-Murdoch surface elasticity model, proposed formulation is applicable to perform the existence of an inevitable parameter of materials via size-dependent behavior and also to strongly demonstrate the influence of out-of-plane contribution of residual surface tension on material stiffness. When compared to molecular dynamics simulations, this modified continuum model is an alternative in terms of dramatically reduction in computational resources with an acceptable level of accuracy. Such attractive approach offers an alternative for studying the mechanical properties and mechanical deformation for indenters of arbitrary axisymmetric profiles. This fundamental development can have a direct impact on nano-indentation applications since the indentation techniques have been widely used for measuring mechanical properties in the nano-scale such as hardness and elastic modulus (e.g., Hainsworth and Page, 1994; Armstrong et al., 1995; Beegan et al., 2007; Yang and Li, 1995; Yang and Li, 1997). By using depth-sensing indentation tests with either spherical or conical indenters, Young's modulus can be calculated from the slope of the linear portion of the unloading curves in the load versus penetration depth while hardness can be calculated from data along the loading curves (Doerner and Nix, 1986; Oliver and Pharr, 1992).

The developed numerical technique should enhance and strengthen the capability in the modeling of nano-sized crack problems using an alternative, computationally cheap continuum-

based model along with the proper treatment of surface stress effects via Gurtin-Murdoch surface elasticity model. The developed mathematical model and the implemented numerical procedure allow more practical planar nano-sized fracture problems to be investigated, e.g. cracks of arbitrary shapes under general loading conditions. Availability of a computational tool of such high capability should be very significant in the parametric study to investigate and gain an insight into various crucial responses of interest in the nano-scale level such as the size-dependent behavior of an elastic field and all other related quantities.

CHAPTER II

ELASTIC LAYER UNDER SURFACE LOADING

In this chapter, the complete solution of an axisymmetric problem for an infinite, rigid-based elastic layer under the action of surface loads and the surface energy effects is presented. The corresponding boundary value problem is formulated based on a classical theory of linear elasticity for the bulk and a complete Gurtin-Murdoch constitutive relation for modeling the surface energy effects. Love's strain potential technique and Hankel integral transform are adopted to obtain the general solution for the bulk whereas the surface equations and conditions at the rigid based supply sufficient boundary conditions to determine all arbitrary constants. A selected numerical technique for efficiently and accurately evaluating all involved integrals is then outlined. After the technique is verified with available benchmark solutions, extensive studies for both cases of axisymmetric normal and axisymmetric tangential surface loads are investigated to understand the nano-scale influence through the surface stress effects (with/without the contribution of residual surface tension) and size dependent behaviors. Moreover, numerical results of a layer under a unit normal point load, a unit normal ring load and a unit tangential ring load, which are benefit for solving nano-indentations problem, are also demonstrated and fully discussed.

2.1 Formulation

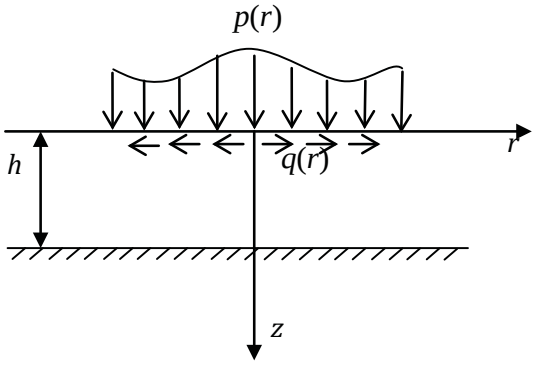

Figure 2.1 A three-dimensional, infinite, rigid-based, elastic layer subjected to axisymmetric surface loading

Consider a three-dimensional, infinite, rigid-based elastic layer of thickness h under the action of arbitrary axisymmetric surface loads as shown schematically in Figure 2.1. The reference cylindrical coordinate system is chosen such that the origin is located at the free surface and the positive z-axis directs downward whereas other axes follow the right-hand rule. The normal surface load and the tangential surface load are denoted by $p = p(r)$ and $q = q(r)$, respectively. In the modeling, the entire domain is treated as a body consisting of two different parts, the bulk which is homogeneous and isotropic and occupies a region defined by $0 < z \leq h$, and the zero-

thickness layer, which occupies the plane z = 0 and is perfectly bonded to the bulk. In the present study, the medium is assumed to be free of the body force and remote loadings. The primary objective is to determine the complete responses (e.g. the displacement and stress fields) within the bulk due to the arbitrary (axisymmetric) applied surface loads and the presence of the surface energy effects.

2.1.1 Basic field equations

For the bulk, the governing field equations follow directly the classical theory of linear isotropic elasticity (e.g. Barber, 1992; Timoshenko et al., 1951). In the absence of body forces and under axisymmetric deformation, the equilibrium equations, constitutive laws and strain-displacement relations expressed in terms of cylindrical coordinates are given by

$$\frac{\partial \sigma_{rr}}{\partial r}+\frac{\partial \sigma_{rz}}{\partial z}+\frac{\sigma_{rr}-\sigma_{\theta\theta}}{r}=0 \tag{2.1a}$$

$$\frac{\partial \sigma_{rz}}{\partial r}+\frac{\partial \sigma_{zz}}{\partial z}+\frac{\sigma_{rz}}{r}=0 \tag{2.1b}$$

$$\sigma_{rr}=(\lambda+2\mu)\varepsilon_{rr}+\lambda\varepsilon_{\theta\theta}+\lambda\varepsilon_{zz} \tag{2.2a}$$

$$\sigma_{\theta\theta}=\lambda\varepsilon_{rr}+(\lambda+2\mu)\varepsilon_{\theta\theta}+\lambda\varepsilon_{zz} \tag{2.2b}$$

$$\sigma_{zz}=\lambda\varepsilon_{rr}+\lambda\varepsilon_{\theta\theta}+(\lambda+2\mu)\varepsilon_{zz} \tag{2.2c}$$

$$\sigma_{rz}=2\mu\varepsilon_{rz} \tag{2.2d}$$

$$\varepsilon_{rr}=\frac{\partial u_r}{\partial r} \tag{2.3a}$$

$$\varepsilon_{\theta\theta}=\frac{u_r}{r} \tag{2.3b}$$

$$\varepsilon_{zz}=\frac{\partial u_z}{\partial z} \tag{2.3c}$$

$$\varepsilon_{rz}=\varepsilon_{zr}=\frac{1}{2}\left(\frac{\partial u_r}{\partial z}+\frac{\partial u_z}{\partial r}\right) \tag{2.3d}$$

where $\{\sigma_{rr},\sigma_{\theta\theta},\sigma_{zz},\sigma_{rz}\}$ are non-zero stress components; $\{\varepsilon_{rr},\varepsilon_{\theta\theta},\varepsilon_{zz},\varepsilon_{rz}\}$ are non-zero strain components; $\{u_r,u_z\}$ are non-zero displacement components; and μ and λ are Lamé constants of the bulk material.

For the surface, the equilibrium conditions on the surface in terms of the generalized Young-Laplace equation (Povestenko, 1993), a complete Gurtin-Murdoch constitutive relation (Gurtin-Murdoch 1975, 1978) and strain displacement relation are given, for the case of axisymmetry and flat surface, by

$$\frac{d\sigma_{rr}^{s}}{dr}+\frac{\sigma_{rr}^{s}-\sigma_{\theta\theta}^{s}}{r}+\sigma_{rz}\big|_{z=0}+q(r)=0 \tag{2.4a}$$

$$\frac{d\sigma_{rz}^{s}}{dr}+\frac{\sigma_{rz}^{s}}{r}+\sigma_{zz}\big|_{z=0}+p(r)=0 \tag{2.4b}$$

$$\sigma_{rr}^{s} = \tau^{s} + (2\mu^{s} + \lambda^{s})\varepsilon_{rr}^{s} + (\lambda^{s} + \tau^{s})\varepsilon_{\theta\theta}^{s} \tag{2.5a}$$

$$\sigma_{\theta\theta}^{s} = \tau^{s} + (2\mu^{s} + \lambda^{s})\varepsilon_{\theta\theta}^{s} + (\lambda^{s} + \tau^{s})\varepsilon_{rr}^{s} \tag{2.5b}$$

$$\sigma_{rz}^{s} = \tau^{s} \frac{du_{z}^{s}}{dr} \tag{2.5c}$$

$$\varepsilon_{rr}^{s} = \frac{du_{r}^{s}}{dr} \tag{2.6}$$

$$\varepsilon_{\theta\theta}^{s} = \frac{u_{r}^{s}}{r} \tag{2.7}$$

where the superscript 's' is used to denote the quantities corresponding to the surface; μ^{s} and λ^{s} are surface Lamé constants; and τ^{s} is the residual surface tension under unstrained conditions. By combining equations (2.4)-(2.7), it leads to two governing field equations for the surface in terms of the surface displacement as follows:

$$\frac{d\bar{\tau}^{s}}{d\bar{r}}\left(1+\frac{\bar{u}_{r}^{s}}{\bar{r}}\right)+\frac{2(\bar{\lambda}+1)}{\bar{\lambda}+2}\alpha\left(\frac{d^{2}\bar{u}_{r}^{s}}{d\bar{r}^{2}}+\frac{1}{\bar{r}}\frac{d\bar{u}_{r}^{s}}{d\bar{r}}-\frac{\bar{u}_{r}^{s}}{\bar{r}^{2}}\right)+2(\bar{\lambda}+1)\bar{\sigma}_{rz}\Big|_{\bar{z}=0}+\bar{q}(\bar{r})=0 \tag{2.8}$$

$$\frac{d}{d\bar{r}}\left(\bar{\tau}^{s}\frac{d\bar{u}_{z}^{s}}{d\bar{r}}\right)+\frac{\bar{\tau}^{s}}{\bar{r}}\frac{d\bar{u}_{z}^{s}}{d\bar{r}}+2(\bar{\lambda}+1)\bar{\sigma}_{zz}\Big|_{z=0}+\bar{p}(\bar{r})=0 \tag{2.9}$$

where various normalized quantities appearing in (2.8) and (2.9) are defined by $\bar{\tau}^{s} = \tau^{s}/\mu\Lambda$, $\bar{u}_{r}^{s} = u_{r}^{s}/\Lambda$, $\bar{u}_{z}^{s} = u_{z}^{s}/\Lambda$, $\bar{t}_{r}^{s} = t_{r}^{s}/2(\lambda+\mu)$, $\bar{t}_{z}^{s} = t_{z}^{s}/2(\lambda+\mu)$, $\bar{\lambda} = \lambda/\mu$, $\bar{r} = r/\Lambda$, $\bar{z} = z/\Lambda$, $\bar{q}(\bar{r}) = q(r)/\mu$, $\bar{p}(\bar{r}) = p(r)/\mu$, $\Lambda = \kappa^{S}(\lambda+2\mu)/2\mu(\lambda+\mu)$, and $\kappa^{S} = 2\mu_{S} + \lambda_{S}$.

2.1.2 General solution for bulk

A general solution for the normalized displacement and normalized stress of a set of governing equations (2.1)-(2.3) can readily be obtained in terms of Love's strain potential Φ as follows (e.g., Sneddon, 1951; Selvadurai, 2000):

$$\bar{u}_{r} = -(\bar{\lambda}+1)\frac{\partial^{2}\Phi}{\partial\bar{r}\partial\bar{z}} \tag{2.10a}$$

$$\bar{u}_{z} = (\bar{\lambda}+2)\nabla^{2}\Phi - (\bar{\lambda}+1)\frac{\partial^{2}\Phi}{\partial\bar{z}^{2}} \tag{2.10b}$$

$$\bar{\sigma}_{rr} = \frac{\bar{\lambda}}{2(\bar{\lambda}+1)}\nabla^{2}\left(\frac{\partial\Phi}{\partial\bar{z}}\right) - \frac{\partial^{3}\Phi}{\partial\bar{r}^{2}\partial\bar{z}} \tag{2.10c}$$

$$\bar{\sigma}_{\theta\theta} = \frac{\bar{\lambda}}{2\left(\bar{\lambda}+1\right)}\nabla^{2}\left(\frac{\partial\Phi}{\partial\bar{z}}\right) - \frac{1}{\bar{r}}\frac{\partial^{2}\Phi}{\partial\bar{r}\partial\bar{z}} \tag{2.10d}$$

$$\bar{\sigma}_{zz} = \frac{(3\bar{\lambda}+4)}{2\left(\bar{\lambda}+1\right)}\nabla^{2}\left(\frac{\partial\Phi}{\partial\bar{z}}\right) - \frac{\partial^{3}\Phi}{\partial^{3}\bar{z}} \tag{2.10e}$$

$$\bar{\sigma}_{rz} = \frac{(\bar{\lambda}+2)}{2\left(\bar{\lambda}+1\right)}\frac{\partial}{\partial \bar{r}}(\nabla^2\Phi) - \frac{\partial^3\Phi}{\partial^2 \bar{z}\,\partial \bar{r}} \tag{2.10f}$$

where $\nabla^2 = \frac{\partial^2}{\partial \bar{r}^2} + \frac{1}{\bar{r}}\frac{\partial}{\partial \bar{r}} + \frac{\partial^2}{\partial \bar{z}^2}$ is the axisymmetric Laplace's operator, $\bar{u}_r = u_r / \Lambda$, $\bar{u}_z = u_z / \Lambda$, $\bar{\sigma}_{rr} = \sigma_{rr} / 2(\lambda+\mu)$, and $\bar{\sigma}_{\theta\theta} = \sigma_{\theta\theta} / 2(\lambda+\mu)$. For the above field to be an elastic state, the Love's strain potential Φ must be bi-harmonic or, equivalently, satisfy the following equation

$$\nabla^4\Phi = 0 \tag{2.11}$$

where $\nabla^4 = \nabla^2 \cdot \nabla^2$. Applying Hankel integral transform to the above equation yields

$$\left(\frac{d^2}{d\bar{z}^2} - \bar{\xi}^2\right)^2 G(\bar{\xi}, \bar{z}) = 0 \tag{2.12}$$

where

$$G(\bar{\xi}, \bar{z}) = \int_0^\infty \Phi(\bar{r}, \bar{z}) J_0(\bar{\xi}\bar{r})\bar{r}\,d\bar{r} \tag{2.13}$$

with $J_n(\bar{\xi})$ denoting the Bessel function of the first kind of order *n*. A general solution of the homogeneous ordinary differential equation (2.12) is given by

$$G(\bar{\xi}, \bar{z}) = (A + B\bar{z})e^{-\bar{\xi}\bar{z}} + (C + D\bar{z})e^{\bar{\xi}\bar{z}} \tag{2.14}$$

where *A*, *B*, *C*, and *D* are arbitrary functions of $\bar{\xi}$, and can be determined from boundary conditions. By employing Hankel integral transform inversion, equations (2.10a)-(2.10f) can be written as

$$\bar{u}_r = (\bar{\lambda}+1)\int_0^\infty \bar{\xi}^2 \frac{dG}{d\bar{z}} J_1(\bar{\xi}\bar{r})\,d\bar{\xi} \tag{2.15a}$$

$$\bar{u}_z = \int_0^\infty \bar{\xi}\left[\frac{d^2G}{d\bar{z}^2} - (\bar{\lambda}+2)\bar{\xi}^2 G\right] J_0(\bar{\xi}\bar{r})\,d\bar{\xi} \tag{2.15b}$$

$$\bar{\sigma}_{rr} = \left(\int_0^\infty \bar{\xi}\left[\frac{\bar{\lambda}+2}{2(\bar{\lambda}+1)}\bar{\xi}^2\frac{dG}{\partial \bar{z}} + \frac{\bar{\lambda}}{2(\bar{\lambda}+1)}\frac{d^3G}{d\bar{z}^3}\right] J_0(\bar{\xi}\bar{r})\,d\bar{\xi}\right) - \frac{1}{\bar{r}}\int_0^\infty \bar{\xi}^2\frac{dG}{d\bar{z}} J_1(\bar{\xi}\bar{r})\,d\bar{\xi} \tag{2.15c}$$

$$\bar{\sigma}_{\theta\theta} = \frac{\bar{\lambda}}{2\left(\bar{\lambda}+1\right)}\int_0^\infty \bar{\xi}\left[\frac{d^3G}{d\bar{z}^3} - \bar{\xi}^2\frac{dG}{d\bar{z}}\right] J_0(\bar{\xi}\bar{r})\,d\bar{\xi} + \frac{1}{\bar{r}}\int_0^\infty \bar{\xi}^2\frac{dG}{d\bar{z}} J_1(\bar{\xi}\bar{r})\,d\bar{\xi} \tag{2.15d}$$

$$\bar{\sigma}_{zz} = \int_0^{\infty} \bar{\xi} \left[\frac{\left(\bar{\lambda}+2\right)}{2\left(\bar{\lambda}+1\right)} \frac{d^3 G}{d\bar{z}^3} - \frac{(3\bar{\lambda}+4)}{2\left(\bar{\lambda}+1\right)} \bar{\xi}^2 \frac{dG}{d\bar{z}} \right] J_0(\bar{\xi}\bar{r}) d\bar{\xi} \tag{2.15e}$$

$$\bar{\sigma}_{rz} = \int_0^{\infty} \bar{\xi}^2 \left[\frac{\bar{\lambda}}{2\left(\bar{\lambda}+1\right)} \frac{d^2 G}{d\bar{z}^2} + \frac{(\bar{\lambda}+2)}{2\left(\bar{\lambda}+1\right)} \bar{\xi}^2 G(\bar{\xi}, \bar{z}) \right] J_1(\bar{\xi}\bar{r}) d\bar{\xi} \tag{2.15f}$$

Finally, by inserting the general solution for the function G given by (2.14), the displacement and stress fields can finally be expressed in terms of the four arbitrary functions A, B, C, and D as

$$\bar{u}_r = (\bar{\lambda}+1) \int_0^{\infty} \bar{\xi}^2 \left\{ \left[-A\bar{\xi} + B(1-\bar{\xi}\bar{z}) \right] e^{-\bar{\xi}\bar{z}} + \left[C\bar{\xi} + D(1+\bar{\xi}\bar{z}) \right] e^{\bar{\xi}\bar{z}} \right\} J_1(\bar{\xi}\bar{r}) d\bar{\xi} \tag{2.16a}$$

$$\bar{u}_z = -(\bar{\lambda}+1) \int_0^{\infty} \bar{\xi}^2 \left\{ \left[A\bar{\xi} + B\left(\frac{2}{(\bar{\lambda}+1)} + \bar{\xi}\bar{z}\right) \right] e^{-\bar{\xi}\bar{z}} + \left[C\bar{\xi} - D\left(\frac{2}{(\bar{\lambda}+1)} - \bar{\xi}\bar{z}\right) \right] e^{\bar{\xi}\bar{z}} \right\} J_0(\bar{\xi}\bar{r}) d\bar{\xi} \tag{2.16b}$$

$$\begin{aligned} \bar{\sigma}_{rr} = & \int_0^{\infty} \bar{\xi}^3 \left\{ \left[-A\bar{\xi} + B\left(\frac{2\bar{\lambda}+1}{\bar{\lambda}+1} - \bar{\xi}\bar{z} \right) \right] e^{-\bar{\xi}\bar{z}} + \left[C\bar{\xi} + D\left(\frac{2\bar{\lambda}+1}{\bar{\lambda}+1} + \bar{\xi}\bar{z} \right) \right] e^{\bar{\xi}\bar{z}} \right\} J_0(\bar{\xi}\bar{r}) d\bar{\xi} \\ & - \frac{1}{\bar{r}} \int_0^{\infty} \bar{\xi}^2 \left(\left[-A\bar{\xi} + B(1-\bar{\xi}\bar{z}) \right] e^{-\bar{\xi}\bar{z}} + \left[C\bar{\xi} + D(1+\bar{\xi}\bar{z}) \right] e^{\bar{\xi}\bar{z}} \right) J_1(\bar{\xi}\bar{r}) d\bar{\xi} \end{aligned} \tag{2.16c}$$

$$\begin{aligned} \bar{\sigma}_{\theta\theta} = & \frac{\bar{\lambda}}{\bar{\lambda}+1} \int_0^{\infty} \bar{\xi}^3 \left\{ B e^{-\bar{\xi}\bar{z}} + D e^{\bar{\xi}\bar{z}} \right\} J_0(\bar{\xi}\bar{r}) d\bar{\xi} \\ & + \frac{1}{\bar{r}} \int_0^{\infty} \bar{\xi}^2 \left(\left[-A\bar{\xi} + B(1-\bar{\xi}\bar{z}) \right] e^{-\bar{\xi}\bar{z}} + \left[C\bar{\xi} + D(1+\bar{\xi}\bar{z}) \right] e^{\bar{\xi}\bar{z}} \right) J_1(\bar{\xi}\bar{r}) d\bar{\xi} \end{aligned} \tag{2.16d}$$

$$\bar{\sigma}_{zz} = \int_0^{\infty} \bar{\xi}^3 \left\{ \left[A\bar{\xi} + B\left(\frac{1}{\bar{\lambda}+1} + \bar{\xi}\bar{z} \right) \right] e^{-\bar{\xi}\bar{z}} + \left[-C\bar{\xi} + D\left(\frac{1}{\bar{\lambda}+1} - \bar{\xi}\bar{z} \right) \right] e^{\bar{\xi}\bar{z}} \right\} J_0(\bar{\xi}\bar{r}) d\bar{\xi} \tag{2.16e}$$

$$\bar{\sigma}_{rz} = \int_0^{\infty} \bar{\xi}^3 \left\{ \left[A\bar{\xi} - B\left(\frac{\bar{\lambda}}{\bar{\lambda}+1} - \bar{\xi}\bar{z} \right) \right] e^{-\bar{\xi}\bar{z}} + \left[C\bar{\xi} + D\left(\frac{\bar{\lambda}}{\bar{\lambda}+1} + \bar{\xi}\bar{z} \right) \right] e^{\bar{\xi}\bar{z}} \right\} J_1(\bar{\xi}\bar{r}) d\bar{\xi} \tag{2.16f}$$

2.1.3 Solution of particular boundary value problem

To obtain the complete solution of a particular boundary value problem, the four arbitrary functions A, B, C and D must be determined. This can be achieved by enforcing the boundary conditions at the top and bottom surfaces of the bulk (i.e. at $z = 0$ and $z = h$). By utilizing the surface equations (2.8) and (2.9) along with assuming that the residual surface tension τ^s is constant throughout, the normal and shear stress components $\bar{\sigma}_{zz}$ and $\bar{\sigma}_{rz}$ on the top surface of the bulk must satisfy the following relations:

$$\bar{\sigma}_{zz}\big|_{\bar{z}=0} = -\frac{\beta\bar{\tau}^s}{2(\bar{\lambda}+1)}\left(\frac{d^2\bar{u}_z}{d\bar{r}^2}+\frac{1}{\bar{r}}\frac{d\bar{u}_z}{d\bar{r}}\right)-\frac{\bar{p}(\bar{r})}{2(\bar{\lambda}+1)} \tag{2.17}$$

$$\bar{\sigma}_{rz}\big|_{\bar{z}=0} = -\frac{\alpha}{(\bar{\lambda}+2)}\left(\frac{d^2\bar{u}_r}{d\bar{r}^2}+\frac{1}{\bar{r}}\frac{d\bar{u}_r}{d\bar{r}}-\frac{\bar{u}_r}{\bar{r}^2}\right)-\frac{\bar{q}(\bar{r})}{2(\bar{\lambda}+1)} \tag{2.18}$$

where α is equal to 1 if the surface effect is not considered, otherwise it is zero and β is equal to 1 if the out-of-plane term is taken into account in the mathematical model, otherwise it is zero. The continuity of the displacement across the interface of the bulk and surface has also been employed, i.e. $\bar{u}_r = \bar{u}_r^s$ and $\bar{u}_z = \bar{u}_z^s$. Due to the fully fixed rigid-based condition, all components of the displacement vanish at $\bar{z} = \bar{h}$ where $\bar{h} = h/\Lambda$, i.e.

$$\bar{u}_r\big|_{\bar{z}=\bar{h}} = 0 \tag{2.19}$$

$$\bar{u}_z\big|_{\bar{z}=\bar{h}} = 0 \tag{2.20}$$

By taking Hankel integral transform of all four boundary conditions (2.17)-(2.20) along with exploiting the relations (2.16a)-(2.16f), it leads to a system of four linear algebraic equations for *A*, *B*, *C* and *D*

$$\begin{aligned}
&A\left(\bar{\xi}(\bar{\lambda}+1)+\beta\frac{\bar{\tau}^s}{2}\bar{\xi}^2(\bar{\lambda}+1)\right)+B\left(1+\beta\bar{\tau}^s\bar{\xi}\right)\\
&+C\left(-\bar{\xi}(\bar{\lambda}+1)+\beta\frac{\bar{\tau}^s}{2}\bar{\xi}^2(\bar{\lambda}+1)\right)+D\left(1-\beta\bar{\tau}^s\bar{\xi}\right)=\frac{Z(\bar{\xi})}{2\bar{\xi}^2}
\end{aligned} \tag{2.21}$$

$$\begin{aligned}
&A\left((\bar{\lambda}+1)\bar{\xi}+\alpha\frac{(\bar{\lambda}+1)^2}{\bar{\lambda}+2}\bar{\xi}^2\right)+B\left(-\bar{\lambda}-\alpha\frac{(\bar{\lambda}+1)^2}{\bar{\lambda}+2}\bar{\xi}\right)\\
&+C\left((\bar{\lambda}+1)\bar{\xi}-\alpha\frac{(\bar{\lambda}+1)^2}{\bar{\lambda}+2}\bar{\xi}^2\right)+D\left(\bar{\lambda}-\alpha\frac{(\bar{\lambda}+1)^2}{\bar{\lambda}+2}\bar{\xi}\right)=\frac{R(\bar{\xi})}{2\bar{\xi}^2}
\end{aligned} \tag{2.22}$$

$$\left[-A\bar{\xi}+B(1-\bar{\xi}\bar{h})\right]e^{-\bar{\xi}\bar{h}}+\left[C\bar{\xi}+D(1+\bar{\xi}\bar{h})\right]e^{\bar{\xi}\bar{h}}=0 \tag{2.23}$$

$$\left[A\bar{\xi}+B\left(\frac{2}{\bar{\lambda}+1}+\bar{\xi}\bar{h}\right)\right]e^{-\bar{\xi}\bar{h}}+\left[C\bar{\xi}+D\left(-\frac{2}{\bar{\lambda}+1}+\bar{\xi}\bar{h}\right)\right]e^{\bar{\xi}\bar{h}}=0 \tag{2.24}$$

where the functions $Z(\bar{\xi})$ and $R(\bar{\xi})$ are given in terms of the surface loads $\bar{p}(\bar{r})$ and $\bar{q}(\bar{r})$ by

$$Z\left(\bar{\xi}\right) = -\int_0^\infty \bar{p}(\bar{r})J_0(\bar{\xi}\bar{r})\bar{r}d\bar{r} \tag{2.25}$$

$$R\left(\bar{\xi}\right) = -\int_0^\infty \bar{q}(\bar{r})J_1(\bar{\xi}\bar{r})\bar{r}d\bar{r} \tag{2.26}$$

Equations (2.21)-(2.24) are sufficient for uniquely determining *A*, *B*, *C*, and *D* as functions of the transform parameter $\bar{\xi}$ and the applied surface loads $Z(\bar{\xi})$ and $R(\bar{\xi})$ and the final explicit solution is given by

$$A=\frac{1}{4}\left[\frac{A_{Z0}+\alpha A_{Z1}}{F}\right]\frac{Z(\bar{\xi})}{\bar{\xi}^3}+\frac{1}{4}\left[\frac{A_{R0}+\beta A_{R1}}{F}\right]\frac{R(\bar{\xi})}{\bar{\xi}^3} \tag{2.27a}$$

$$B=\frac{1}{4}\left[\frac{B_{Z0}+\alpha B_{Z1}}{F}\right]\frac{Z(\bar{\xi})}{\bar{\xi}^2}+\frac{1}{4}\left[\frac{B_{R0}+\beta B_{R1}}{F}\right]\frac{R(\bar{\xi})}{\bar{\xi}^2} \tag{2.27b}$$

$$C=\frac{1}{4}\left[\frac{C_{Z0}+\alpha C_{Z1}}{F}\right]\frac{Z(\bar{\xi})}{\bar{\xi}^3}+\frac{1}{4}\left[\frac{C_{R0}+\beta C_{R1}}{F}\right]\frac{R(\bar{\xi})}{\bar{\xi}^3} \tag{2.27c}$$

$$D=\frac{1}{4}\left[\frac{D_{Z0}+\alpha D_{Z1}}{F}\right]\frac{Z(\bar{\xi})}{\bar{\xi}^2}+\frac{1}{4}\left[\frac{D_{R0}+\beta D_{R1}}{F}\right]\frac{R(\bar{\xi})}{\bar{\xi}^2} \tag{2.27d}$$

where

$$\begin{aligned}
A_{Z0}&=\frac{\bar{\lambda}(\bar{\lambda}+3)}{(\bar{\lambda}+1)^2}e^{2\bar{\xi}\bar{h}}+2\bar{\xi}^2\bar{h}^2-\frac{2\bar{\xi}\bar{h}\bar{\lambda}}{\bar{\lambda}+1}+\frac{\bar{\lambda}^2+3\bar{\lambda}+4}{(\bar{\lambda}+1)^2}\\
A_{Z1}&=\frac{\bar{\xi}}{\bar{\lambda}+2}\left((\bar{\lambda}+3)(e^{2\bar{\xi}\bar{h}}-1)-2\bar{\xi}\bar{h}(\bar{\xi}\bar{h}-1)(\bar{\lambda}+1)\right)\\
A_{R0}&=\frac{\bar{\lambda}+3}{(\bar{\lambda}+1)^2}e^{2\bar{\xi}\bar{h}}+\frac{3\bar{\lambda}+5}{(\bar{\lambda}+1)^2}+\frac{2\bar{\xi}\bar{h}}{\bar{\lambda}+1}+2\bar{\xi}^2\bar{h}^2\\
A_{R1}&=\frac{\bar{\tau}^s\bar{\xi}}{2}\left[\frac{2(\bar{\lambda}+3)}{(\bar{\lambda}+1)^2}(e^{2\bar{\xi}\bar{h}}-1)-\frac{4\bar{\xi}\bar{h}}{\bar{\lambda}+1}-2\bar{\xi}^2\bar{h}^2\right]
\end{aligned} \tag{2.28a}$$

$$\begin{aligned}
B_{Z0}&=(1-2\bar{\xi}\bar{h})+\frac{\bar{\lambda}+3}{\bar{\lambda}+1}e^{2\bar{\xi}\bar{h}}\\
B_{Z1}&=\frac{\bar{\xi}}{\bar{\lambda}+2}\left((e^{2\bar{\xi}\bar{h}}-1)(\bar{\lambda}+3)+2\bar{\xi}\bar{h}(\bar{\lambda}+1)\right)\\
B_{R0}&=-(1+2\bar{\xi}\bar{h})-\frac{\bar{\lambda}+3}{\bar{\lambda}+1}e^{2\bar{\xi}\bar{h}}\\
B_{R1}&=\frac{\bar{\tau}^s\bar{\xi}}{2}\left[\frac{\bar{\lambda}+3}{\bar{\lambda}+1}(1-e^{2\bar{\xi}\bar{h}})+2\bar{\xi}\bar{h}\right]
\end{aligned} \tag{2.28b}$$

$$\begin{aligned}
C_{Z0}&=-\frac{\bar{\lambda}(\bar{\lambda}+3)}{(\bar{\lambda}+1)^2}e^{-2\bar{\xi}\bar{h}}-2\bar{\xi}^2\bar{h}^2-\frac{2\bar{\xi}\bar{h}\bar{\lambda}}{\bar{\lambda}+1}-\frac{\bar{\lambda}^2+3\bar{\lambda}+4}{(\bar{\lambda}+1)^2}\\
C_{Z1}&=\frac{\bar{\xi}}{\bar{\lambda}+2}\left((\bar{\lambda}+3)(e^{-2\bar{\xi}\bar{h}}-1)-2\bar{\xi}\bar{h}(1+\bar{\xi}\bar{h})(\bar{\lambda}+1)\right)\\
C_{R0}&=\frac{\bar{\lambda}+3}{(\bar{\lambda}+1)^2}e^{-2\bar{\xi}\bar{h}}+\frac{3\bar{\lambda}+5}{(\bar{\lambda}+1)^2}-\frac{2\bar{\xi}\bar{h}}{\bar{\lambda}+1}+2\bar{\xi}^2\bar{h}^2\\
C_{R1}&=\frac{\bar{\tau}^s\bar{\xi}}{2}\left[-\frac{2(\bar{\lambda}+3)}{(\bar{\lambda}+1)^2}(e^{-2\bar{\xi}\bar{h}}-1)-\frac{4\bar{\xi}\bar{h}}{\bar{\lambda}+1}+2\bar{\xi}^2\bar{h}^2\right]
\end{aligned} \tag{2.28c}$$

$$
\begin{aligned}
D_{Z0} &= (1+2\bar{\xi}\bar{h}) + \frac{\bar{\lambda}+3}{\bar{\lambda}+1}e^{-2\bar{\xi}\bar{h}} \\
D_{Z1} &= \frac{\bar{\xi}}{\bar{\lambda}+2}\left((1-e^{-2\bar{\xi}\bar{h}})(\bar{\lambda}+3)+2\bar{\xi}\bar{h}(\bar{\lambda}+1)\right) \\
D_{R0} &= (1-2\bar{\xi}\bar{h}) + \frac{\bar{\lambda}+3}{\bar{\lambda}+1}e^{-2\bar{\xi}\bar{h}} \\
D_{R1} &= \frac{\bar{\tau}^s\bar{\xi}}{2}\left[\frac{\bar{\lambda}+3}{\bar{\lambda}+1}(1-e^{-2\bar{\xi}\bar{h}}) - 2\bar{\xi}\bar{h}\right]
\end{aligned}
\tag{2.28d}
$$

$$
\begin{aligned}
F = &\left[\frac{\bar{\lambda}^2+4\bar{\lambda}+5}{\bar{\lambda}+1} + 2\bar{h}\bar{\xi}^2(\bar{h}+\alpha)(\bar{\lambda}+1) + (\bar{\lambda}+3)\left(\cosh(2\bar{\xi}\bar{h}) + \alpha\bar{\xi}\sinh(2\bar{\xi}\bar{h})\right)\right] \\
&+\beta\frac{\bar{\tau}^s\bar{\xi}}{2}\left[(\bar{\lambda}+3)\frac{\bar{\lambda}+2}{\bar{\lambda}+1}\sinh(2\bar{\xi}\bar{h}) - 2\bar{\xi}\bar{h}(\bar{\lambda}+2) + \frac{\bar{\xi}\alpha}{\bar{\lambda}+2}\left((\bar{\lambda}+3)^2\cosh(2\bar{\xi}\bar{h}) - (\bar{\lambda}+3)^2 - 2\bar{\xi}^2\bar{h}^2(\bar{\lambda}+1)\right)\right]
\end{aligned}
\tag{2.28e}
$$

Once the functions *A*, *B*, *C*, and *D* are obtained from (2.27)-(2.28), both the displacement and stress at any point within the bulk can be computed from (2.16a)-(2.16f). Numerical evaluation of all involved integrals is briefly discussed in the next chapter.

It is evident that by setting the parameters α and β to zero, the solution obtained is identical to that of a classical problem of a three-dimensional, infinite elastic layer under surface loadings (Sneddon, 1951; Selvadurai, 2000). Furthermore, by setting β to zero, the above results reduce to those presented by Zhao and Rajapakse (2009) and Zhao (2009). These two special benchmark solutions can be employed in the verification procedure. In addition, results for the special case of a half space can also be obtained by simply taking sufficiently large layer thickness *h*.

2.2 Numerical Implementation

Although all functions *A*, *B*, *C*, and *D* are obtained in a closed form in terms of the transform parameter $\bar{\xi}$, determination of the displacement and stress fields still requires the evaluation of integrals corresponding to Hankel transform inversion. It is apparent that all involved integrals contain relatively complex integrands and they cannot be directly integrated to obtain a closed form elastic field. In this section, a selected numerical technique for efficiently and accurately evaluating those integrals is outlined below.

2.2.1 Truncation

It is evident that all integrals appearing in (2.16a)-(2.16f) are improper integrals with their lower and upper limits equal to zero and infinity, respectively. To evaluate such integrals numerically, it is common to truncate the domain of integration from $[0,\infty)$ to $[0,\bar{\xi}_R]$ where $\bar{\xi}_R$ is a finite real number. The approximate displacement and stress fields in terms of the truncated integrals are given by

$$
\bar{u}_r = (\bar{\lambda}+1)\int_0^{\bar{\xi}_R}\bar{\xi}^2\left\{\left[-A\bar{\xi}+B(1-\bar{\xi}\bar{z})\right]e^{-\bar{\xi}\bar{z}} + \left[C\bar{\xi}+D(1+\bar{\xi}\bar{z})\right]e^{\bar{\xi}\bar{z}}\right\}J_1(\bar{\xi}\bar{r})d\bar{\xi} \tag{2.29a}
$$

$$
\bar{u}_z = -(\bar{\lambda}+1)\int_0^{\bar{\xi}_R}\bar{\xi}^2\left\{\left[A\bar{\xi}+B(\frac{2}{(\bar{\lambda}+1)}+\bar{\xi}\bar{z})\right]e^{-\bar{\xi}\bar{z}} + \left[C\bar{\xi}-D(\frac{2}{(\bar{\lambda}+1)}-\bar{\xi}\bar{z})\right]e^{\bar{\xi}\bar{z}}\right\}J_0(\bar{\xi}\bar{r})d\bar{\xi} \tag{2.29b}
$$

$$\bar{\sigma}_{rr} = \int_0^{\bar{\xi}_R} \bar{\xi}^3 \left\{ \left[-A\bar{\xi} + B\left(\frac{2\bar{\lambda}+1}{\bar{\lambda}+1} - \bar{\xi}\bar{z} \right) \right] e^{-\bar{\xi}\bar{z}} + \left[C\bar{\xi} + D\left(\frac{2\bar{\lambda}+1}{\bar{\lambda}+1} + \bar{\xi}\bar{z} \right) \right] e^{\bar{\xi}\bar{z}} \right\} J_0(\bar{\xi}\bar{r}) d\bar{\xi}$$

$$-\frac{1}{\bar{r}} \int_0^{\bar{\xi}_R} \bar{\xi}^2 \left(\left[-A\bar{\xi} + B(1-\bar{\xi}\bar{z}) \right] e^{-\bar{\xi}\bar{z}} + \left[C\bar{\xi} + D(1+\bar{\xi}\bar{z}) \right] e^{\bar{\xi}\bar{z}} \right) J_1(\bar{\xi}\bar{r}) d\bar{\xi} \qquad (2.29c)$$

$$\bar{\sigma}_{\theta\theta} = \frac{\bar{\lambda}}{\bar{\lambda}+1} \int_0^{\bar{\xi}_R} \bar{\xi}^3 \left\{ Be^{-\bar{\xi}\bar{z}} + De^{\bar{\xi}\bar{z}} \right\} J_0(\bar{\xi}\bar{r}) d\bar{\xi}$$

$$+\frac{1}{\bar{r}} \int_0^{\bar{\xi}_R} \bar{\xi}^2 \left(\left[-A\bar{\xi} + B(1-\bar{\xi}\bar{z}) \right] e^{-\bar{\xi}\bar{z}} + \left[C\bar{\xi} + D(1+\bar{\xi}\bar{z}) \right] e^{\bar{\xi}\bar{z}} \right) J_1(\bar{\xi}\bar{r}) d\bar{\xi}$$

(2.29d)

$$\bar{\sigma}_{zz} = \int_0^{\bar{\xi}_R} \bar{\xi}^3 \left\{ \left[A\bar{\xi} + B\left(\frac{1}{\bar{\lambda}+1} + \bar{\xi}\bar{z} \right) \right] e^{-\bar{\xi}\bar{z}} + \left[-C\bar{\xi} + D\left(\frac{1}{\bar{\lambda}+1} - \bar{\xi}\bar{z} \right) \right] e^{\bar{\xi}\bar{z}} \right\} J_0(\bar{\xi}\bar{r}) d\bar{\xi} \qquad (2.29e)$$

$$\bar{\sigma}_{rz} = \int_0^{\bar{\xi}_R} \bar{\xi}^3 \left\{ \left[A\bar{\xi} - B\left(\frac{\bar{\lambda}}{\bar{\lambda}+1} - \bar{\xi}\bar{z} \right) \right] e^{-\bar{\xi}\bar{z}} + \left[C\bar{\xi} + D\left(\frac{\bar{\lambda}}{\bar{\lambda}+1} + \bar{\xi}\bar{z} \right) \right] e^{\bar{\xi}\bar{z}} \right\} J_1(\bar{\xi}\bar{r}) d\bar{\xi} \qquad (2.29f)$$

While the convergence of the above approximate solution to an analytical solution is ensured as $\bar{\xi}_R$ approaches infinity, it is standard, in the numerical calculation, to choose a sufficiently large number $\bar{\xi}_R$ such that the error from the approximation is less than a specified tolerance.

2.2.2 Interval subdivision

Due to the oscillating nature of their integrands, the numerical integration of involved integrals in (2.16a)-(2.16f) by using Gaussian quadrature over a single interval requires a large number of integrations points. To enhance the accuracy and computational efficiency, the interval [0, $\bar{\xi}_R$] is first partitioned into *N* sub-intervals denoted by [$\bar{\xi}_0 = 0$, $\bar{\xi}_1$], [$\bar{\xi}_1$, $\bar{\xi}_2$], [$\bar{\xi}_2$, $\bar{\xi}_3$], …, [$\bar{\xi}_{N-1}$, $\bar{\xi}_N = \bar{\xi}_R$] and the integral over the interval [0, $\bar{\xi}_R$] is obtained from the sum of all sub-integrals over each sub-interval as follows:

$$\int_0^{\bar{\xi}_R} f(\bar{\xi}) d\bar{\xi} = \int_{\bar{\xi}_{0=0}}^{\bar{\xi}_1} f(\bar{\xi}) d\bar{\xi} + \int_{\bar{\xi}_1}^{\bar{\xi}_2} f(\bar{\xi}) d\bar{\xi} + \ldots + \int_{\bar{\xi}_{N-2}}^{\bar{\xi}_{N-1}} f(\bar{\xi}) d\bar{\xi} + \int_{\bar{\xi}_{N-1}}^{\bar{\xi}_N = \bar{\xi}_R} f(\bar{\xi}) d\bar{\xi} \qquad (2.30)$$

where $f = f(\bar{\xi})$ denotes any integrand. As the number of sub-intervals increases, the oscillating behavior of the integrand in each sub-interval should disappear, and they can accurately be integrated by using low-order Gaussian quadrature.

2.2.3 Numerical quadrature

By using the change of variable, the Gaussian quadrature formula for each sub-interval in (2.30) is given by

$$\int_{\bar{\xi}_{i-1}}^{\bar{\xi}_i} f(\bar{\xi})d\bar{\xi} = \int_{-1}^{1} f(\bar{\xi}(\xi^*))Jd\xi^* = \sum_{i=1}^{n} f(\bar{\xi}(\xi_i^*))Jw_i \tag{2.31}$$

where $\bar{\xi} = (1-\xi^*)\bar{\xi}_{i-1}/2 + (1+\xi^*)\bar{\xi}_i/2$, $(\bar{\xi}_i - \bar{\xi}_{i-1})/2$ denotes the Jacobian of transformation, ξ_i^* is the location of an integration point, w_i is the corresponding weight, and n is the number of integration points.

2.2.4 Convergence study

In the present study, extensive numerical experiments are to be performed to investigate the influence of the truncation parameter $\bar{\xi}_R$, the number of sub-intervals N, and the number of integration points n on the accuracy of the numerical integration. Such three parameters must be chosen properly to ensure the accuracy of the numerical results while consuming reasonable computational time.

Both the number of integration points and the number of sub-intervals have a direct impact on the accuracy of the numerical integration for a fixed truncation parameter $\bar{\xi}_R$. In general, by increasing the number of sub-intervals, each sub-integral over each sub-interval requires less number of integration points since the oscillating behavior of the integrand gradually disappears. In the present study, for a fixed truncation parameter $\bar{\xi}_R$, the number of sub-intervals N is increased until the integral can be integrated correctly (for a specified tolerance) by using a low order Gaussian quadrature over each sub-interval. The ratio $\bar{\xi}_R / N$ is then computed and used to indicate the size of the sub-interval over which the integrand is sufficiently well-behaved to be integrated using low order Gaussian quadrature. Finally, a proper choice of the truncation parameter $\bar{\xi}_R$ is obtained by increasing such upper limit until the value of the integral converges or remains unchanged (for a specified tolerance). It is important to remark that in such process, the number of sub-intervals must be increased accordingly in order to maintain the size of the sub-intervals ($\bar{\xi}_R / N$) to be sufficiently small to allow the integration by low-order Gaussian quadrature.

2.3 Numerical Results

Extensive studies for both cases of axisymmetric normal and axisymmetric tangential surface loads are investigated to understand the nano-scale influence through the surface stress effects (with/without the contribution of residual surface tension) and size dependent behaviors. Moreover, numerical results of a layer under a unit normal point load, a unit normal ring load and a unit tangential ring load, which are benefit for solving nano-indentations problem, are also demonstrated and fully discussed.

2.3.1 Verification

Numerical results obtained from the developed computer program are verified with various benchmark solutions. For examples, numerical solutions without surface energy effects of an elastic layer under normal concentrated load are compared with analytical solutions presented by Bumister (1943, 1945) and those of a half-space subjected to uniformly distributed vertical load

are verified with solutions of Ahlvin and Ulery (1962). Furthermore, numerical results with no surface energy effects and numerical results accounted for surface energy effects without the contribution of the out-of-plane term of an elastic layer under uniformly normal distributed load are compared with those proposed by Zhao (2009). As evident from results presented further below, numerical solutions obtained from the present study exhibit excellent agreement with the benchmark solutions.

2.3.1.1 Infinite rigid-based elastic layer under normal point force

Consider a normal point load $\overline{P}_{pt} = P_{pt} / \mu\Lambda^2$ acting to the surface of a rigid-based layer with the normalized thickness $\overline{h} = 1.0$ and the Poisson's ratio $\upsilon = 0.2$ as shown in Figure 2.2. Without consideration of surface energy effects, the analytical solution derived by Burmister (1943, 1945) and tabulated by Poulos (1967b) are employed to verify the accuracy of the present study. Numerical solutions for this classical case can readily be obtained in the present study by setting $\alpha = 0$ and $\beta = 0$. The radial and vertical displacements at the surface and non-zero stress components at $\overline{z} = 0.1$ along the radial direction are reported in Tables 2.1-2.3. It is obvious that numerical results from the present study show good agreement with the analytical solutions given by Burmister (1943, 1945).

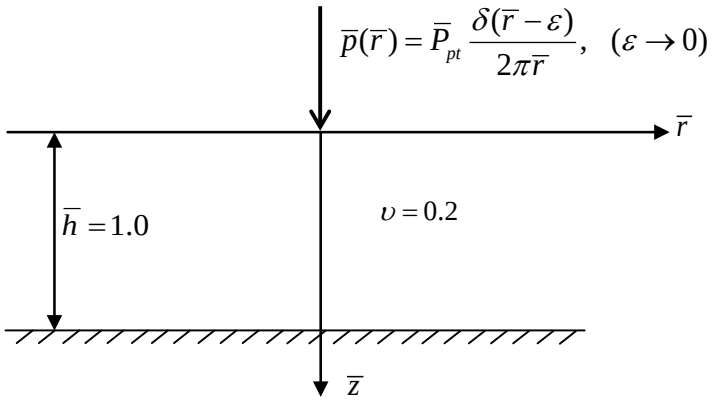

Figure 2.2 Three-dimensional, infinite, rigid-based, elastic layer subjected to a normal point load

2.3.1.2 Elastic half-space under uniformly distributed normal traction

A three-dimensional, elastic half-space with Poisson's ratio $\upsilon = 0.2$ under the action of a uniformly distributed normal traction p_0 over a circular area of normalized radius $\overline{a} = a / \Lambda$ shown in Figure 2.3 is considered (excluding the surface energy effects). In this case, the exact solution tabulated by Ahlvin and Ulery (1962) has been employed as a benchmark solution. Again, in the analysis, α and β are set to be zero in order to specialize the problem into the classical case and the normalized thickness $\overline{h}$ must be chosen to be sufficiently large to represent the elastic half-space. Results for non-zero displacement and stress components are reported in Table 2.4 along with those of Ahlvin and Ulery (1962). It is evident that solutions obtained from the current study are almost indistinguishable from the reference results.

Table 2.1 Normalized vertical and radial displacements of a three-dimensional, infinite, rigid-based, elastic layer subjected to a normal point load

$\bar{r}$	$2\pi\bar{h}\bar{E}\bar{u}_r / \bar{P}_{pt}$		$2\pi\bar{h}\bar{E}\bar{u}_z / \bar{P}_{pt}$	
	Burmister (1943, 1945)	**Current study**	**Burmister (1943, 1945)**	**Current study**
0.05	-14.362	-14.344	35.921	35.310
0.1	-7.124	-7.172	16.728	16.554
0.2	-3.455	-3.477	7.162	7.195
0.3	-2.184	-2.178	4.016	4.050
0.4	-1.523	-1.512	2.478	2.473
0.5	-1.064	-1.109	1.599	1.579
0.6	-0.824	-0.830	1.048	1.048
0.7	-0.62	-0.620	0.69	0.704
0.8	-0.465	-0.461	0.45	0.458

Table 2.2 Normalized vertical and radial stress components of a three-dimensional, infinite, rigid-based, elastic layer subjected to a normal point load

$\bar{r}$	$4\pi\bar{h}^2(\bar{\lambda}+1)\bar{\sigma}_{zz} / \bar{P}_{pt}$		$4\pi\bar{h}^2(\bar{\lambda}+1)\bar{\sigma}_{rr} / \bar{P}_{pt}$	
	Burmister (1943, 1945)	**Current study**	**Burmister (1943, 1945)**	**Current study**
0	300	300	-30.71	-30.72
0.1	53.08	53.06	34.75	34.75
0.2	5.415	5.395	12.5	12.49
0.3	0.994	0.974	3.347	3.344
0.4	0.293	0.273	0.614	0.611
0.5	0.124	0.103	-0.259	-0.262
0.6	0.067	0.048	-0.528	-0.530
0.7	0.041	0.025	-0.578	-0.579
0.8	0.026	0.013	-0.544	-0.544
0.9	0.016	0.006	-0.479	-0.478

Table 2.3 Normalized shear and hoop stress components of a three-dimensional, infinite, rigid-based, elastic layer subjected to a normal point load

$\bar{r}$	$4\pi\bar{h}^2(\bar{\lambda}+1)\bar{\sigma}_{rz}/\bar{P}_{pt}$		$4\pi\bar{h}^2(\bar{\lambda}+1)\bar{\sigma}_{\theta\theta}/\bar{P}_{pt}$	
	Burmister (1943, 1945)	**Current study**	**Burmister (1943, 1945)**	**Current study**
0	0	0.000	-30.71	-30.720
0.1	53	53.003	-4.342	-4.355
0.2	10.68	10.676	2.237	2.224
0.3	2.765	2.765	1.996	1.983
0.4	0.909	0.908	1.349	1.337
0.5	0.326	0.324	0.877	0.865
0.6	0.102	0.099	0.566	0.554
0.7	0.005	0.002	0.363	0.352
0.8	-0.038	-0.043	0.231	0.221
0.9	-0.056	-0.061	0.144	0.135

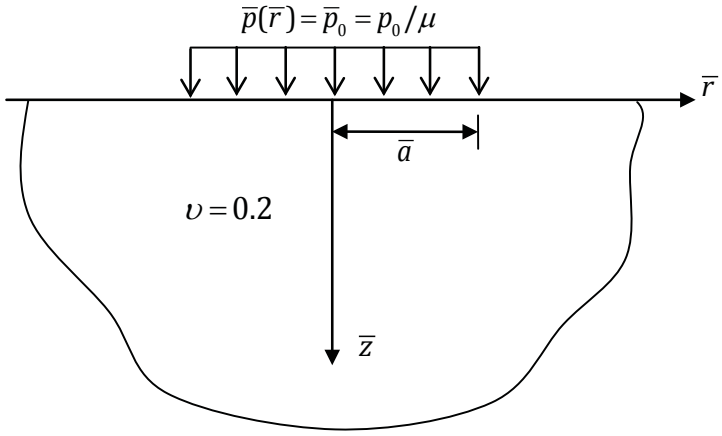

Figure 2.3 Three-dimensional, infinite, elastic half-space subjected to a uniformly distributed normal traction

2.3.1.3 Infinite rigid-based elastic layer under uniformly distributed normal traction

Consider an infinite rigid-based elastic layer under uniformly distributed normal traction p_0 acting over a circular area of normalized radius $\bar{a} = 10.0$ and with the normalized layer thickness $\bar{h} = 30$ as shown in Figure 2.4. To allow a direct comparison of available results proposed by Zhao (2009), the same set of material constants obtained from atomistic simulation (Miller and Shenoy, 2000; Shenoy, 2005) is utilized, and they are summarized in Table 2.5. Results for the classical case and the case accounting for the surface energy effects but ignoring the out-of-plane term can be obtained by simply setting $\alpha = 0, \beta = 0$ and $\alpha = 1, \beta = 0$, respectively. By comparing results for the surface displacement and stresses at $\bar{z} = 0.1$ along the radial direction with those

presented by Zhao (2009) for $\bar{h}/\bar{a}=3$, it is found that solutions obtained from the present study are in excellent agreement with the benchmark solutions as shown in Figures 2.5-2.7.

Table 2.4 Normalized displacement and stress components of a three-dimensional, infinite, elastic half-space subjected to a uniformly distributed normal traction

$\bar{z}/\bar{a}$	$2(\bar{\lambda}+1)\bar{\sigma}_{zz}/\bar{p}_0$		$2(\bar{\lambda}+1)\bar{\sigma}_{rr}/\bar{p}_0$		$2(\bar{\lambda}+1)\bar{\sigma}_{\theta\theta}/\bar{p}_0$		$\bar{u}_z/\bar{p}_0$	
	Ahlvin and Ulery (1962)	**Current study**	**Ahlvin and Ulery (1962)**	**Current study**	**Ahlvin and Ulery (1962)**	**Current study**	**Ahlvin and Ulery (1962)**	**Current study**
0	1.000	0.993	0.700	0.695	0.700	0.695	0.800	0.800
0.1	0.999	0.999	0.581	0.581	0.581	0.581	0.769	0.769
0.2	0.992	0.992	0.468	0.468	0.468	0.468	0.736	0.736
0.3	0.976	0.976	0.367	0.367	0.367	0.367	0.702	0.702
0.4	0.949	0.949	0.280	0.280	0.280	0.280	0.667	0.667
0.5	0.911	0.911	0.208	0.208	0.208	0.208	0.633	0.633
0.6	0.864	0.864	0.151	0.151	0.151	0.151	0.599	0.599
0.7	0.811	0.811	0.106	0.106	0.106	0.106	0.566	0.566
0.8	0.756	0.756	0.072	0.072	0.072	0.072	0.535	0.535
0.9	0.701	0.701	0.047	0.047	0.047	0.047	0.505	0.505
1	0.646	0.646	0.028	0.028	0.028	0.028	0.478	0.478
1.2	0.547	0.547	0.005	0.005	0.005	0.005	0.429	0.429
1.5	0.424	0.424	-0.010	-0.010	-0.010	-0.010	0.368	0.368
2	0.284	0.284	-0.016	-0.016	-0.016	-0.016	0.294	0.294
2.5	0.200	0.200	-0.014	-0.014	-0.014	-0.014	0.243	0.243
3	0.146	0.146	-0.012	-0.012	-0.012	-0.012	0.207	0.207
4	0.087	0.087	-0.008	-0.008	-0.008	-0.008	0.158	0.158
5	0.057	0.057	-0.005	-0.005	-0.005	-0.005	0.128	0.128
6	0.040	0.040	-0.004	-0.004	-0.004	-0.004	0.107	0.107
7	0.030	0.030	-0.003	-0.003	-0.003	-0.003	0.092	0.092
8	0.023	0.023	-0.002	-0.002	-0.002	-0.002	0.081	0.081

Table 2.5 Material properties used in numerical study

Model Parameter	**Value (unit)**
λ	$58.17\text{x}10^9$ (N/m^2)
μ	$26.13\text{x}10^9$ (N/m^2)
λ^s	6.8511 (N/m)
μ^s	-0.376 (N/m)
τ^s	1 (N/m)

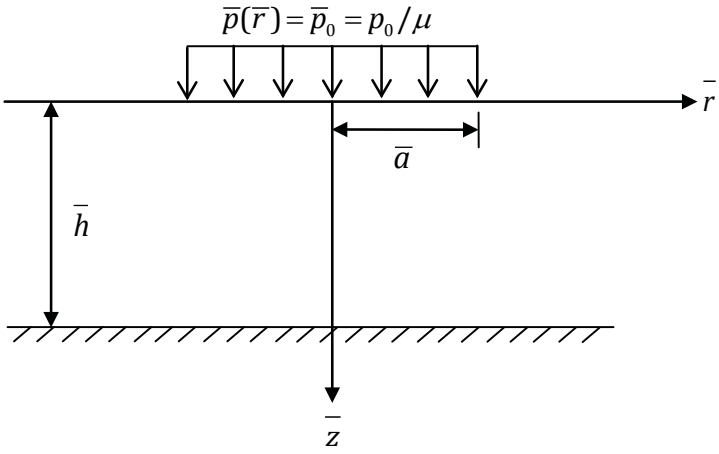

Figure 2.4 Three-dimensional, infinite, rigid-based, elastic layer subjected to a uniformly distributed normal traction

2.3.2 Layer under various surface loads

After the formulation and numerical implementation are verified for both the classical case and the case accounting for the surface stress effects but ignoring the out-of-plane term, the proposed model (including the out-of-plane term) is then utilized to investigate the influence of the surface stress effects on elastic fields and demonstrate the significant role of the out-of-plane term in Gurtin-Murdoch surface elasticity model. By using material properties summarized in Table 2.5, numerical results and size-dependent behaviors for both normal and tangential directions of axisymmetric surface loads are illustrated and discussed.

2.3.2.1 Uniformly distributed normal traction

Consider an infinite, rigid-based elastic layer under uniform normal traction p_0 acting on a circular region of radius a as shown in Figure 2.4. Results for both radial and vertical displacements on the surface along the radial direction for $\bar{a} = 10.0$ and various normalized thicknesses are shown in Figure 2.8(a)-(b), respectively. It is apparent from this set of results that a model incorporating the out-of-plane term predicts much lower surface displacement or, equivalently, renders materials stiffer while the solution obtained from a model excluding the out-of-plane term exhibits significant influence of the surface energy effects only in the case of the radial displacement. Hence, the influence of the out-of-plane term is significant and, in general, cannot be neglected. In addition, results for all cases show similar trend for various $\bar{h}$.

For non-zero stress components, results are reported for $\bar{h} = 10$ and $\bar{a} = 1$ at three different normalized depths ($\bar{z} = 0.25$, $\bar{z} = 0.5$, $\bar{z} = 1.0$). The variation of the normalized vertical stress $4\pi(\bar{\lambda}+1)\bar{\sigma}_{zz}/\bar{p}_0$ in the radial direction is shown in Figure 2.9(a). Clearly, the vertical stresses for all cases reach their maximum at $\bar{r} = 0$ and rapidly decrease to zero when $\bar{r}$ is near the edge of the surface loading, i.e. $\bar{r}/\bar{a} = 1$. Regarding to the presence of surface energy effects, values of the vertical stress are lesser within the surface loading region $\bar{r}/\bar{a} \le 1.0$ and slightly higher for $\bar{r}/\bar{a} > 1.0$. Moreover, the influence of surface energy effects exhibits significant role in the region relatively close to the surface. It is interesting to point out that all such behaviors are more apparent in the current model, which integrates the out-of-plane contribution of the residual surface tension into the analysis.

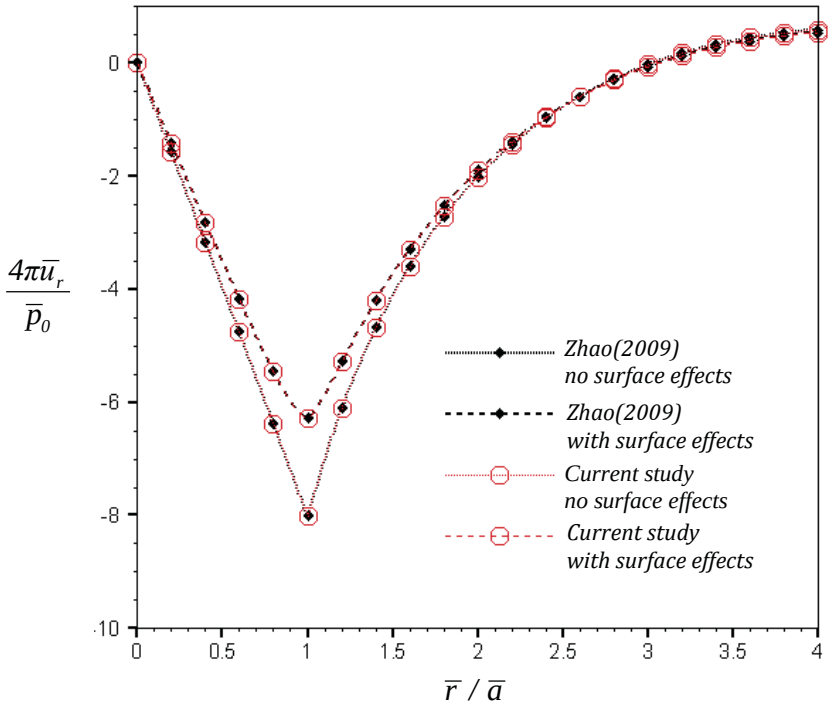

(a)

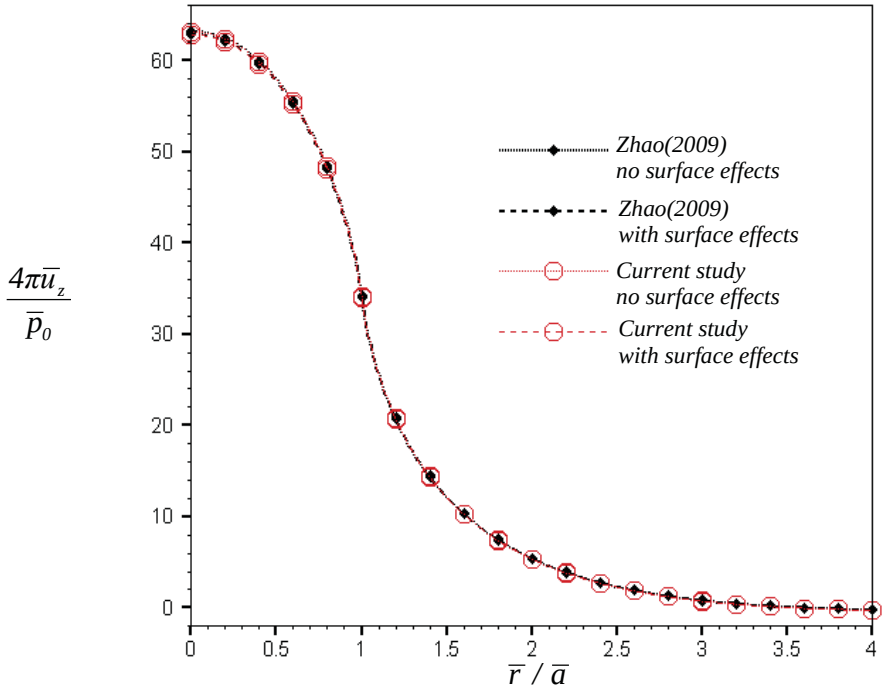

(b)

Figure 2.5 Normalized displacement profiles of an elastic layer under a uniformly distrubuted normal traction: (a) radial displacement and (b) vertical displacement

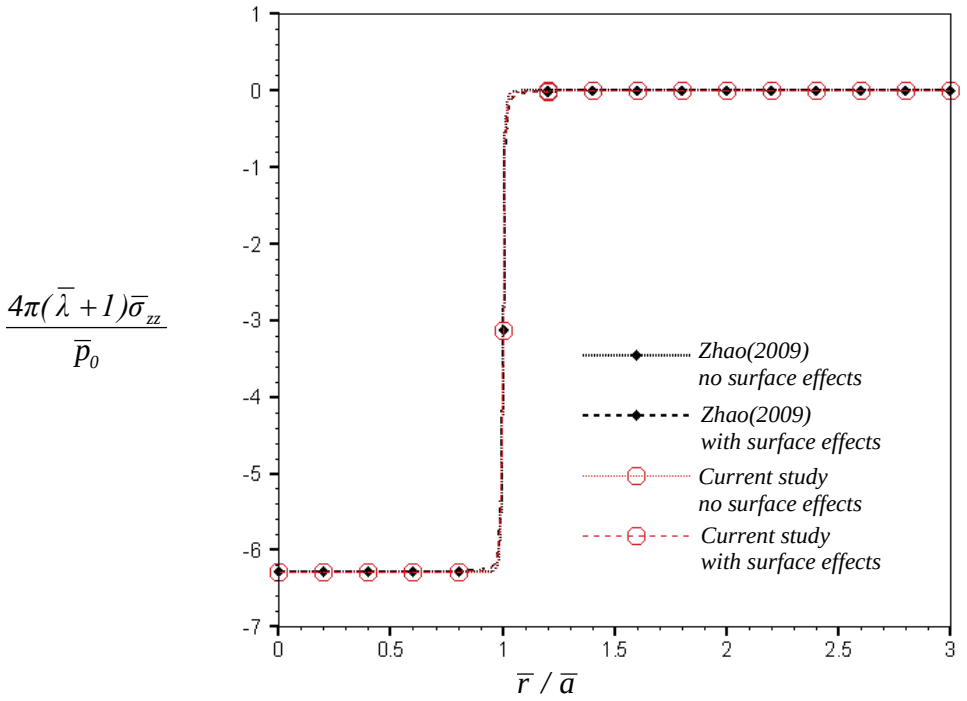

(a)

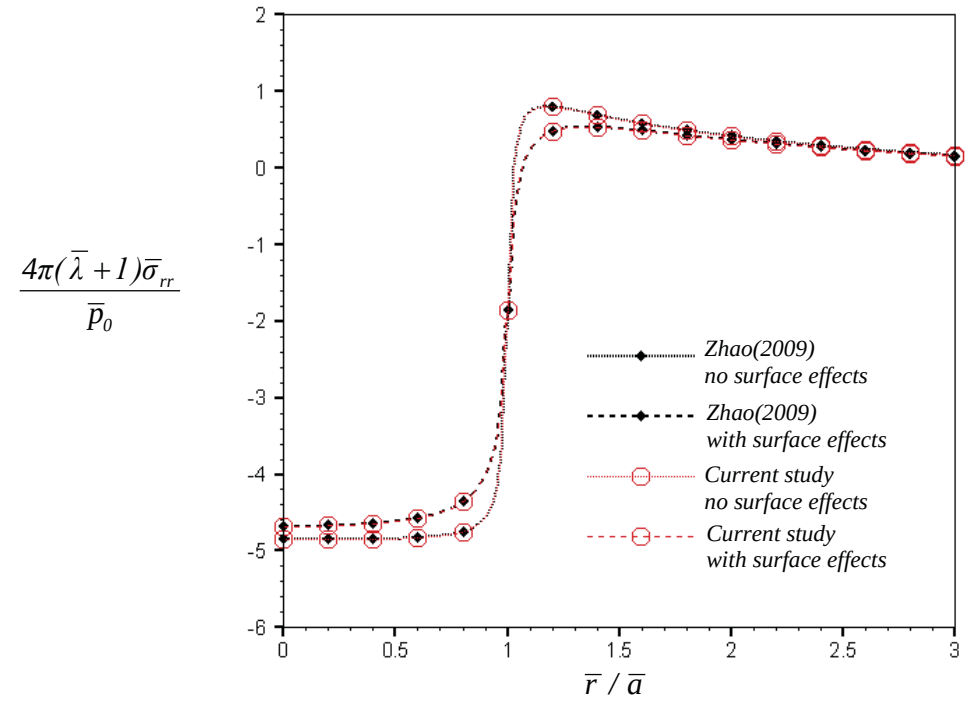

(b)

Figure 2.6 Normalized stress profiles of an elastic layer under a uniformly distrubuted normal traction: (a) vertical stress and (b) radial stress

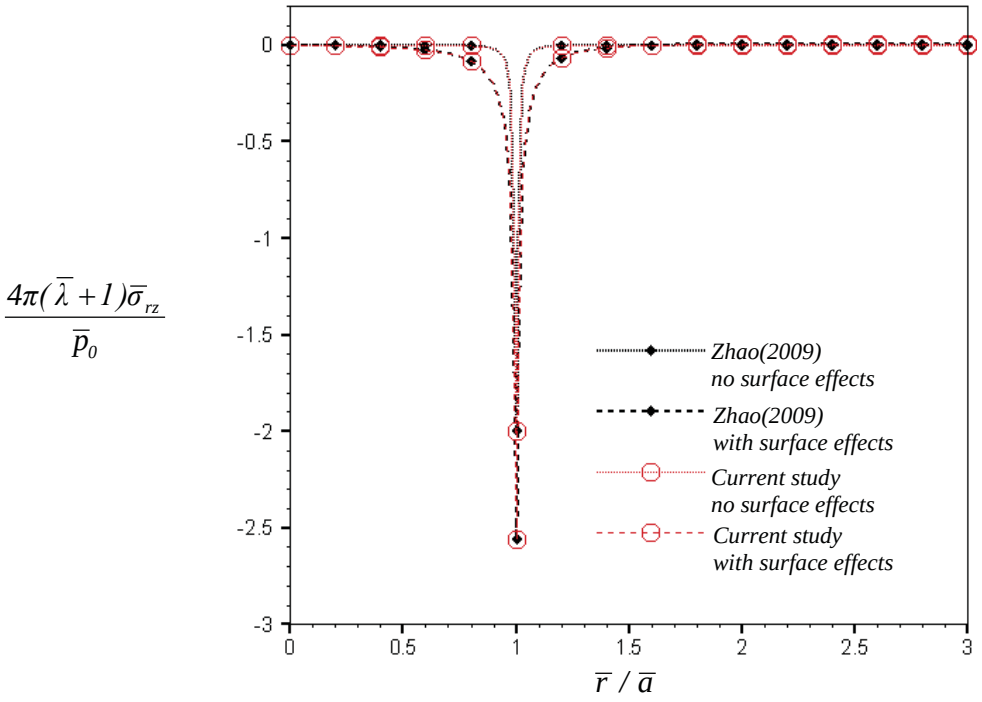

(a)

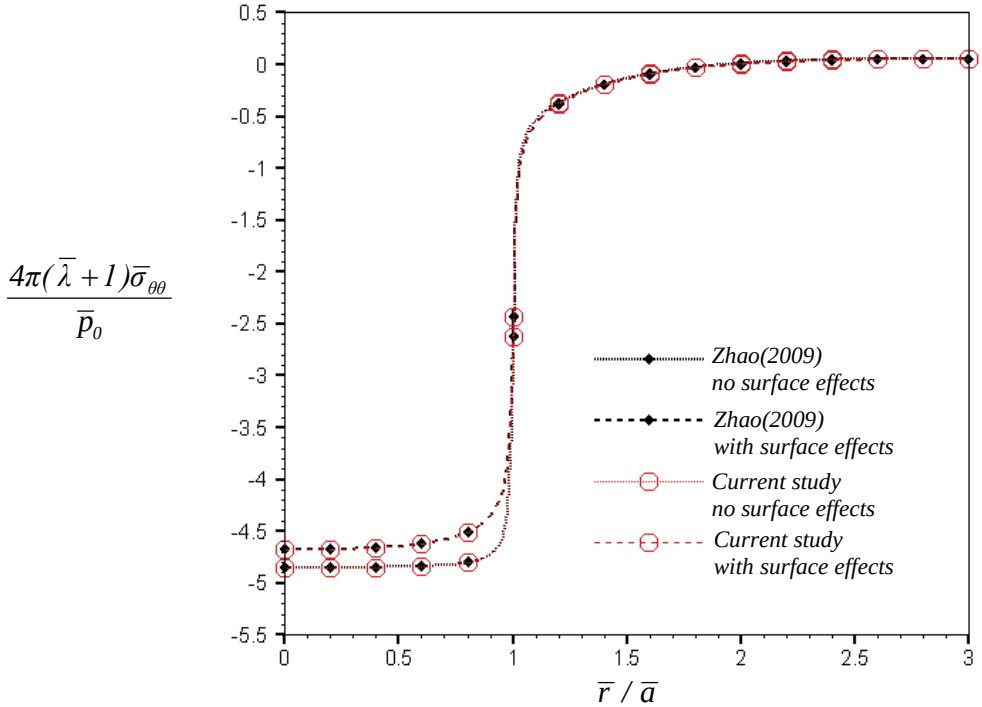

(b)

Figure 2.7 Normalized stress profiles of an elastic layer under a uniformly distrubuted normal traction: (a) shear stress and (b) hoop stress

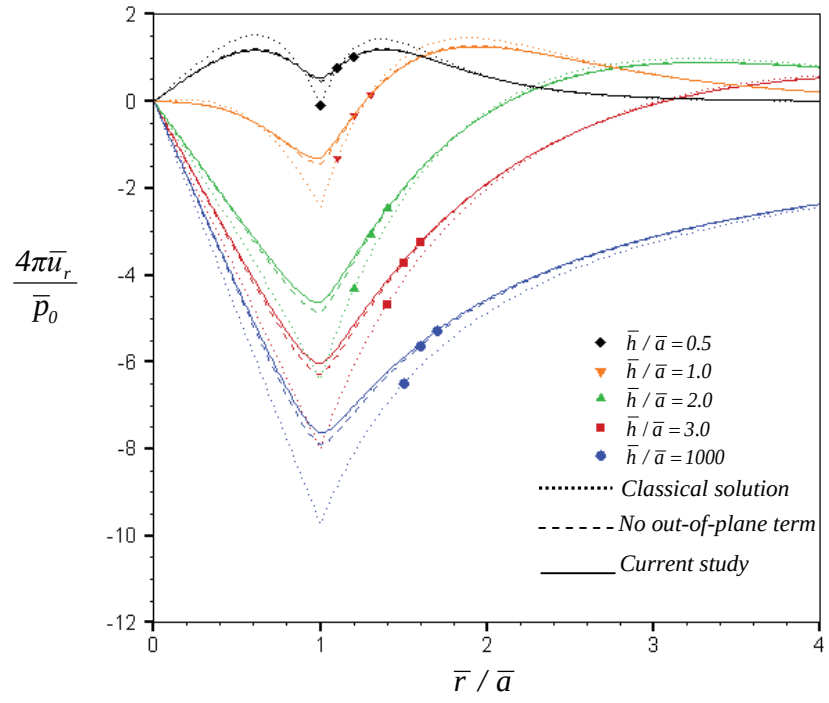

(a)

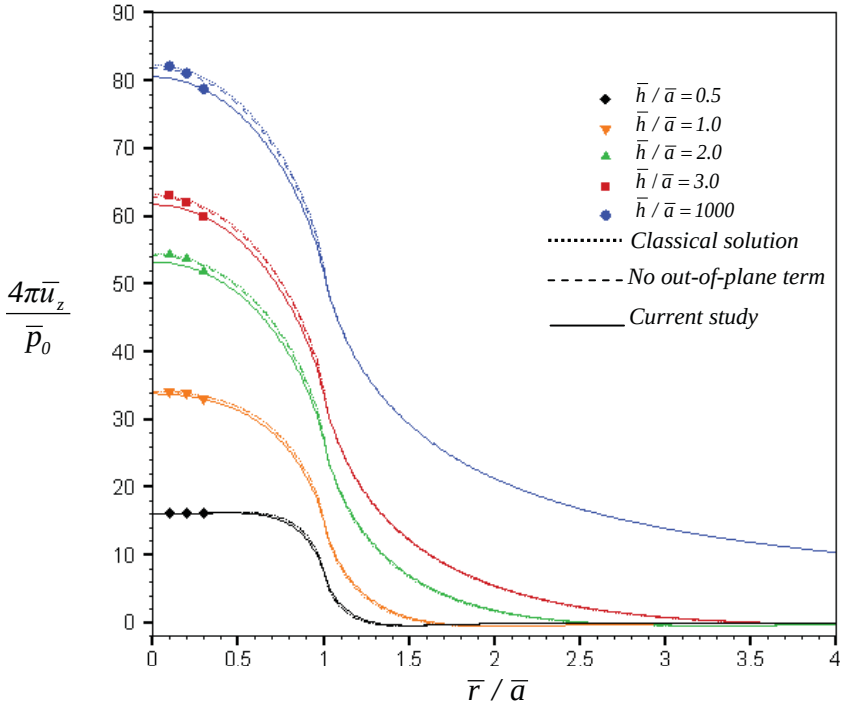

(b)

Figure 2.8 Normalized displacement profiles of an elastic layer under a uniformly distrubuted normal traction: (a) radial displacement and (b) vertical displacement

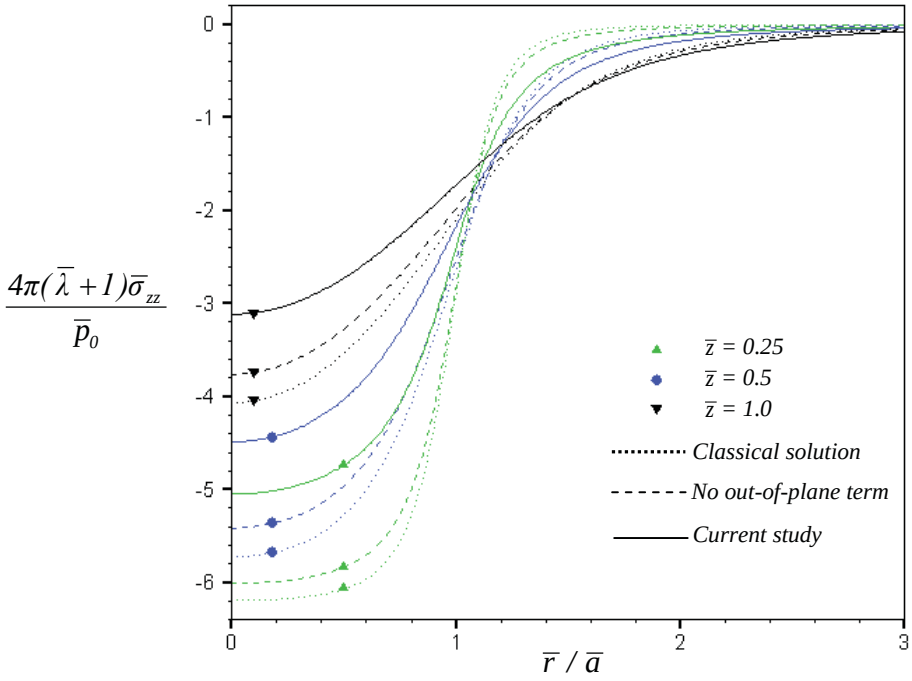

(a)

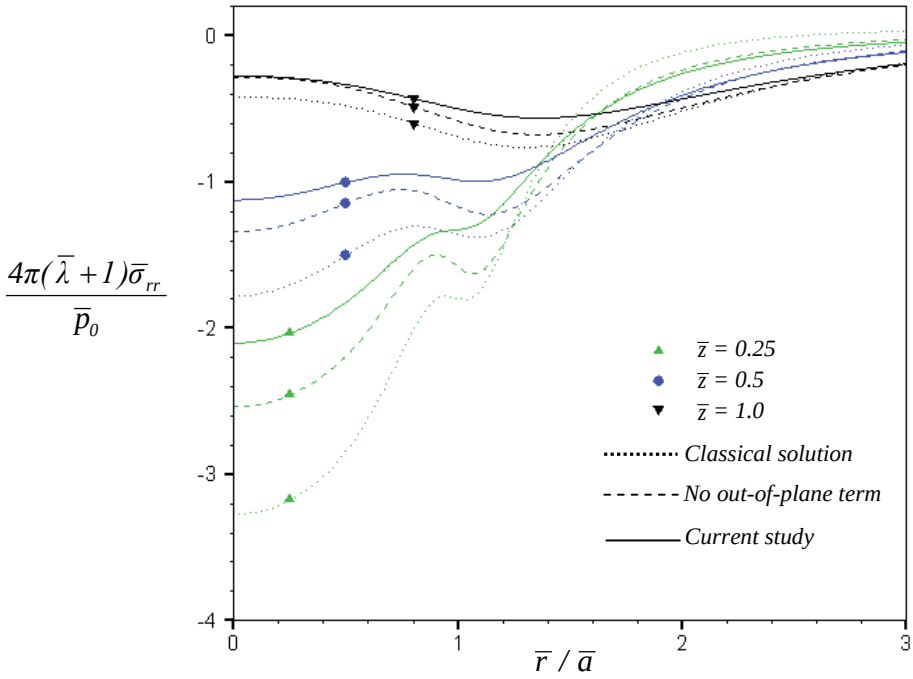

(b)

Figure 2.9 Normalized stress profiles of an elastic layer under a uniformly distrubuted normal traction: (a) vertical stress and (b) radial stress

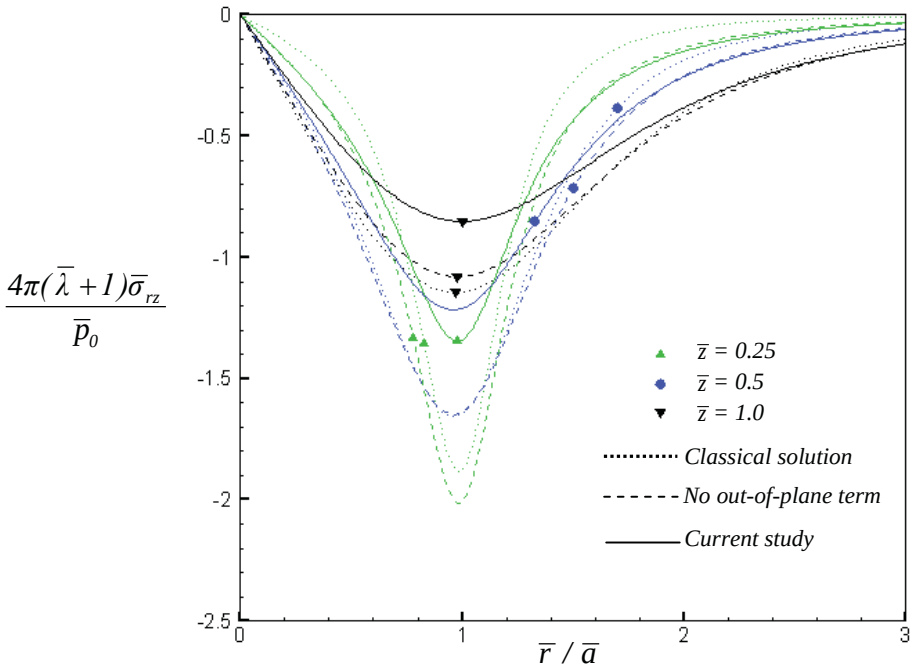

(a)

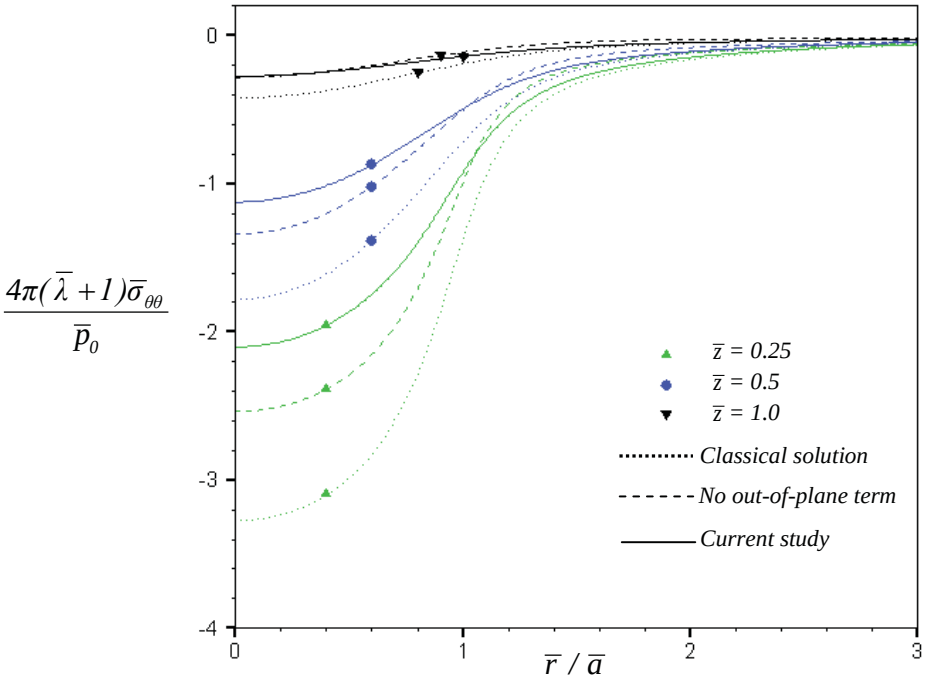

(b)

Figure 2.10 Normalized stress profiles of an elastic layer under a uniformly distrubuted normal traction: (a) shear stress and (b) hoop stress

Results for the normalized shear stress $4\pi(\bar{\lambda}+1)\bar{\sigma}_{rz}/\bar{p}_0$ are reported in Figure 2.10(a) for various depths. Behaviors of the shear stress for all three models along the radial direction exhibit the similar trend. In particular, the shear stress vanishes at $\bar{r}=0$ due to the symmetry, rapidly increases to reach its peak at the edge of the surface loading (i.e. $\bar{r}/\bar{a}=1$), and promptly decreases thereafter. It is worth noting that in the region very near the edge of surface loading the surface energy effects significantly lower the magnitude of shear stress, especially in a model including the out-of-plane contribution of the residual surface tension. As anticipated, the influence of surface stresses is quite large in a region near the surface and insignificant in a region far away from the surface.

Variation along the radial direction of the normalized radial stress $4\pi(\bar{\lambda}+1)\bar{\sigma}_{rr}/\bar{p}_0$ and normalized hoop stress $4\pi(\bar{\lambda}+1)\bar{\sigma}_{\theta\theta}/\bar{p}_0$ are respectively presented for various depths in Figure 2.9(b) and 2.10(b). Again, results obtained from all three models possess the similar trend, i.e., starting with their maximum value and gradually decreasing as $\bar{r}$ increases. This observed behavior excludes the case of the radial stress at $\bar{z}=1.0$ since such stress starts at a certain value, gradually reaches its peak, and then slowly decays. However, the surface energy effects on these two stress components are similar to those on the vertical stress, i.e. lower stress within a region under the surface loading and slightly higher stress in the outside region. In addition, strong influence of the surface stresses is observed in the region near the surface. Through the proper normalization, solutions obtained by a model without the surface energy effects exhibit no size-dependency. However, this is not true for results predicted by models incorporating the surface energy effects. The size-dependent behavior can be observed due to the presence of an intrinsic length scale associated with the presence of the surface stresses. In this study, the size-dependency of all normalized stresses is investigated by varying the radius of surface loading while maintaining the ratio $\bar{h}/\bar{a}$. Results are reported in Figures 2.11-2.14 for $\bar{h}/\bar{a}=3$. In particular, Figures 2.11(a), 2.12(a), 2.13(a) and 2.14(a) show the variation along the radial direction of non-zero stress components at $\bar{z}/\bar{a}=0.1$ for three different radius whereas Figures 2.11(b), 2.12(b), 2.13(b) and 2.14(b) present the relationship between normalized stress components and the radius of surface loading for three various depths and $\bar{r}/\bar{a}=0.5$.

Unlike the classical solutions, the results from the two models accounting for surface energy effects depend strongly on the normalized radius $\bar{a}$ for small $\bar{a}$, and such dependence becomes negligible as $\bar{a}$ increases. In particular, the results predicted by the model considering the out-of-plane contribution of residual surface tension exhibit much stronger size dependency than that excluding the out-of-plane term. In addition, this set of results confirms the necessity to consider the surface effects when responses in a region very close to the surface are of interest.

2.3.2.2 Linearly distributed tangential traction

Consider an infinite, rigid-based elastic layer subjected to a linearly distributed tangential traction in a circular region of radius *a* as shown in Figure 2.15. This traction is normalized such that $\bar{q}(\bar{r})=\bar{q}_0\bar{r}/\bar{a}$ where $\bar{q}_0=q_0/\mu$, $\bar{a}=a/\Lambda$, and q_0 is the maximum traction at the edge of surface loading. Results for radial and vertical displacements for different layer thicknesses are shown in Figures 2.16(a)-(b), respectively. It is obvious from these results that the presence of surface energy effects significantly lowers the magnitude of the displacement. However, the out-of-plane contribution of residual surface tension has a strong influence only on the vertical displacement and becomes negligible for the radial displacement. Moreover, when varying the layer thickness, both radial and vertical displacements are higher as the layer thickness increases.

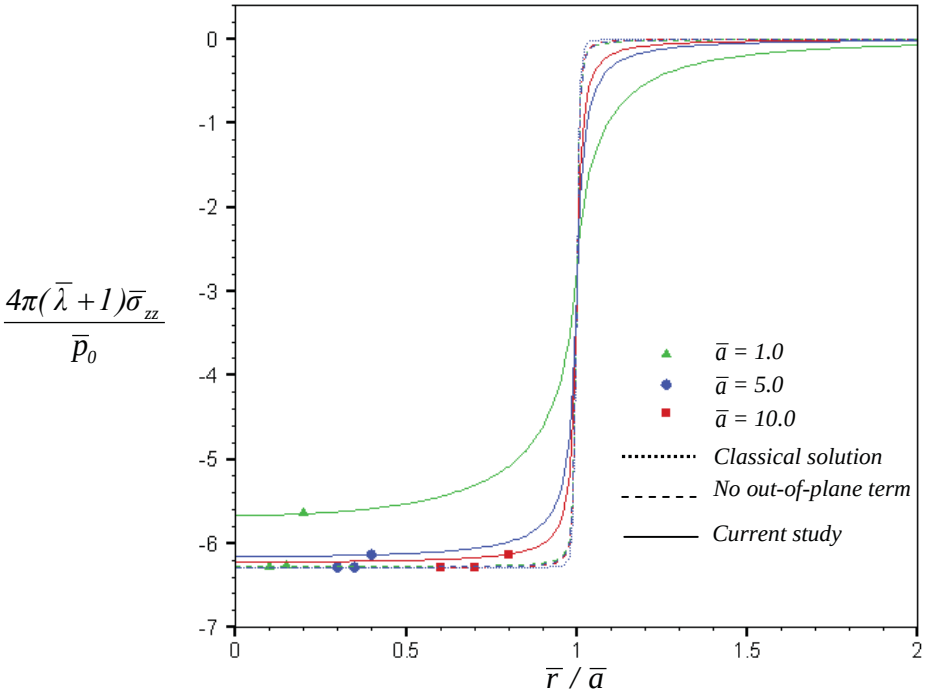

(a)

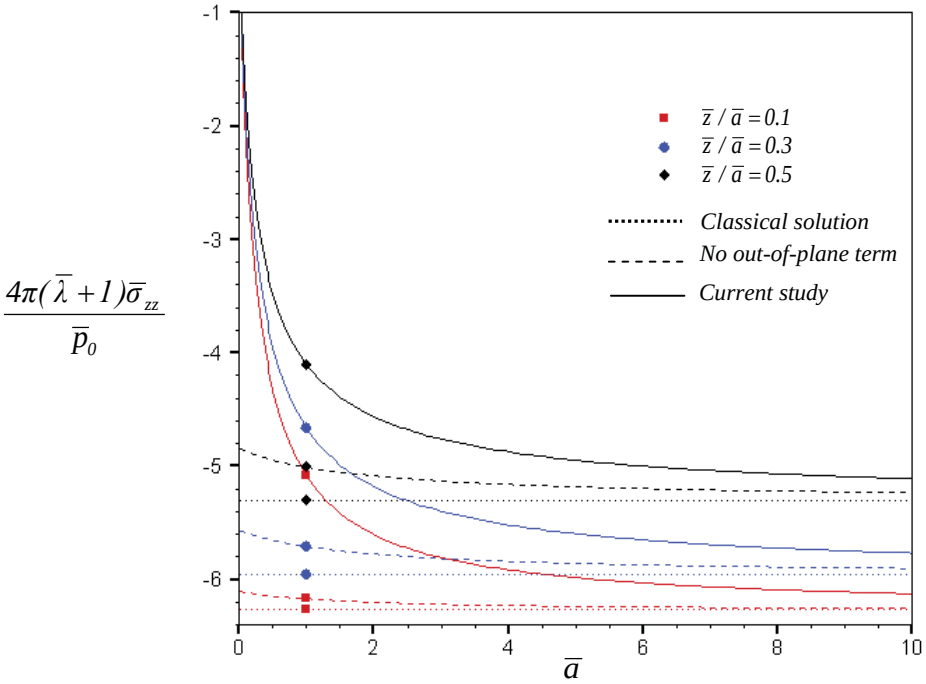

(b)

Figure 2.11 Normalized vertical stress of elastic layer under a uniformly distrubuted normal traction for $\bar{h}/\bar{a}=3$: (a) profile along radial direction and (b) at $\bar{r}/\bar{a}=0.5$

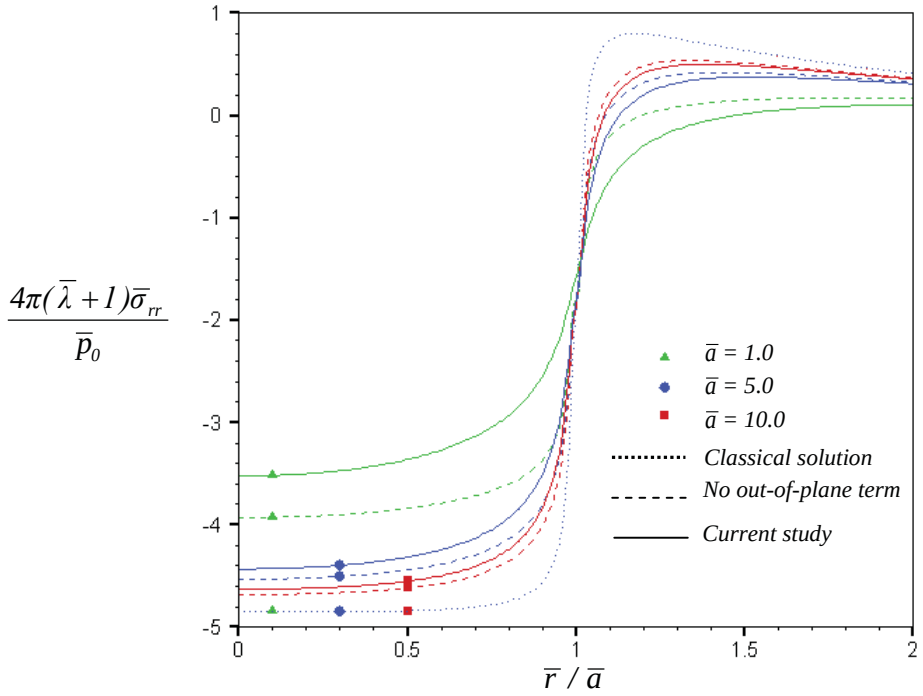

(a)

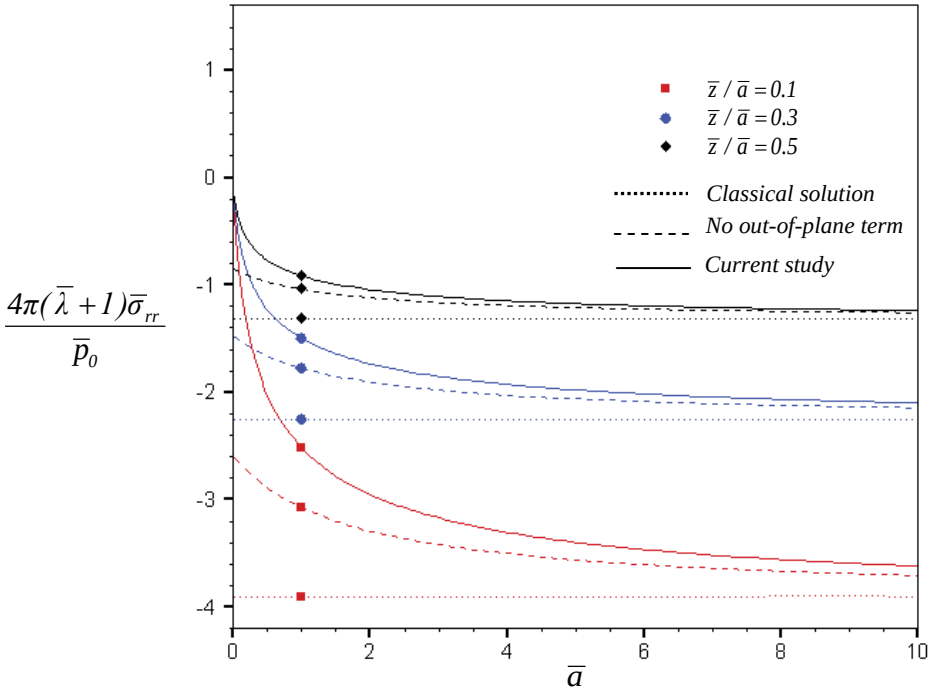

(b)

Figure 2.12 Normalized radial stress of an elastic layer under a uniformly distrubuted normal traction for $\bar{h} / \bar{a} = 3$: (a) profile along radial direction and (b) at $\bar{r} / \bar{a} = 0.5$

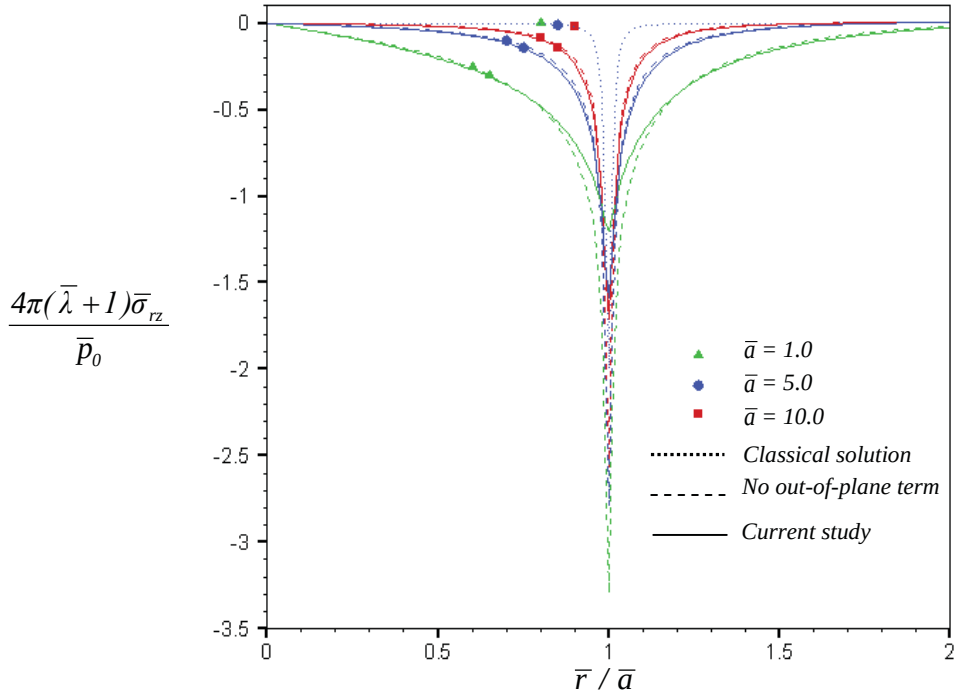

(a)

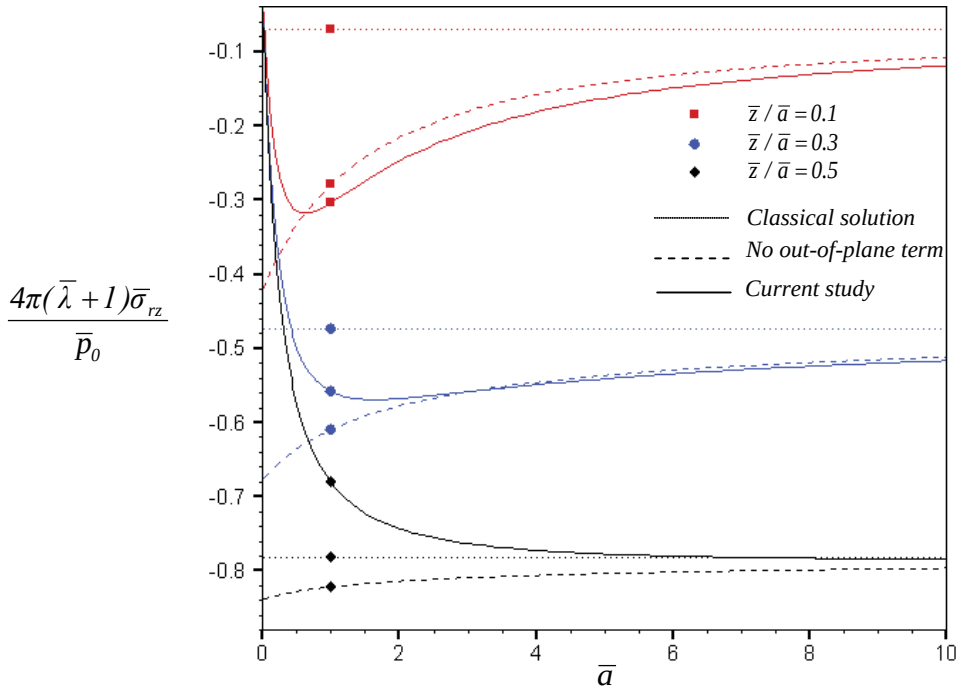

(b)

Figure 2.13 Normalized shear stress of an elastic layer under a uniformly distrubuted normal traction for $\bar{h}/\bar{a}=3$: (a) profile along radial direction and (b) at $\bar{r}/\bar{a}=0.5$

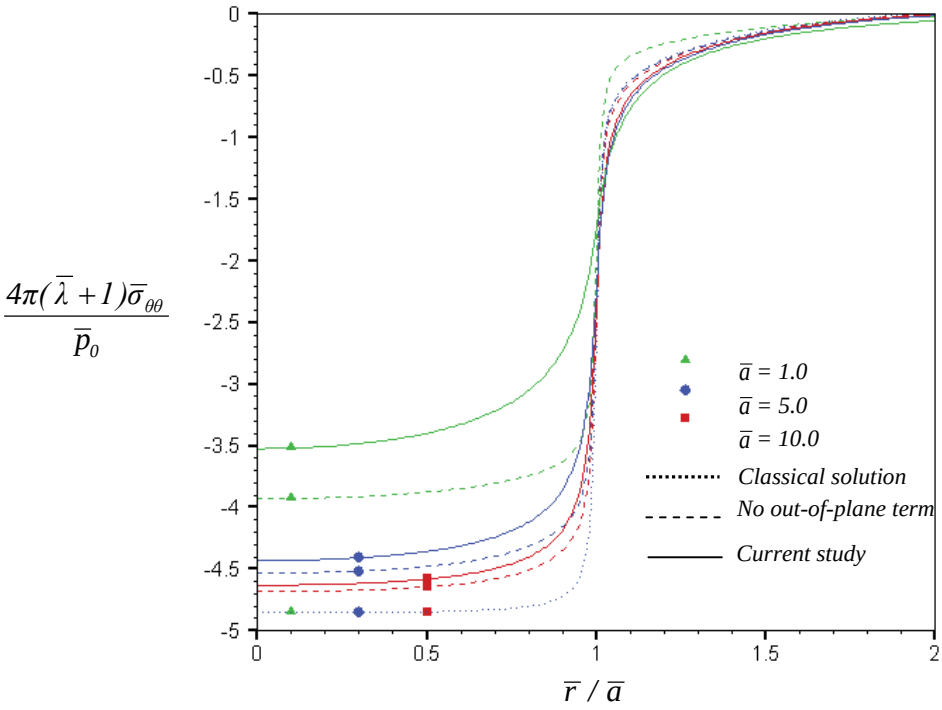

(a)

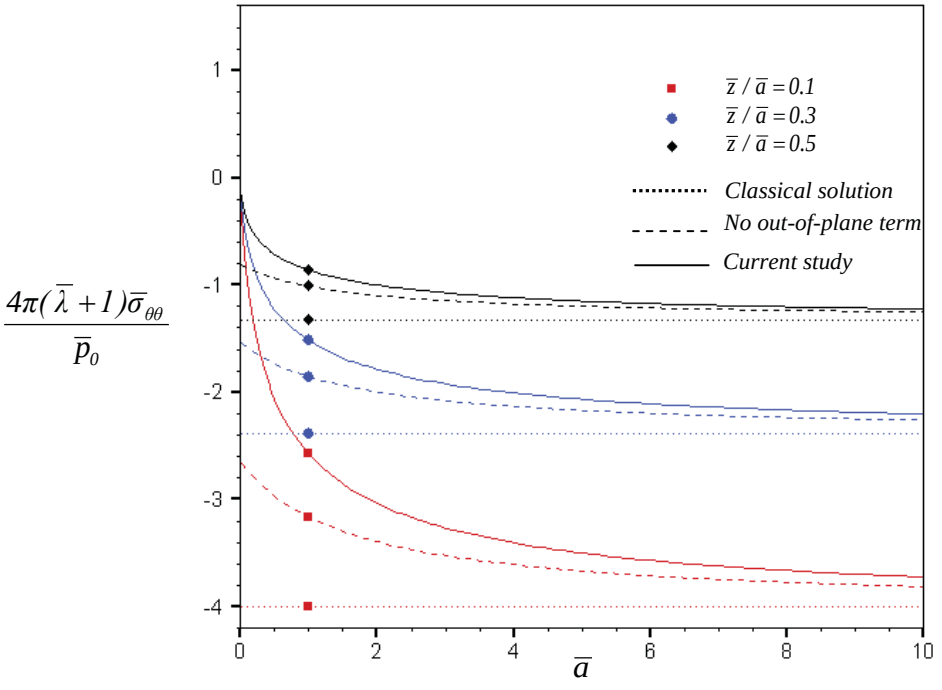

(b)

Figure 2.14 Normalized hoop stress of an elastic layer under a uniformly distrubuted normal traction for $\bar{h}/\bar{a}=3$: (a) profile along radial direction and (b) at $\bar{r}/\bar{a}=0.5$

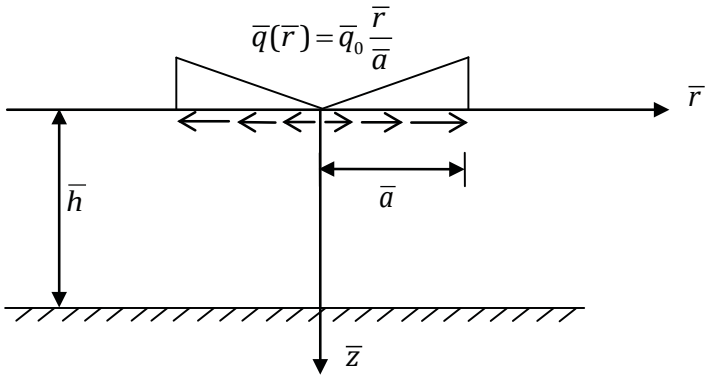

Figure 2.15 Three-dimensional, infinite, rigid-based, elastic layer subjected to a linearly distributed tangential traction

The results for stress components are obtained for $\bar{h} = 10$, $\bar{a} = 1$, and three different normalized depths (i.e., $\bar{z} = 0.25, \bar{z} = 0.5, \bar{z} = 1.0$). Profiles of the normalized vertical stresses $4\pi(\bar{\lambda}+1)\bar{\sigma}_{zz} / \bar{q}_0$ and the normalized radial stresses $4\pi(\bar{\lambda}+1)\bar{\sigma}_{rr} / \bar{q}_0$ along the radial direction are reported in Figure 2.17. At a small depth, the tensile stress is observed within a region of surface loading, and it gradually changes to the compressive stress when passing the edge of a loading region. The vertical stress and radial stress profiles also show the strong influence of the surface energy effects for the region relatively near the surface. Moreover, the discrepancy of the results predicted by the two models, with and without the out-of-plane contribution of residual surface tension, is more apparent for the vertical stress but negligible for the radial stress.

Results for the normalized shear stress $4\pi(\bar{\lambda}+1)\bar{\sigma}_{rz} / \bar{q}_0$ are shown in Figure 2.18(a) for various depths. For this particular loading condition, the shear stress increases to reach its peak near the edge of loading region and then abruptly decreases to zero after passing the edge of loading region. Again, the influence of surface stresses on this shear stress component is more apparent for the region close to the surface. From the profiles of normalized hoop stress $4\pi(\bar{\lambda}+1)\bar{\sigma}_{\theta\theta} / \bar{q}_0$ shown in Figure 2.18(b), the results obtained from the two models including the surface energy effects are significantly different from the classical solution, and such discrepancy increases when the depth decreases. It is worth noting that the contribution of the out-of-plane term is insignificant since the two models yield almost identical hoop stress.

To demonstrate the size-dependent behavior of a layer subjected to a linearly distributed tangential load, a scheme similar to that used to study a layer subjected to uniformly distributed normal traction is employed. The layer thickness and the radius of loading region are varied while their ratios are fixed (i.e., $\bar{h} / \bar{a} = 3$). The variation along the radial direction of non-zero stress components at $\bar{z} / \bar{a} = 0.1$ for three different radius are reported in Figures 2.19(a), 2.20(a), 2.21(a) and 2.22(a) whereas the relationship between normalized stress components and the radius of loading region for three various depths and $\bar{r} / \bar{a} = 0.5$ are shown in Figures 2.19(b), 2.20(b), 2.21(b) and 2.22(b). Unlike the case of uniformly distributed normal load, the out-of-plane contribution of the residual surface tension has significant influences only on the vertical stress. However, the solutions obtained from the two models accounting for the surface energy effects still show the size-dependency. As the radius $\bar{a}$ and the depth where the responses are determined decrease, the surface energy effects become more important.

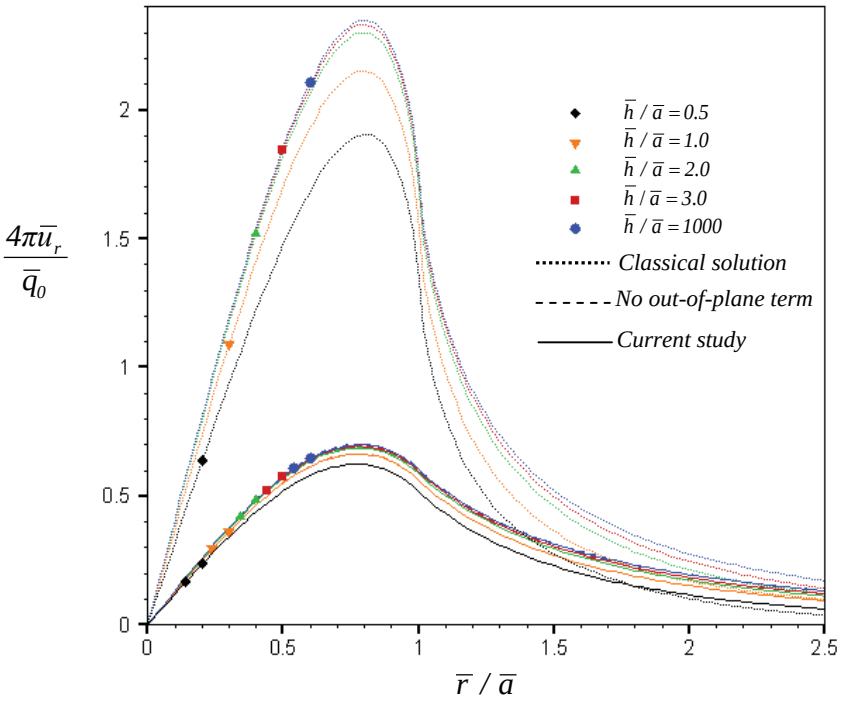

(a)

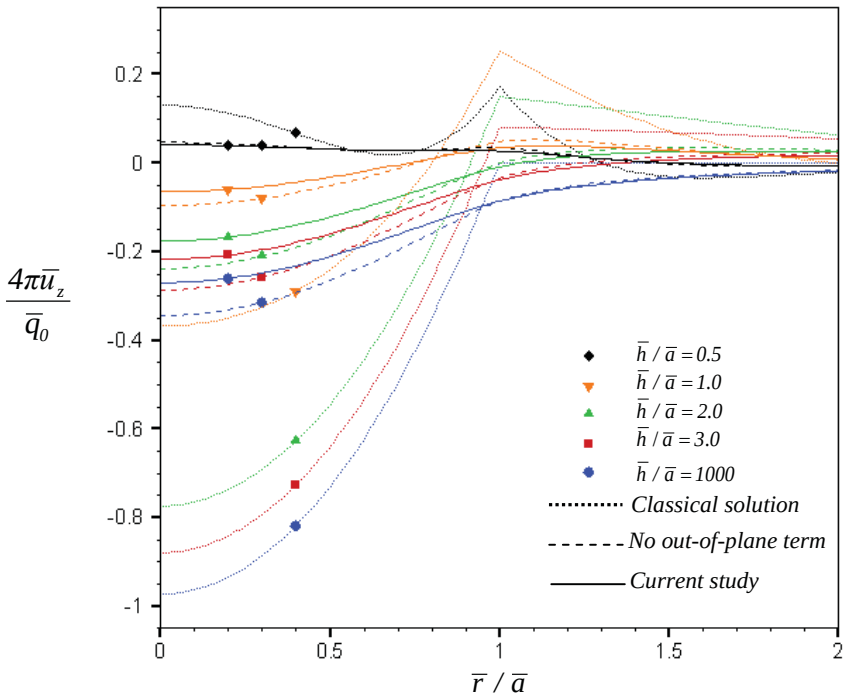

(b)

Figure 2.16 Normalized displacement profiles of an elastic layer under a linearly distrubuted tangential load: (a) radial displacement and (b) vertical displacement

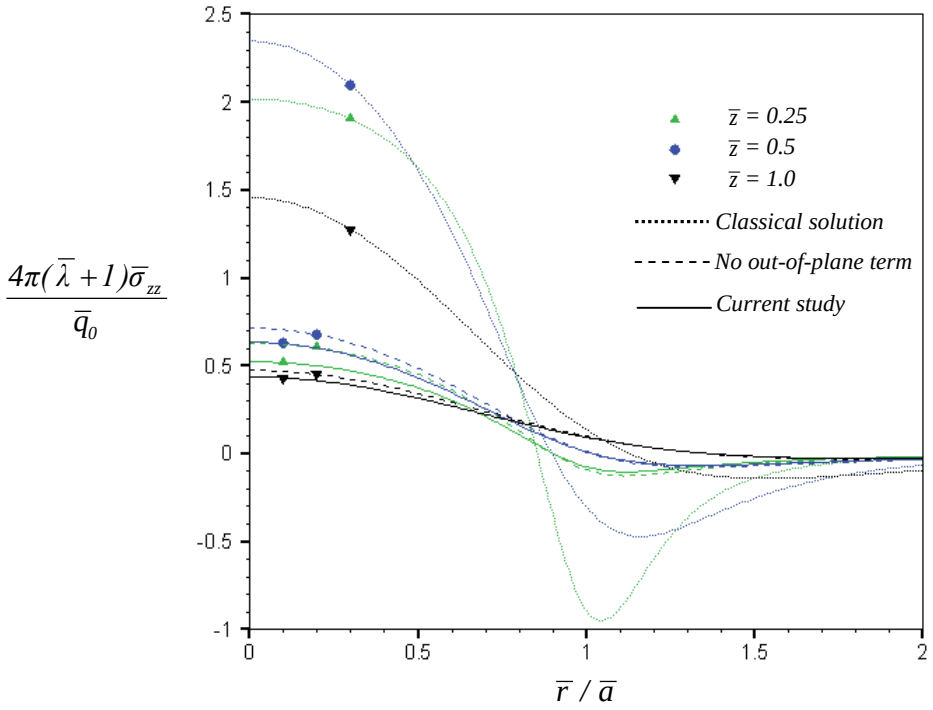

(a)

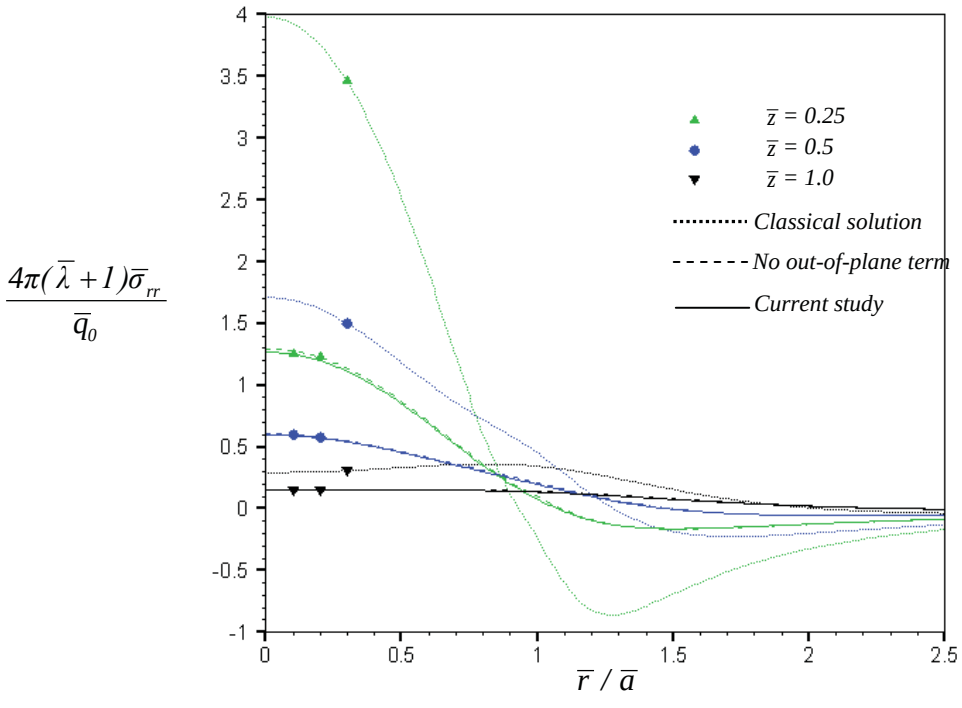

(b)

Figure 2.17 Normalized stress profiles of an elastic layer under a linearly distrubuted tangential load: (a) vertical stress and (b) radial stress

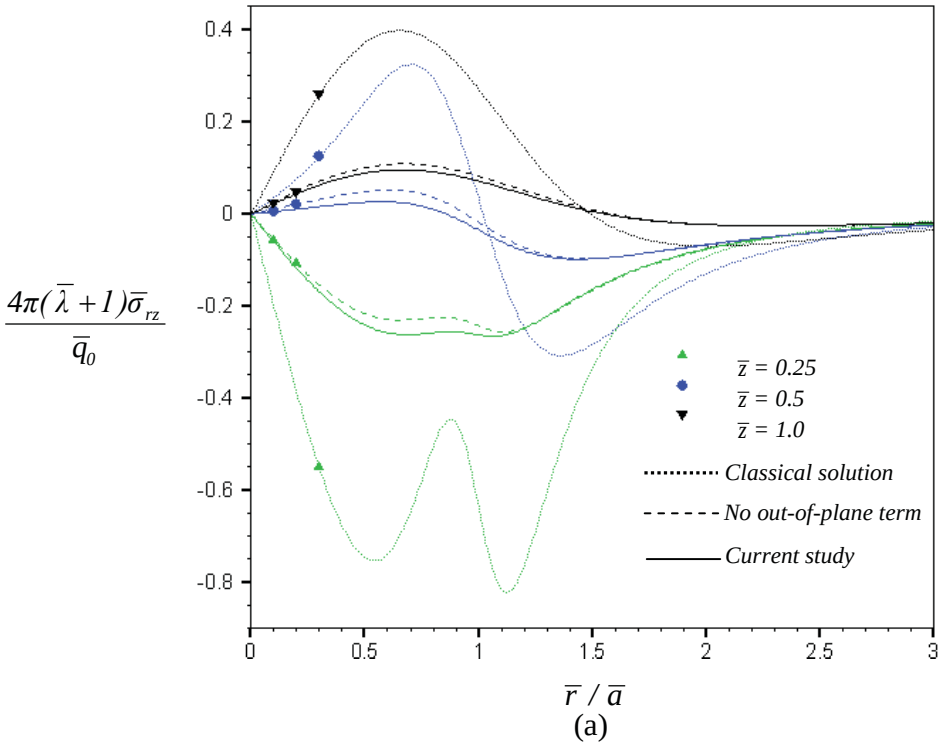

(a)

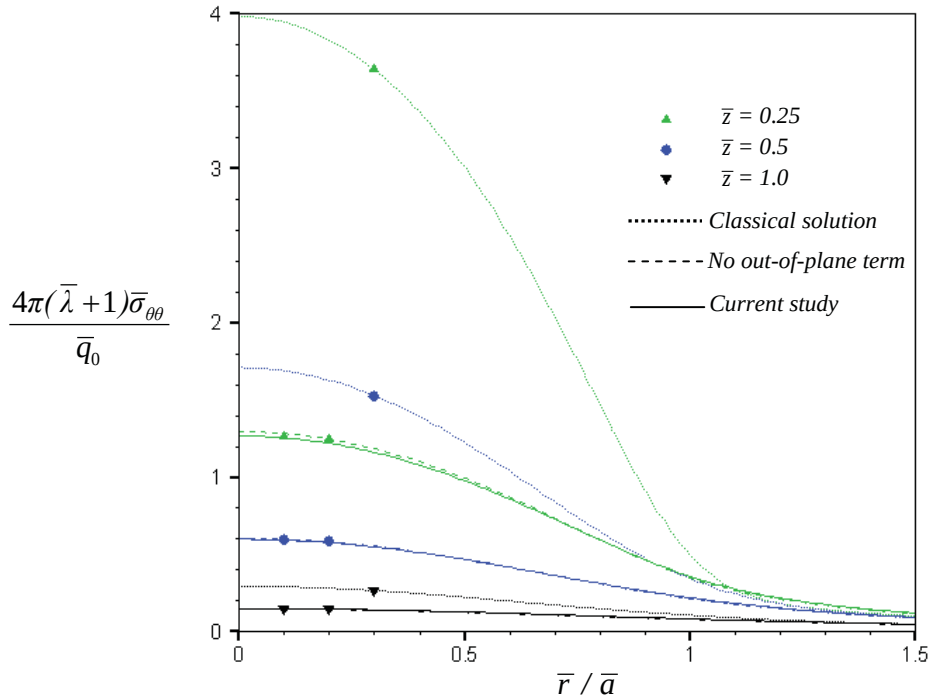

(b)

Figure 2.18 Normalized stress profiles of an elastic layer under a linearly distrubuted tangential load: (a) shear stress and (b) hoop stress

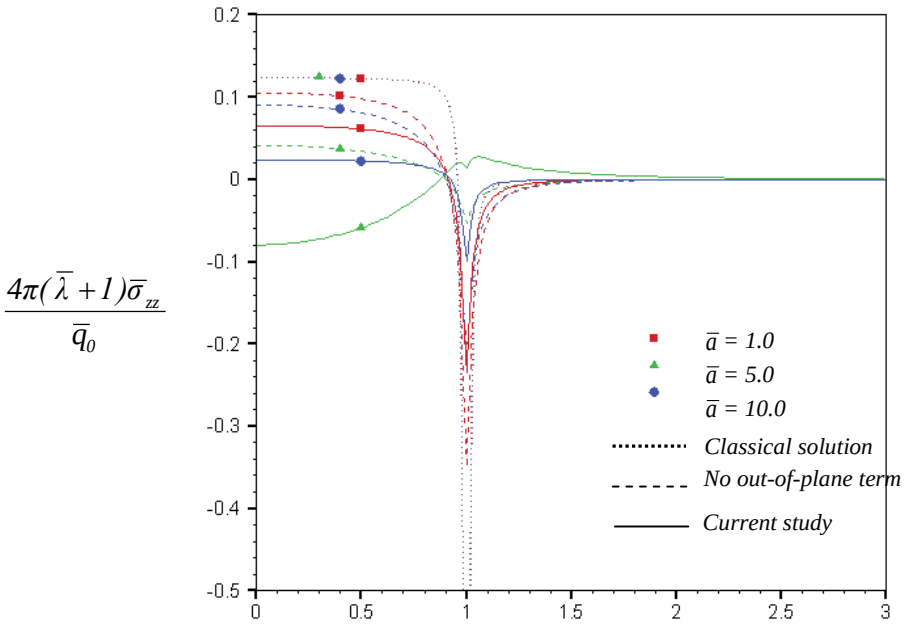

(a)

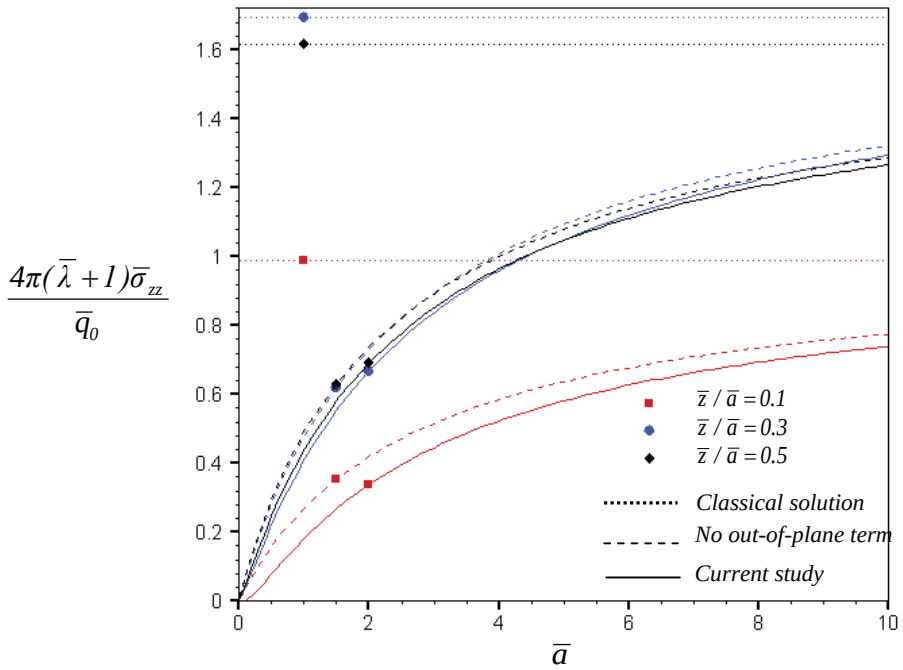

(b)

Figure 2.19 Normalized vertical stress of an elastic layer under a linearly distrubuted tangential load for $\bar{h} / \bar{a} = 3$: (a) profile along radial direction and (b) at $\bar{r} / \bar{a} = 0.5$

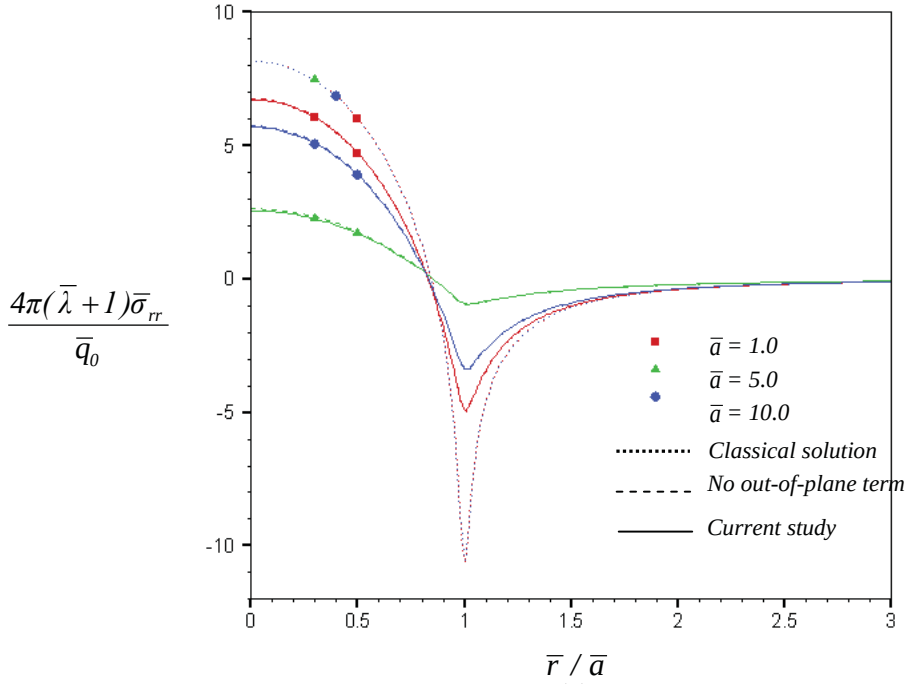

(a)

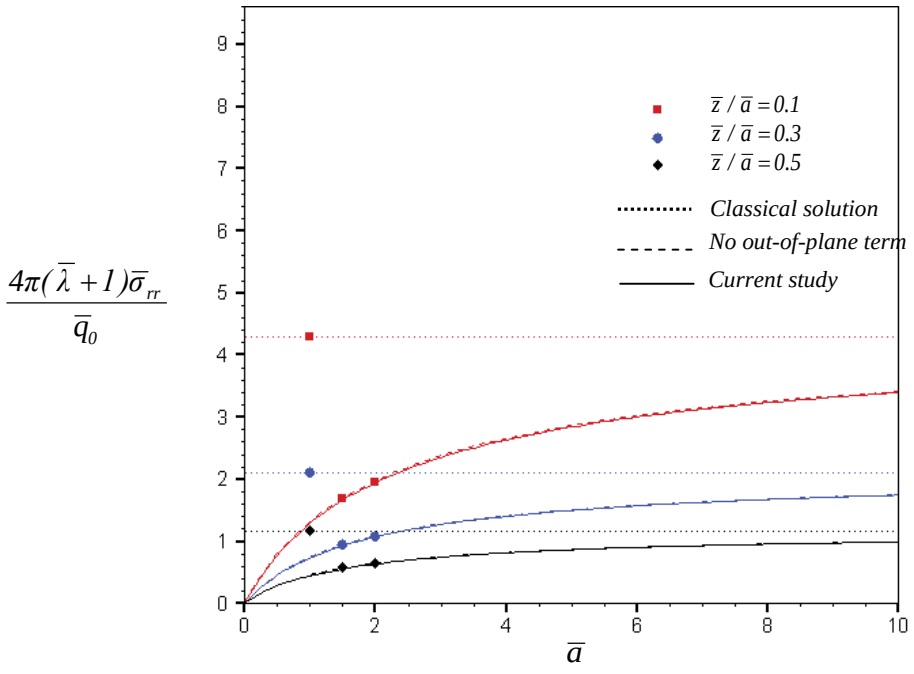

(b)

Figure 2.20 Normalized radial stress of an elastic layer under a linearly distrubuted tangential load for $\bar{h} / \bar{a} = 3$: (a) profile along radial direction and (b) at $\bar{r} / \bar{a} = 0.5$

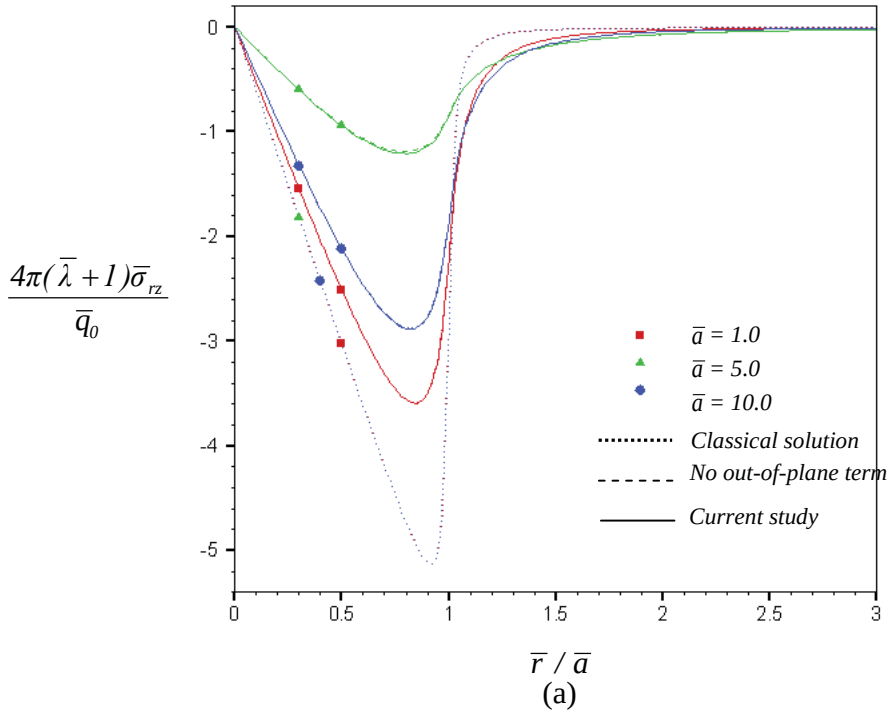

(a)

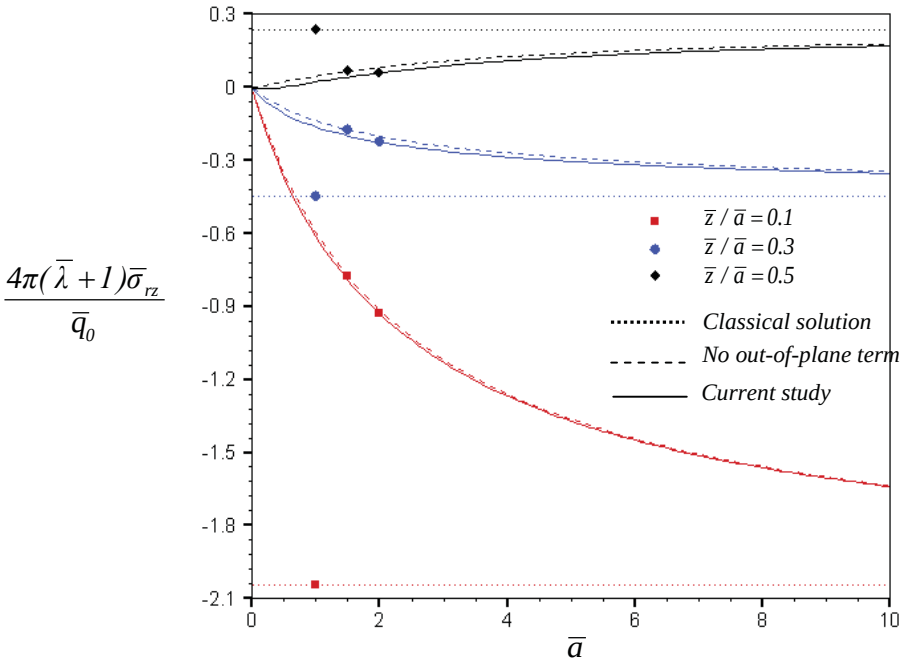

(b)

Figure 2.21 Normalized shear stress of an elastic layer under a linearly distrubuted tangential load for $\bar{h} / \bar{a} = 3$: (a) profile along radial direction and (b) at $\bar{r} / \bar{a} = 0.5$

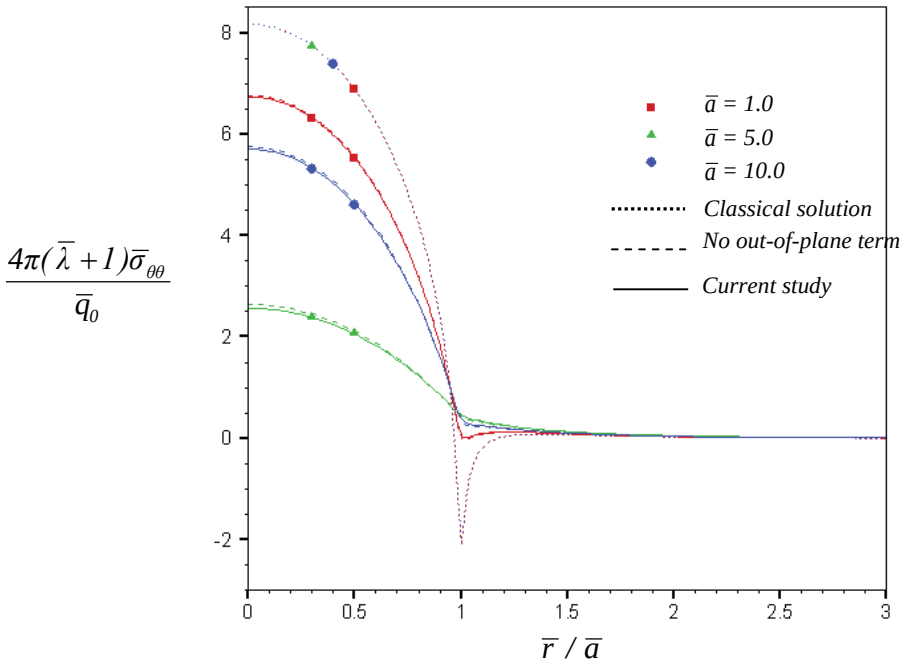

(a)

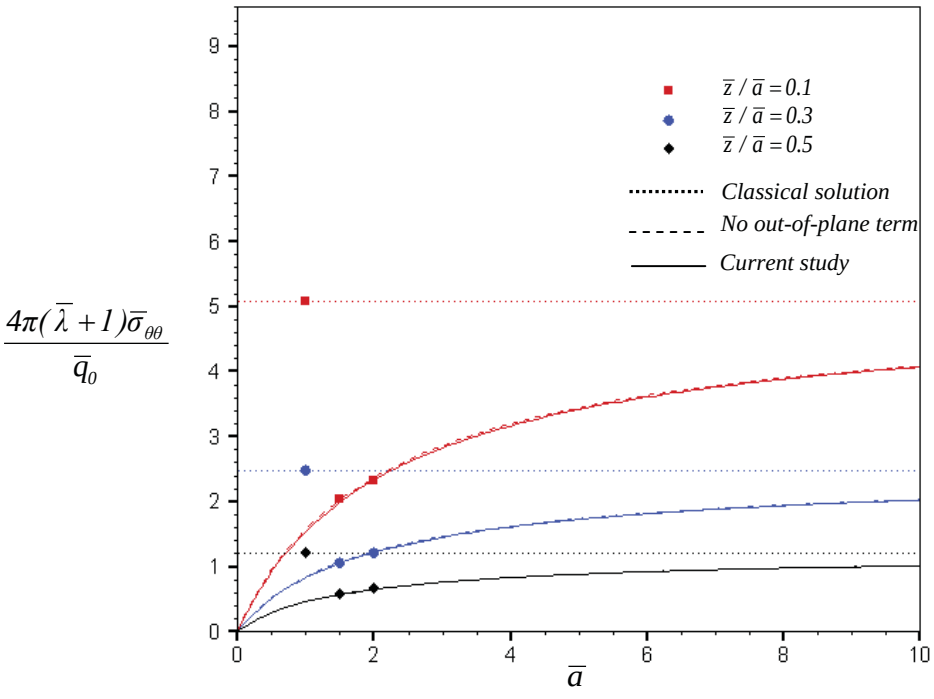

(b)

Figure 2.22 Normalized hoop stress of an elastic layer under a linearly distrubuted tangential load for $\bar{h} / \bar{a} = 3$: (a) profile along radial direction and (b) at $\bar{r} / \bar{a} = 0.5$

2.3.3 Fundamental solutions

Since the formulation has been established for arbitrary axisymmetric surface loading, general results can be further specialized to construct certain useful fundamental solutions. For instance, the solutions associated with a layer subjected to a normal concentrated load at the origin, a normal ring load at any radius a and a tangential ring load at any radius a can readily be obtained. These fundamental solutions constitute the basis for solving other related boundary value problems such as nano-indentation problems.

2.3.3.1 Layer under normal concentrated load

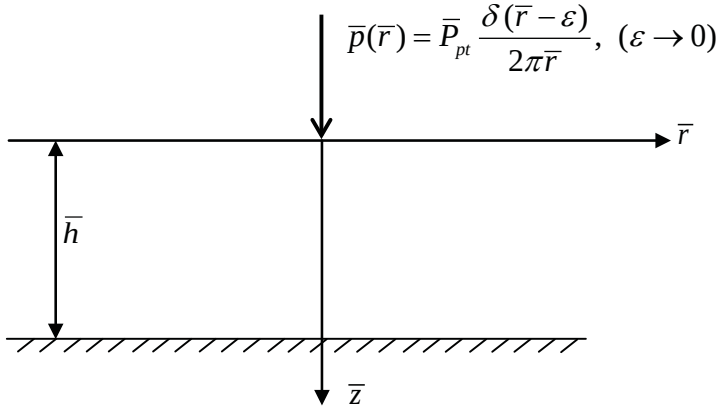

Figure 2.23 Three-dimensional, infinite, rigid-based, elastic layer subjected to a normal concentrated load

Consider a three-dimensional, infinite, rigid-based, elastic layer subjected to a normal concentrated load P_{pt} as shown in figure 2.23. The concentrated load P_{pt} is normalized such that $\bar{P}_{pt} = P_{pt} / \mu\Lambda^2$. Profiles of the normalized radial displacement $2\pi\bar{h}\bar{E}\bar{u}_r / \bar{P}_{pt}$ and the normalized vertical displacement $2\pi\bar{h}\bar{E}\bar{u}_r / \bar{P}_{pt}$ at the surface obtained by three different models are reported for four different layer thicknesses ($\bar{h} = 0.5, \bar{h} = 1.0$, $\bar{h} = 2.0$, and $\bar{h} = 3.0$) in Figure 2.24(a) and 2.24(b), respectively. It is found that the normalized radial displacement is singular at $\bar{r} = 0$ except for the solution obtained from a model accounting for the out-of-plane contribution of residual surface stress. On the other hand, the results of normalized vertical displacement tend to be infinite under the concentrated load for all cases and reduce rapidly when $\bar{r}$ increases. In addition, the similar behavior is observed for all layer thicknesses under consideration, and the magnitude of the displacement is higher as the layer thickness increases.

In order to clearly demonstrate the influence of surface energy effects on the stress field, the layer thickness is chosen to be sufficiently large (i.e. $\bar{h} = 10$). Numerical results of all normalized non-zero stress components are reported along the radial direction for various depths in Figures 2.25-2.26. Clearly, the normalized vertical stress $4\pi\bar{h}^2(\bar{\lambda}+1)\bar{\sigma}_{zz} / \bar{P}_{pt}$ reaches its peak at $\bar{r} = 0$, and then decrease monotonically to zero as $\bar{r}$ increases. The normalized radial stress $4\pi\bar{h}^2(\bar{\lambda}+1)\bar{\sigma}_{rr} / \bar{P}_{pt}$ decreases from a positive value to a negative value for small $\bar{r}$, and then

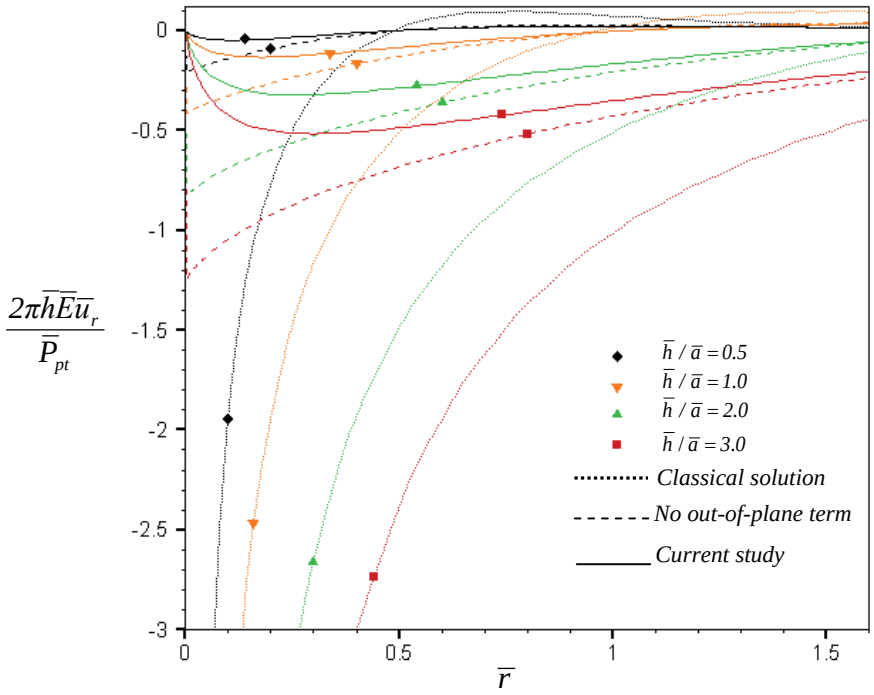

(a)

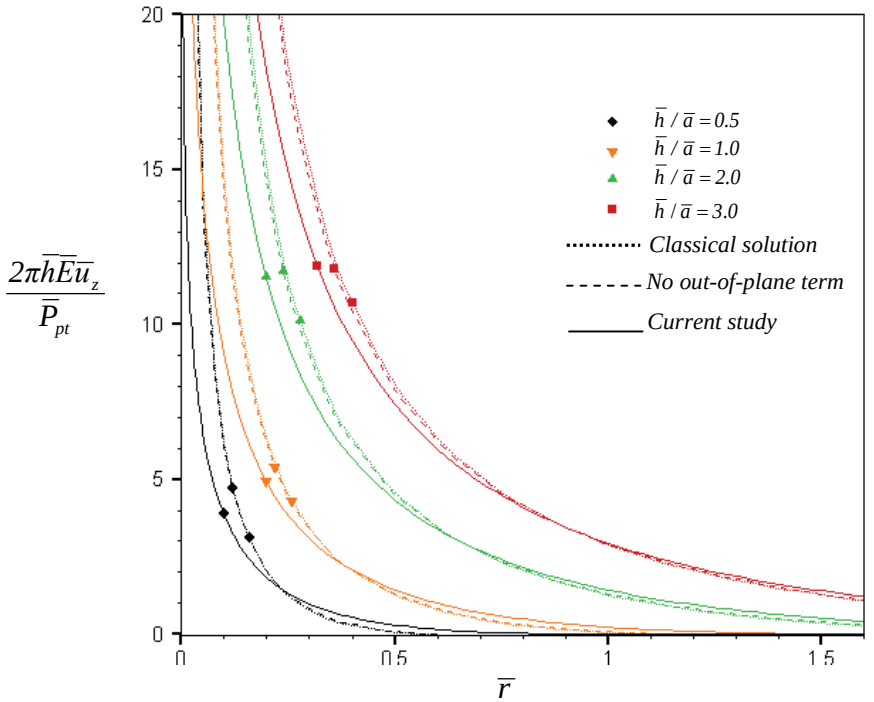

(b)

Figure 2.24 Normalized displacement profiles of an elastic layer under a normal concentrated load: (a) radial displacement and (b) vertical displacement

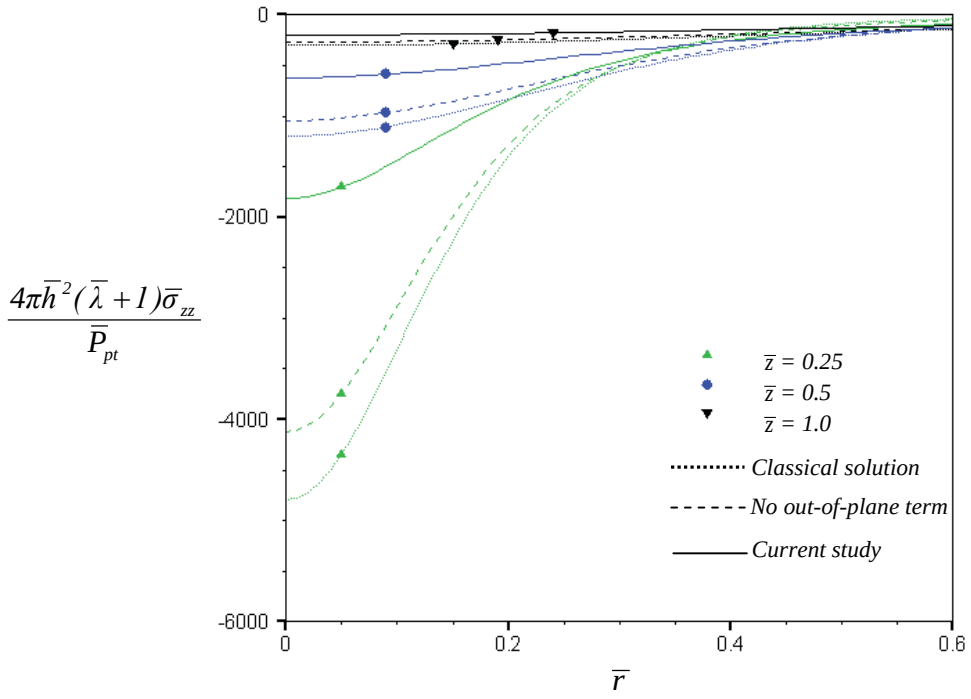

(a)

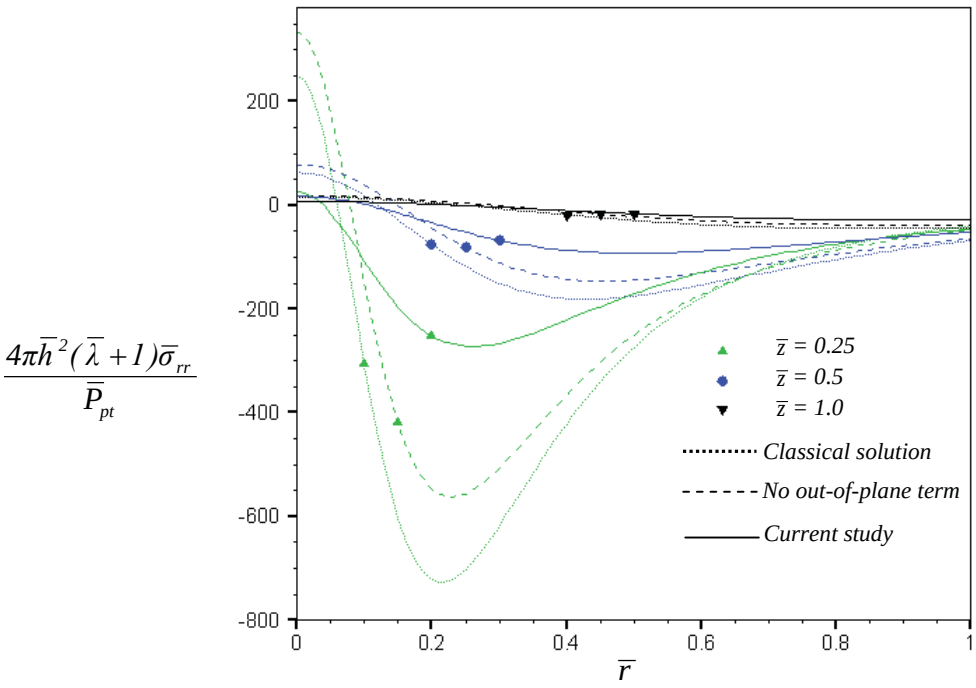

(b)

Figure 2.25 Normalized stress profiles of an elastic layer under a normal concentrated load: (a) vertical stress and (b) radial stress

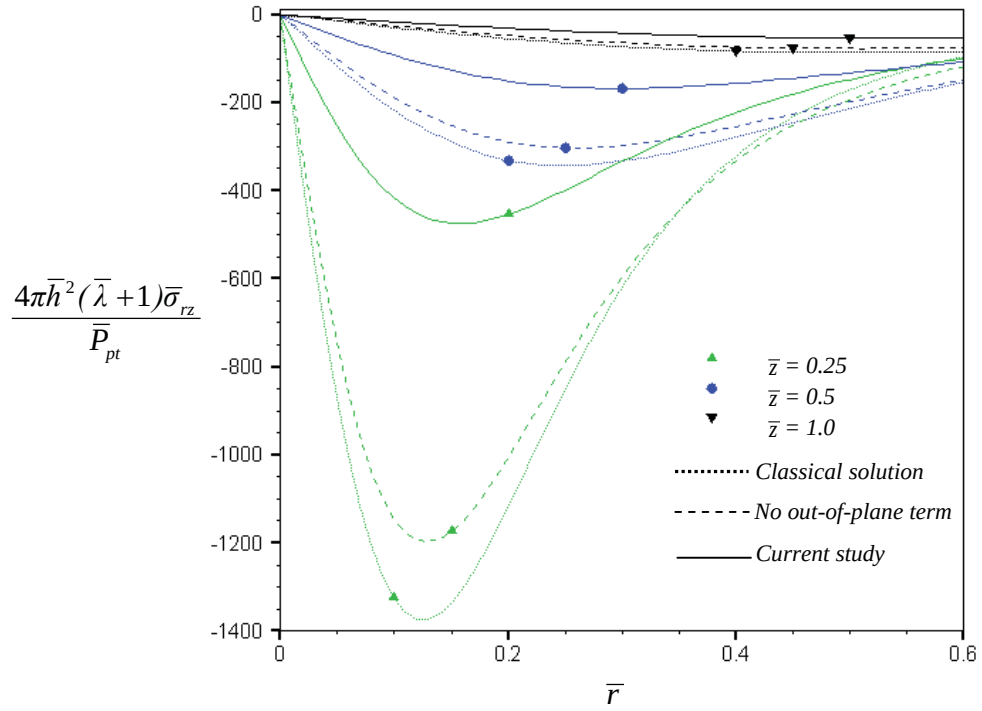

(a)

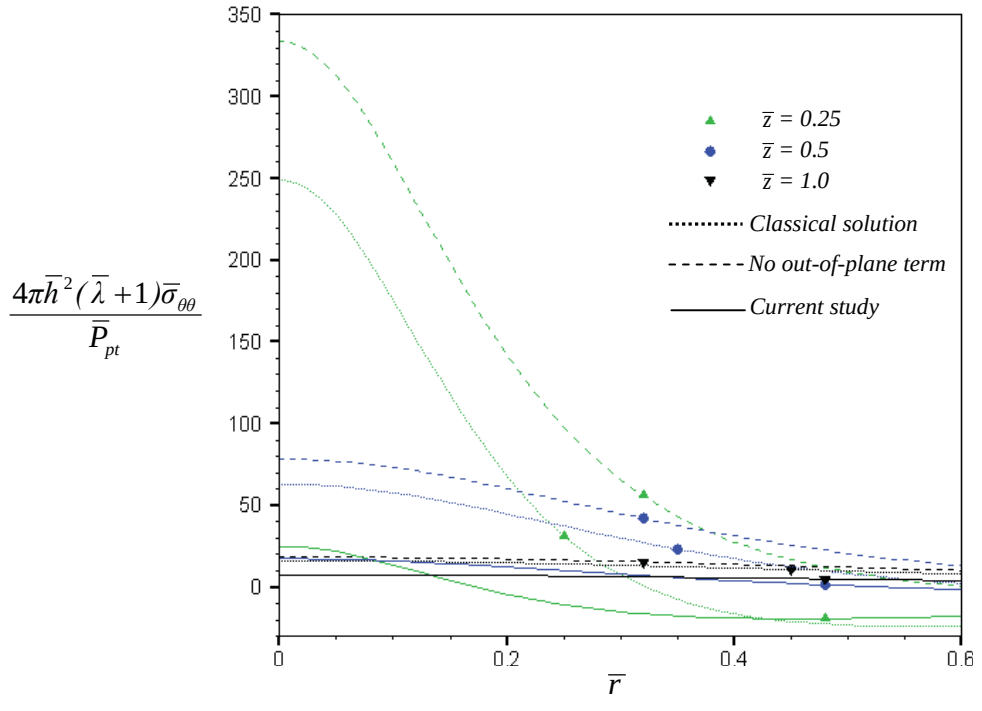

(b)

Figure 2.26 Normalized stress profiles of an elastic layer under a normal concentrated load: (a) shear stress and (b) hoop stress

attains its maximum negative value in the range $0.2 < \bar{r} < 0.5$. Thereafter, it magnitude gradually reduces to zero in the region further away from the concentrated load. Due to the symmetry, the normalized shear stress vanishes at $\bar{r} = 0$, then rapidly increases to reach its peak, and gradually decreases to zero for a large $\bar{r}$. It is obvious that presence of surface energy effects generally reduce the magnitude of all stress components when compared to their classical counterpart except for the normalized hoop stress, whose values predicted by the model accounting for surface energy effects but without the out-of-plane contribution of residual surface stress. In that case, the hoop stresses are much larger than those obtained from the classical model.

2.3.3.2 Layer under normal ring load

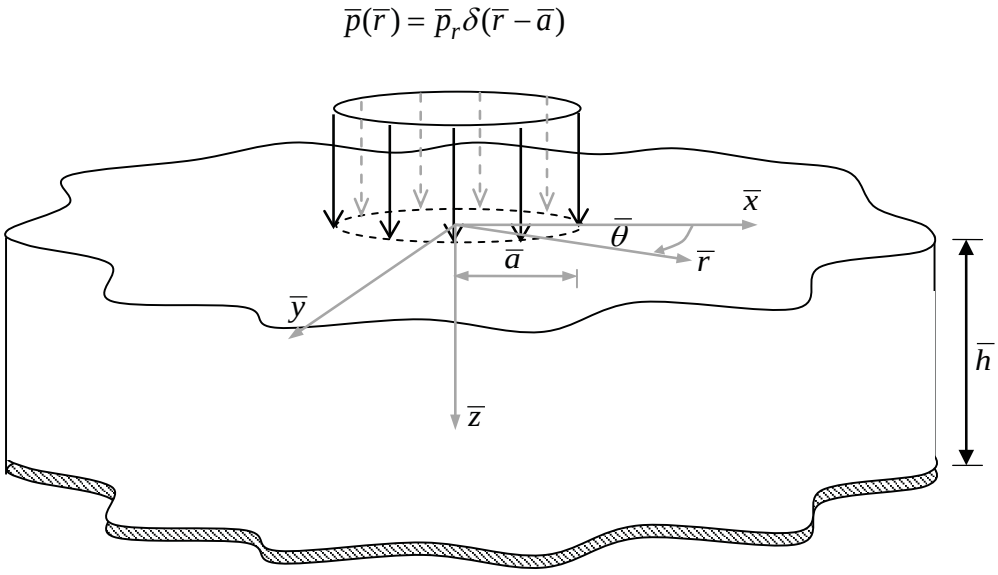

Figure 2.27 Three-dimensional, infinite, rigid-based, elastic layer subjected to a normal ring load

Consider a three-dimensional, infinite, rigid-based, elastic layer subjected to a normal ring load p_r at the radius a as shown in figure 2.27. The ring load and the radius *a* are normalized such that $\bar{p}_r = p_r / \mu\Lambda$ and $\bar{a} = a / \Lambda$. Results for the normalized radial displacement $4\pi\bar{h}\bar{u}_r / \bar{p}_r$ and the normalized vertical displacement $4\pi\bar{h}\bar{u}_z / \bar{p}_r$ at the surface are plotted along the radial direction as shown in Figure 2.28 for four different thicknesses ($\bar{h} = 0.5, \bar{h} = 1.0, \bar{h} = 2.0$, and $\bar{h} = 3.0$) and $\bar{a} = 1$. It is apparent from the obtained results in Figure 2.28(a) that the radial displacement for the classical case exhibits rapid variation at location of the applied ring load while those obtained from the other two models are finite and smooth, which are significantly different from the classical one. It can also be seen from Figure 2.28(b) that the vertical displacements predicted by the classical model and a model considering the surface energy effect without the out-of-plane term are slightly different, and singular at the location of applied load. On the other hand, the vertical displacements obtained from the model incorporating the out-of-plane term are finite, which are quite different from the other two solutions.

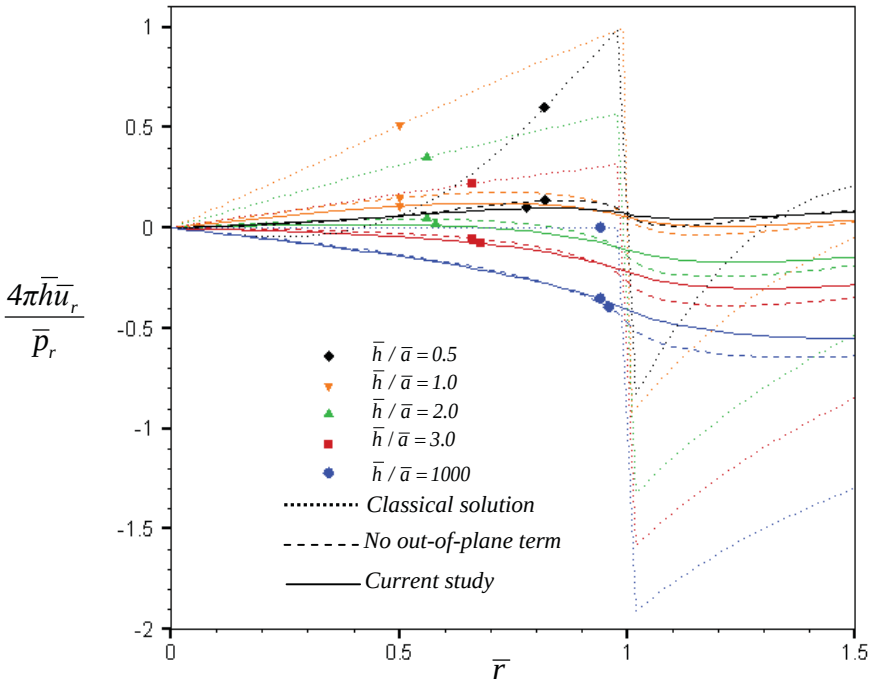

(a)

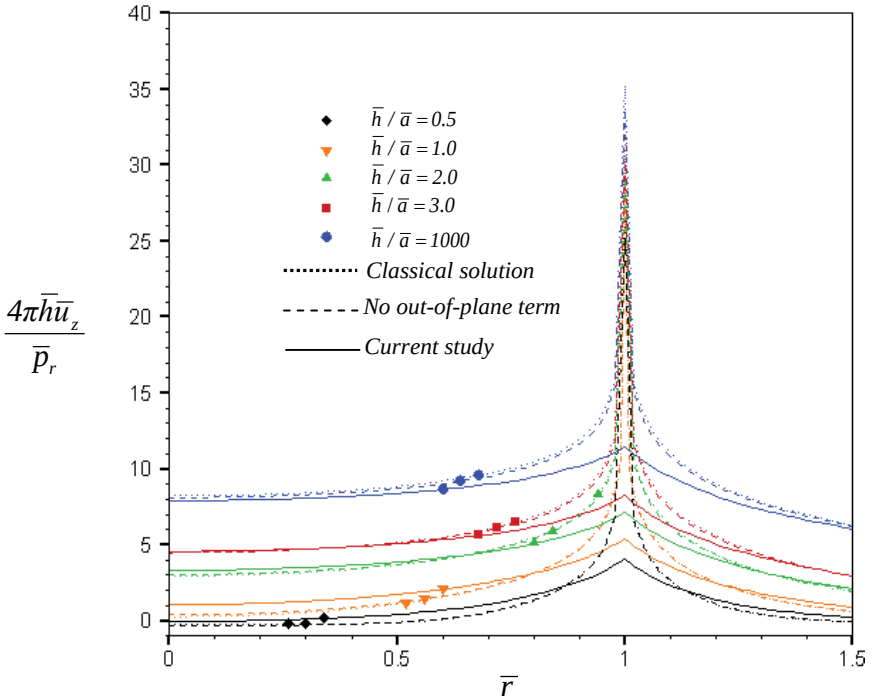

(b)

Figure 2.28 Normalized displacement profiles of an elastic layer under a normal ring load: (a) radial displacement and (b) vertical displacement

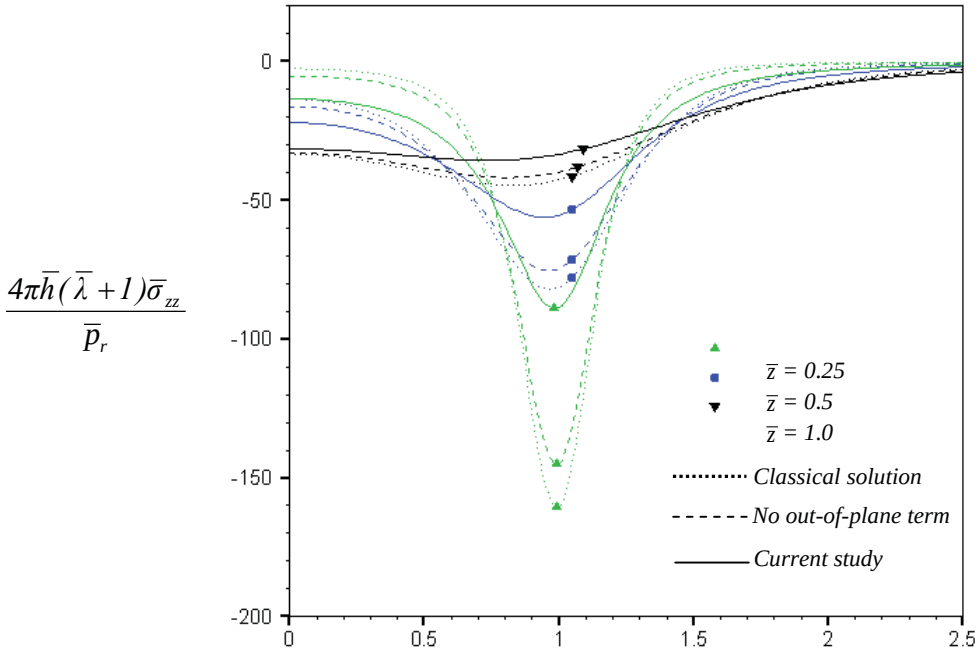

(a)

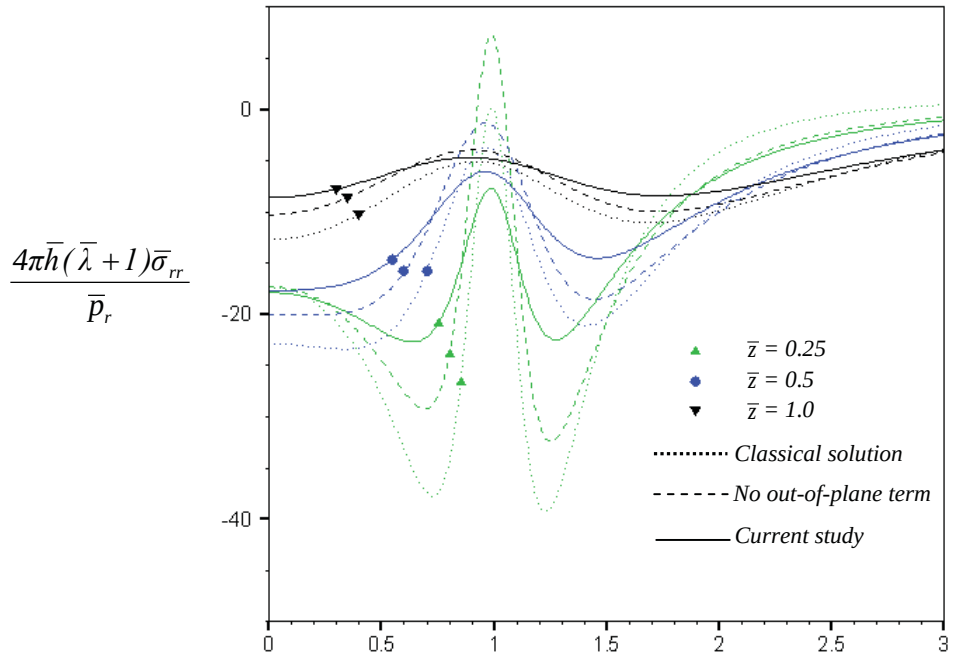

(b)

Figure 2.29 Normalized stress profiles of an elastic layer under a normal ring load: (a) vertical stress and (b) radial stress

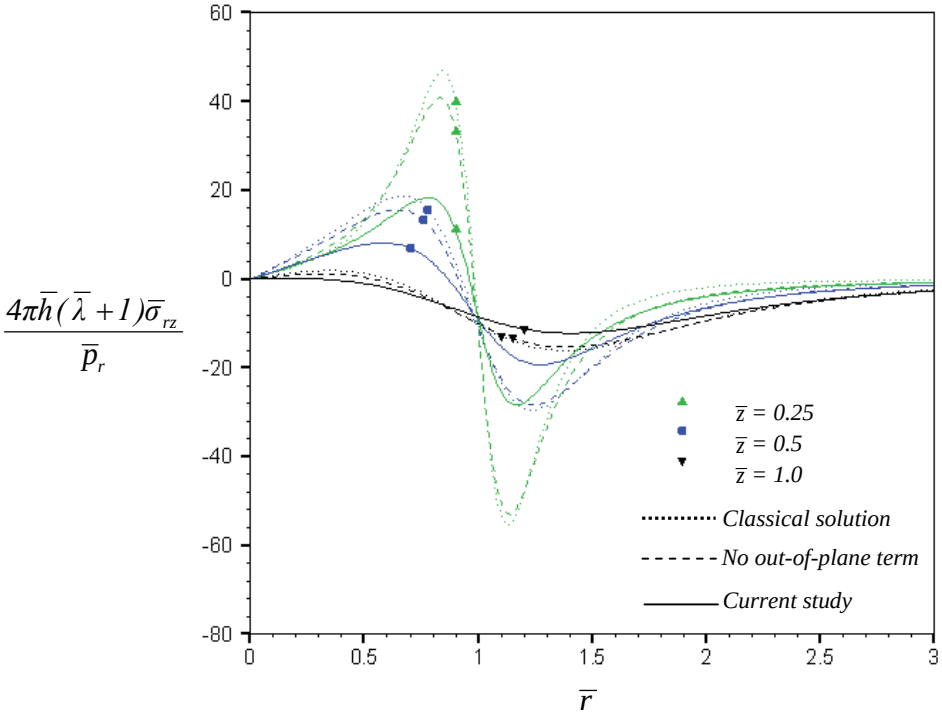

(a)

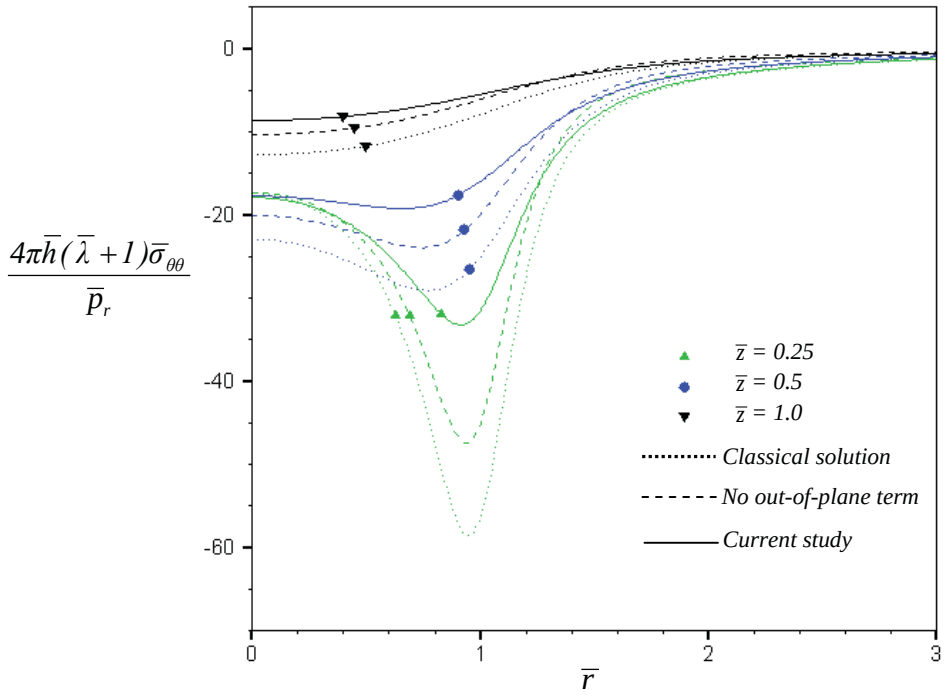

(b)

Figure 2.30 Normalized stress profiles of an elastic layer under a normal ring load: (a) shear stress and (b) hoop stress

The numerical results for stresses within the bulk obtained from all three models are also reported for various depths and $\bar{h}=10$ in Figures 2.29-2.30. Similar to the previous observation, the influence of the surface stresses on the stress field within the bulk is more significant when the location to determine the responses is relatively close to the surface.

2.3.3.3 Layer under tangential ring load

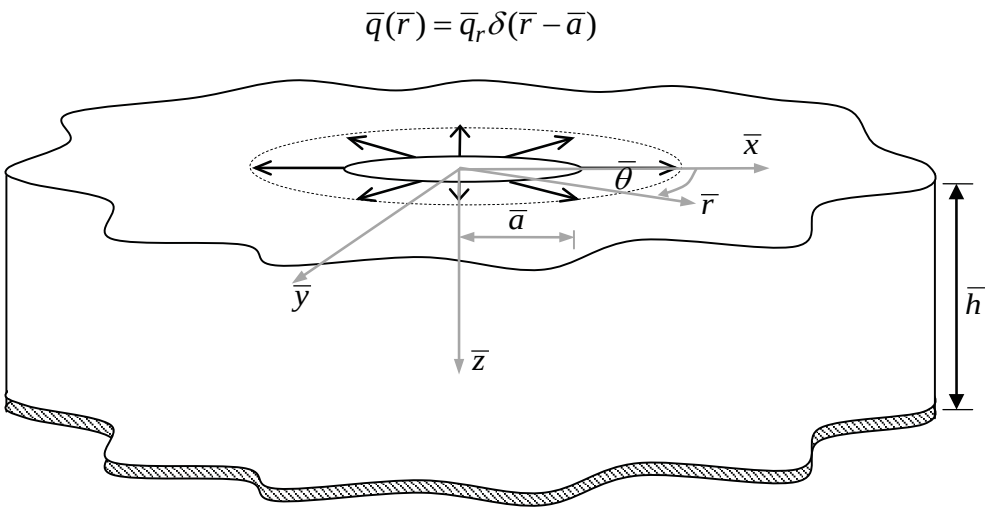

Figure 2.31 Three-dimensional, infinite, rigid-based, elastic layer subjected to a tangential ring load

Consider a three-dimensional, infinite, rigid-based, elastic layer subjected to a unit tangential ring load q_r at the radius a as shown in figure 2.31. The ring load and the radius are normalized such that $\bar{q}_r = q_r / \mu\Lambda$ and $\bar{a} = a/\Lambda$. Results for the normalized radial displacement $4\pi\bar{h}\bar{u}_r / \bar{q}_r$ and the normalized vertical displacement $4\pi\bar{h}\bar{u}_z / \bar{q}_r$ at the surface are plotted along the radial direction as shown in Figures 2.32(a) and 2.32(b) for four different thicknesses ($\bar{h}=0.5$, $\bar{h}=1.0$, $\bar{h}=2.0$, and $\bar{h}=3.0$) and $\bar{a}=1$. For this particular loading condition, both the radial and vertical displacements obtained from the classical model are singular at the location of the applied ring load whereas those obtained from the two models accounting for the surface energy effects are finite everywhere. While results obtained from the two models exhibit huge discrepancy from the classical solution, the contribution of out-of-plane term is insignificant especially for the radial displacement.

Figures 2.33-2.34 demonstrate profiles of normalized stress components for a layer subjected to a tangential ring load for the layer thickness $\bar{h}=10$ and various depths. It is obviously seen that the presence of the surface energy effects reduces the magnitude of the stresses especially in the region closed to the surface. Moreover, for the normalized vertical stress and normalized shear stress, such behavior is more evident when the out-of-plane contribution of the residual surface stress is taken into account.

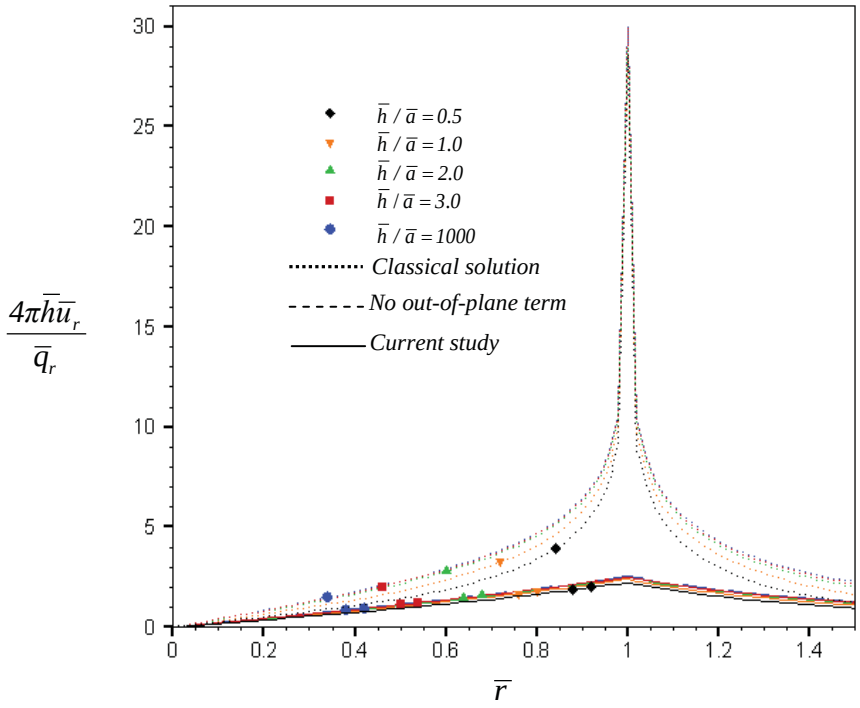

(a)

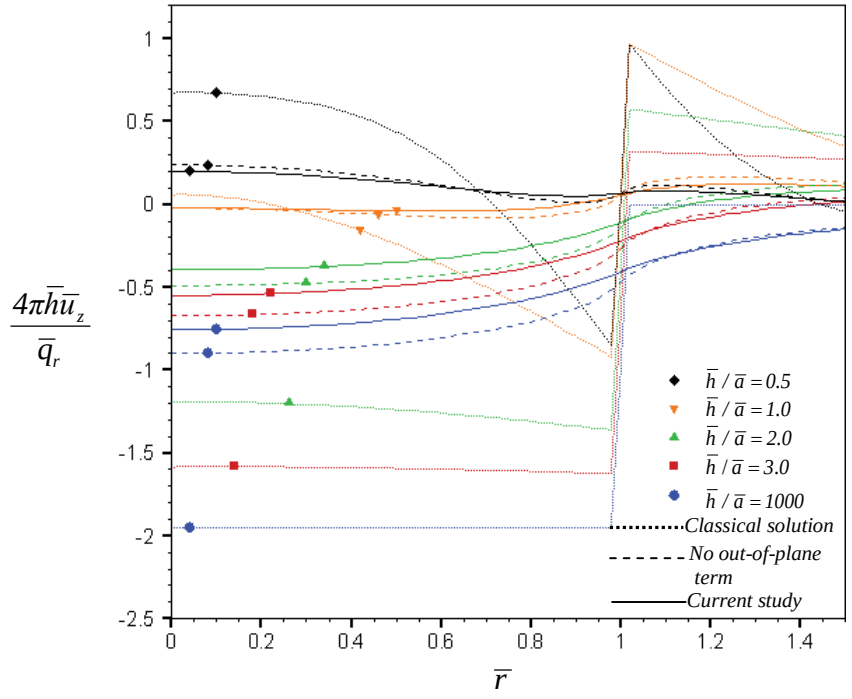

(b)

Figure 2.32 Normalized displacement profiles of an elastic layer under tangential ring load: (a) radial displacement and (b) vertical displacement

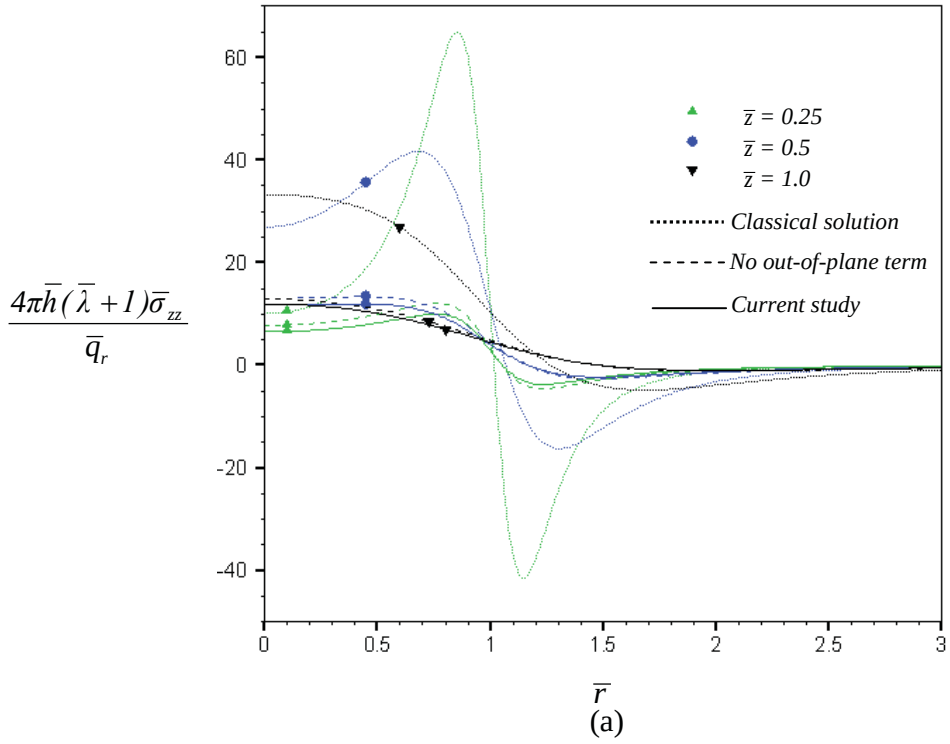

(a)

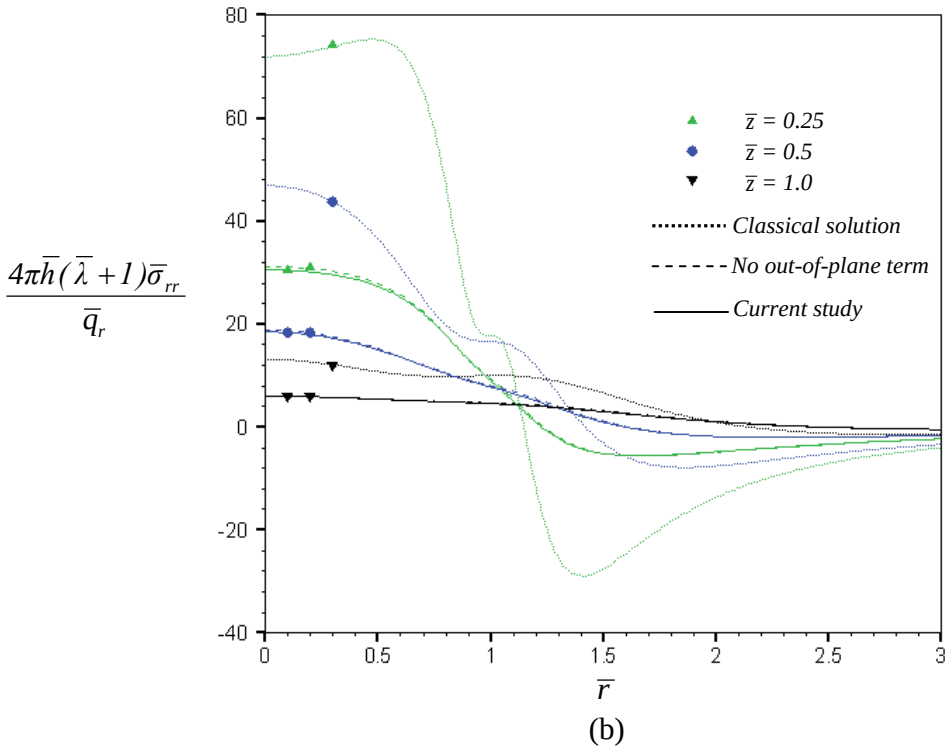

(b)

Figure 2.33 Normalized stress profiles of an elastic layer under tangential ring load: (a) vertical stress and (b) radial stress

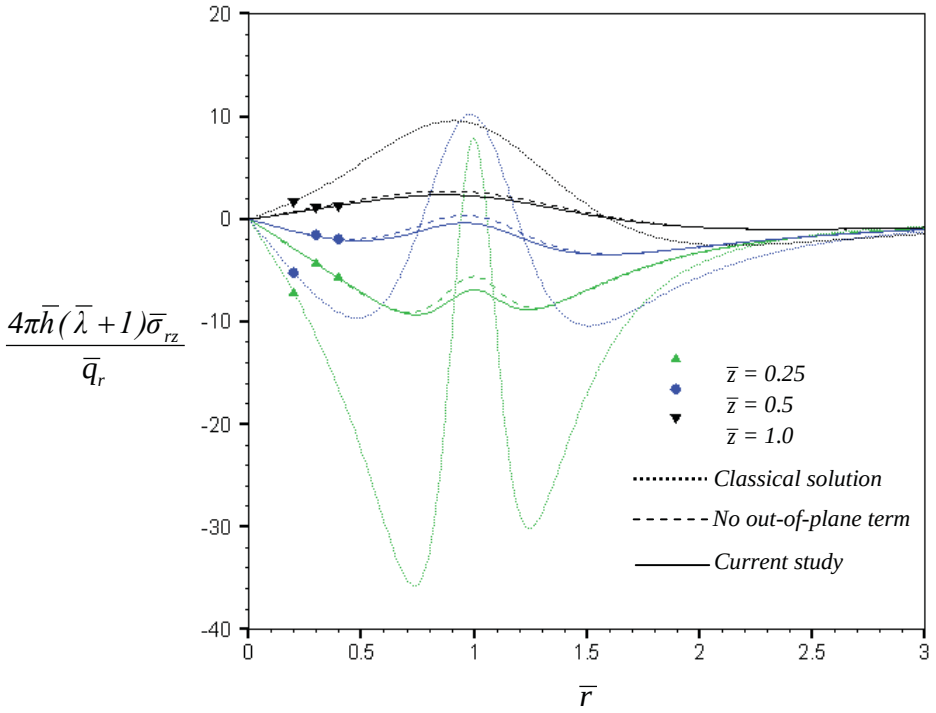

(a)

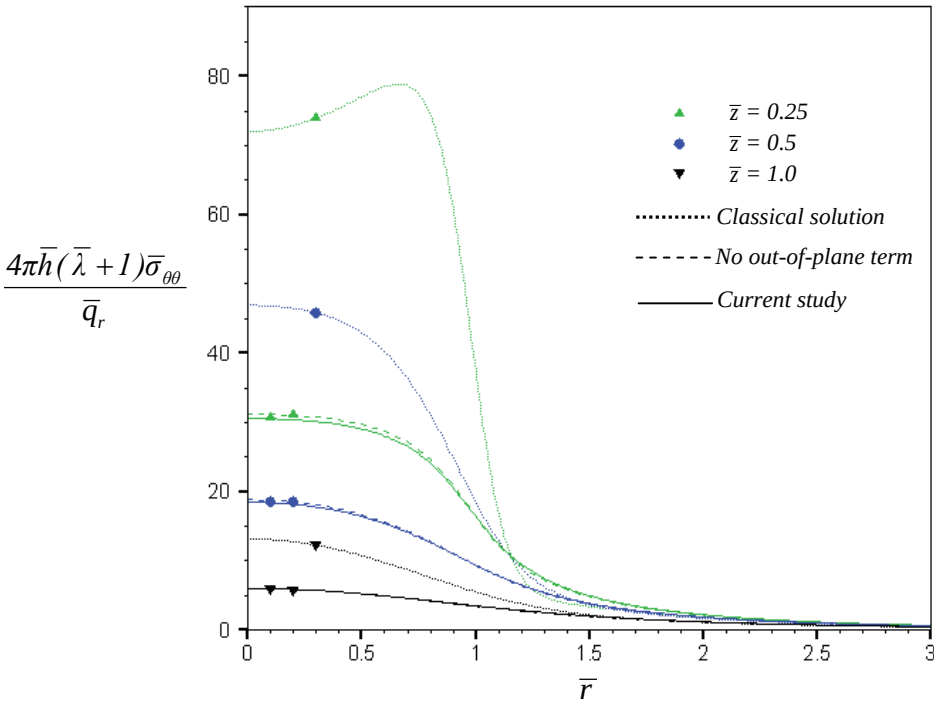

(b)

Figure 2.34 Normalized stress profiles of an elastic layer under tangential ring load: (a) shear stress and (b) hoop stress

2.3.3.4 Applications of fundamental solutions

Results obtained above for three special loading conditions can be employed to construct Green functions useful for various boundary value problems. To demonstrate their vast applications, let us consider a three-dimensional, infinite, rigid-based, elastic layer subjected to any axisymmetric normal traction $p(r)$ and tangential traction $q(r)$. Once solutions of all field quantities due to both unit normal and unit tangential ring loads are determined, they can be utilized along with a method of superposition to obtain integral relations for both the displacement and stress on the surface and within the bulk due to the traction $p(r)$ and $q(r)$. For instance, the radial and tangential displacements at any distance r^* on the surface are given by

$$u_r(r^*) = \int_0^\infty U_r^N(r^*,r)p(r)dr + \int_0^\infty U_r^T(r^*,r)q(r)dr \tag{2.32}$$

$$u_z(r^*) = \int_0^\infty U_z^N(r^*,r)p(r)dr + \int_0^\infty U_z^T(r^*,r)q(r)dr \tag{2.33}$$

where $U_r^N(r^*,r)$ and $U_z^N(r^*,r)$ are radial and tangential displacements at any distance r^* on the surface due to a unit normal ring load applied to the layer at the radius r and $U_r^T(r^*,r)$ and $U_z^T(r^*,r)$ are radial and tangential displacements at any distance r^* on the surface due to a unit tangential ring load applied to the layer at the radius r. Other field quantities at any point (r^*, z^*) within the bulk, denoted generically by $R(r^*,z^*)$, can also be obtained in a similar fashion as

$$R(r^*,z^*) = \int_0^\infty R^N(r^*,z^*,r)p(r)dr + \int_0^\infty R^T(r^*,z^*,r)q(r)dr \tag{2.34}$$

where, again, $R^N(r^*,z^*,r)$ and $R^T(r^*,z^*,r)$ are responses at any point (r^*, z^*) within the bulk due to a unit normal ring load and unit tangential ring load applied to the layer at the radius r, respectively. Clearly, for a problem where the surface traction $p(r)$ and $q(r)$ are fully prescribed, the integral relations (2.32)-(2.34) can be directly employed to determine all field quantities.

For nano-indentation problems, both normal traction $p(r)$ and tangential traction $q(r)$ under the indenter are unknown a priori and they must be determined before the integral relation (2.34) can be used. For a special case of axisymmetric, rigid, frictionless nano-indentation problems, the tangential traction $q(r)$ vanishes and vertical displacement under the indenter is fully prescribed via its known profile v^p and the prescribed indentation depth d. The integral relation (2.33) for any r^* under the indenter becomes

$$u_z(r^*) = \int_0^a U_z^N(r^*,r)p(r)dr = d + v^p(r^*) \quad , \quad r^* \le a \tag{2.35}$$

where a denotes the contact radius. The integral equation (2.35) can be solved to obtain the unknown contact pressure $p(r)$. Once $p(r)$ is determined, all other field quantities can readily be obtained from the integral relation (2.34).

For axisymmetric, rigid, fully bonded nano-indentation problems, the radial displacement under the indenter identically vanishes and the vertical displacement under the indenter is fully prescribed via its known profile v^p and the prescribed indentation depth d. The integral relations (2.32) and (2.33) for any r^* under the indenter becomes

$$u_r(r^*) = \int_0^a U_r^N(r^*,r)p(r)dr + \int_0^a U_r^T(r^*,r)q(r)dr = 0 \quad , \quad r^* \le a \tag{2.36}$$

$$u_z(r^*) = \int_0^a U_z^N(r^*,r)p(r)dr + \int_0^a U_z^T(r^*,r)q(r)dr = d + v^p(r^*) \quad , \quad r^* \le a \tag{2.37}$$

The two integral equations (2.36)-(2.37) are sufficient for solving the unknown traction $p(r)$ and $q(r)$. Once the traction is obtained, all other field quantities can be computed from the integral relation (2.34).

For axisymmetric, rigid, rough nano-indentation problems, the tangential traction $q(r)$ can be related to the normal traction $p(r)$ via an appropriate friction model and, again, the vertical displacement under the indenter is fully prescribed via its known profile v^p and the prescribed indentation depth d. The integral relation (2.33) for any r^* under the indenter becomes

$$u_z(r^*) = \int_0^a U_z^N(r^*,r)p(r)dr + \int_0^a U_z^T(r^*,r)f(p(r))dr = d + v^p(r^*) \quad , \quad r^* \le a \tag{2.38}$$

where a function f denotes the relation between p and q. The integral equation (2.38) can be employed to solve for the unknown normal traction $p(r)$. Once $p(r)$ is determined, the tangential traction can readily be obtained and all other field quantities are computed from the integral relation (2.34).

By following the same strategy, solutions of all field quantities due to a unit normal concentrated load applied to the surface of a layer can be utilized as Green functions to establish integral relations for field quantities due to arbitrary normal traction on the surface. In addition, the integral relation for the vertical displacement on the surface can be employed to form the integral equation governed the unknown pressure under the rigid, frictionless indenter of arbitrary profiles.

CHAPTER III

NANO-INDENTATION

In this chapter, the formulation of boundary value problem associated with an axisymmetric, frictionless, rigid punch acting on a half-space is first presented. The Hankel integral transform is then applied to reduce the corresponding mixed boundary conditions to a set of dual integral equations. These integral equations are further reduced to a Fredholm integral equation of the second kind that is well-suited for constructing numerical solutions. Due to the complexity of the key governing equation, numerical schemes are adopted to construct approximate solutions. Several components essential for numerical implementations such as the domain truncation, the discretization of the primary unknown function, the collocation scheme, linear solvers, and Hankel transform inversion are briefly summarized. The solution procedure is implemented to determine the complete elastic fields for indentors of both smooth and non-smooth contacts. The accuracy of the present numerical scheme is verified by comparing with analytical solutions of the classical case for both profiles. Once the method is fully tested, it is applied to solve more complex indentation problems accounted for surface stress effects in which analytical solutions do not exist. In the analysis, indentors with flat-ended and paraboloidal profiles are chosen to represent the non-smooth and smooth contacts respectively. Numerical results for three different models (i.e. classical solution with no surface stress effects and solutions accounted for surface stress effects with and without the out-of-plane contribution of the residual surface tension) are fully compared and discussed.

3.1 Formulation

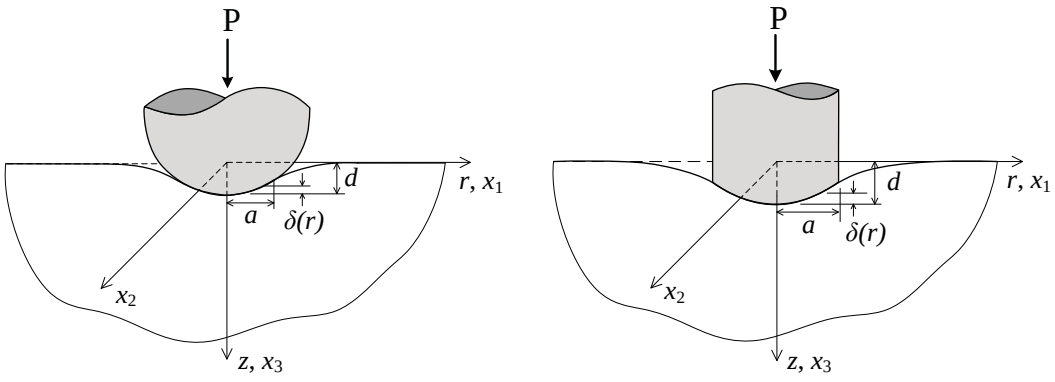

(a) (b)

Figure 3.1 Indentation of half-space by axisymmetric rigid frictionless punch: smooth contact and (b) non-smooth contact

Consider a homogeneous, isotropic, elastic half-space indented by an axisymmetric frictionless rigid punch as shown schematically in Figure 3.1. The profile of the punch, denoted by a

function $\delta = \delta(r)$, is defined for convenience and without loss by choosing $\delta = 0$ at $r = 0$. The radius of a contact region and the indentation depth resulting from a resultant force P at the center of the punch are denoted by a and d, respectively. In this study, the profile of the punch is assumed to be smooth (i.e. the unit normal vector to the surface of the punch or, equivalently, $d\delta/dr$ is well-defined) at any point within the contact region except along the boundary $r = a$ where the profile is allowed to be non-smooth. A punch with well-defined $d\delta/dr$ for $r \leq a$ is termed a smooth-contact punch (see Figure 3.1(a)) whereas a punch with well-defined $d\delta/dr$ only for $r < a$ is termed a non-smooth-contact punch (see Figure 3.1(b)). In the present study, the pressure distribution exerted by the punch and the complete elastic fields within the half-space accounted for surface energy effects are to be determined.

3.1.1 Basic equations

Behavior of the half-space (bulk) is governed by a classical theory of elasticity. In the absence of body force, the governing field equations (i.e. equilibrium equations, constitutive relations and strain-displacement relations) can be expressed as

$$\sigma_{ij,j} = 0 \tag{3.1}$$

$$\sigma_{ij} = 2\mu\varepsilon_{ij} + \lambda\delta_{ij}\varepsilon_{kk} \tag{3.2}$$

$$\varepsilon_{ij} = \frac{1}{2}\left(u_{i,j} + u_{j,i}\right) \tag{3.3}$$

where u_i, σ_{ij} and ε_{ij} denote components of the displacement, stress and strain tensors, respectively; δ_{ij} is a Kronecker-delta symbol; and μ and λ are Lamé constants of a bulk material. Note that lower-case indices range from 1 to 3, and repeated indices imply the summation over their range.

A surface of the half-space is regarded as a negligibly thin membrane adhered perfectly to the bulk without slipping and its behavior (which is different from the bulk) is modeled by Gurtin-Murdoch continuum model of surface elasticity. The equilibrium conditions on the surface in terms of the generalized Young-Laplace equation (Povestenko, 1993), surface constitutive relations and strain-displacement relationship, when specialized to this particular case, are given by (Gurtin and Murdoch, 1975; Gurtin and Murdoch, 1978; Gurtin et al., 1998)

$$\sigma^s_{i\alpha,\alpha} + \sigma_{i3} + t_i^0 = 0 \tag{2.4}$$

$$\sigma^s_{\beta\alpha} = \tau^s\delta_{\beta\alpha} + 2\left(\mu^s - \tau^s\right)\varepsilon^s_{\beta\alpha} + \left(\lambda^s + \tau^s\right)\varepsilon^s_{\gamma\gamma}\delta_{\beta\alpha} + \tau^s u^s_{\beta,\alpha}\ , \quad \sigma^s_{3\alpha} = \tau^s u^s_{3,\alpha} \tag{2.5}$$

$$\varepsilon^s_{\alpha\beta} = \frac{1}{2}\left(u^s_{\alpha,\beta} + u^s_{\beta,\alpha}\right) \tag{2.6}$$

where the superscript ‘s’ is used to denote the quantities corresponding to the surface; μ^s and λ^s are surface Lamé constants; τ^s is the residual surface tension under unstrained conditions; and t_i^0 denotes the prescribed traction on the surface. It is important to emphasize here that Greek indices range from 1 to 2 and, once again, repeated indices imply the summation over their range. When specialized to an axisymmetric case, the corresponding elastic fields can be

obtained by solving, in a cylindrical coordinate system (r,θ,z), the following biharmonic equation (Sneddon, 1951; Selvadurai, 2000)

$$\nabla^4\Phi = 0 \tag{3.7}$$

where Φ is Love's strain potential. The displacement and stress fields are given in terms of Φ as follows:

$$\sigma_{rr} = \lambda\nabla^2\left(\frac{\partial\Phi}{\partial z}\right) - 2(\lambda+\mu)\frac{\partial^3\Phi}{\partial r^2\partial z} \tag{3.8a}$$

$$\sigma_{\theta\theta} = \lambda\nabla^2\left(\frac{\partial\Phi}{\partial z}\right) - \frac{2(\lambda+\mu)}{r}\frac{\partial^2\Phi}{\partial r\partial z} \tag{3.8b}$$

$$\sigma_{zz} = (3\lambda+4\mu)\nabla^2\left(\frac{\partial\Phi}{\partial z}\right) - 2(\lambda+\mu)\frac{\partial^3\Phi}{\partial z^3} \tag{3.8c}$$

$$\sigma_{rz} = (\lambda+2\mu)\frac{\partial}{\partial r}\left(\nabla^2\Phi\right) - 2(\lambda+\mu)\frac{\partial^3\Phi}{\partial z^2\partial r} \tag{3.8d}$$

$$u_r = -\frac{\lambda+\mu}{\mu}\frac{\partial^2\Phi}{\partial r\partial z} \tag{3.8e}$$

$$u_z = \frac{\lambda+2\mu}{\mu}\nabla^2\Phi - \frac{\lambda+\mu}{\mu}\frac{\partial^2\Phi}{\partial z^2} \tag{3.8f}$$

By applying Hankel integral transforms, the biharmonic equation (3.7) is reduced to

$$\left(\frac{d^2}{dz^2} - \xi^2\right)^2 G(\xi,z) = 0 \tag{3.9}$$

where $J_n(\xi)$ denotes the first order Bessel functions of order *n* and

$$G(\xi,z) = \int_0^\infty r\Phi J_0(\xi r)\,dr \tag{3.10}$$

The general solution of (3.9) is given by

$$G(\xi,z) = (A+Bz)e^{-\xi z} + (C+Dz)e^{\xi z} \tag{3.11}$$

where A, B, C and D are arbitrary functions of ξ that can be determined from boundary conditions. Accordingly, the general solutions for displacements and stresses can be transformed into the relations involving $G(\xi,z)$ and its derivatives with respect to z by using Hankel inversion and the relations (3.8a)-(3.8f). Those solutions are expressed as

$$\sigma_{rr}=\int_0^\infty \xi\left[\lambda\frac{d^3G}{dz^3}+(\lambda+2\mu)\xi^2\frac{dG}{dz}\right]J_0(\xi r)\,d\xi-\frac{2(\lambda+\mu)}{r}\int_0^\infty \xi^2\frac{dG}{dz}J_1(\xi r)\,d\xi \tag{3.12a}$$

$$\sigma_{\theta\theta}=\lambda\int_0^\infty \xi\left[\frac{d^3G}{dz^3}-\xi^2\frac{dG}{dz}\right]J_0(\xi r)\,d\xi+\frac{2(\lambda+\mu)}{r}\int_0^\infty \xi^2\frac{dG}{dz}J_1(\xi r)\,d\xi \tag{3.12b}$$

$$\sigma_{zz}=\int_0^\infty \xi\left[(\lambda+2\mu)\frac{d^3G}{dz^3}-(3\lambda+4\mu)\xi^2\frac{dG}{dz}\right]J_0(\xi r)\,d\xi \tag{3.12c}$$

$$\sigma_{rz}=\int_0^\infty \xi^2\left[\lambda\frac{d^2G}{dz^2}+(\lambda+2\mu)\xi^2G\right]J_1(\xi r)\,d\xi \tag{3.12d}$$

$$u_r=\frac{\lambda+\mu}{\mu}\int_0^\infty \xi^2\frac{dG}{dz}J_1(\xi r)\,d\xi \tag{3.12e}$$

$$u_z=\int_0^\infty \xi\left[\frac{d^2G}{dz^2}-\frac{\lambda+2\mu}{\mu}\xi^2G\right]J_0(\xi r)\,d\xi \tag{3.12f}$$

Note that u_θ, $\sigma_{r\theta}$ and $\sigma_{z\theta}$ vanish due to axisymmetric deformations, and all non-zero variables are independent of θ. By invoking the remote condition associated with the vanishing displacements and stresses as $z\to\infty$, *C* and *D* must vanish, and the function $G(\xi,z)$ reduces to

$$G(\xi,z)=(A+Bz)e^{-\xi z} \tag{3.13}$$

Upon substituting (3.13) into (3.12), the expression for the components of stresses and displacements are then given in terms of *A* and *B* by

$$\begin{aligned}\frac{\sigma_{rr}}{2(\lambda+\mu)}&=\int_0^\infty \xi^3\left[-\xi A+\left(\frac{2\lambda+\mu}{\lambda+\mu}-\xi z\right)B\right]e^{-\xi z}J_0(\xi r)\,d\xi\\&\quad-\frac{1}{r}\int_0^\infty \xi^2\left[-\xi A+(1-\xi z)B\right]e^{-\xi z}J_1(\xi r)\,d\xi\end{aligned} \tag{3.14}$$

$$\begin{aligned}\frac{\sigma_{\theta\theta}}{2(\lambda+\mu)}&=\frac{\lambda}{\lambda+\mu}\int_0^\infty \xi^3 Be^{-\xi z}J_0(\xi r)\,d\xi\\&\quad+\frac{1}{r}\int_0^\infty \xi^2\left[-\xi A+(1-\xi z)B\right]e^{-\xi z}J_1(\xi r)\,d\xi\end{aligned} \tag{3.15}$$

$$\frac{\sigma_{zz}}{2(\lambda+\mu)}=\int_0^\infty \xi^3\left[\xi A+\left(\frac{\mu}{\lambda+\mu}+\xi z\right)B\right]e^{-\xi z}J_0(\xi r)\,d\xi \tag{3.16}$$

$$\frac{\sigma_{rz}}{2(\lambda+\mu)}=\int_0^\infty \xi^3\left[\xi A-\left(\frac{\lambda}{\lambda+\mu}-\xi z\right)B\right]e^{-\xi z}J_1(\xi r)\,d\xi \tag{3.17}$$

$$u_r=\frac{\lambda+\mu}{\mu}\int_0^\infty \xi^2\left[-\xi A+(1-\xi z)B\right]e^{-\xi z}J_1(\xi r)\,d\xi \tag{3.18}$$

$$u_z = -\frac{\lambda+\mu}{\mu}\int_0^\infty \xi^2 \left[\xi A + \left(\frac{2\mu}{\lambda+\mu} + \xi z \right) B \right] e^{-\xi z} J_0(\xi r)\, d\xi \tag{3.19}$$

3.1.2 Formulation of indentation problem

For the indentation problem shown in Figure 3.1, the domain boundary can be decomposed into a surface outside the contact region on which the traction identically vanishes and a surface inside the contact region on which the normal displacement is prescribed while, resulting from the frictionless assumption, the shear traction vanishes. These mixed boundary conditions can be expressed as

$$u_z\big|_{z=0} = d - \delta(r) \qquad ; \quad 0 \le r \le a \tag{3.20}$$

$$\sigma_{zz}\big|_{z=0} + \tau^s \nabla^2 u_z = 0 \qquad ; \quad a < r < \infty \tag{3.21}$$

$$\sigma_{rz}\big|_{z=0} + \kappa^s \left(\frac{d^2 u_r}{dr^2} + \frac{1}{r}\frac{du_r}{dr} - \frac{u_r}{r^2} \right)_{z=0} = 0 \qquad ; \quad 0 \le r < \infty \tag{3.22}$$

where $\kappa^s = 2\mu^s + \lambda^s$ is a surface material constant. Upon substituting (3.17) and (3.18) into the boundary condition (3.22), it leads to a relation between *A* and *B*:

$$A\xi(1+\Lambda_0\xi) = \left(\frac{\lambda}{\lambda+\mu} + \Lambda_0\xi \right) B \tag{3.23}$$

where $\Lambda_0 = \kappa^s / 2\mu$. By enforcing the mixed boundary conditions (3.20) and (3.21) along with the relation (3.23), it yields a pair of integral equations:

$$-\int_0^\infty \xi^2 \left[\frac{(\lambda+2\mu)+(\lambda+3\mu)\Lambda_0\xi}{\mu(1+\Lambda_0\xi)} \right] B J_0(\xi r)\, d\xi = d - \delta(r) \qquad ; \quad 0 \le r \le a \tag{3.24}$$

$$\int_0^\infty \xi^3 \left\{ \frac{2\mu\left[(\lambda+\mu)+(\lambda+2\mu)\Lambda_0\xi\right] + \tau^s\xi\left[(\lambda+2\mu)+(\lambda+3\mu)\Lambda_0\xi\right]}{\mu^2(1+\Lambda_0\xi)} \right\} B J_0(\xi r)\, d\xi = 0$$

$$; \quad a < r < \infty \tag{3.25}$$

The dual integral equations (3.24) and (3.25) constitute a complete set of equations for determining the unknown function $B = B(\xi)$. By introducing two functions $\phi = \phi(\xi)$ and $w = w(\xi)$ such that

$$\phi(\xi) = \xi^3 \left\{ \frac{2\mu\left[(\lambda+\mu)+(\lambda+2\mu)\Lambda_0\xi\right] + \tau^s\xi\left[(\lambda+2\mu)+(\lambda+3\mu)\Lambda_0\xi\right]}{\mu^2(1+\Lambda_0\xi)} \right\} B \tag{3.26}$$

$$\xi^{-1}\phi(\xi)\left[1+w(\xi)\right] = \xi^2 \left[\frac{(\lambda+2\mu)+(\lambda+3\mu)\Lambda_0\xi}{\mu(1+\Lambda_0\xi)} \right] B \tag{3.27}$$

the dual integral equations (3.24) and (3.25) can further be simplified to

$$\int_0^\infty \bar{\xi}^{-1}\bar{\phi}\left(\bar{\xi}\right)\left[1+w\left(\bar{\xi}\right)\right]J_0\left(\bar{\xi}\bar{r}\right)d\bar{\xi} = \bar{f}\left(\bar{r}\right) \quad ; \quad 0 \le \bar{r} \le 1 \tag{3.28}$$

$$\int_0^\infty \bar{\phi}\left(\bar{\xi}\right)J_0\left(\bar{\xi}\bar{r}\right)d\bar{\xi} = 0 \quad ; \quad 1 < \bar{r} < \infty \tag{3.29}$$

where $\bar{f}(\bar{r}) = f(\bar{r})/a = -[\bar{d} - \bar{\delta}(\bar{r})]$, $\bar{\delta}(\bar{r}) = \delta(\bar{r})/a$, $\bar{d} = d/a$, $\bar{\xi} = \xi a$, $\bar{r} = r/a$, and $\bar{\phi} = \bar{\phi}\left(\bar{\xi}\right) = \phi\left(\bar{\xi}\right)/a$. The function $\bar{\phi} = \bar{\phi}\left(\bar{\xi}\right)$ becomes the primary unknown of the dual integrals (3.28) and (3.29) whereas the function $w = w\left(\bar{\xi}\right)$ is known and can be obtained directly from (3.26) and (3.27) as

$$w\left(\bar{\xi}\right) = \frac{(\bar{\lambda}+2)+(\bar{\lambda}+3)\bar{\Lambda}_0\bar{\xi}}{2\left[\left(\bar{\lambda}+1\right)+\left(\bar{\lambda}+2\right)\bar{\Lambda}_0\bar{\xi}\right]+\bar{\tau}^s\bar{\xi}\left[\left(\bar{\lambda}+2\right)+\left(\bar{\lambda}+3\right)\bar{\Lambda}_0\bar{\xi}\right]} - 1 \tag{3.30}$$

where $\bar{\lambda} = \lambda/\mu$, $\bar{\Lambda}_0 = \Lambda_0/a$ and $\bar{\tau^s} = \tau^s/(\mu a)$. It is evident from (3.30) that the function $w = w\left(\bar{\xi}\right)$ possesses a limit equal to -1 as $\bar{\xi} \to \infty$.

The solution of dual integral equations of the type (3.28) and (3.29) has been extensively studied by Mandal (1988) and Sneddon (1966). Following their procedures, such a set of dual integral equations can be reduced to a Fredholm integral equation of the second kind as

$$\bar{\phi}\left(\bar{\xi}\right) = \frac{2\bar{\xi}}{\pi}\int_0^1 \cos\left(\bar{\xi}t\right)dt\,\frac{d}{dt}\int_0^t \frac{uf\left(u\right)du}{\sqrt{t^2-u^2}} - \frac{\bar{\xi}}{\pi}\int_0^\infty \frac{w\left(u\right)\bar{\phi}\left(u\right)}{u}\left\{\frac{\sin\left(u+\bar{\xi}\right)}{u+\bar{\xi}} + \frac{\sin\left(u-\bar{\xi}\right)}{u-\bar{\xi}}\right\}du \tag{3.31}$$

It can be seen from (3.31) that the function $f\left(u\right)$ is merely related to the indenter profile and the function $w\left(u\right)$ is related to the boundary conditions involving the surface energy parameters. This single integral equation (3.31) is in a form well-suited for constructing numerical solutions for $\bar{\phi} = \bar{\phi}\left(\bar{\xi}\right)$. Once the function $\bar{\phi} = \bar{\phi}\left(\bar{\xi}\right)$ is solved, the functions *A* and *B* can be subsequently determined from (3.23) and (3.26), respectively, and the complete elastic fields within the half-space can also be obtained from (3.14)-(3.19). In addition, the magnitude of the total indentation force *P* producing the indentation depth *d* can be obtained by integrating the contact pressure, i.e. the left hand side of Eq. (3.21), over the area of the contact region.

In the absence of surface energy effects, above formulation can readily be specialized to a special case of a classical indentation problem by setting $\bar{\Lambda}_0 = 0$ and $\bar{\tau^s} = 0$. The function $w = w(\bar{\xi})$ in (3.30) simply reduces to a constant w^* given below:

$$w^* = \frac{\bar{\lambda}+2}{2\left(\bar{\lambda}+1\right)} - 1 \tag{3.32}$$

The dual integral equations (3.24) and (3.25) now become

$$\int_0^\infty \bar{\xi}^{-1}\bar{\phi}\left(\bar{\xi}\right)J_0\left(\bar{\xi}\bar{r}\right)d\bar{\xi} = f^*\left(\bar{r}\right) \quad ; \quad 0 \le \bar{r} \le 1 \tag{3.33}$$

$$\int_0^\infty \bar{\phi}\left(\bar{\xi}\right)J_0\left(\bar{\xi}\bar{r}\right)d\bar{\xi} = 0 \quad ; \quad 1 < \bar{r} < \infty \tag{3.34}$$

where $f^*\left(\bar{r}\right) = \bar{f}\left(\bar{r}\right)/w^*$. A set of dual integral equations (3.33) and (3.34) was solved analytically by Sneddon (1965).

3.2 Numerical Implementations

Due to the complexity of the Fredholm integral equation of the second kind formulated in Chapter II, numerical schemes are necessarily adopted to construct approximate solutions. In this chapter, several components essential for such numerical implementation (e.g. domain truncation, discretization of the primary unknown function $\bar{\phi} = \bar{\phi}(\bar{\xi})$, collocation, linear solvers, Hankel transform inversion, etc.) are briefly summarized.

3.2.1 Domain truncation

It is evident that the second integral of the Fredholm integral equation (3.31) is an improper integral with an infinite upper limit and the involved primary unknown function $\bar{\phi} = \bar{\phi}(\bar{\xi})$ is defined on a semi-infinite interval [0, ∞). Before constructing an approximate solution for $\bar{\phi} = \bar{\phi}(\bar{\xi})$, the domain of integration of the improper integral is first truncated from [0, ∞) to [0, $\bar{\xi}_R$] where $\bar{\xi}_R$ is a finite real number. The truncated Fredholm integral equation is given by

$$\bar{\phi}(\bar{\xi}) = \frac{2\bar{\xi}}{\pi}\int_0^1 \cos(\bar{\xi}t)dt\,\frac{d}{dt}\int_0^t \frac{uf(u)du}{\sqrt{t^2-u^2}} - \frac{\bar{\xi}}{\pi}\int_0^{\bar{\xi}_R} \frac{w(u)\bar{\phi}(u)}{u}\left\{\frac{\sin(u+\bar{\xi})}{u+\bar{\xi}} + \frac{\sin(u-\bar{\xi})}{u-\bar{\xi}}\right\}du \tag{3.35}$$

3.2.2 Discretization

The unknown function $\bar{\phi} = \bar{\phi}(\bar{\xi})$ over the entire truncated domain [0, $\bar{\xi}_R$] can be discretized in the form

$$\bar{\phi}(\bar{\xi}) = \bar{\xi}\sum_{j=1}^{n}\alpha_j\psi_j(\bar{\xi}) \tag{3.36}$$

where α_j are unknown nodal quantities to be determined, $\psi_j(\xi)$ are nodal basis functions, and n is the number of nodes resulting from the discretization. It is worth noting that the approximation (3.36) results from a special property of the function ϕ at the origin; more specifically, this function vanishes at the origin of order $\mathcal{O}(\bar{\xi})$. Note also that, in the present study, the nodal basis functions are systematically constructed in an element-wise fashion based on standard isoparametric, quadratic elements.

Upon inserting the approximation (3.36) into (3.35) and then dividing the entire equation by $\bar{\xi}$, it leads to a discretized integral equation

$$\sum_{j=1}^{n} \mathcal{M}_j(\bar{\xi})\alpha_j = \mathcal{F}(\bar{\xi}) \tag{3.37}$$

where the integrals $\mathcal{M}_j(\bar{\xi})$ and $\mathcal{F}(\bar{\xi})$ are defined on the truncated domain [0, ξ_R] by

$$\mathcal{M}_j(\bar{\xi}) = \psi_j(\bar{\xi}) + \int_0^{\bar{\xi}_R} \psi_j(u)K(\bar{\xi},u)du \tag{3.38}$$

$$\mathcal{F}(\bar{\xi}) = \frac{2}{\pi}\int_0^1 \cos(\bar{\xi}t)dt \frac{d}{dt}\int_0^t \frac{uf(u)du}{\sqrt{t^2-u^2}} \tag{3.39}$$

$$K(\bar{\xi},u) = \frac{w(u)}{\pi}\left\{\frac{\sin(u+\bar{\xi})}{u+\bar{\xi}} + \frac{\sin(u-\bar{\xi})}{u-\bar{\xi}}\right\} \tag{3.40}$$

It can readily be verified that the kernel $K(\bar{\xi}, u)$ is regular for any pair of points ($\bar{\xi}$, u) and, as a result, $\mathcal{M}_j(\bar{\xi})$ involves only an regular integral for all $\bar{\xi} \in [0, \bar{\xi}_R]$. The integral $\mathcal{F}(\bar{\xi})$ is given in terms of a double line integral whose inner integrand involves the prescribed profile of the punch and is only weakly singular at $u = t$. To obtain a better form well-suited for numerical integration, an integration by parts is performed along with applying a special variable transformation (i.e. $u = t\sin\theta$) to remove such singularity and this, finally, leads to

$$\mathcal{F}(\bar{\xi}) = \frac{2\bar{\xi}}{\pi}\int_0^1 \sin(\bar{\xi}t)\int_0^{\pi/2} uf(u)\big|_{u=t\sin\theta} d\theta dt + \frac{2\cos(\bar{\xi})}{\pi}\int_0^{\pi/2} uf(u)\big|_{u=\sin\theta} d\theta \tag{3.41}$$

3.2.3 Collocation method

To obtain a sufficient number of equations to solve for the unknown constants α_j, a collocation-based technique is utilized. In particular, the discretized integral equation (3.3) is collocated (or, equivalent, forced to be satisfied) at all nodes $\bar{\xi} = \bar{\xi}_i$ (for i = 1, 2, 3, ..., n), and this leads to a set of n linear algebraic equations governing the nodal quantities α_j as follows

$$\mathbf{M}\boldsymbol{\alpha} = \mathbf{F} \tag{3.42}$$

where $\boldsymbol{\alpha} = \{\alpha_1, \alpha_2, ..., \alpha_n\}^T$ is vector of nodal quantities and entries of the coefficient matrix **M** and the prescribed vector **F** are given by

$$[\mathbf{M}]_{ij} = \mathcal{M}_j(\bar{\xi}_i) = \psi_j(\bar{\xi}_i) + \int_0^{\bar{\xi}_R} \psi_j(u)K(\bar{\xi}_i,u)du \tag{3.43}$$

$$[\mathbf{F}]_i = \mathcal{F}(\bar{\xi}_i) = \frac{2\bar{\xi}_i}{\pi}\int_0^1 \sin(\bar{\xi}_i t)\int_0^{\pi/2} uf(u)\big|_{u=t\sin\theta} d\theta dt + \frac{2\cos(\bar{\xi}_i)}{\pi}\int_0^{\pi/2} uf(u)\big|_{u=\sin\theta} d\theta \tag{3.44}$$

3.2.4 Construction of M and F

It is evident from (3.43) and (3.44) that entries of the matrix **M** and the prescribed vector **F** involve only regular integrals. Thus, a standard Gaussian quadrature can be used to efficiently and accurately evaluate such integrals. While every entry of the matrix **M** is given in terms of a definite integral over the truncated domain [0, $\bar{\xi}_R$], this matrix can be efficiently constructed in an element-wise fashion and the contribution from all elements to the global matrix **M** can readily be treated using a standard assembly procedure (e.g., Hughes, 2000). It is worth noting that for some special punch profiles, the integral $\mathcal{F}(\bar{\xi})$ admits an explicit expression and, as a result, construction of the corresponding vector **F** requires no numerical integration. For instance, the integral $\mathcal{F}(\bar{\xi})$ can be obtained for a flat-ended cylindrical indenter (i.e. $\bar{\delta}(\bar{r}) = 0$) and a paraboloidal indenter (i.e. $\bar{\delta}(\bar{r}) = \alpha a \bar{r}^2$ where α is a constant representing the slenderness of the punch profile) as

Flat-ended cylindrical indenter: $\mathcal{F}(\bar{\xi}) = -\dfrac{2\bar{d}}{\pi\bar{\xi}}\sin(\bar{\xi})$ (3.45)

Paraboloidal indenter: $\mathcal{F}(\bar{\xi}) = -\dfrac{2\bar{d}}{\pi\bar{\xi}}\sin(\bar{\xi}) + \dfrac{4\alpha a}{\pi\bar{\xi}^3}\left\{2\bar{\xi}\cos(\bar{\xi}) + (-2+\bar{\xi}^2)\sin(\bar{\xi})\right\}$ (3.46)

3.2.5 Linear solvers

It is evident from equation (3.43) that the coefficient matrix **M** is non-symmetric and fully dense. To solve a system of linear equations (3.42), either a direct solver based on the LU-decomposition method or an iterative solver adopted from the stabilized bi-conjugate gradient method is employed. Once the nodal quantities α_j are known, the approximate solution for $\bar{\phi} = \bar{\phi}(\bar{\xi})$ can readily be obtained from (3.36) for any $\bar{\xi}$ in the truncated domain [0, $\bar{\xi}_R$].

3.2.6 Determination of field quantities

Once the numerical solution $\bar{\phi} = \bar{\phi}(\bar{\xi})$ is obtained, functions $\bar{A} = \bar{A}(\bar{\xi}) = A(\bar{\xi})/a^5$ and $\bar{B} = \bar{B}(\bar{\xi}) = B(\bar{\xi})/a^4$ can be obtained at any $\bar{\xi} \in [0, \bar{\xi}_R]$ by directly solving the relations (3.23) and (2.25) via proper normalization. The explicit formula for $\bar{A} = \bar{A}(\bar{\xi})$ and $\bar{B} = \bar{B}(\bar{\xi})$ in terms of $\bar{\phi} = \bar{\phi}(\bar{\xi})$ is given by

$$A(\bar{\xi}) = \frac{\left(\dfrac{\bar{\lambda}}{\bar{\lambda}+1} + \bar{\Lambda}_0\bar{\xi}\right)\bar{\phi}\left(\bar{\xi}\right)}{\bar{\xi}^4\left\{2\left[\left(\bar{\lambda}+1\right)+\left(\bar{\lambda}+2\right)\bar{\Lambda}_0\bar{\xi}\right]+\overline{\tau^s}\bar{\xi}\left[\left(\bar{\lambda}+2\right)+\left(\bar{\lambda}+3\right)\bar{\Lambda}_0\bar{\xi}\right]\right\}} \tag{3.47}$$

$$B(\bar{\xi}) = \frac{\left(1+\bar{\Lambda}_0\bar{\xi}\right)\bar{\phi}\left(\bar{\xi}\right)}{\bar{\xi}^3\left\{2\left[\left(\bar{\lambda}+1\right)+\left(\bar{\lambda}+2\right)\bar{\Lambda}_0\bar{\xi}\right]+\overline{\tau^s}\bar{\xi}\left[\left(\bar{\lambda}+2\right)+\left(\bar{\lambda}+3\right)\bar{\Lambda}_0\bar{\xi}\right]\right\}} \tag{3.48}$$

The stress and displacement fields within the elastic half-space can then be obtained from the integrals (3.14)-(3.19) via proper normalization and with the upper limited being replaced by $\bar{\xi}_R$, i.e.

$$\begin{aligned}\bar{\sigma}_{rr}(\bar{r},\bar{z}) = \frac{\sigma_{rr}}{2(\lambda+\mu)} &= \int_0^{\bar{\xi}_R} \bar{\xi}^3 \left[-\bar{\xi}\bar{A} + \left(\frac{2\bar{\lambda}+1}{\bar{\lambda}+1} - \bar{\xi}\bar{z} \right) \bar{B} \right] e^{-\bar{\xi}\bar{z}} J_0(\bar{\xi}\bar{r})\, d\bar{\xi} \\ &- \frac{1}{\bar{r}} \int_0^{\bar{\xi}_R} \bar{\xi}^2 \left[-\bar{\xi}\bar{A} + (1-\bar{\xi}\bar{z})\bar{B} \right] e^{-\bar{\xi}\bar{z}} J_1(\bar{\xi}\bar{r})\, d\bar{\xi}\end{aligned} \tag{3.49}$$

$$\begin{aligned}\bar{\sigma}_{\theta\theta}(\bar{r},\bar{z}) = \frac{\sigma_{\theta\theta}}{2(\lambda+\mu)} &= \frac{\bar{\lambda}}{\bar{\lambda}+1} \int_0^{\bar{\xi}_R} \bar{\xi}^3 \bar{B} e^{-\bar{\xi}\bar{z}} J_0(\bar{\xi}\bar{r})\, d\bar{\xi} \\ &+ \frac{1}{\bar{r}} \int_0^{\bar{\xi}_R} \bar{\xi}^2 \left[-\bar{\xi}\bar{A} + (1-\bar{\xi}\bar{z})\bar{B} \right] e^{-\bar{\xi}\bar{z}} J_1(\bar{\xi}\bar{r})\, d\bar{\xi}\end{aligned} \tag{3.50}$$

$$\bar{\sigma}_{zz}(\bar{r},\bar{z}) = \frac{\sigma_{zz}}{2(\lambda+\mu)} = \int_0^{\bar{\xi}_R} \bar{\xi}^3 \left[\bar{\xi}\bar{A} + \left(\frac{1}{\bar{\lambda}+1} + \bar{\xi}\bar{z} \right) \bar{B} \right] e^{-\bar{\xi}\bar{z}} J_0(\bar{\xi}\bar{r})\, d\bar{\xi} \tag{3.51}$$

$$\bar{\sigma}_{rz}(\bar{r},\bar{z}) = \frac{\sigma_{rz}}{2(\lambda+\mu)} = \int_0^{\bar{\xi}_R} \bar{\xi}^3 \left[\bar{\xi}\bar{A} - \left(\frac{\bar{\lambda}}{\bar{\lambda}+1} - \bar{\xi}\bar{z} \right) \bar{B} \right] e^{-\bar{\xi}\bar{z}} J_1(\bar{\xi}\bar{r})\, d\bar{\xi} \tag{3.52}$$

$$\bar{u}_r(\bar{r},\bar{z}) = \frac{u_r}{a} = (\bar{\lambda}+1) \int_0^{\bar{\xi}_R} \bar{\xi}^2 \left[-\bar{\xi}\bar{A} + (1-\bar{\xi}\bar{z})\bar{B} \right] e^{-\bar{\xi}\bar{z}} J_1(\bar{\xi}\bar{r})\, d\bar{\xi} \tag{3.53}$$

$$\bar{u}_z(\bar{r},\bar{z}) = \frac{u_z}{a} = -(\bar{\lambda}+1) \int_0^{\bar{\xi}_R} \bar{\xi}^2 \left[\bar{\xi}\bar{A} + \left(\frac{2}{\bar{\lambda}+1} + \bar{\xi}\bar{z} \right) \bar{B} \right] e^{-\bar{\xi}\bar{z}} J_0(\bar{\xi}\bar{r})\, d\bar{\xi} \tag{3.54}$$

where $\bar{z} = z/a$. To evaluate such truncated Hankel transform inversions for any pair of points $(\bar{r}, \bar{z})$, standard Gaussian quadrature is again employed. It is important to point out that presence of the exponential term $e^{-\bar{\xi}\bar{z}}$ in the integrand significantly increases the rate of decay of the unfavorable oscillated behavior arising from the Bessel functions $J_n(\bar{\xi})$ for $\bar{z} > 0$ and, as a result, the associated integrals converges very rapidly with a relatively low $\bar{\xi}_R$. On the contrary, such exponential term becomes one on a free surface of the half-space (i.e. $\bar{z} = 0$) and, due to the slow rate of decay of the Bessel functions, it generally requires a sufficiently large $\bar{\xi}_R$ for those integrals associated with $\bar{z} = 0$ to achieve their converged value.

Once the elastic fields within the half-space are obtained, other interesting quantities can also be computed. For instance, the normalized contact pressure under the punch, denoted by $\bar{p} = \bar{p}(\bar{r})$, can readily be obtained from

$$\bar{p}(\bar{r}) = \frac{p}{2(\lambda+\mu)} = -\left[\bar{\sigma}_{zz}(\bar{r},\bar{z}=0) + \frac{\bar{\tau}^s \nabla^2 \bar{u}_z(\bar{r},\bar{z}=0)}{2(\bar{\lambda}+1)} \right] \qquad ; \quad 0 \le \bar{r} < 1 \tag{3.55}$$

It is remarked that the Laplacian of the normal displacement appearing on the right hand side of (3.55) can directly be evaluated using the prescribed boundary condition (3.20). The normalized indentation force $\overline{P}$ can further be computed by integrating the contact pressure $\overline{p} = \overline{p}(\overline{r})$ over the contact region:

$$\overline{P} = \frac{P}{2a^2(\lambda+\mu)} = -\int_0^{2\pi}\int_0^1 \overline{p}(\overline{r})\overline{r}d\overline{r}d\theta = -2\pi\int_0^1 \overline{p}(\overline{r})\overline{r}d\overline{r} \tag{3.56}$$

3.2.7 Determination of contact radius *a* for smooth-contact punch

For a smooth-contact punch, the contact radius *a* is unknown a priori and must be determined first before other quantities of interest can be obtained. It is remarked first that once the contact radius *a* is known, there is no difference of a solution procedure for both smooth-contact and nonsmooth-contact punch. To solve for a final contact region *a* that corresponds to a given indentation depth *d*, a physically admissible condition associated with the continuity of the vertical stress at $r = a$ is utilized. However, the explicit or close-form relationship between those two parameters (*a* and *d*) cannot be obtained due to the complexity of the boundary value problem accounted for the surface energy effects.

3.2.8 Convergence study

For the proposed numerical technique, three key factors that affect the accuracy of the approximate solutions are the truncation parameter $\overline{\xi}_R$, the number of elements employed in the discretization, and the number of integration points used in standard Gaussian quadrature. Extensive numerical experiments have been performed to choose a proper truncated domain, the level of mesh refinement and optimal quadrature to ensure the convergence and accuracy of numerical results. Such investigation is briefly discussed below.

The number of Gauss points required in the numerical integration can be significant to accurately integrate oscillating and complex integrands (resulting from the Bessel functions, $\overline{\phi} = \overline{\phi}(\overline{\xi})$, the kernel $K(\overline{\xi}, u)$). From numerical experiments, it is found that as the size of elements decreases (i.e. the number of elements in the discretization increases), it only requires few Gauss points to achieve highly accurate results since the integrand on each element exhibits milder variation without oscillating behavior.

To investigate the level of mesh refinement required to obtain the converged results, we perform experiments for a given truncated domain $[0, \overline{\xi}_R]$. A series of meshes on the fixed $[0, \overline{\xi}_R]$ is constructed and then used in the analysis. The number of elements (*N*) in the discretization is increased until a converged solution (for a specified tolerance) is obtained for a fixed $\overline{\xi}_R$. By repeating the analysis for various $\overline{\xi}_R$, a ratio $N/\overline{\xi}_R$ (representing the level of mesh refinement) to ensure the good discretization is found approximately equal to 1.

To obtain a proper truncated domain that optimizes the computational cost but, at the same time, yields accurate results, we next investigate the convergence of approximate solutions with respect to the truncated parameter $\overline{\xi}_R$. From such study, it can be concluded that the truncated parameter $\overline{\xi}_R$ to attain a converged results for the non-smooth contact punch is much larger than that for the smooth contact punch. This is due primarily to the singularity induced at the boundary of the contact region of the non-smooth contact punch. Suggested by various

experiments, the truncated parameter $\overline{\xi}_R$ in the analysis of non-smooth contact and smooth contact punches equal to 10,000 and 1,000 respectively.

3.3 Numerical Results

The solution procedure described in section 3.2 is implemented as an in-house computer code to determine the complete elastic fields for punches of both smooth and non-smooth contacts. The accuracy of the present numerical scheme is first verified by comparing with analytical solutions of the classical case (no surface energy effects) for both categories. Once the method is tested, it is then applied to solve more complex indentation problems accounted for surface stress effects in which analytical solutions do not exist. In the analysis, punches with flat-ended and paraboloidal profiles are chosen to represent the non-smooth and smooth contacts, respectively. Numerical results for three different models (i.e. classical solution with no surface stress effects and solutions accounted for surface stress effects with and without the out-of-plane contribution of the residual surface tension) are fully compared and discussed.

3.3.1 Verification with analytical solutions

Consider a rigid frictionless punch with a flat-ended cylindrical profile (i.e. $\delta(r) = 0$) and a paraboloidal profile (i.e. $\delta(r) = \alpha r^2$ where α is a constant) indented on an isotropic, elastic half-space as shown schematically in Figure 3.2(a) and Figure 3.2(b) respectively. Note that for both punch profiles the total indentation depth at the tip of the punch d and the final radius of contact a are associated with the total indentation force P. With no surface surface effect, the analytical solutions derived by Sneddon (1965) are employed to validate the proposed formulation and numerical implementations. In numerical experiments, the present solution scheme is specialized to treat the classical case by setting $\overline{\Lambda}_0 = 0$ and $\overline{\tau^s} = 0$. According to Sneddon (1965), the distribution of contact pressure under the punch p_c, the shape of the deformed boundary $u_z(r, 0)$ and the total indentation force P_c required to produce the indentation depth d for flat-ended cylindrical and paraboloidal punches are summarized below.

(a) Flat-ended Cylindrical Punch

$$p_c = \frac{4\mu(\lambda+\mu)d}{\pi(\lambda+2\mu)a}\frac{1}{\sqrt{1-(r/a)^2}} \quad ; \quad 0 \le r < a \tag{3.57}$$

$$u_z(r,0) = \frac{2d}{\pi}\sin^{-1}(a/r) \quad ; \quad r > a \tag{3.58}$$

$$P_c = \frac{8\mu(\lambda+\mu)}{\lambda+2\mu}ad \tag{3.59}$$

(b) Paraboloidal Punch

$$a_c^{\,2} = \frac{d}{2\alpha} \tag{3.60}$$

$$p_c = \frac{8\mu(\lambda+\mu)d}{\pi a(\lambda+2\mu)}\sqrt{1-(r/a)^2} \quad ; \quad 0 \le r < a \tag{3.61}$$

$$u_z(r,0) = \frac{d}{\pi}\left\{(2-(r/a)^2)\sin^{-1}(a/r) + \frac{r}{a}\sqrt{1-(a/r)^2}\right\} \qquad ; \quad r > a \tag{3.62}$$

$$P_c = \frac{32\mu(\lambda+\mu)}{3(\lambda+2\mu)}\alpha a^3, \tag{3.63}$$

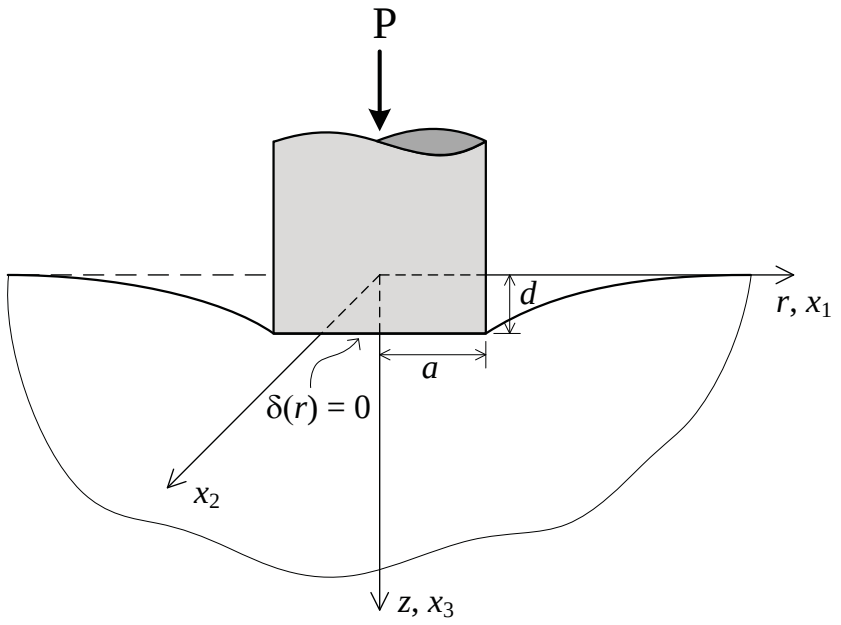

(a)

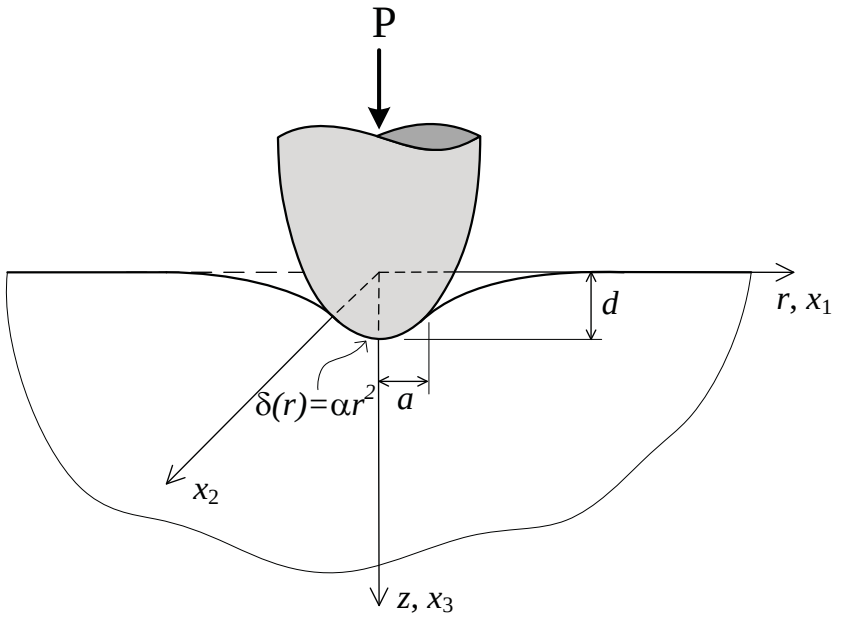

(b)

Figure 3.2 Indentation of half-space by axisymmetric rigid frictionless punch: flat-ended cylindrical punch and (b) paraboloidal punch

Though the properties of elastic materials in the present study can be arbitrary, to simply compare some elastic quantities with those obtained by Zhao (2009), the same set of material properties is uitilized. Aluminum is used for the bulk material (Meyers and Chawla, 1999) whereas Al [1 1 1] is employed for the surface (Miller and Shenoy, 2000). All material constants are summarized in Table 3.1. In the numerical study, it is convenient to introduce following non-dimensional quantities: $r_0 = r/\Lambda_0$; $z_0 = z/\Lambda_0$; $a_0 = a/\Lambda_0$; $d_0 = d/\Lambda_0$ and $\alpha_0 = \alpha \Lambda_0$. It is worth noting that although the classical solution is independent of Λ_0, use of this parameter in the non-dimensionalization allows a direct comparison between non-classical and classical solutions.

In the case of flat-ended cylindrical punch with contact radius $a_0 = 0.5$, comparisons betwen the cuurent solutions and the classical solutions for the contact pressure and the vertical displacement are presented in Figure 3.3(a) and Figure 3.3(b) respectively. It is evidently found that numerical results obtained from the present study are almost indistinguishable from the exact solutions proposed by Sneddon (1965). Another comparison is performed for the case of paraboloidal punch with $\alpha_0 = 0.5$. It can be obviously seen from Figure 3.4(a) and Figure 3.4(b) that two numerical solutions obtained from the present scheme, one is the contact pressure and the other is the vertical displacement at the free surface, once again exhibit excellent agreement with the corresponding analytical solutions. This additionally confirms the accuracy of the present technique.

3.3.2 Punch with surface stress effects

From the high accuracy of numerical solutions obtained for the classical case, the proposed scheme is now convincingly applied to investigate the indentation problems with the surface stress effects being incorporated. To allow comparisons with results obtained from Zhao (2009) and demonstrate the significant role of the surface residual tension τ^s, Gurtin-Murdoch model without the out-of-plane contribution of τ^s is also considered. Selected numerical results are reported and dicussed for both punch profiles as follows.

3.3.2.1 Flat-ended cylindrical punch

The case of a flat-ended cylindrical punch indented on the half-space with a specified contact radius *a* and indentation depth *d* shown in Figure 3.2(a) is first examined. Note that this punch is an example of a non-smooth contact punch since $d\delta/dr$ is not well-defined at $r = a$. The corresponding elastic fields within the half-space are reported in Figures 3.5-3.8.

It can be obviously seen from Figure 3.5 that the distribution of the contact pressure under the punch accounted for the surface effects possesses the same trend as that for the classical solution in which the singularity still exists at the boundary of the punch. Due to the integration of the out-of-plane contribution of the surface tension, the predicted contact pressure for this particular model is considerably less than those obtained from the other two models (i.e. the classical model and Gurtin-Murdoch model without the out-of-plane contribution of τ^s). In the analysis, three values of the contact radii, $a_0 = 0.5$, 1.0 and 1.5, are considered to study the size-dependent behavior and found that when the radius of a punch is smaller and in the same order as Λ_0, the effects of surface stresses are comparatively larger. It is interesting to point out that when the contact pressure *p* has been normalized in a proper manner (i.e. normalized as $\pi p a_0/4\mu d_0$), size-dependent behavior due to the influence of surface energy effects is significantly demonstrated. This phenomenon cannot be certainly observed in the classical model (only one single dotted line is shown in spite of changing the contact radius a_0). It implies that

the classical model ignores an inevitable material parameter (i.e. the intrinsic length Λ_0) and, as a result, it predicts erroneous solutions when the radius of a punch is very small. However, the contact pressure under the larger punch (i.e. larger contact radius a_0) for both models, accounted for the surface energy effects, converges monotonically to the classical solution.

The variations of normalized vertical stresses, $\pi\sigma_{zz}/4\mu d_0$, along the radial direction at four depths, z_0 = 0.1, 0.5, 1.0 and 1.5, with contact radius a_0 = 0.5 are shown in Figure 3.6. The vertical stress profiles indicate the strong influence of the surface energy effects for region relatively closed to the punch. In particular, at very small depth (i.e. z_0 = 0.1), the vertical stress increases monotonically and reaches their peak values near r_0/a_0 = 1 and then starts to drop rapidly when r_0 increases. At larger depths, the vertical stress reaches its maximum at r_0 = 0 and decreases monotonically to zero at relatively large r_0. It is evident that an ideal surface attached to the bulk of the current model distributes the localized indentation force to an area outside the contact region. As a direct consequence, the current model (i.e. Gurtin-Murdoch model with the out-of-plane contribution of τ^s) predicts the lower vertical stress under the punch and higher vertical stress outside the contact region than those obtained from the other two models. However, such discrepancy becomes insignificant in the region far away from the punch.

Numerical results of normalized shear stresses, $\pi\sigma_{rz}/4\mu d_0$, and radial stresses, $\pi\sigma_{rr}/4\mu d_0$, at various depths with contact radius a_0 = 0.5 are also presented in Figure 3.7(a) and Figure 3.7(b) respectively. Similar to the vertical stresses, the magnitudes of shear stresses along the radial direction predicted by the current model are generally lower and higher respectively than those obtained from the other two models for regions inside and outside the contact area. The shear stress at any depth vanishes at r_0 = 0 because of the axisymmetry, and it reaches its peak value near the edge of the punch (r_0/a_0 = 1) and, thereafter, decreases rapidly with r_0. However, such behavior is not observed for the radial stress, for instance, the magnitude of radial stress at z_0 = 0.5 obtained from the current model lies between those predicted by the other two models for a region inside the contact. As expected, the shear and radial stresses obtained from all three models for relatively large r_0 possess the same trend and decay monotonically to zero. The inflence of surface energy effects is extremely small for $z_0 \geq 1.5$ as clearly demonstrated by small discrepancy between the solutions obtained from the current and classical models.

According to results shown in Figure 3.8(a) for the normalized vertical displacement, $u_z/\Lambda_0 d_0$, along the radial direction at five depths, z_0 = 0.0, 0.1, 0.5, 1.0 and 1.5, with contact radius a_0 = 0.5, one predicted by the current model is comparatively higher than those obtained from the other two models due to the need of higher indentation force to produce the same indentation depth. Unlike the stress solutions, vertical displacements exhibit a slower decay rate as z_0 increases while they still gradually converge to the classical solutions. As the final illustration of elastic fields for this particular punch, the normalized radial displacement, $u_r/\Lambda_0 d_0$, at four dfifferent depths, z_0 = 0.1, 0.5, 1.0 and 1.5, with the same contact radius a_0 = 0.5 is reported in Figure 3.8(b). Clearly, the radial displacement increases rapidly from zero at r_0 = 0 to its peak value at relatively small r_0 and then gradually decreases with r_0. It should be noted that the surface energy effects only influence the magnitude of the radial displacement whereas its distribution along the radial direction predicted by all three models is quite similar.

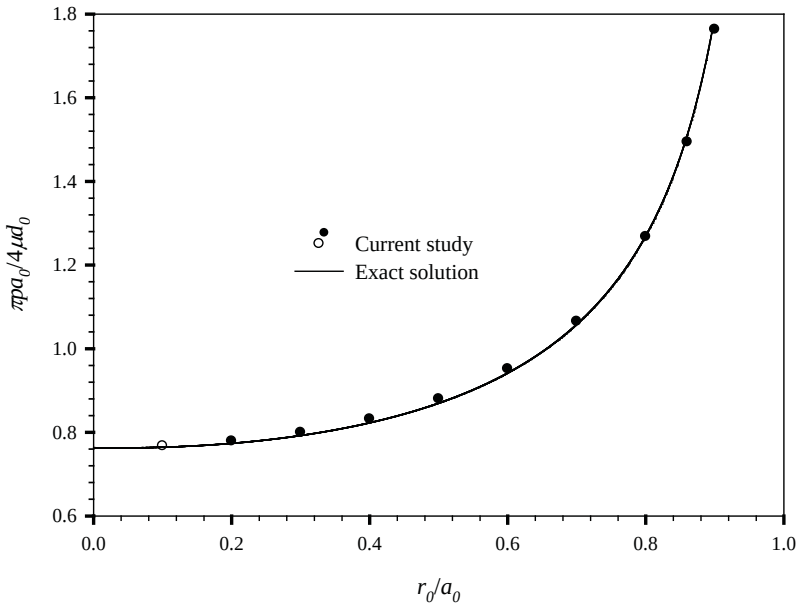

(a)

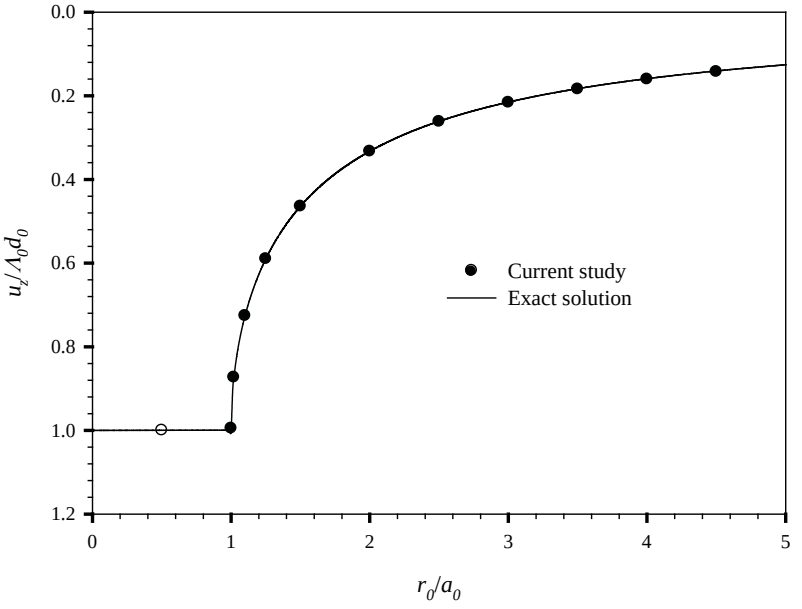

(b)

Figure 3.3 Comparisons of classical numerical solutions with exact solutions for flat-ended cylindrical punch: (a) normalized contact pressure and (b) normalized vertical displacement

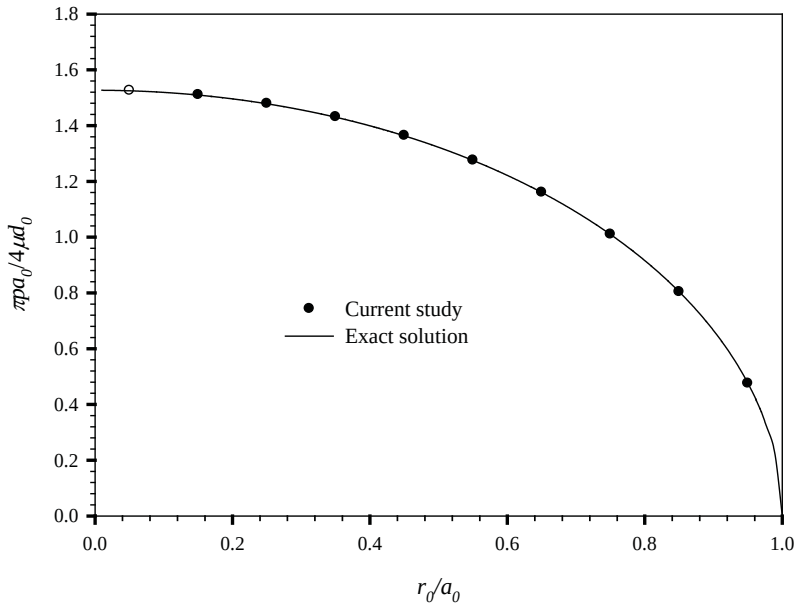

(a)

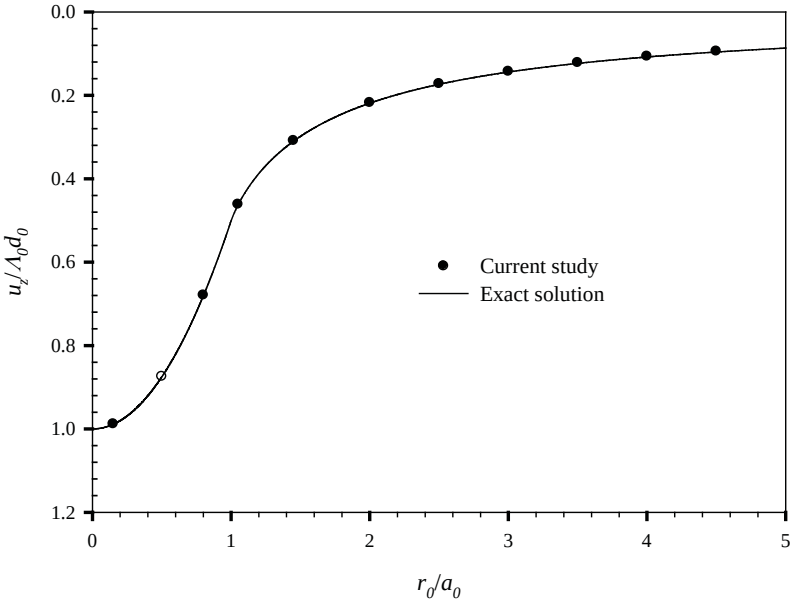

(b)

Figure 3.4 Comparisons of classical numerical solutions with exact solutions for paraboloidal punch: (a) normalized contact pressure and (b) normalized vertical displacement

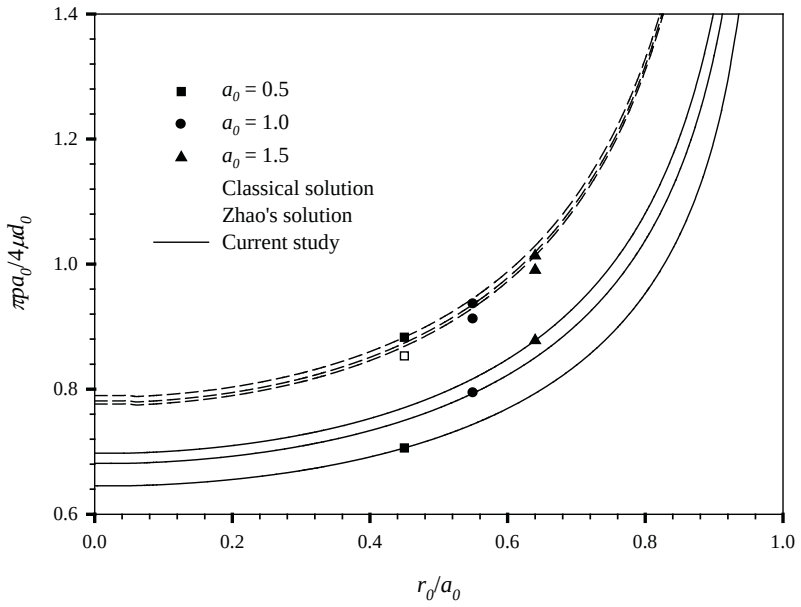

Figure 3.5 Distribution of normalized contact pressure under flat-ended cylindrical punch with various contact radii

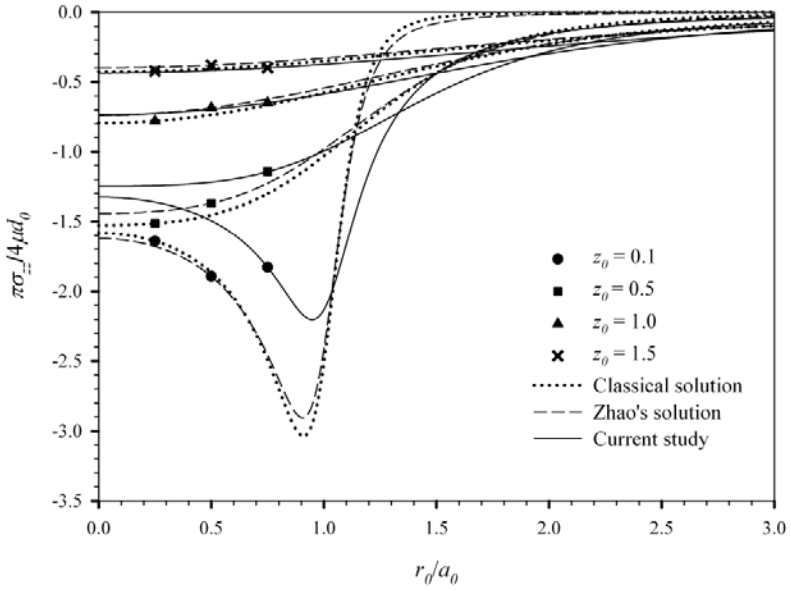

Figure 3.6 Normalized vertical stress profiles of flat-ended cylindrical punch with contact radius $a_0 = 0.5$ at various depths

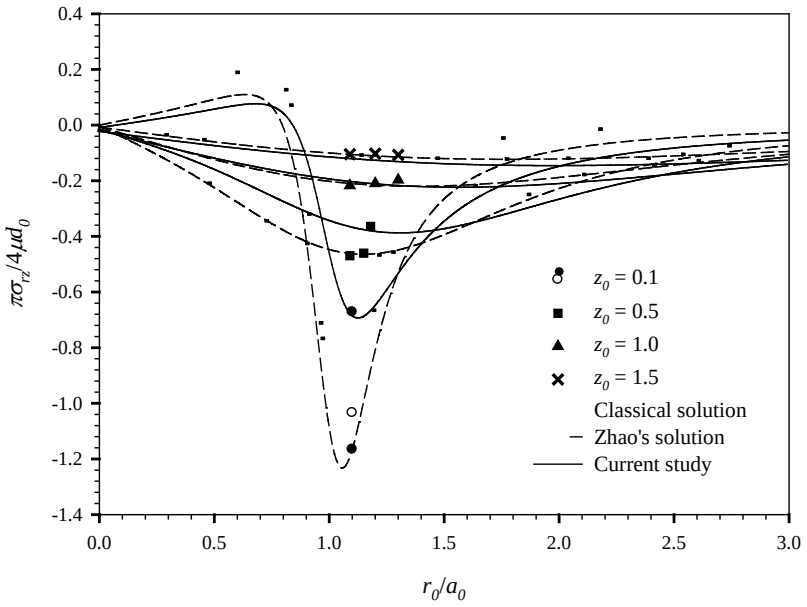

(a)

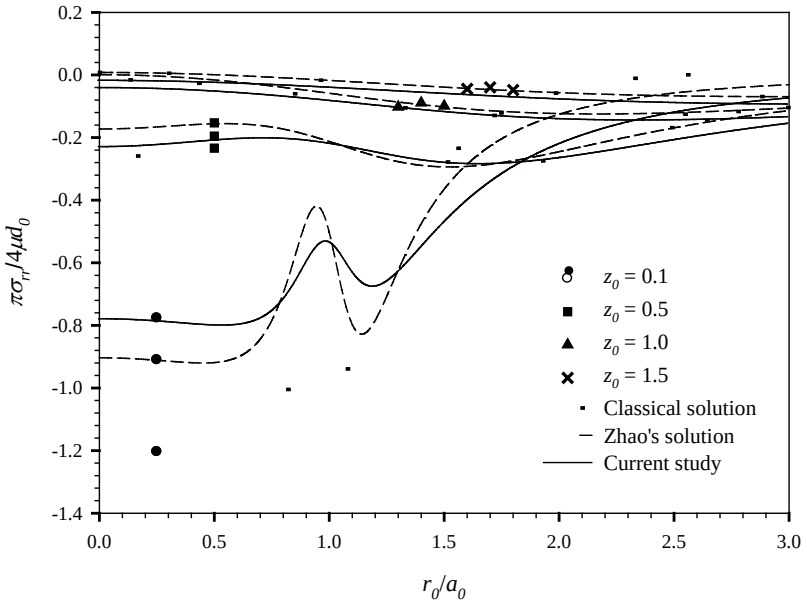

(b)

Figure 3.7 Normalized stress profiles of flat-ended cylindrical punch with contact radius a_0 = 0.5 at various depths: (a) shear stress and (b) radial stress

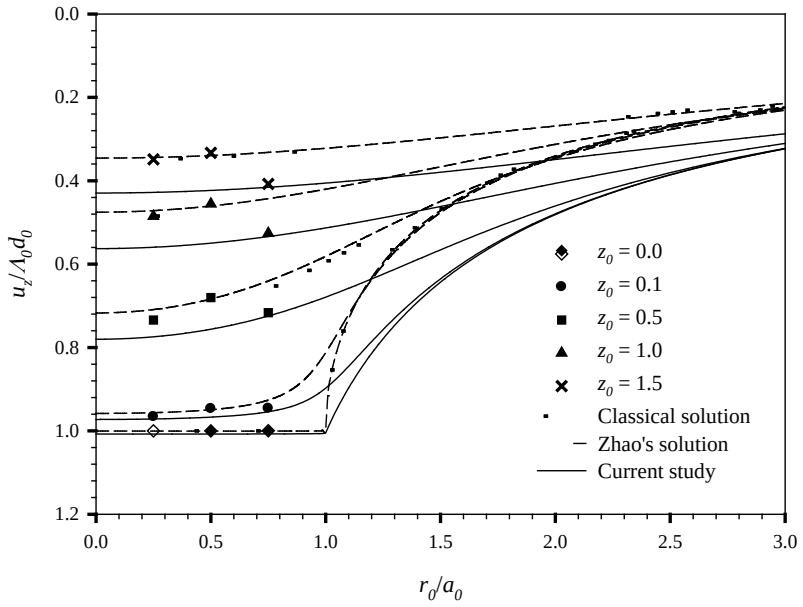

(a)

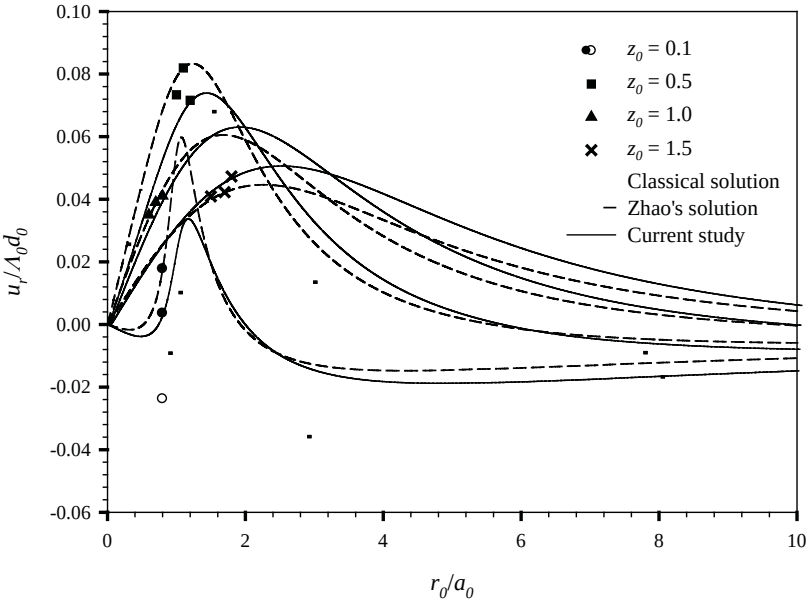

(b)

Figure 3.8 Normalized displacement profiles of flat-ended cylindrical punch with contact radius a_0 = 0.5 at various depths: (a) vertical displacement and (b) radial displacement

3.3.2.2 Paraboloidal punch

Consider next a paraboloidal punch with α_0 = 0.5 acting on the half-space with the indentation depth d and final contact radius a as shown in Figure 3.2(b). This punch belongs to a class of smooth contact punches since $d\delta/dr$ is well-defined at $r = a$ where a is unknown a priori. Note again that the final contact radius a is determined by enforcing the continuity condition of the vertical stress beneath the punch at $r = a$. Numerical results for elastic fields of this particular punch profile are reported in Figures 3.9-3.12, additionally, some interesting results demonstrating size-dependent behavior and material stiffness due to surface energy effects are finally shown in Figures 3.13-3.15 and all crucial remarks are summarized as follows.

To demonstrate the size-dependency resulting from the influence of surface energy effects, the distribution of normalized contact pressure under a paraboloidal punch, $\pi p a_0/4\mu d_0$, is first presented in Figure 3.9 for three values of the contact radii, a_0 = 0.5, 0.8 and 1.0. Interestingly, the contact pressure predicted by the current model becomes finite at the boundary while those obtained from the classical case and Zhao's model vanish at the boundary of the contact region. Unlike the results for the flat-ended cylindrical punch, the contact pressure obtained from the current model is significantly larger than those obtained from the other two models. However, such discrepancy becomes smaller when the contact radius is larger. Note that upon the proper normalization the distribution of the contact pressure for the classical case is obviously independent of the contact radius, and exhibits no size-dependency.

Normalized vertical stress profiles for the paraboloidal punch with a fixed contact radius a_0 = 0.5 at five depths, z_0 = 0.0, 0.1, 0.5, 1.0 and 1.5, are reported in Figure 3.10. It is important to emphasize that due to the enforcement of continuity of the vertical stress at $r = a$, the singularity behavior at the boundary of the contact region disappears for this particular punch profile similar to what observed in the case of flat-ended punch. The maximum value of the vertical stress occurs at the origin and rapidly decays to zero as r_0 increases. Clearly, the distribution of the vertical stress along the radial direction at a very small depth exhibits significant difference from the case of the flat-ended punch. Once again, the vertical stress close to the free surface predicted by the current model deviates from those obtained from the classical and Zhao's models. This implies that the stress field depends significantly on the surface energy effects and the out-of-plane contribution of the residual surface tension.

Figures 3.11(a) and 3.11(b) show the normalized shear and radial stresses along the radial direction with contact radius a_0 = 0.5 at four different depths, z_0 = 0.1, 0.5, 1.0 and 1.5. Similar to the case of flat-ended punch, the shear stress at each depth increases from zero at r_0 = 0 to its peak value near the punch boundary (r_0/a_0 = 1) and then decays rapidly as r_0 increases. On the other hand, the radial stress decreases monotonically from its maximum value at r_0 = 0 as r_0 increases. Again, the surface energy exhibits significant influence on both shear and radial stresses only in a local region very near the punch, and its contribution becomes negligible at regions very far from the punch. The influence of surface energy on the vertical and radial displacements is also clearly demonstrated by the results shown in Figures 3.12(a) and 3.12(b). The vertical displacement predicted by the current model is comparatively higher with a slower decay rate when compared to those obtained from the other two models. This observed behavior is similar to the case of flat-ended punch.

To further demonstrate the size-dependent behavior, the relationship between the ratio a_0/a_c (where a_c denotes the contact radius for the classical case) and the contact radius a_0 of a paraboloidal punch is investigated as shown in Figure 3.13. Due to the influence of surface energy effects, it is evident that the contact radius is smaller than that obtained from the classical

case for the same indentation depth. This implies that presence of the surface stress renders the material stiffer. In particular, the difference from the classical solution is less than 1% for Zhao's model and up to 30% for the current model. It appears that the out-of-plane contribution of residual surface tension has a significant influence on material stiffness, and the surface energy effects play a prominent role in mechanical properties of materials.

Another set of results that confirms the size-dependent behavior of predicted solutions when the surface energy effects are incorporated is associated with the relationship between the normalized indentation force, P/P_c, and the contact radius a_0 for flat-ended cylindrical and paraboloidal punches as shown in Figure 3.14. It is obviously seen that when the radius of the punch becomes smaller the indentation force required to produce the same indentation depth is relatively higher due to the surface energy effects. The discrepancy is more pronounced for the results predicted by the current model when compared to Zhao's solutions. This implies that the stiffness of materials characterized by the indentation experiment does not only depend on the penetration depth but also the radius of the punch. In particular, at the contact radius $a_0 = 0.1$, results obtained from Zhao's model are approximately 5% higher than the classical solution for both punch profiles whereas those predicted by a model accounted for the out-of-plane contribution of the residual surface tension are up to 120% and 160% higher than that obtained from the classical model for paraboloidal and flat-ended punches respectively.

To clearly demonstrate the influence of surface energy effects on the material stiffness, the relationship between normalized indentation force, $P/4\mu\Lambda_0^2$, and the indentation depth d_0 for both punch profiles are presented in Figures 3.15(a) and 3.15(b). It can be concluded from these results that the indentation force for both punches predicted by the current model is significantly higher than those obtained from the classical model and Zhao's model. This additionally confirms that materials become stiffer due to the presence of the surface stress effects and the out-of-plane contribution of the residual surface tension amplifies such influence. It is also important to emphasize that the discrepancy of results for the flat-ended cylindrical punch is more pronounced than that for the paraboloidal punch due to the non-smoothness of the punch profile and the singularity of stress field introduced at the boundary of the contact region.

Table 3.1 Material properties used in numerical study

Model Parameter	Value (unit)
λ	58.17×10^9 (N/m^2)
μ	26.13×10^9 (N/m^2)
Λ_0	0.16707 (nm)
λ^s	6.8511 (N/m)
μ^s	-0.376 (N/m)
τ^s	1 (N/m)

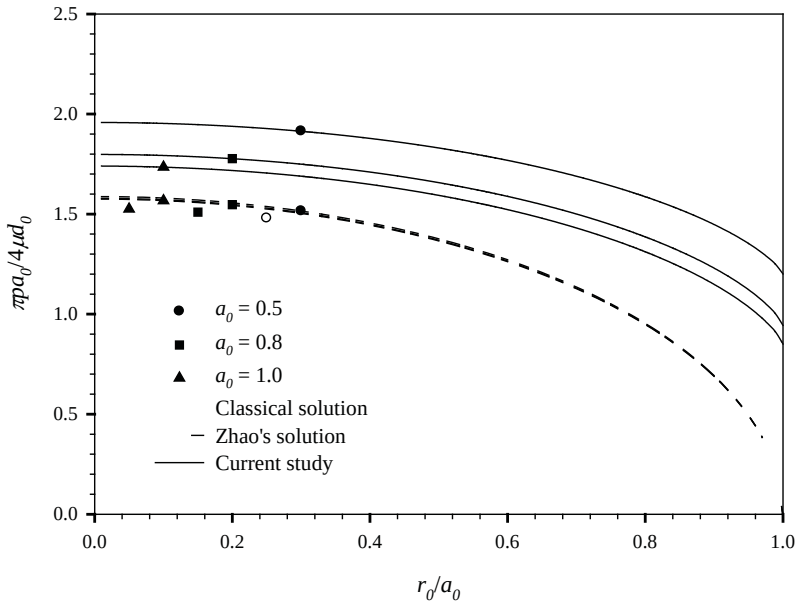

Figure 3.9 Distribution of normalized contact pressure under paraboloidal punch with various contact radii

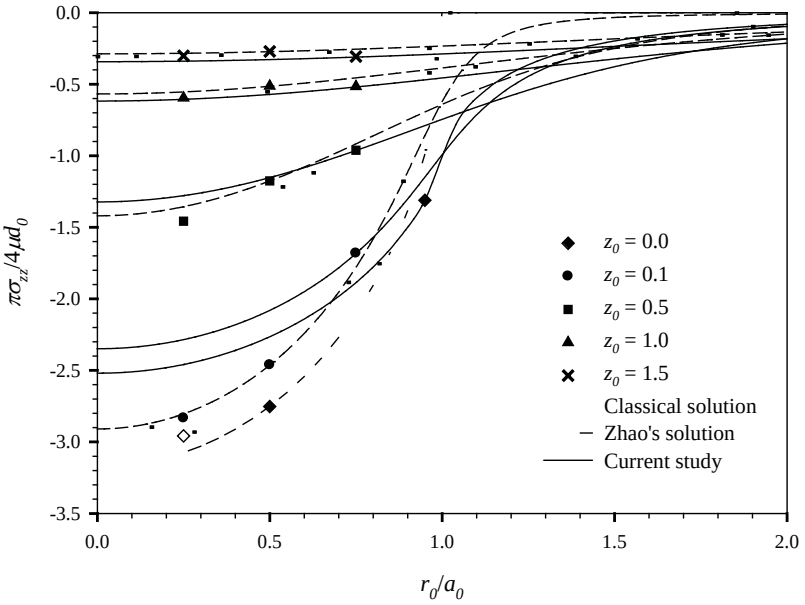

Figure 3.10 Normalized vertical stress profiles of paraboloidal punch with contact radius a_0 = 0.5 at various depths

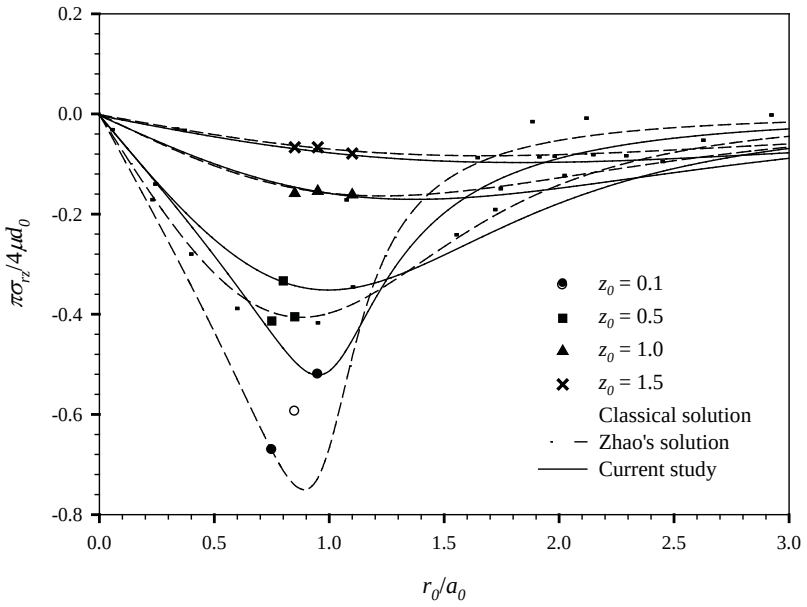

(a)

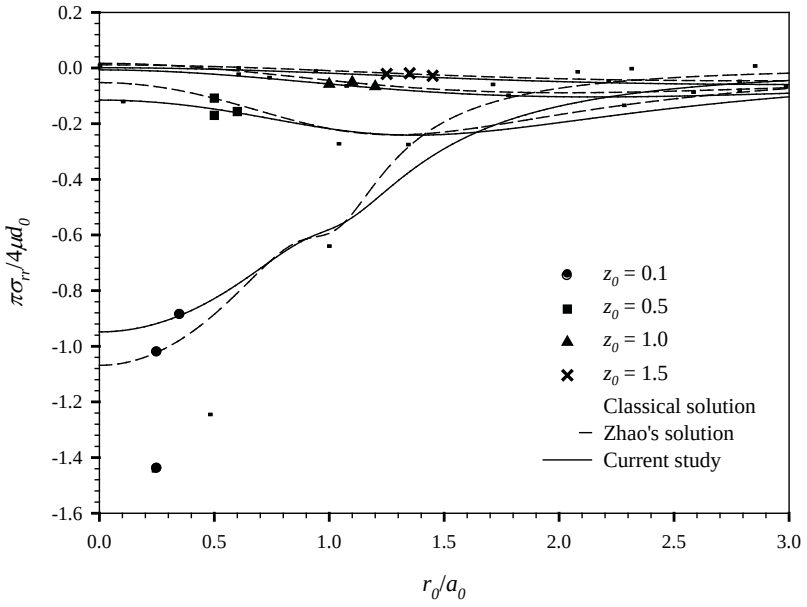

(b)

Figure 3.11 Normalized stress profiles of paraboloidal punch with contact radius a_0 = 0.5 at various depths: (a) shear stress and (b) radial stress

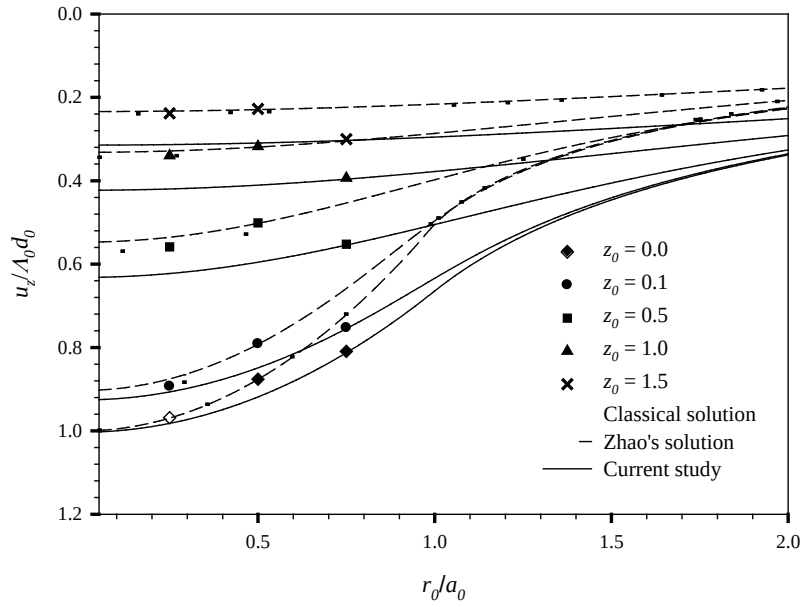

(a)

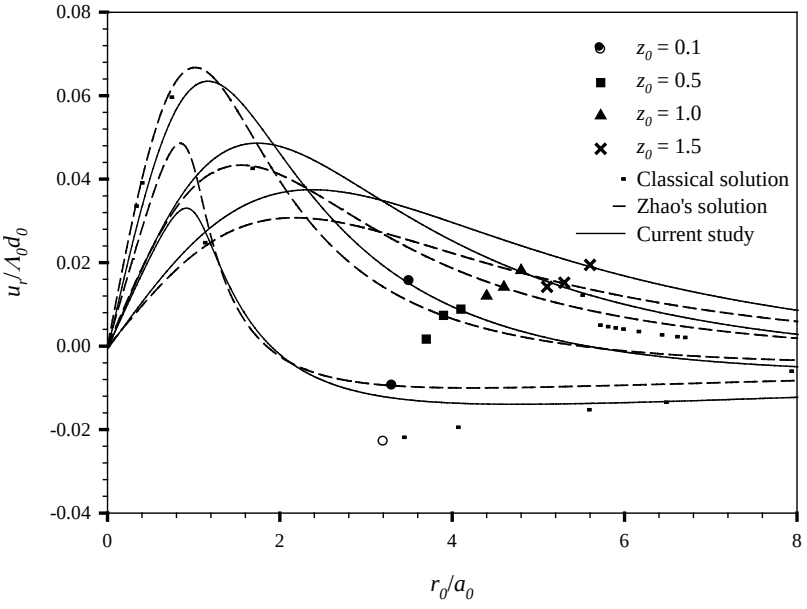

(b)

Figure 3.12 Normalized displacement profiles of paraboloidal punch with contact radius $a_0 = 0.5$ at various depths: (a) vertical displacement and (b) radial displacement

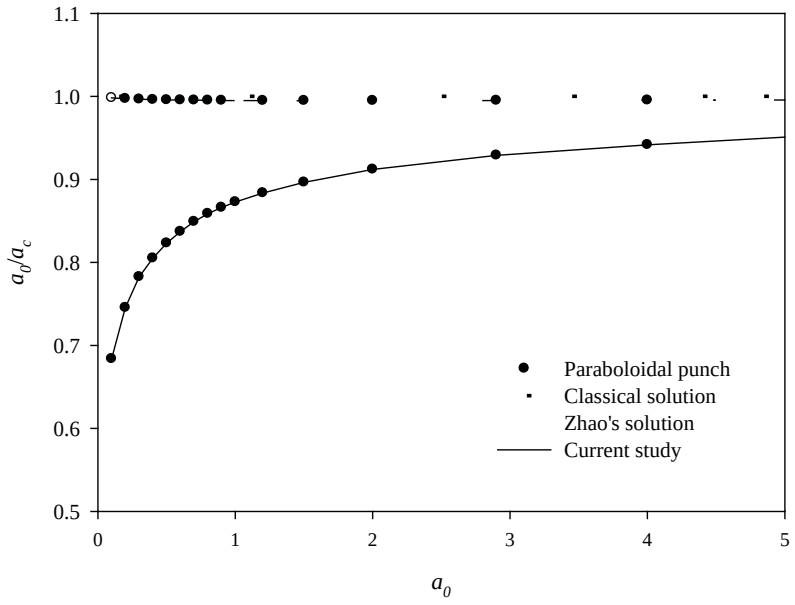

Figure 3.13 Variation of a_0/a_c versus contact radius a_0.

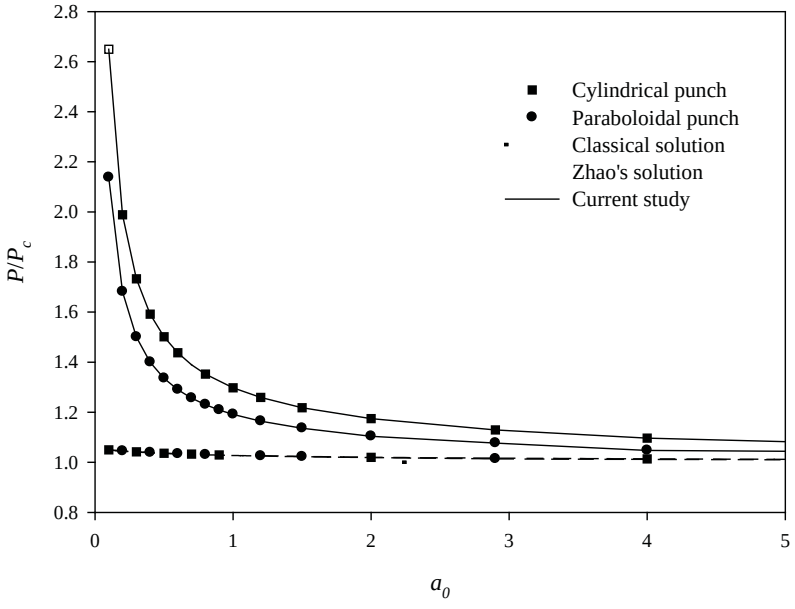

Figure 3.14 Variation of normalized indentation force versus contact radius a_0

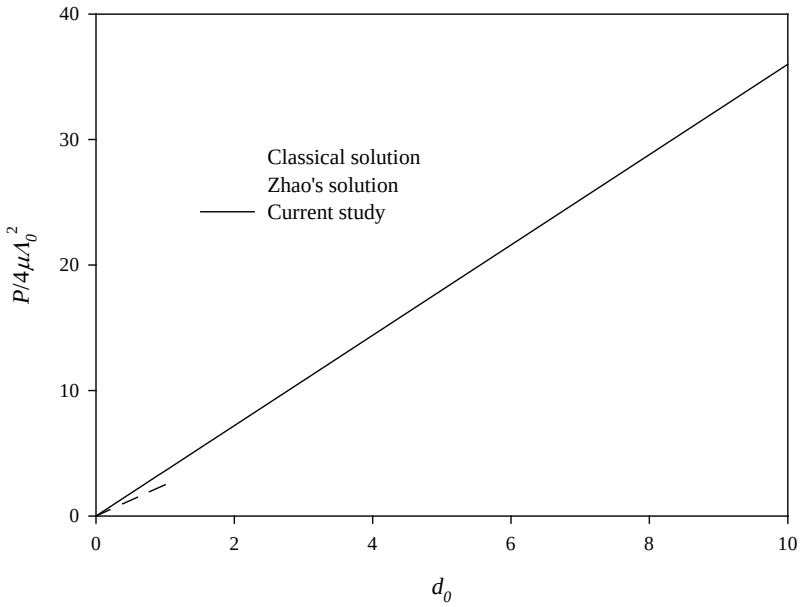

(a)

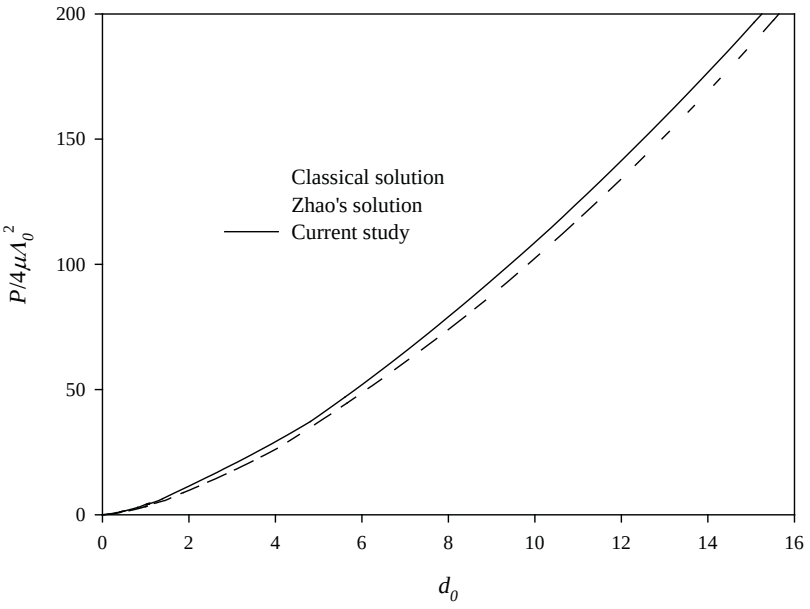

(b)

Figure 3.15 Relationship between normalized indentation force and indentation depth d_0: (a) flat-ended cylindrical punch and (b) paraboloidal punch

CHAPTER IV

NANO-CRACKS

This chapter begins with the clear problem description and essential assumptions for the formulation of boundary value problem related to nano-cracks in three-dimensional infinite elastic media. All basic field equations and the development of governing equations for both the bulk material and the crack surface are then presented. Next, the fully coupled system of weak-form equations governing the primary unknowns on the crack surface is derived. Essential components required in the numerical implementation including the discretization and numerical integration are briefly discussed. In general, standard procedures for the weakly singular SGBEM (e.g., Li and Mear 1998, Li *et al.* 1998, Rungamornrat 2006, Rungamornrat and Mear 2008) and those for the standard finite element method (e.g., Bathe 1990, Hughes 2000, Zienkiewicz and Taylor 2000) are utilized to form the discretized system of linear algebraic equations. To verify the formulation and numerical implementation of the proposed method for solving nano-sized cracks problems, a penny-shaped crack embedded in an isotropic, linearly elastic, unbounded domain under pure mode-I loading conditions is considered first. Results of the crack opening displacement and the vertical stress in the vicinity of the crack front are compared with existing benchmark solutions (Intarit *et al.* 2012, Intarit 2013). Once the technique is fully tested, the parametric study is performed for this particular problem to elucidate the influence of surface stresses and the size-dependent behaviors of the predicted solutions. Then, the same penny-shaped crack is investigated for mixed-mode loading conditions. To further demonstrate the capability of the current method in solving cracks of arbitrary shapes and multiple cracks, an elliptical crack under mode-I and mixed-mode loading conditions and two coplanar cracks under mode-I loading are considered respectively in the remaining of this chapter.

4.1 Formulation

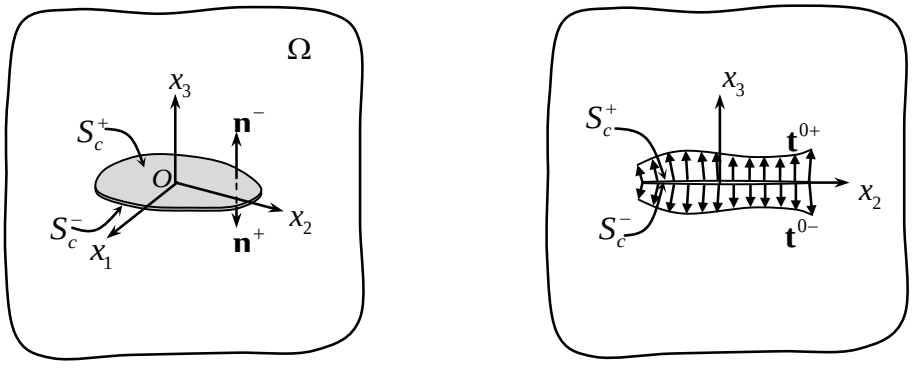

(a) (b)

Figure 4.1 (a) Schematic of three-dimensional infinite elastic medium containing an isolated crack and (b) prescribed traction on crack surfaces.

Consider a three-dimensional, linearly elastic, infinite medium Ω containing an isolated, planar crack of arbitrary shape with a selected reference Cartesian coordinate system $\{O;\ x_1;\ x_2;\ x_3\}$, as shown schematically in Figure 4.1(a).

The crack is represented by two geometrically identical surfaces, denoted by S_c^+ and S_c^-, with the corresponding outward unit normal vectors $\mathbf{n}^+$ and $\mathbf{n}^-$ oriented perpendicular to the x_3-axis for convenience in further development. In the present study, the medium is assumed free of body forces and remote loading, but subjected to prescribed, self-equilibrated, normal traction $\mathbf{t}^{0+}$ and $\mathbf{t}^{0-}$ on the crack surfaces S_c^+ and S_c^- respectively (see Figure 4.1(b)). An infinitesimally thin layer on each crack surface possesses a constant residual surface tension τ^s (under unstrained conditions) and the surface Lamé constants λ^s and μ^s, whereas the rest of the medium, termed the "*bulk material*", is made of a homogeneous, isotropic, linearly elastic material with shear modulus μ and Poisson's ratio ν.

A clear problem statement of the present study is to determine the complete elastic field including the displacements and stresses within the bulk material by taking the influence of surface stresses into account. Fracture-related information such as the relative crack-face displacement and the local stress field in the vicinity of the crack front is also of primary interest.

4.1.1 Domain decomposition

In the formulation of the boundary value problem, the medium is decomposed into three parts: the bulk material, the zero-thickness layer S_c^+ and the zero-thickness layer S_c^- as shown in Figure 4.2. The bulk material is simply the whole medium without the two infinitesimally thin layers on the crack surfaces. Since both layers have zero thickness, the geometry of the bulk material is therefore identical to that of the whole medium (i.e. it can also be completely described by the region Ω and the two crack surfaces S_c^+ and S_c^-).

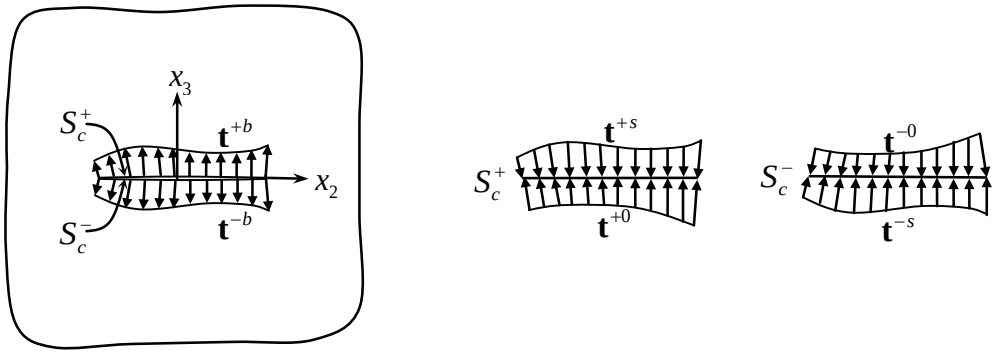

(a) (b) (c)

Figure 4.2 Schematics of (a) the bulk material, (b) the zero-thickness layer S_c^+ and (c) the zero-thickness layer S_c^-.

The key difference between the bulk material and the original medium is that the bulk material is homogeneous and the crack surfaces S_c^+ and S_c^- in the bulk material part are subjected to unknown tractions (exerted directly by the two layers) $\mathbf{t}^{+b}$ and $\mathbf{t}^{-b}$, respectively. The layer S_c^+ is treated as a two-sided surface with one side subjected to the prescribed traction $\mathbf{t}^{+0}$ and the other side subjected to the traction $\mathbf{t}^{+s}$ exerted by the bulk material (Figure 4.2(b)). Similarly, the layer S_c^- is treated as a two-sided surface with one side subjected to the prescribed traction $\mathbf{t}^{-0}$ and the other side subjected to the traction $\mathbf{t}^{-s}$ exerted by the bulk material (Figure 4.2(c)). In what follows, Greek subscripts denote field quantities associated with the surface and take the values 1, 2 while the Latin subscripts take the values 1, 2, 3. It is remarked that, in the development to follow, it will suffice to make reference to the single crack surface $S_c \equiv S_c^+$.

4.1.2 Governing equations of bulk material

Since the bulk material is made of homogeneous, isotropic, linear elastic material, its behavior is governed by the classical theory of linear elasticity. From results developed in the work of Rungamornrat and Mear (2008a) and Rungamornrat and Senjuntichai (2009), the displacement and stress components at any interior point $\mathbf{x}$, denoted respectively by $u_p(\mathbf{x})$ and $\sigma_{ij}(\mathbf{x})$, can be expressed in terms of the traction data $\mathbf{t}^{+b}$ and $\mathbf{t}^{-b}$ and the displacement data $\mathbf{u}^{+b}$ and $\mathbf{u}^{-b}$ on the crack surfaces S_c^+ and S_c^- as

$$\begin{aligned} u_p(\mathbf{x}) = & \int_{S_c} U_j^p(\boldsymbol{\xi}-\mathbf{x}) t_j^{b\Sigma}(\boldsymbol{\xi}) dS(\boldsymbol{\xi}) \\ & + \int_{S_c} G_{mj}^p(\boldsymbol{\xi}-\mathbf{x}) D_m u_j^{b\Delta}(\boldsymbol{\xi}) dS(\boldsymbol{\xi}) - \int_{S_c} H_{ij}^p(\boldsymbol{\xi}-\mathbf{x}) n_i(\boldsymbol{\xi}) u_j^{b\Delta}(\boldsymbol{\xi}) dS(\boldsymbol{\xi}) \end{aligned} \tag{4.1}$$

$$\begin{aligned} \sigma_{ij}(\mathbf{x}) = & \int_{S_c} \varepsilon_{irt} C_{lk,t}^{ij}(\boldsymbol{\xi}-\mathbf{x}) D_l u_k^{b\Delta}(\boldsymbol{\xi}) dS(\boldsymbol{\xi}) \\ & + \int_{S_c} \varepsilon_{irt} G_{tj,r}^p(\boldsymbol{\xi}-\mathbf{x}) t_p^{b\Sigma}(\boldsymbol{\xi}) dS(\boldsymbol{\xi}) - \int_{S_c} H_{ij}^p(\boldsymbol{\xi}-\mathbf{x}) t_p^{b\Sigma}(\boldsymbol{\xi}) dS(\boldsymbol{\xi}) \end{aligned} \tag{4.2}$$

where $D_t(\cdot) = \varepsilon_{tmj} n_m \partial(\cdot)/\partial \xi_j$ is a surface differential operator, $t_j^{b\Sigma} = t_j^{+b} + t_j^{-b}$, $u_j^{b\Delta} = u_j^{+b} - u_j^{-b}$, ε_{irt} is the standard alternating symbol, the kernels $\{U_j^p, G_{mj}^p, C_{mj}^{tk}, H_{ij}^p\}$ for isotropic elastic materials are given explicitly by

$$U_j^p(\boldsymbol{\xi}-\mathbf{x}) = \frac{1}{16\pi(1-\nu)\mu r}\left[(3-4\nu)\delta_{pj} + \frac{(\xi_p - x_p)(\xi_j - x_j)}{r^2}\right] \tag{4.3}$$

$$G_{mj}^p(\boldsymbol{\xi}-\mathbf{x}) = \frac{1}{8\pi(1-\nu)r}\left[(1-2\nu)\varepsilon_{mpj} + \frac{(\xi_p - x_p)(\xi_a - x_a)}{r^2}\varepsilon_{ajm}\right] \tag{4.4}$$

$$C_{mj}^{tk}(\boldsymbol{\xi}-\mathbf{x}) = \frac{\mu}{4\pi(1-\nu)r}\left[(1-\nu)\delta_{tk}\delta_{mj} + 2\nu\delta_{km}\delta_{tj} - \delta_{kj}\delta_{tm} - \frac{(\xi_k - x_k)(\xi_j - x_j)}{r^2}\delta_{tm}\right] \tag{4.5}$$

$$H_{ij}^p(\boldsymbol{\xi}-\mathbf{x}) = -\frac{(\xi_i - x_i)\delta_{jp}}{4\pi r^3} \tag{4.6}$$

with $r = \|\boldsymbol{\xi} - \mathbf{x}\|$, and ν, μ are Poisson's ratio and the shear modulus respectively. The boundary integral relations (3.1) and (3.2) allow the displacement and stress at any interior point to be determined once the data $\mathbf{t}^{+b}$, $\mathbf{t}^{-b}$, $\mathbf{u}^{+b}$ and $\mathbf{u}^{-b}$ are known. To establish the boundary integral equations governing the unknown data $\mathbf{t}^{+b}$, $\mathbf{t}^{-b}$, $\mathbf{u}^{+b}$ and $\mathbf{u}^{-b}$, the integral relations (4.1) and (4.2) are utilized along with the limiting process to any point on the crack surface and the standard integration by parts procedure using Stokes' theorem to obtain the weak-form equations. The final weak-form, boundary integral equations are given by (see details of the development in Rungamornrat and Mear (2008a) and Rungamornrat and Senjuntichai (2009))

$$\begin{aligned}
\frac{1}{2}\int_{S_c} \tilde{t}_p^{\Sigma}(\mathbf{y}) u_p^{b\Sigma}(\boldsymbol{\xi}(\mathbf{y}))\, dS(\mathbf{y}) = & \int_{S_c} \tilde{t}_p^{\Sigma}(\mathbf{y}) \int_{S_c} U_j^p(\boldsymbol{\xi} - \boldsymbol{\eta}) t_j^{b\Sigma}(\boldsymbol{\eta})\, dS(\boldsymbol{\eta})\, dS(\boldsymbol{\xi}) \\
& + \int_{S_c} \tilde{t}_p^{\Sigma}(\mathbf{y}) \int_{S_c} G_{mj}^p(\boldsymbol{\xi} - \boldsymbol{\eta}) D_m u_j^{b\Delta}(\boldsymbol{\eta})\, dS(\boldsymbol{\eta})\, dS(\boldsymbol{\xi}) \\
& - \int_{S_c} \tilde{t}_p^{\Sigma}(\mathbf{y}) \int_{S_c} H_{ij}^p(\boldsymbol{\xi} - \mathbf{y}) n_i(\boldsymbol{\eta}) u_j^{b\Delta}(\boldsymbol{\eta})\, dS(\boldsymbol{\eta})\, dS(\boldsymbol{\xi})
\end{aligned} \tag{4.7}$$

$$\begin{aligned}
-\frac{1}{2}\int_{S_c} \tilde{u}_k^{\Delta}(\mathbf{y}) t_k^{b\Delta}(\boldsymbol{\xi}(\mathbf{y}))\, dS(\mathbf{y}) = & \int_{S_c} D_t \tilde{u}_k^{\Delta}(\boldsymbol{\xi}(\mathbf{y})) \int_{S_c} C_{mj}^{tk}(\boldsymbol{\xi} - \boldsymbol{\eta}) D_m u_j^{b\Delta}(\boldsymbol{\eta})\, dS(\boldsymbol{\eta})\, dS(\boldsymbol{\xi}) \\
& + \int_{S_c} D_t \tilde{u}_k^{\Delta}(\mathbf{y}) \int_{S_c} G_{tk}^j(\boldsymbol{\xi} - \boldsymbol{\eta}) t_j^{b\Sigma}(\boldsymbol{\eta})\, dS(\boldsymbol{\eta})\, dS(\boldsymbol{\xi}) \\
& + \int_{S_c} \tilde{u}_k^{\Delta}(\mathbf{y}) \int_{S_c} H_{lk}^j(\boldsymbol{\eta} - \mathbf{y}) n_l(\boldsymbol{\xi}) t_j^{b\Sigma}(\boldsymbol{\eta})\, dS(\boldsymbol{\eta})\, dS(\boldsymbol{\xi})
\end{aligned} \tag{4.8}$$

where $u_j^{b\Sigma} = u_j^{+b} + u_j^{-b}$, $t_j^{b\Delta} = t_j^{+b} - t_j^{-b}$, and $\{\tilde{t}_p^{\Sigma},\ \tilde{u}_k^{\Delta}\}$ are sufficiently smooth test functions. The pair of equations (4.7) and (4.8) has been well recognized as the weak-form boundary integral equations for the sum of the displacement $u_j^{b\Sigma}$ and the jump of the traction $t_j^{b\Delta}$ across the crack surface respectively. It is worth noting that both integral equations contain only weakly singular kernels $\{U_j^p, G_{mj}^p, C_{mj}^{tk}, H_{ij}^p n_j\}$ of $\mathcal{O}(1/r)$. This positive feature renders all involved double surface integrals to exist in an ordinary sense, and their validity requires only C^0- boundary data.

4.1.3 Governing equations of two layers

The two layers S_c^+ and S_c^- shown in Figures 4.2(b) and 4.2(c) are considered as infinitesimally thin membranes adhered perfectly to the bulk material. The behavior of these two layers is modeled by the full version of Gurtin-Murdoch surface elasticity theory. The equilibrium equations, the surface constitutive relations and the strain-displacement relationship of the layers S_c^+ and S_c^- are therefore given by (Gurtin and Murdoch, 1975; Gurtin and Murdoch, 1978; Gurtin *et al.*, 1998)

$$\sigma_{i\beta,\beta}^s + t_i^s + t_i^o = 0 \tag{4.9}$$

$$\sigma_{\alpha\beta}^s = \tau^s \delta_{\alpha\beta} + \left(\lambda^s + \tau^s\right)\varepsilon_{\gamma\gamma}^s \delta_{\alpha\beta} + 2\left(\mu^s - \tau^s\right)\varepsilon_{\alpha\beta}^s + \tau^s u_{\alpha,\beta}^s \quad , \quad \sigma_{3\beta}^s = \tau^s u_{3,\beta}^s \tag{4.10}$$

$$\varepsilon_{\alpha\beta}^s = \tfrac{1}{2}\left(u_{\alpha,\beta}^s + u_{\beta,\alpha}^s\right) \tag{4.11}$$

where $\sigma_{i\beta}^{s}$, $\varepsilon_{\alpha\beta}^{s}$, u_i^s represent stress, strain and displacement components within the layer. It is important to remark that, in this case, the full version of Gurtin-Murdoch surface elasticity theory including both the surface Lamé constants (or in-plane elastic constants), and the residual surface tension is considered. This model should suit the treatment of general loading conditions when both the normal and tangential traction can be applied simultaneously on the crack surfaces.

To construct the weak-form equation, the equilibrium equation (4.9) is multiplied by a sufficiently smooth test function $\tilde{u}_i^s$ and the result is integrated over the entire crack surface to obtain

$$\int_{S_c} \tilde{u}_\alpha^s \sigma_{\alpha\beta,\beta}^s dS + \int_{S_c} \tilde{u}_3^s \sigma_{3\beta,\beta}^s dS + \int_{S_c} \tilde{u}_i^s t_i^s dS + \int_{S_c} \tilde{u}_i^s t_i^0 dS = 0 \tag{4.12}$$

By performing the integration by parts of the first term using the Gauss-divergence theorem, it leads to

$$\int_{S_c} \tilde{u}_{\alpha,\beta}^s \sigma_{\alpha\beta}^s dS + \int_{S_c} \tilde{u}_{3,\beta}^s \sigma_{3\beta}^s dS - \int_{S_c} \tilde{u}_i^s t_i^s dS = \int_{\partial S_c} \tilde{u}_\alpha^s \sigma_{\alpha\beta}^s n_\beta dS + \int_{\partial S_c} \tilde{u}_3^s \sigma_{3\beta}^s n_\beta dS + \int_{S_c} \tilde{u}_i^s t_i^0 dS \tag{4.13}$$

Substituting (4.10) into (4.13) finally yields

$$\begin{aligned} &\lambda^s \int_{S_c} \tilde{u}_{\alpha,\alpha}^s u_{\gamma,\gamma}^s dS + \frac{\mu^s}{2} \int_{S_c} \left(\tilde{u}_{\alpha,\beta}^s + \tilde{u}_{\beta,\alpha}^s\right)\left(u_{\alpha,\beta}^s + u_{\beta,\alpha}^s\right) dS + \tau^s \int_{S_c} \tilde{u}_{3,\beta}^s u_{3,\beta}^s dS - \int_{S_c} \tilde{u}_i^s t_i^s dS = \\ &\lambda^s \int_{\partial S_c} \tilde{u}_\alpha^s n_\alpha u_{\gamma,\gamma}^s d\Gamma + \frac{\mu^s}{2} \int_{\partial S_c} \left(\tilde{u}_\alpha^s n_\beta + \tilde{u}_\beta^s n_\alpha\right)\left(u_{\alpha,\beta}^s + u_{\beta,\alpha}^s\right) d\Gamma + \tau^s \int_{\partial S_c} \tilde{u}_3^s u_{3,\beta}^s n_\beta d\Gamma + \int_{S_c} \tilde{u}_i^s t_i^0 dS \end{aligned} \tag{4.14}$$

Note that the weak-form equation (4.14) applies to both crack surfaces. In particular, the weak-form equations for the surface S_c^+ and surface S_c^- can be obtained explicitly by

$$\begin{aligned} &\lambda^s \int_{S_c} \tilde{u}_{\alpha,\alpha}^{s+} u_{\gamma,\gamma}^{s+} dS + \frac{\mu^s}{2} \int_{S_c} \left(\tilde{u}_{\alpha,\beta}^{s+} + \tilde{u}_{\beta,\alpha}^{s+}\right)\left(u_{\alpha,\beta}^{s+} + u_{\beta,\alpha}^{s+}\right) dS + \tau^s \int_{S_c} \tilde{u}_{3,\beta}^{s+} u_{3,\beta}^{s+} dS - \int_{S_c} \tilde{u}_i^{s+} t_i^{s+} dS = \\ &\lambda^s \int_{\partial S_c} \tilde{u}_\alpha^{s+} n_\alpha u_{\gamma,\gamma}^{s+} d\Gamma + \frac{\mu^s}{2} \int_{\partial S_c} \left(\tilde{u}_\alpha^{s+} n_\beta + \tilde{u}_\beta^{s+} n_\alpha\right)\left(u_{\alpha,\beta}^{s+} + u_{\beta,\alpha}^{s+}\right) d\Gamma + \tau^s \int_{\partial S_c} \tilde{u}_3^{s+} u_{3,\beta}^{s+} n_\beta d\Gamma + \int_{S_c} \tilde{u}_i^{s+} t_i^{0+} dS \end{aligned} \tag{4.15}$$

$$\begin{aligned} &\lambda^s \int_{S_c} \tilde{u}_{\alpha,\alpha}^{s-} u_{\gamma,\gamma}^{s-} dS + \frac{\mu^s}{2} \int_{S_c} \left(\tilde{u}_{\alpha,\beta}^{s-} + \tilde{u}_{\beta,\alpha}^{s-}\right)\left(u_{\alpha,\beta}^{s-} + u_{\beta,\alpha}^{s-}\right) dS + \tau^s \int_{S_c} \tilde{u}_{3,\beta}^{s-} u_{3,\beta}^{s-} dS - \int_{S_c} \tilde{u}_i^{s-} t_i^{s-} dS = \\ &\lambda^s \int_{\partial S_c} \tilde{u}_\alpha^{s-} n_\alpha u_{\gamma,\gamma}^{s-} d\Gamma + \frac{\mu^s}{2} \int_{\partial S_c} \left(\tilde{u}_\alpha^{s-} n_\beta + \tilde{u}_\beta^{s-} n_\alpha\right)\left(u_{\alpha,\beta}^{s-} + u_{\beta,\alpha}^{s-}\right) d\Gamma + \tau^s \int_{\partial S_c} \tilde{u}_3^{s-} u_{3,\beta}^{s-} n_\beta d\Gamma + \int_{S_c} \tilde{u}_i^{s-} t_i^{0-} dS \end{aligned} \tag{4.16}$$

where the superscripts "+" and "–" are added to differentiate quantities defined on each crack surface. Since the boundary integral equations governing the bulk material are derived in terms of the unknown sum and jump of quantities across the crack surface, it is natural to establish the

weak-form equations governing the surface in terms of the same type of unknowns. This can be readily accomplished by forming two linear combinations of (4.15) and (4.16) as follows: (i) choosing $\tilde{u}_i^{s+} = \tilde{u}_i^{s-} \equiv \tilde{u}_i^{s\Sigma}$ and then adding (4.15) to (4.16) and (ii) choosing $\tilde{u}_i^{s+} = \tilde{u}_i^{s-} \equiv \tilde{u}_i^{s\Delta}$ and then subtracting (4.15) from (4.16). Such pair of equivalent weak-form equations is given by

$$\begin{aligned}
&\lambda^s \int_{S_c} \tilde{u}_{\alpha,\alpha}^{s\Sigma} u_{\gamma,\gamma}^{s\Sigma} dS + \frac{\mu^s}{2} \int_{S_c} \left(\tilde{u}_{\alpha,\beta}^{s\Sigma} + \tilde{u}_{\beta,\alpha}^{s\Sigma}\right)\left(u_{\alpha,\beta}^{s\Sigma} + u_{\beta,\alpha}^{s\Sigma}\right) dS + \tau^s \int_{S_c} \tilde{u}_{3,\beta}^{s\Sigma} u_{3,\beta}^{s\Sigma} dS - \int_{S_c} \tilde{u}_i^{s\Sigma} t_i^{s\Sigma} dS = \\
&\lambda^s \int_{\partial S_c} \tilde{u}_\alpha^{s\Sigma} n_\alpha u_{\gamma,\gamma}^{s\Sigma} d\Gamma + \frac{\mu^s}{2} \int_{\partial S_c} \left(\tilde{u}_\alpha^{s\Sigma} n_\beta + \tilde{u}_\beta^{s\Sigma} n_\alpha\right)\left(u_{\alpha,\beta}^{s\Sigma} + u_{\beta,\alpha}^{s\Sigma}\right) d\Gamma + \tau^s \int_{\partial S_c} \tilde{u}_3^{s\Sigma} u_{3,\beta}^{s\Sigma} n_\beta d\Gamma + \int_{S_c} \tilde{u}_i^{s\Sigma} t_i^{0\Sigma} dS
\end{aligned} \tag{4.17}$$

$$\begin{aligned}
&\lambda^s \int_{S_c} \tilde{u}_{\alpha,\alpha}^{s\Delta} u_{\gamma,\gamma}^{s\Delta} dS + \frac{\mu^s}{2} \int_{S_c} \left(\tilde{u}_{\alpha,\beta}^{s\Delta} + \tilde{u}_{\beta,\alpha}^{s\Delta}\right)\left(u_{\alpha,\beta}^{s\Delta} + u_{\beta,\alpha}^{s\Delta}\right) dS + \tau^s \int_{S_c} \tilde{u}_{3,\beta}^{s\Delta} u_{3,\beta}^{s\Delta} dS - \int_{S_c} \tilde{u}_i^{s\Delta} t_i^{s\Delta} dS = \\
&\lambda^s \int_{\partial S_c} \tilde{u}_\alpha^{s\Delta} n_\alpha u_{\gamma,\gamma}^{s\Delta} d\Gamma + \frac{\mu^s}{2} \int_{\partial S_c} \left(\tilde{u}_\alpha^{s\Delta} n_\beta + \tilde{u}_\beta^{s\Delta} n_\alpha\right)\left(u_{\alpha,\beta}^{s\Delta} + u_{\beta,\alpha}^{s\Delta}\right) d\Gamma + \tau^s \int_{\partial S_c} \tilde{u}_3^{s\Delta} u_{3,\beta}^{s\Delta} n_\beta d\Gamma + \int_{S_c} \tilde{u}_i^{s\Delta} t_i^{0\Delta} dS
\end{aligned} \tag{4.18}$$

where superscripts "Σ" and "Δ" indicate the sum and jump of quantities across the crack surface. It should be remarked further that since the jump of the displacement along the crack-front vanishes identically, the test function $\tilde{u}_i^{s\Delta}$ is chosen to satisfy the homogeneous condition $\tilde{u}_i^{s\Delta} = 0$ on ∂S_c. The weak-form equations (4.17) and (4.18) now take the form

$$\begin{aligned}
&\lambda^s \int_{S_c} \tilde{u}_{\alpha,\alpha}^{s\Sigma} u_{\gamma,\gamma}^{s\Sigma} dS + \frac{\mu^s}{2} \int_{S_c} \left(\tilde{u}_{\alpha,\beta}^{s\Sigma} + \tilde{u}_{\beta,\alpha}^{s\Sigma}\right)\left(u_{\alpha,\beta}^{s\Sigma} + u_{\beta,\alpha}^{s\Sigma}\right) dS + \tau^s \int_{S_c} \tilde{u}_{3,\beta}^{s\Sigma} u_{3,\beta}^{s\Sigma} dS - \int_{S_c} \tilde{u}_i^{s\Sigma} t_i^{s\Sigma} dS = \\
&\lambda^s \int_{\partial S_c} \tilde{u}_\alpha^{s\Sigma} n_\alpha u_{\gamma,\gamma}^{s\Sigma} d\Gamma + \frac{\mu^s}{2} \int_{\partial S_c} \left(\tilde{u}_\alpha^{s\Sigma} n_\beta + \tilde{u}_\beta^{s\Sigma} n_\alpha\right)\left(u_{\alpha,\beta}^{s\Sigma} + u_{\beta,\alpha}^{s\Sigma}\right) d\Gamma + \tau^s \int_{\partial S_c} \tilde{u}_3^{s\Sigma} u_{3,\beta}^{s\Sigma} n_\beta d\Gamma + \int_{S_c} \tilde{u}_i^{s\Sigma} t_i^{0\Sigma} dS
\end{aligned} \tag{4.19}$$

$$\begin{aligned}
&\lambda^s \int_{S_c} \tilde{u}_{\alpha,\alpha}^{s\Delta} u_{\gamma,\gamma}^{s\Delta} dS + \frac{\mu^s}{2} \int_{S_c} \left(\tilde{u}_{\alpha,\beta}^{s\Delta} + \tilde{u}_{\beta,\alpha}^{s\Delta}\right)\left(u_{\alpha,\beta}^{s\Delta} + u_{\beta,\alpha}^{s\Delta}\right) dS + \tau^s \int_{S_c} \tilde{u}_{3,\beta}^{s\Delta} u_{3,\beta}^{s\Delta} dS - \int_{S_c} \tilde{u}_i^{s\Delta} t_i^{s\Delta} dS = \\
&\qquad \int_{S_c} \tilde{u}_i^{s\Delta} t_i^{0\Delta} dS
\end{aligned} \tag{4.20}$$

Equations (4.19) and (4.20) constitute a set of weak-form equations governing the unknown quantities $\{ u_i^{s\Sigma}, t_i^{s\Sigma}, u_i^{s\Delta}, t_i^{s\Delta} \}$.

4.1.3.1 Special case with only residual surface tension

It has been pointed out by various investigators that the influence of the surface Lamé constants on the out-of-plane responses in the local region very near the surface is negligibly weak (Intarit *et al.* 2012, Nan and Wang 2012, Intarit 2013, Pinyochotiwong *et al.* 2013). The simplified version of the Gurtin-Murdoch model without the in-plane surface elasticity is therefore considered suitable for modeling planar cracks subjected to pure mode-I loading conditions. By

simply setting the surface Lamé constants λ^s and μ^s to zero in the constitutive relation for the surface (4.10), it leads to

$$\sigma^s_{\alpha\beta} = \tau^s\delta_{\alpha\beta} + \tau^s\varepsilon^s_{\gamma\gamma}\delta_{\alpha\beta} - 2\,\tau^s\varepsilon^s_{\alpha\beta} + \tau^s u^s_{\alpha,\beta} \quad , \quad \sigma^s_{3\beta} = \tau^s u^s_{3,\beta} \tag{4.21}$$

Since the same equilibrium equation and strain-displacement relation as those employed in the general case (i.e. equations (4.9) and (4.11)) are also considered, the model is not restricted mathematically to applied traction normal to the crack surface although it is physically suitable for treating pure mode-I loading conditions. Due to the vanishing of the term $\sigma^s_{\alpha\beta,\beta}$, which can readily be verified by the relation (4.21), the equilibrium equation (4.9) then implies that the applied shear traction is transmitted directly to the crack surface of the bulk medium. To construct the weak-form statement for this particular case, the procedure similar to that employed in the previous section is adopted. The final weak-form equations of the two layers take the following form:

$$\tau^s\int_{S_c}\tilde{u}^{s\Sigma}_{3,\beta}u^{s\Sigma}_{3,\beta}dS - \int_{S_c}\tilde{u}^{s\Sigma}_i t^{s\Sigma}_i dS = \int_{\partial S_c}\tilde{u}^{s\Sigma}_3\sigma^{s\Sigma}_{3\beta}n_\beta dS + \int_{S_c}\tilde{u}^{s\Sigma}_i t^{0\Sigma}_i dS \tag{4.22}$$

$$\tau^s\int_{S_c}\tilde{u}^{s\Delta}_{3,\beta}u^{s\Delta}_{3,\beta}dS - \int_{S_c}\tilde{u}^{s\Delta}_i t^{s\Delta}_i dS = \int_{S_c}\tilde{u}^{s\Delta}_i t^{0\Delta}_i dS \tag{4.23}$$

4.1.3.2 Special case with only in-plane surface elasticity

Another simplified version of the Gurtin-Murdoch model considered in the present study is the one with only the effect of the in-plane surface elasticity being treated. The simplified constitutive relation of the layers S_c^+ and S_c^- is obtained by substituting the residual surface tension τ^s to zero in (4.10), and this results in

$$\sigma^s_{\alpha\beta} = \lambda^s\varepsilon^s_{\gamma\gamma}\delta_{\alpha\beta} + 2\,\mu^s\varepsilon^s_{\alpha\beta} \quad , \quad \sigma^s_{3\beta} = 0 \tag{4.24}$$

It is evident from (4.24) that this simplified model always predicts zero out-of-plane shear stresses and this result, when combined with the equilibrium equation (4.9), dictates that the applied normal traction is transmitted directly to the crack surface of the bulk material. Similar to the previous special case, this simplified model is still applicable to general loading conditions on the crack surface. To obtain the weak-form statement for this particular case, the procedure similar to that employed in the general case is utilized and the resulting weak-form equations are given by

$$\begin{aligned}&\lambda^s\int_{S_c}\tilde{u}^{s\Sigma}_{\alpha,\alpha}u^{s\Sigma}_{\gamma,\gamma}dS + \frac{\mu^s}{2}\int_{S_c}\left(\tilde{u}^{s\Sigma}_{\alpha,\beta} + \tilde{u}^{s\Sigma}_{\beta,\alpha}\right)\left(u^{s\Sigma}_{\alpha,\beta} + u^{s\Sigma}_{\beta,\alpha}\right)dS - \int_{S_c}\tilde{u}^{s\Sigma}_i t^{s\Sigma}_i dS = \\ &\lambda^s\int_{\partial S_c}\tilde{u}^{s\Sigma}_\alpha n_\alpha u^{s\Sigma}_{\gamma,\gamma}d\Gamma + \frac{\mu^s}{2}\int_{\partial S_c}\left(\tilde{u}^{s\Sigma}_\alpha n_\beta + \tilde{u}^{s\Sigma}_\beta n_\alpha\right)\left(u^{s\Sigma}_{\alpha,\beta} + u^{s\Sigma}_{\beta,\alpha}\right)d\Gamma + \int_{S_c}\tilde{u}^{s\Sigma}_i t^{0\Sigma}_i dS\end{aligned} \tag{4.25}$$

$$\lambda^s \int_{S_c} \tilde{u}^{s\Delta}_{\alpha,\alpha} u^{s\Delta}_{\gamma,\gamma} dS + \frac{\mu^s}{2} \int_{S_c} \left(\tilde{u}^{s\Delta}_{\alpha,\beta} + \tilde{u}^{s\Delta}_{\beta,\alpha} \right) \left(u^{s\Delta}_{\alpha,\beta} + u^{s\Delta}_{\beta,\alpha} \right) dS - \int_{S_c} \tilde{u}^{s\Delta}_i t^{s\Delta}_i dS = \int_{S_c} \tilde{u}^{s\Delta}_i t^{0\Delta}_i dS \tag{4.26}$$

4.1.4 Governing equations of whole medium

Since the two layers S_c^+ and S_c^- are adhered perfectly to the bulk material, the displacements and traction along the interface of the two layers and the bulk material must be continuous. This yields the following continuity conditions:

$$u^{s\Delta}_i = u^{b\Delta}_i \equiv u^{\Delta}_i \tag{4.27}$$

$$u^{s\Sigma}_i = u^{b\Sigma}_i \equiv u^{\Sigma}_i \tag{4.28}$$

$$t^{s\Delta}_i = -t^{b\Delta}_i \equiv -t^{\Delta}_i \tag{4.29}$$

$$t^{s\Sigma}_i = -t^{b\Sigma}_i \equiv -t^{\Sigma}_i \tag{4.30}$$

Substituting (4.27) - (4.30) into (4.7), (4.8), (4.19) and (4.20), leads to a system of four equations involving four unknown functions $\{u_i^{\Sigma}, t_i^{\Sigma}, u_i^{\Delta}, t_i^{\Delta}\}$ as follows:

$$\begin{aligned}
\frac{1}{2}\int_{S_c} \tilde{t}^{\Sigma}_p(\mathbf{y}) u^{\Sigma}_p(\boldsymbol{\xi}) d\mathbf{y} dS(\mathbf{y}) \boldsymbol{\xi} = & \int_{S_c} \tilde{t}^{\Sigma}_p(\mathbf{y}) \int_{S_c} U^p_j(\quad - \quad) t^{\Sigma}_j(\quad) dS(\quad) dS(\quad) \\
& + \int_{S_c} \tilde{t}^{\Sigma}_p(\mathbf{y}) \boldsymbol{\xi} \int_{S_c} G^p_{mj}(\quad - \boldsymbol{\xi}) D_m u^{\Delta}_j(\quad) d\mathbf{y} dS(\quad) dS(\quad) \\
& - \int_{S_c} \tilde{t}^{\Sigma}_p(\mathbf{y}) \boldsymbol{\xi} \int_{S_c} H^p_{ij}(\boldsymbol{\xi} - \mathbf{y}) \boldsymbol{\xi} n_i(\quad) \mathbf{y} u^{\Delta}_j(\quad) dS(\quad) dS(\quad)
\end{aligned} \tag{4.31}$$

$$\begin{aligned}
-\frac{1}{2}\int_{S_c} \tilde{u}^{\Delta}_k(\mathbf{y}) t^{\Delta}_k(\boldsymbol{\xi}) d\mathbf{y} dS(\mathbf{y}) = & \int_{S_c} \boldsymbol{\xi} D_t \tilde{u}^{\Delta}_k(\boldsymbol{\xi}) \int_{S_c} \mathbf{y} C^{tk}_{mj}(\quad - \quad) D_m u^{\Delta}_j(\quad) dS(\quad) dS(\quad) \\
& + \int_{S_c} D_t \tilde{u}^{\Delta}_k(\mathbf{y}) \boldsymbol{\xi} \int_{S_c} \mathbf{y} G^j_{tk}(\boldsymbol{\xi} - \quad) t^{\Sigma}_j(\quad) d\mathbf{y} dS(\quad) dS(\quad) \\
& + \int_{S_c} \tilde{u}^{\Delta}_k(\mathbf{y}) \boldsymbol{\xi} \int_{S_c} \mathbf{y} H^j_{lk}(\mathbf{y} - \quad) \boldsymbol{\xi}_l(\quad) t^{\Sigma}_j(\quad) d\mathbf{y} dS(\quad) dS(\quad)
\end{aligned} \tag{4.32}$$

$$\begin{aligned}
& \lambda^s \int_{S_c} \tilde{u}^{s\Sigma}_{\alpha,\alpha} u^{\Sigma}_{\gamma,\gamma} dS + \frac{\mu^s}{2} \int_{S_c} \left(\tilde{u}^{s\Sigma}_{\alpha,\beta} + \tilde{u}^{s\Sigma}_{\beta,\alpha} \right) \left(u^{\Sigma}_{\alpha,\beta} + u^{\Sigma}_{\beta,\alpha} \right) dS + \tau^s \int_{S_c} \tilde{u}^{s\Sigma}_{3,\beta} u^{\Sigma}_{3,\beta} dS + \int_{S_c} \tilde{u}^{s\Sigma}_i t^{\Sigma}_i dS = \\
& \lambda^s \int_{\partial S_c} \tilde{u}^{s\Sigma}_{\alpha} n_{\alpha} u^{\Sigma}_{\gamma,\gamma} d\Gamma + \frac{\mu^s}{2} \int_{\partial S_c} \left(\tilde{u}^{s\Sigma}_{\alpha} n_{\beta} + \tilde{u}^{s\Sigma}_{\beta} n_{\alpha} \right) \left(u^{\Sigma}_{\alpha,\beta} + u^{\Sigma}_{\beta,\alpha} \right) d\Gamma + \tau^s \int_{\partial S_c} \tilde{u}^{s\Sigma}_3 u^{\Sigma}_{3,\beta} n_{\beta} d\Gamma + \int_{S_c} \tilde{u}^{s\Sigma}_i t^{0\Sigma}_i dS
\end{aligned} \tag{4.33}$$

$$\lambda^s \int_{S_c} \tilde{u}^{s\Delta}_{\alpha,\alpha} u^{\Delta}_{\gamma,\gamma} dS + \frac{\mu^s}{2} \int_{S_c} \left(\tilde{u}^{s\Delta}_{\alpha,\beta} + \tilde{u}^{s\Delta}_{\beta,\alpha} \right) \left(u^{\Delta}_{\alpha,\beta} + u^{\Delta}_{\beta,\alpha} \right) dS + \tau^s \int_{S_c} \tilde{u}^{s\Delta}_{3,\beta} u^{\Delta}_{3,\beta} dS + \int_{S_c} \tilde{u}^{s\Delta}_i t^{\Delta}_i dS = \int_{S_c} \tilde{u}^{s\Delta}_i t^{0\Delta}_i dS \tag{4.34}$$

It is obvious from (4.32) and (4.34) that terms involving the unknown jump of the traction t_i^{Δ} are similar and, by choosing $\tilde{u}^{s\Delta}_i = \tilde{u}^{\Delta}_i$, the two equations can be combined and those terms containing t_i^{Δ} can be eliminated. The above system (4.31)-(4.34) now becomes a system of three equations involving three unknown functions $\{u_i^{\Sigma}, t_i^{\Sigma}, u_i^{\Delta}\}$ given by

$$
\begin{aligned}
\mathcal{A}(\tilde{\mathbf{u}}^{s\Sigma},\mathbf{u}^{\Sigma}) &+ \mathcal{B}(\tilde{\mathbf{u}}^{s\Sigma},\mathbf{t}^{\Sigma}) && = \mathcal{R}_1(\tilde{\mathbf{u}}^{s\Sigma}) \\
\mathcal{B}(\tilde{\mathbf{t}}^{\Sigma},\mathbf{u}^{\Sigma}) &+ \mathcal{C}(\tilde{\mathbf{t}}^{\Sigma},\mathbf{t}^{\Sigma}) + \mathcal{D}(\tilde{\mathbf{t}}^{\Sigma},\mathbf{u}^{\Delta}) && = 0 \\
\mathcal{D}(\mathbf{t}^{\Sigma},\tilde{\mathbf{u}}^{\Delta}) &+ \mathcal{E}(\tilde{\mathbf{u}}^{\Delta},\mathbf{u}^{\Delta}) && = \mathcal{R}_2(\tilde{\mathbf{u}}^{\Delta})
\end{aligned}
\tag{4.35}
$$

where the bilinear integral operators $\mathcal{A}$, $\mathcal{B}$, $\mathcal{C}$, $\mathcal{D}$, $\mathcal{E}$ are defined by

$$
\begin{aligned}
\mathcal{A}(\mathbf{X},\mathbf{Y}) &= \frac{\lambda^s}{2}\int_{S_c} X_{\alpha,\alpha}Y_{\gamma,\gamma}dS + \frac{\mu^s}{4}\int_{S_c}\left(X_{\alpha,\beta}+X_{\beta,\alpha}\right)\left(Y_{\alpha,\beta}+Y_{\beta,\alpha}\right)dS + \frac{\tau^s}{2}\int_{S_c} X_{3,\beta}Y_{3,\beta}dS \\
&-\left[\frac{\lambda^s}{2}\int_{\partial S_c} X_{\alpha}n_{\alpha}Y_{\gamma,\gamma}d\Gamma + \frac{\mu^s}{4}\int_{\partial S_c}\left(X_{\alpha}n_{\beta}+X_{\beta}n_{\alpha}\right)\left(Y_{\alpha,\beta}+Y_{\beta,\alpha}\right)d\Gamma + \frac{\tau^s}{2}\int_{\partial S_c} X_3 Y_{3,\beta}n_{\beta}d\Gamma\right]
\end{aligned}
\tag{4.36}
$$

$$
\mathcal{B}(\mathbf{X},\mathbf{Y}) = \frac{1}{2}\int_{S_c} X_p(\mathbf{y})Y_p(\mathbf{y})dS(\mathbf{y}) \tag{4.37}
$$

$$
\mathcal{C}(\mathbf{X},\mathbf{Y}) = -\int_{S_c} X_p(\mathbf{y})\int_{S_c} U_j^p(\boldsymbol{\xi}-\mathbf{y})Y_j(\boldsymbol{\xi})dS(\boldsymbol{\xi})dS(\mathbf{y}) \tag{4.38}
$$

$$
\begin{aligned}
\mathcal{D}(\mathbf{X},\mathbf{Y}) &= -\int_{S_c} X_p(\mathbf{y})\int_{S_c} G_{mj}^p(\boldsymbol{\xi}-\mathbf{y})D_m Y_j(\boldsymbol{\xi})dS(\boldsymbol{\xi})dS(\mathbf{y}) \\
&+\int_{S_c} X_p(\mathbf{y})\int_{S_c} H_{ij}^p(\boldsymbol{\xi}-\mathbf{y})n_i(\boldsymbol{\xi})Y_j(\boldsymbol{\xi})dS(\boldsymbol{\xi})dS(\mathbf{y})
\end{aligned}
\tag{4.39}
$$

$$
\mathcal{E}(\mathbf{X},\mathbf{Y}) = -\int_{S_c} D_t X_k(\mathbf{y})\int_{S_c} C_{mj}^{tk}(\boldsymbol{\xi}-\mathbf{y})D_m Y_j(\boldsymbol{\xi})dS(\boldsymbol{\xi})dS(\mathbf{y}) + \mathcal{F}(\mathbf{X},\mathbf{Y}) \tag{4.40}
$$

$$
\mathcal{F}(\mathbf{X},\mathbf{Y}) = \frac{\lambda^s}{2}\int_{S_c} X_{\alpha,\alpha}Y_{\beta,\beta}dS + \frac{\mu^s}{4}\int_{S_c}\left(X_{\alpha,\beta}+X_{\beta,\alpha}\right)\left(Y_{\alpha,\beta}+Y_{\beta,\alpha}\right)dS + \frac{\tau^s}{2}\int_{S_c} X_{3,\beta}Y_{3,\beta}dS \tag{4.41}
$$

and the linear integral operators $\{\mathcal{R}_1, \mathcal{R}_2\}$ are defined, in terms of prescribed data $\mathbf{t}^{0\Sigma}$ and $\mathbf{t}^{0\Delta}$, by

$$
\mathcal{R}_1(\mathbf{X}) = \frac{1}{2}\int_{S_c} X_l(\mathbf{y})t_l^{0\Sigma}(\mathbf{y})dS(\mathbf{y}) \tag{4.42}
$$

$$
\mathcal{R}_2(\mathbf{X}) = \frac{1}{2}\int_{S_c} X_l(\mathbf{y})t_l^{0\Delta}(\mathbf{y})dS(\mathbf{y}) \tag{4.43}
$$

4.1.4.1 Special case with only residual surface tension

For the special case when only the residual surface tension is considered, the fully coupled system of governing equations (4.35) can readily be simplified by ignoring the surface elastic constants, and they can be expressed as

$$
\begin{aligned}
\bar{\mathcal{A}}(\tilde{\mathbf{u}}^{s\Sigma},\mathbf{u}^{\Sigma}) &+ \mathcal{B}(\tilde{\mathbf{u}}^{s\Sigma},\mathbf{t}^{\Sigma}) && = \mathcal{R}_1(\tilde{\mathbf{u}}^{s\Sigma}) \\
\mathcal{B}(\tilde{\mathbf{t}}^{\Sigma},\mathbf{u}^{\Sigma}) &+ \mathcal{C}(\tilde{\mathbf{t}}^{\Sigma},\mathbf{t}^{\Sigma}) &+ \mathcal{D}(\tilde{\mathbf{t}}^{\Sigma},\mathbf{u}^{\Delta}) &= 0 \\
& \mathcal{D}(\mathbf{t}^{\Sigma},\tilde{\mathbf{u}}^{\Delta}) &+ \bar{\mathcal{E}}(\tilde{\mathbf{u}}^{\Delta},\mathbf{u}^{\Delta}) &= \mathcal{R}_2(\tilde{\mathbf{u}}^{\Delta})
\end{aligned}
\tag{4.44}
$$

where the additional bilinear integral operators $\bar{\mathcal{A}}$ and $\bar{\mathcal{E}}$ are defined by

$$
\bar{\mathcal{A}}(\mathbf{X},\mathbf{Y}) = \frac{\tau^s}{2}\int_{S_c} X_{3,\beta}Y_{3,\beta}dS - \frac{\tau^s}{2}\int_{\partial S_c} X_3 Y_{3,\beta}n_\beta d\Gamma \tag{4.45}
$$

$$
\bar{\mathcal{E}}(\mathbf{X},\mathbf{Y}) = -\int_{S_c} D_t X_k(\mathbf{y})\int_{S_c} C_{mj}^{tk}(\boldsymbol{\xi}-\mathbf{y})D_m Y_j(\boldsymbol{\xi})dS(\boldsymbol{\xi})dS(\mathbf{y}) + \bar{\mathcal{F}}(\mathbf{X},\mathbf{Y}) \tag{4.46}
$$

$$
\bar{\mathcal{F}}(\mathbf{X},\mathbf{Y}) = \frac{\tau^s}{2}\int_{S_c} X_{3,\beta}Y_{3,\beta}dS \tag{4.47}
$$

It is remarked that the system (4.44) still contains three equations and involves three unknown functions $\{u_i^{\Sigma}, t_i^{\Sigma}, u_i^{\Delta}\}$.

4.1.4.2 Special case with only in-plane surface elasticity

For the special case when only the in-plane surface elasticity is considered, the fully coupled system of governing equations can readily be obtained by setting the residual surface tension to zero in (4.35), and the final result is given by

$$
\begin{aligned}
\hat{\mathcal{A}}(\tilde{\mathbf{u}}^{s\Sigma},\mathbf{u}^{\Sigma}) &+ \mathcal{B}(\tilde{\mathbf{u}}^{s\Sigma},\mathbf{t}^{\Sigma}) && = \mathcal{R}_1(\tilde{\mathbf{u}}^{s\Sigma}) \\
\mathcal{B}(\tilde{\mathbf{t}}^{\Sigma},\mathbf{u}^{\Sigma}) &+ \mathcal{C}(\tilde{\mathbf{t}}^{\Sigma},\mathbf{t}^{\Sigma}) &+ \mathcal{D}(\tilde{\mathbf{t}}^{\Sigma},\mathbf{u}^{\Delta}) &= 0 \\
& \mathcal{D}(\mathbf{t}^{\Sigma},\tilde{\mathbf{u}}^{\Delta}) &+ \hat{\mathcal{E}}(\tilde{\mathbf{u}}^{\Delta},\mathbf{u}^{\Delta}) &= \mathcal{R}_2(\tilde{\mathbf{u}}^{\Delta})
\end{aligned}
\tag{4.48}
$$

where the additional bilinear integral operators $\hat{\mathcal{A}}$ and $\hat{\mathcal{E}}$ are defined by

$$
\begin{aligned}
\hat{\mathcal{A}}(\mathbf{X},\mathbf{Y}) = {} & \frac{\lambda^s}{2}\int_{S_c} X_{\alpha,\alpha}Y_{\gamma,\gamma}dS + \frac{\mu^s}{4}\int_{S_c}\left(X_{\alpha,\beta}+X_{\beta,\alpha}\right)\left(Y_{\alpha,\beta}+Y_{\beta,\alpha}\right)dS \\
& - \frac{\lambda^s}{2}\int_{\partial S_c} X_\alpha n_\alpha Y_{\gamma,\gamma}d\Gamma - \frac{\mu^s}{4}\int_{\partial S_c}\left(X_\alpha n_\beta + X_\beta n_\alpha\right)\left(Y_{\alpha,\beta}+Y_{\beta,\alpha}\right)d\Gamma
\end{aligned}
\tag{4.49}
$$

$$
\hat{\mathcal{E}}(\mathbf{X},\mathbf{Y}) = -\int_{S_c} D_t X_k(\mathbf{y})\int_{S_c} C_{mj}^{tk}(\boldsymbol{\xi}-\mathbf{y})D_m Y_j(\boldsymbol{\xi})dS(\boldsymbol{\xi})dS(\mathbf{y}) + \hat{\mathcal{F}}(\mathbf{X},\mathbf{Y}) \tag{4.50}
$$

$$
\hat{\mathcal{F}}(\mathbf{X},\mathbf{Y}) = \frac{\lambda^s}{2}\int_{S_c} X_{\alpha,\alpha}Y_{\beta,\beta}dS + \frac{\mu^s}{4}\int_{S_c}\left(X_{\alpha,\beta}+X_{\beta,\alpha}\right)\left(Y_{\alpha,\beta}+Y_{\beta,\alpha}\right)dS \tag{4.51}
$$

Again, the system (4.48) still contains three equations and involves the same three unknown functions $\{u_i^{\Sigma}, t_i^{\Sigma}, u_i^{\Delta}\}$.

4.2 Numerical Implementations

In this section, essential components required in the numerical implementation including the discretization and numerical integration are briefly discussed. In general, standard procedures for the weakly singular SGBEM (e.g., Li and Mear 1998, Li *et al.* 1998, Rungamornrat 2006, Rungamornrat and Mear 2008) and those for the standard finite element method (e.g., Bathe 1990, Hughes 2000, Zienkiewicz and Taylor 2000) are utilized to form the discretized system of linear algebraic equations.

4.2.1 Discretization

Standard Galerkin approximation is employed in the discretization of the system of governing equations (4.35), (4.44), and (4.48). Since all involved boundary integrals governing the bulk material contain only weakly singular kernels of $\mathcal{O}(1/r)$, continuous (C^0) interpolation functions are utilized everywhere in the approximation of both trial and test functions. In particular, the following approximation for the test functions and the trial functions is introduced:

$$\tilde{u}_i^{s\Sigma} = \sum_{p=1}^{N} \tilde{U}_{3(p-1)+i}^{s\Sigma} \Phi_p \; ; \qquad u_i^{\Sigma} = \sum_{q=1}^{N} U_{3(q-1)+i}^{\Sigma} \Phi_q \tag{4.52}$$

$$\tilde{u}_i^{\Delta} = \sum_{p=1}^{N} \tilde{U}_{3(p-1)+i} \Phi_p \; ; \qquad u_i^{\Delta} = \sum_{q=1}^{N} U_{3(q-1)+i}^{\Delta} \Phi_q \tag{4.53}$$

$$\tilde{t}_i^{\Sigma} = \sum_{p=1}^{N} \tilde{T}_{3(p-1)+i} \Phi_p \; ; \qquad t_i^{\Sigma} = \sum_{q=1}^{N} T_{3(q-1)+i}^{\Sigma} \Phi_q \tag{4.54}$$

where N is the number of nodal points; Φ_p is nodal basis functions at the node p; Φ_q is nodal basis functions at the node q; $U_{3(q-1)+i}^{\Sigma}$, $U_{3(q-1)+i}^{\Delta}$, and $T_{3(q-1)+i}^{\Sigma}$ are nodal degrees of freedom associated with the sum of the displacement, the jump of the displacement and the sum of the traction across the crack surfaces, respectively; and $\tilde{U}_{3(p-1)+i}^{s\Sigma}$, $\tilde{U}_{3(p-1)+i}$, and $\tilde{T}_{3(p-1)+i}$ are arbitrary nodal quantities.

4.2.1.1 General case

Substituting (4.52)-(4.54) into (4.35) along with using the arbitrariness of $\tilde{U}_{3(p-1)+i}^{s\Sigma}$, $\tilde{U}_{3(p-1)+i}$, and $\tilde{T}_{3(p-1)+i}$, leads to a system of linear algebraic equations as

$$\begin{bmatrix} \mathbf{A} & \mathbf{B} & \mathbf{0} \\ \mathbf{B}^T & \mathbf{C} & \mathbf{D} \\ \mathbf{0} & \mathbf{D}^T & \mathbf{E} \end{bmatrix} \begin{Bmatrix} \mathbf{U}^{\Sigma} \\ \mathbf{T}^{\Sigma} \\ \mathbf{U}^{\Delta} \end{Bmatrix} = \begin{Bmatrix} \mathbf{R}_1 \\ \mathbf{0} \\ \mathbf{R}_2 \end{Bmatrix} \tag{4.55}$$

where the sub-matrices $\mathbf{A}, \mathbf{B}, \mathbf{C}, \mathbf{D}, \mathbf{E}$ are associated with the bilinear operators $\mathcal{A}, \mathcal{B}, \mathcal{C}, \mathcal{D}, \mathcal{E}$; sub-vectors $\mathbf{R}_1, \mathbf{R}_2$ correspond to the linear operators $\mathcal{R}_1, \mathcal{R}_2$; $\mathbf{U}^{\Sigma}$ is a vector of nodal quantities of the sum of the displacement; $\mathbf{U}^{\Delta}$ is a vector of nodal quantities of the

jump of the displacement; and $\mathbf{T}^{\Sigma}$ is a vector of nodal quantities of the sum of the traction. The sub-matrices $\mathbf{A}$, $\mathbf{B}$, $\mathbf{C}$, $\mathbf{D}$, $\mathbf{E}$ and sub-vectors $\mathbf{R}_1$, $\mathbf{R}_2$ are given explicitly by

$$
\begin{aligned}
[\mathbf{A}]_{3(p-1)+\alpha,3(q-1)+\beta} = & \frac{\lambda^s}{2}\int_{S_c}\Phi_{p,\alpha}(\underset{\sim}{y})\Phi_{q,\beta}(\underset{\sim}{y})dS(\underset{\sim}{y}) - \frac{\lambda^s}{2}\int_{\partial S_c}\Phi_{p}(\underset{\sim}{y})\Phi_{q,\beta}(\underset{\sim}{y})n_\alpha d\Gamma(\underset{\sim}{y}) \\
& + \frac{\mu^s}{2}\left(\int_{S_c}\Phi_{p,\beta}(\underset{\sim}{y})\Phi_{q,\alpha}(\underset{\sim}{y})dS(\underset{\sim}{y}) + \delta_{\alpha\beta}\int_{S_c}\Phi_{p,\gamma}(\underset{\sim}{y})\Phi_{q,\gamma}(\underset{\sim}{y})dS(\underset{\sim}{y})\right) \\
& - \frac{\mu^s}{2}\left(\int_{\partial S_c}\Phi_{p}(\underset{\sim}{y})\Phi_{q,\alpha}(\underset{\sim}{y})n_\beta d\Gamma(\underset{\sim}{y}) + \delta_{\alpha\beta}\int_{\partial S_c}\Phi_{p}(\underset{\sim}{y})\Phi_{q,\gamma}(\underset{\sim}{y})n_\gamma d\Gamma(\underset{\sim}{y})\right)
\end{aligned}
\tag{4.56}
$$

$$
[\mathbf{A}]_{3(p-1)+3,3(q-1)+3} = \frac{\tau^s}{2}\int_{S_c}\Phi_{p,\gamma}(\underset{\sim}{y})\Phi_{q,\gamma}(\underset{\sim}{y})dS(\underset{\sim}{y}) - \frac{\tau^s}{2}\int_{\partial S_c}\Phi_{p}(\underset{\sim}{y})\Phi_{q,\gamma}(\underset{\sim}{y})n_\gamma d\Gamma(\underset{\sim}{y}) \tag{4.57}
$$

$$
[\mathbf{B}]_{3(p-1)+i,3(q-1)+j} = \frac{1}{2}\int_{S_c}\delta_{ij}\Phi_{p}(\underset{\sim}{y})\Phi_{q}(\underset{\sim}{y})dS(\underset{\sim}{y}) \tag{4.58}
$$

$$
[\mathbf{C}]_{3(p-1)+i,3(q-1)+j} = -\int_{S_c}\Phi_{p}(\underset{\sim}{y})\int_{S_c}U^i_j(\xi-\underset{\sim}{y})\Phi_{q}(\xi)dS(\xi)dS(\underset{\sim}{y}) \tag{4.59}
$$

$$
\begin{aligned}
[\mathbf{D}]_{3(p-1)+i,3(q-1)+j} = & -\int_{S_c}\Phi_{p}(\underset{\sim}{y})\int_{S_c}G^i_{mj}(\boldsymbol{\xi}-\underset{\sim}{y})D_m\Phi_{q}(\boldsymbol{\xi})dS(\boldsymbol{\xi})dS(\underset{\sim}{y}) \\
& + \int_{S_c}\Phi_{p}(\underset{\sim}{y})\int_{S_c}H^i_{mj}(\boldsymbol{\xi}-\underset{\sim}{y})n_m(\boldsymbol{\xi})\Phi_{q}(\boldsymbol{\xi})dS(\boldsymbol{\xi})dS(\underset{\sim}{y})
\end{aligned}
\tag{4.60}
$$

$$
[\mathbf{E}]_{3(p-1)+i,3(q-1)+j} = -\int_{S_c}D_t\Phi_{p}(\underset{\sim}{y})\int_{S_c}C^{ti}_{mj}(\boldsymbol{\xi}-\underset{\sim}{y})D_m\Phi_{q}(\boldsymbol{\xi})dS(\boldsymbol{\xi})dS(\underset{\sim}{y}) + [\mathbf{F}]_{3(p-1)+i,3(q-1)+j} \tag{4.61}
$$

$$
\begin{aligned}
[\mathbf{F}]_{3(p-1)+\alpha,3(q-1)+\beta} = & \frac{\lambda^s}{2}\int_{S_c}\Phi_{p,\alpha}(\underset{\sim}{y})\Phi_{q,\beta}(\underset{\sim}{y})dS(\underset{\sim}{y}) \\
& + \frac{\mu^s}{2}\left(\int_{S_c}\Phi_{p,\beta}(\underset{\sim}{y})\Phi_{q,\alpha}(\underset{\sim}{y})dS(\underset{\sim}{y}) + \delta_{\alpha\beta}\int_{S_c}\Phi_{p,\gamma}(\underset{\sim}{y})\Phi_{q,\gamma}(\underset{\sim}{y})dS(\underset{\sim}{y})\right)
\end{aligned}
\tag{4.62}
$$

$$
[\mathbf{F}]_{3(p-1)+3,3(q-1)+3} = \frac{\tau^s}{2}\int_{S_c}\Phi_{p,\gamma}(\underset{\sim}{y})\Phi_{q,\gamma}(\underset{\sim}{y})dS(\underset{\sim}{y}) \tag{4.63}
$$

$$
[\mathbf{R}_1]_{3(p-1)+i} = \frac{1}{2}\int_{S_c}\Phi_{p}(\underset{\sim}{y})t^{0\Sigma}_i(\underset{\sim}{y})dS(\underset{\sim}{y});\ \ [\mathbf{R}_2]_{3(p-1)+i} = \frac{1}{2}\int_{S_c}\Phi_{p}(\underset{\sim}{y})t^{0\Delta}_i(\underset{\sim}{y})dS(\underset{\sim}{y}) \tag{4.64}
$$

$$
[\mathbf{U}^{\Sigma}]_{3(q-1)+i} = U^{\Sigma}_{3(q-1)+i};\ \ [\mathbf{U}^{\Delta}]_{3(q-1)+i} = U^{\Delta}_{3(q-1)+i};\ \ [\mathbf{T}^{\Sigma}]_{3(q-1)+i} = T^{\Sigma}_{3(q-1)+i} \tag{4.65}
$$

4.2.1.2 Special case with only residual surface tension

By applying the same procedure as that employed in the general case to (4.44), it leads to a system of linear algebraic equations as follows:

$$\begin{bmatrix} \bar{\mathbf{A}} & \mathbf{B} & \mathbf{0} \\ \mathbf{B}^T & \mathbf{C} & \mathbf{D} \\ \mathbf{0} & \mathbf{D}^T & \bar{\mathbf{E}} \end{bmatrix} \begin{Bmatrix} \mathbf{U}^{\Sigma} \\ \mathbf{T}^{\Sigma} \\ \mathbf{U}^{\Delta} \end{Bmatrix} = \begin{Bmatrix} \mathbf{R}_1 \\ \mathbf{0} \\ \mathbf{R}_2 \end{Bmatrix} \tag{4.66}$$

where the sub-matrices $\bar{\mathbf{A}}$, $\mathbf{B}$, $\mathbf{C}$, $\mathbf{D}$, $\bar{\mathbf{E}}$ are associated with the bilinear operators $\bar{\mathcal{A}}$, $\mathcal{B}$, $\mathcal{C}$, $\mathcal{D}$, $\bar{\mathcal{E}}$; sub-vectors $\mathbf{R}_1$, $\mathbf{R}_2$ correspond to the linear operators $\mathcal{R}_1$, $\mathcal{R}_2$; $\mathbf{U}^{\Sigma}$ is a vector of nodal quantities of the sum of the displacement; $\mathbf{U}^{\Delta}$ is a vector of nodal quantities of the jump of the displacement; and $\mathbf{T}^{\Sigma}$ is a vector of nodal quantities of the sum of the traction. The additional sub-matrices $\bar{\mathbf{A}}$ and $\bar{\mathbf{E}}$ are given explicitly by

$$[\bar{\mathbf{A}}]_{3(p-1)+\alpha,3(q-1)+\beta} = 0 \tag{4.67}$$

$$[\bar{\mathbf{A}}]_{3(p-1)+3,3(q-1)+3} = \frac{\tau^s}{2}\int_{S_c} \Phi_{p,\gamma}(\underset{\sim}{y})\Phi_{q,\gamma}(\underset{\sim}{y})dS(\underset{\sim}{y}) - \frac{\tau^s}{2}\int_{\partial S_c} \Phi_{p}(\underset{\sim}{y})\Phi_{q,\gamma}(\underset{\sim}{y})n_\gamma d\Gamma(\underset{\sim}{y}) \tag{4.68}$$

$$[\bar{\mathbf{E}}]_{3(p-1)+i,3(q-1)+j} = -\int_{S_c} D_t\Phi_p(\underset{\sim}{y})\int_{S_c} C^{ti}_{mj}(\boldsymbol{\xi}-\underset{\sim}{y})D_m\Phi_q(\boldsymbol{\xi})dS(\boldsymbol{\xi})dS(\underset{\sim}{y}) + [\bar{\mathbf{F}}]_{3(p-1)+i,3(q-1)+j} \tag{4.69}$$

$$[\bar{\mathbf{F}}]_{3(p-1)+\alpha,3(q-1)+\beta} = 0 \tag{4.70}$$

$$[\bar{\mathbf{F}}]_{3(p-1)+3,3(q-1)+3} = \frac{\tau^s}{2}\int_{S_c} \Phi_{p,\gamma}(\underset{\sim}{y})\Phi_{q,\gamma}(\underset{\sim}{y})dS(\underset{\sim}{y}) \tag{4.71}$$

4.2.1.3 Special case with only in-plane surface elasticity

The discretized system of linear algebraic equations of the governing equations (4.48) can also be obtained in the same manner and the final result is given by

$$\begin{bmatrix} \hat{\mathbf{A}} & \mathbf{B} & \mathbf{0} \\ \mathbf{B}^T & \mathbf{C} & \mathbf{D} \\ \mathbf{0} & \mathbf{D}^T & \hat{\mathbf{E}} \end{bmatrix} \begin{Bmatrix} \mathbf{U}^{\Sigma} \\ \mathbf{T}^{\Sigma} \\ \mathbf{U}^{\Delta} \end{Bmatrix} = \begin{Bmatrix} \mathbf{R}_1 \\ \mathbf{0} \\ \mathbf{R}_2 \end{Bmatrix} \tag{4.72}$$

where the sub-matrices $\hat{\mathbf{A}}$, $\mathbf{B}$, $\mathbf{C}$, $\mathbf{D}$, $\hat{\mathbf{E}}$ are associated with the bilinear operators $\hat{\mathcal{A}}$, $\mathcal{B}$, $\mathcal{C}$, $\mathcal{D}$, $\hat{\mathcal{E}}$; sub-vectors $\mathbf{R}_1$, $\mathbf{R}_2$ correspond to the linear operators $\mathcal{R}_1$, $\mathcal{R}_2$; $\mathbf{U}^{\Sigma}$ is a vector of nodal quantities of the sum of the displacement; $\mathbf{U}^{\Delta}$ is a vector of nodal quantities of the jump of the displacement; and $\mathbf{T}^{\Sigma}$ is a vector of nodal quantities of the sum of the traction. The additional sub-matrices $\hat{\mathbf{A}}$ and $\hat{\mathbf{E}}$ are given explicitly by

$$\begin{aligned}[\hat{\mathbf{A}}]_{3(p-1)+\alpha,3(q-1)+\beta} = {} & \frac{\lambda^s}{2}\int_{S_c} \Phi_{p,\alpha}(\underset{\sim}{y})\Phi_{q,\beta}(\underset{\sim}{y})dS(\underset{\sim}{y}) - \frac{\lambda^s}{2}\int_{\partial S_c} \Phi_{p}(\underset{\sim}{y})\Phi_{q,\beta}(\underset{\sim}{y})n_\alpha d\Gamma(\underset{\sim}{y}) \\ & + \frac{\mu^s}{2}\left(\int_{S_c} \Phi_{p,\beta}(\underset{\sim}{y})\Phi_{q,\alpha}(\underset{\sim}{y})dS(\underset{\sim}{y}) + \delta_{\alpha\beta}\int_{S_c} \Phi_{p,\gamma}(\underset{\sim}{y})\Phi_{q,\gamma}(\underset{\sim}{y})dS(\underset{\sim}{y})\right) \\ & - \frac{\mu^s}{2}\left(\int_{\partial S_c} \Phi_{p}(\underset{\sim}{y})\Phi_{q,\alpha}(\underset{\sim}{y})n_\beta d\Gamma(\underset{\sim}{y}) + \delta_{\alpha\beta}\int_{\partial S_c} \Phi_{p}(\underset{\sim}{y})\Phi_{q,\gamma}(\underset{\sim}{y})n_\gamma d\Gamma(\underset{\sim}{y})\right)\end{aligned} \tag{4.73}$$

$$[\hat{\mathbf{A}}]_{3(p-1)+3,3(q-1)+3} = 0 \tag{4.74}$$

$$[\hat{\mathbf{E}}]_{3(p-1)+i,3(q-1)+j} = -\int_{S_c} D_t \Phi_p(\underset{\sim}{y}) \int_{S_c} C_{mj}^{ti}(\boldsymbol{\xi} - \underset{\sim}{y}) D_m \Phi_q(\boldsymbol{\xi}) dS(\boldsymbol{\xi}) dS(\underset{\sim}{y}) + [\hat{\mathbf{F}}]_{3(p-1)+i,3(q-1)+j} \tag{4.75}$$

$$\begin{aligned}[\hat{\mathbf{F}}]_{3(p-1)+\alpha,3(q-1)+\beta} &= \frac{\lambda^s}{2} \int_{S_c} \Phi_{p,\alpha}(\underset{\sim}{y}) \Phi_{q,\beta}(\underset{\sim}{y}) dS(\underset{\sim}{y}) \\ &+ \frac{\mu^s}{2} \left(\int_{S_c} \Phi_{p,\beta}(\underset{\sim}{y}) \Phi_{q,\alpha}(\underset{\sim}{y}) dS(\underset{\sim}{y}) + \delta_{\alpha\beta} \int_{S_c} \Phi_{p,\gamma}(\underset{\sim}{y}) \Phi_{q,\gamma}(\underset{\sim}{y}) dS(\underset{\sim}{y}) \right)\end{aligned} \tag{4.76}$$

$$[\hat{\mathbf{F}}]_{3(p-1)+3,3(q-1)+3} = 0 \tag{4.77}$$

4.2.2 Numerical integration

To evaluate the sub-matrices $\mathbf{A}$, $\bar{\mathbf{A}}$, $\hat{\mathbf{A}}$, $\mathbf{B}$, $\mathbf{C}$, $\mathbf{D}$, $\mathbf{E}$, $\bar{\mathbf{E}}$, $\hat{\mathbf{E}}$ and sub-vectors $\mathbf{R}_1$, $\mathbf{R}_2$ numerically, the single and double surface integrals must be properly treated. All single surface integrals contain regular integrands, and can be efficiently and accurately integrated using standard Gaussian quadrature. Unlike single surface integrals, double surface integrals can be categorized into three types depending on a pair of elements resulting from the discretization of the surface S_c.

The first type is termed a regular double surface integral since its integrand is not singular with only mild variation. This type of integral arises when both elements in a pair are relatively remote in comparison with their characteristic size. Similar to the single surface integral, all regular double surface integrals can be accurately integrated by Gaussian quadrature. The second type, termed weakly singular double surface integrals, arises when both elements in a pair are identical and, therefore, the integrand is weakly singular due to the involved kernels. Although these integrals exist in an ordinary sense (sense of Riemann), it was pointed out by Xiao (1998) that they cannot be accurately integrated by standard Gaussian quadrature. To circumvent such difficulty, similar techniques based on integrand regularization via a series of transformations proposed by Li *et al.* (1985), Hayami and Brebbia (1988) and Xiao (1998) are employed. The last type of double surface integrals, which are considered most challenging, is a nearly singular integral. The integrand of these integrals is nearly singular since both elements in a pair are relatively close in comparison with their characteristic size and this renders the kernels appearing in those integrals nearly singular and exhibiting rapid variation. Similar to the weakly singular integrals, Gaussian quadrature cannot be used to integrate nearly singular integrals efficiently. Special techniques proposed by Hayami (1992), Hayami and Matsumoto (1994) and Xiao (1998) are adopted to perform the numerical integration.

4.2.3 Shape functions

As clearly discussed in the literature review, the singularity of the stress along the crack front of nano-sized cracks with the presence of surface stresses is still unclear. Some investigators pointed out that the stress along the crack front of nano-sized crack should be finite (e.g., Kim *et al.*, 2010; Kim *et al.*, 2011; Kim *et al.*, 2011; Nan and Wang, 2012). Other studies have concluded in the opposite direction that the stress along crack front of nano-sized crack is still singular; however the order of singularity reduces from square-root singularity to logarithmic

singularity (e.g., Sendova and Walton, 2010; Kim *et al.* 2013). In the current study, it is postulated that the singularity of the stress along the crack front disappears when the surface stresses is taken into account. As a result, standard isoparametric C^0 elements are employed everywhere to approximate all test and trial functions appearing in the governing equations of nano-sized crack problems. However, for some special cases when the influence of the surface stresses is ignored in certain directions, the special crack-tip shape functions proposed by Li *et al.* (1998) to accurately capture the right behavior of the near tip field are still required. The standard isoparametric shape functions can be easily found in Bathe (1990), Hughes (2000) and Zienkiewicz and Taylor (2000). The special crack-tip shape functions can be referred to the work of Li *et al.* (1998). The usage of the shape functions (standard shape functions or special crack-tip shape functions) in the present study can be summarized as follows:

- For the general case, when the full version of Gurtin-Murdoch model is considered, the standard shape functions are used in the approximation of all components of primary unknowns.
- For the special case, when the simplified version of Gurtin-Murdoch model without the surface elastic constants is considered, the special crack-tip shape functions are employed to approximate the in-plane components of $\underset{\sim}{u}^{\Delta}$ and $\underset{\sim}{\tilde{u}}^{\Delta}$ whereas the standard shape functions are utilized to discretize all remaining quantities.

For the special case, when the simplified version of Gurtin-Murdoch model without the residual surface tension is considered, the special crack-tip shape functions are employed to approximate the out-of-plane components of $\underset{\sim}{u}^{\Delta}$ and $\underset{\sim}{\tilde{u}}^{\Delta}$ whereas the standard shape functions are adopted to discretize all remaining quantities.

4.3 Numerical Results

In the analysis, three different levels of mesh refinement are adopted to examine the convergence of numerical results. Nine-node isoparametric elements are used to discretize the entire crack front, whereas the rest of the crack surface is discretized by eight-node and six-node isoparametric elements. Young's modulus and Poisson's ratio for the bulk material are taken as $E = 107\ GPa$ and $\nu = 0.33$, respectively, and the surface elastic constants and the residual surface tension are chosen identical to those utilized by Intarit *et al.* (2012) and Intarit (2013) (i.e. $\lambda^s = 4.4939\ N/m$, $\mu^s = 2.7779\ N/m$, $\tau^s = 0.6056\ N/m$). These above material properties are used for all following numerical examples in this chapter. For convenience in the numerical analysis, all quantities involved in the key governing equations are properly normalized. For instance, the unknown sum of the traction and the prescribed traction on the top surface of the two-thickness layers are normalized by the shear modulus μ (i.e. $t_0^{\Sigma} = t^{\Sigma}/\mu$ and $\sigma_{i0} = \sigma_i^0/\mu$); the unknown sum and jump of the displacement across the crack surface are normalized by a special length scale $\Lambda = \kappa^s/\mu = 0.24983\ nm$ (i.e. $u_0^{\Delta} = u^{\Delta}/\Lambda$ and $u_0^{\Sigma} = u^{\Sigma}/\Lambda$) where $\kappa^s = \left|\lambda^s + 2\mu^s\right|$; and all characteristic lengths representing the geometry of the crack such as the crack radius a, the semi-major axis a, and the semi-minor axis b used in following examples are normalized by the length scale Λ (i.e. $a_0 = a/\Lambda$ and $b_0 = b/\Lambda$).

4.3.1 Penny-shaped crack under pure mode-I loading

As a means for verifying the current technique, the problem of a penny-shaped crack of radius *a* embedded in an isotropic, linear elastic infinite medium is considered (Figure 4.3(a)). The crack is subjected to self-equilibrated, uniformly distributed normal traction $t_3^+ = -t_3^- = \sigma_0$. The three meshes of the crack surface used in the numerical study are shown in Figure 4.3(b).

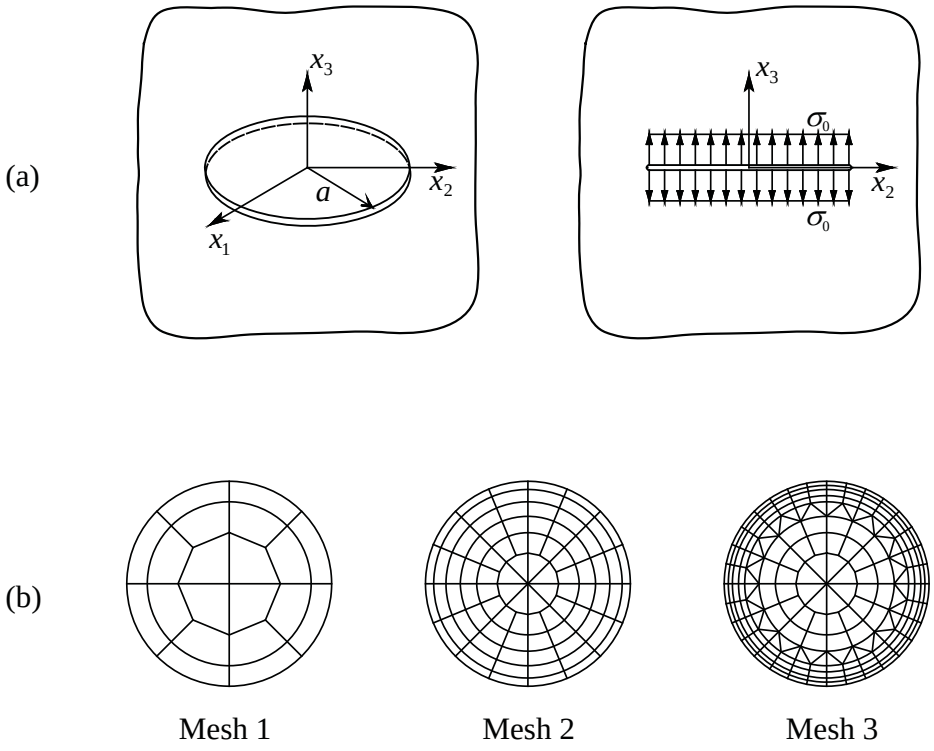

Figure 4.3 (a) Schematic of a penny-shaped crack of radius a embedded in an isotropic, linear elastic infinite medium subjected to uniformly distributed normal traction $t_3^+ = -t_3^- = \sigma_0$; (b) Meshes adopted in the analysis. Mesh 1: 20 elements and 77 nodes. Mesh 2: 88 elements and 297 nodes. Mesh 3: 216 elements and 665 nodes.

4.3.1.1 Verification

This problem has been previously solved by Intarit *et al.* (2012) and Intarit (2013) using Hankel integral transforms along with a solution technique for dual integral equations, and their results are used as the benchmark solution to validate the proposed FEM-SGBEM technique. In this numerical example, results for mode-I loading conditions are presented for three different models. The model-1 represents the classical case without the surface stress effects. It should be noted that, for this particular case, the classical solution of the crack opening displacement and the stress in the vicinity of crack front can be found in Tada *et al.* (2000) and Kachanov *et al.* (2004) respectively. The model-2 is associated with a simplified version of Gurtin-Murdoch surface elasticity model (the first special case), in which the residual surface tension (τ^s) is only considered. The model-3 corresponds a full version of Gurtin-Murdoch surface elasticity model

where both the surface elastic constants (λ^s, μ^s) and the residual surface tension (τ^s) are included.

The normalized crack opening displacement and the normalized vertical stresses near the crack front, when the influence of surface stresses is taken into account, are reported in Figures 4.4-4.5 along with the benchmark solution generated by a technique proposed by Intarit *et al.* (2012) and Intarit (2013). It is seen that the numerical results are slightly mesh dependent and that they are highly accurate and almost indistinguishable from the analytical solution for both the crack opening displacement and near-tip vertical stresses σ_{33} for the model-2 and model-3. It can also be pointed out from the results shown in Figure 4.4 that the two models incorporating the surface stresses with (model-3) and without (model-2) the influence of the in-plane surface elasticity yield results significantly different from those predicted by the classical model (model-1). While both the residual surface tension and the in-plane surface elasticity contribute to such discrepancy, the influence of the residual surface tension seems more significant in the case of mode-I loading conditions. The medium tends to be much stiffer than the classical case, when the full version of the surface stress model is considered in the analysis.

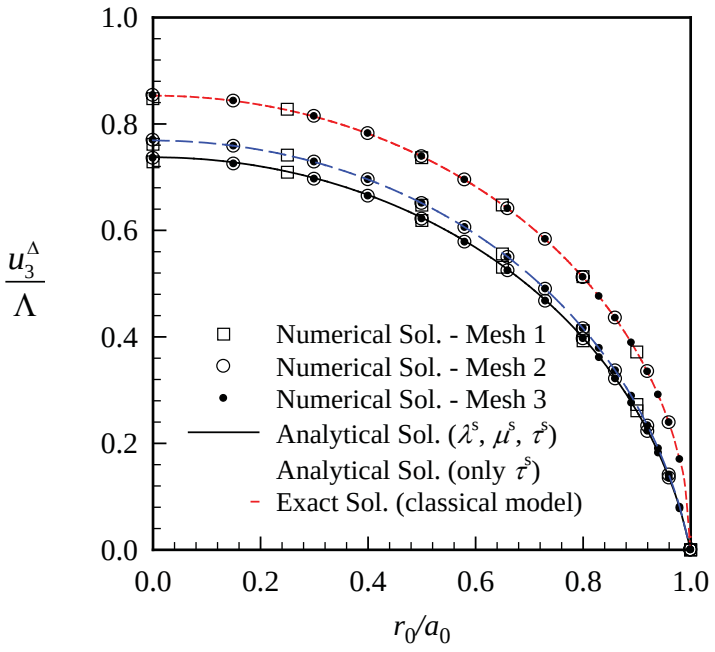

Figure 4.4 Comparison of the normalized crack opening displacements of a penny-shaped crack under uniformly distributed normal traction obtained from three different models for $E = 107\,GPa$, $\nu = 0.33$, $\lambda^s = 4.4939\ N/m$, $\mu^s = 2.7779\ N/m$ and $\tau^s = 0.6056\ N/m$

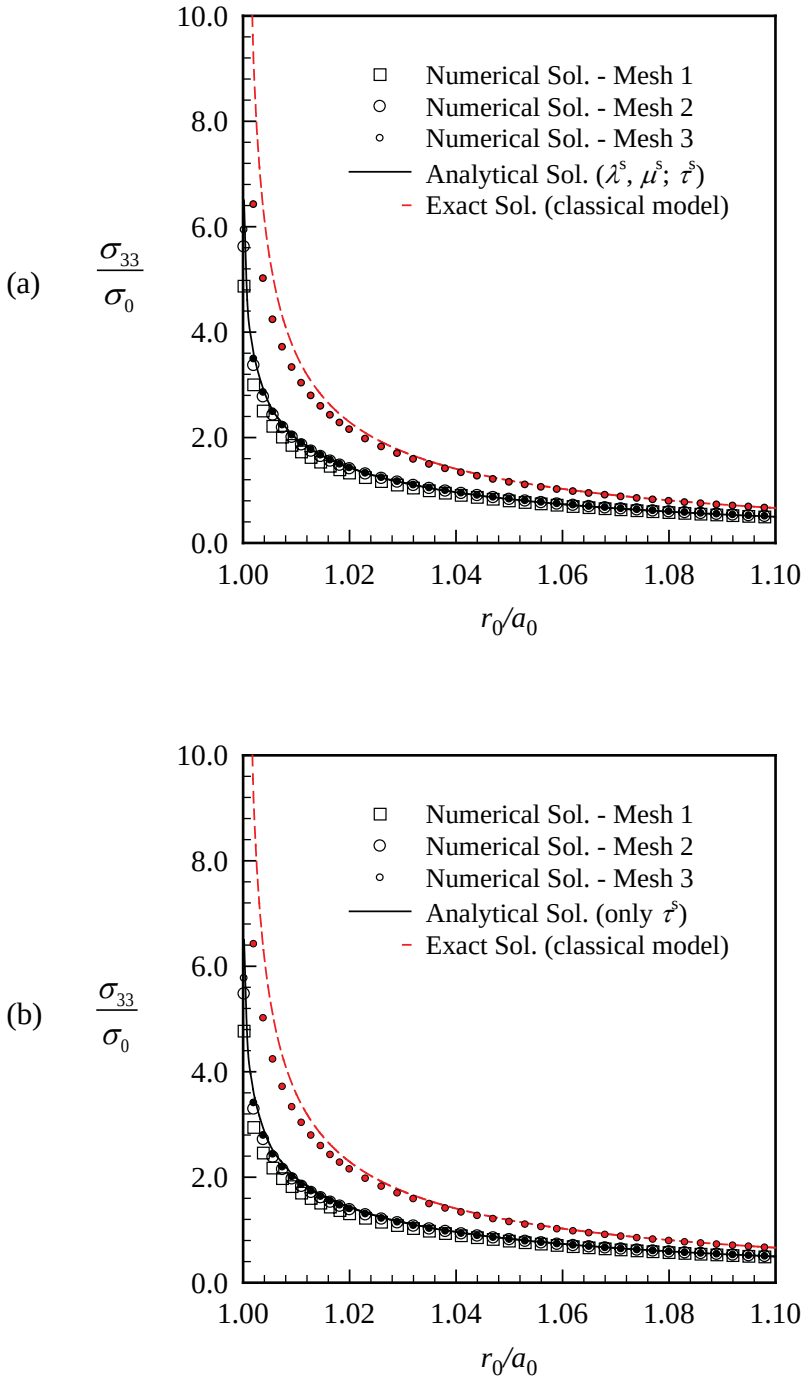

Figure 4.5 Normalized vertical stresses σ_{33}/σ_0 in the vicinity of the crack-front of a penny-shaped crack under uniformly distributed normal traction for $E = 107\,GPa$, $\nu = 0.33$, $\lambda^s = 4.4939\ N/m$, $\mu^s = 2.7779\ N/m$ and $\tau^s = 0.6056\ N/m$: results for (a) model-3 and (b) model-2.

4.3.1.2 Parametric study

To further examine the influence of the residual surface tension (τ^s) on the predicted solution of mode-I crack problems, the normalized crack opening displacement and the normalized vertical stress σ_{33} for different values of the residual surface tension τ^s ranging from 0.1 to 1.0 *N/m* (with the surface elastic constants and the bulk material properties remaining fixed) are shown in Figure 4.6. It can be concluded that the residual surface tension exhibits significant role on the crack opening displacement and the vertical stress σ_{33} for mode-I loading conditions. In particular, as τ^s becomes larger, the deviation of results from the classical case (without the surface stresses) significantly increases and, clearly, it renders the elastic medium much stiffer.

The investigation of the influence of the surface elasticity constants (λ^s, μ^s) on the solution of cracks under mode-I loading conditions is also considered. The normalized crack opening displacement and the normalized vertical stress σ_{33} in the vicinity of the crack front for different values of the surface elasticity constants (λ^s, μ^s) ranging from 0, 0.1, 1 and 10 times of their initial value (with the residual surface tension and the bulk material properties remaining fixed) are reported in Figure 4.7. This numerical study is performed only for the model-3 where the full version of Gurtin-Murdoch surface elasticity is considered. It can be concluded from this set of results that the surface elasticity constants exhibit a little influence on the crack opening displacement but negligible influence on the vertical stress for mode-I loading conditions. However, as the surface elasticity constants become larger, the deviation of results from those predicted by the model-2, slightly, increases and, it clearly makes the bulk material a little stiffer.

To demonstrate the size-dependent behavior of results due to the presence of the surface stresses, the crack opening displacements and the near-tip vertical stresses are illustrated in Figure 4.8 for all three models. It is evident that the predicted solutions apparently exhibit size-dependent behavior by including the surface stress effects in the mathematical model. In particular, the normalized crack opening displacements and the normalized vertical stresses in the vicinity of the crack front of the model-2 and model-3 depend significantly on the crack size. On the contrary, the normalized crack opening displacements and normalized vertical stresses of model-1 are independent of the crack radius upon the proper normalization.

4.3.2 Penny-shaped crack under mixed mode loading

In this section, a penny-shaped crack in an unbounded medium under mixed-mode loading conditions (i.e. mode-II and mode-III loading conditions) is investigated to demonstrate the capability of the proposed FEM-SGBEM coupling in the analysis of nano-sized crack problems. This numerical example should provide the complete information with insight of the influence of surface stresses on elastic responses and fracture data within the context of three-dimensional problems. In the Gurtin-Murdoch surface elasticity model, the surface elastic constants are related to the in-plane terms in the governing equations of the surface and should significantly affects the in-plane behavior of cracks under mixed-mode loading conditions. Therefore, similar to the previous problem, three different models are considered in this case. The model-1 is the classical model when the surface stresses are ignored. The classical solution of the crack sliding displacements and stresses in the vicinity of the crack front can be found in Kachanov *et al.* (2004). The model-2 is associated with a simplified version of Gurtin-Murdoch surface elasticity model where the in-plane surface elasticity is only treated. The last model, the model-3, once again corresponds to the full version of Gurtin-Murdoch model.

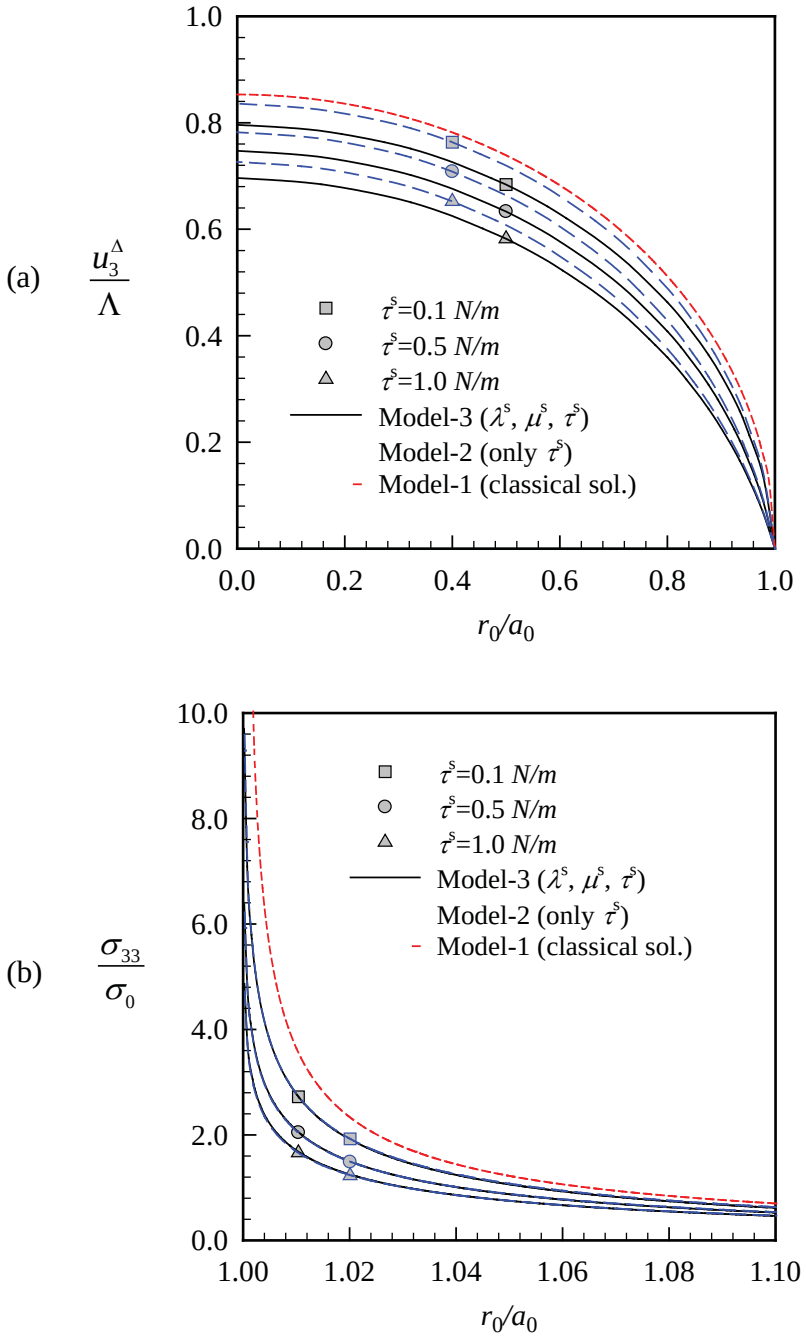

Figure 4.6 Penny-shaped crack under uniformly distributed normal traction for different residual surface tension τ^s ranging from 0.1 to 1 *N/m;* $E = 107\,GPa$, $\nu = 0.33$, $\lambda^s = 4.4939\ N/m$, $\mu^s = 2.7779\ N/m$: (a) normalized crack opening displacements and (b) normalized near-tip vertical stresses σ_{33}/σ_0 obtained by using mesh-3

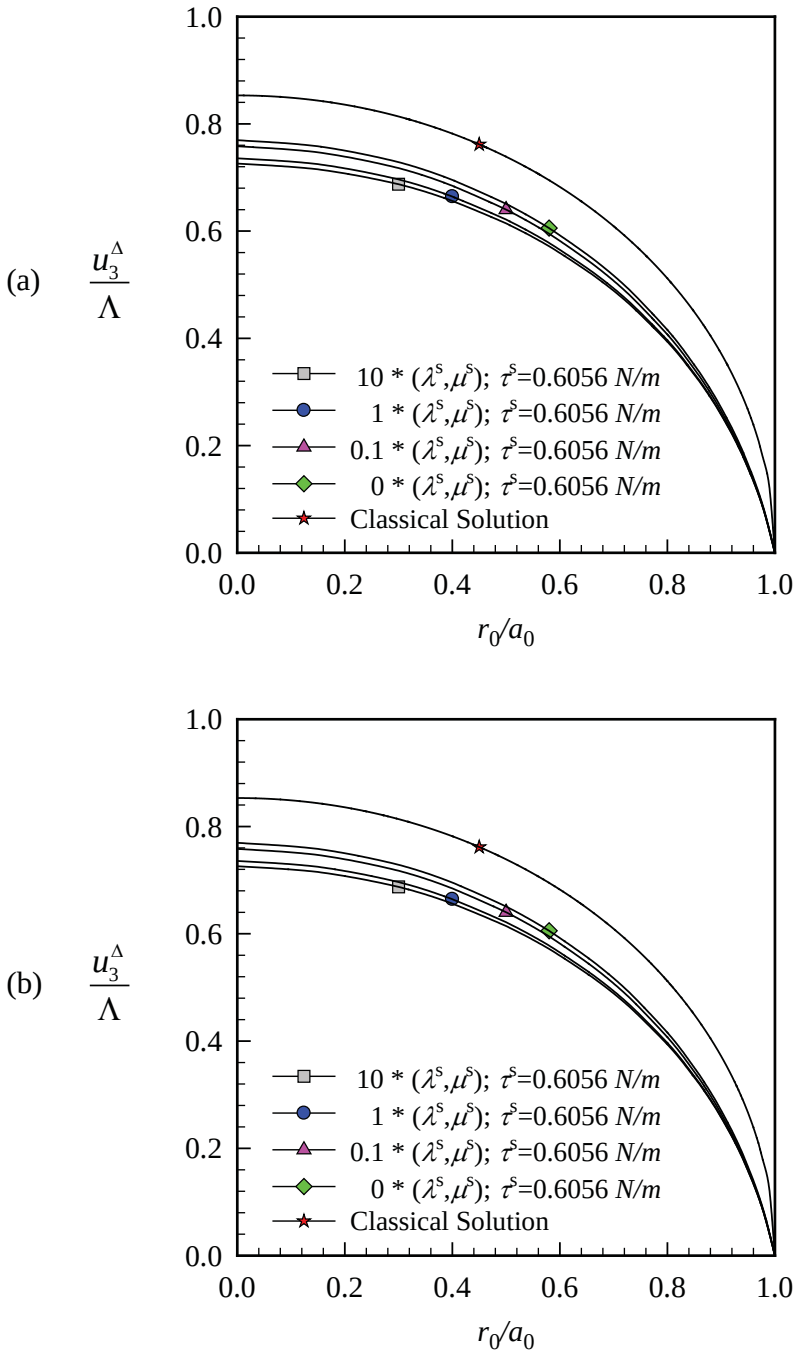

Figure 4.7 Penny-shaped crack under uniformly distributed normal traction, for different surface elasticity constants (λ^s, μ^s) ranging from 0; 0.1; 1 and 10 times of their initial value ($\lambda^s = 4.4939\ N/m,\ \mu^s = 2.7779\ N/m$); $E = 107\,GPa$, $\nu = 0.33$, $\tau^s = 0.6056\ N/m$: (a) normalized crack opening displacements and (b) normalized near-tip vertical stresses obtained by using mesh-3

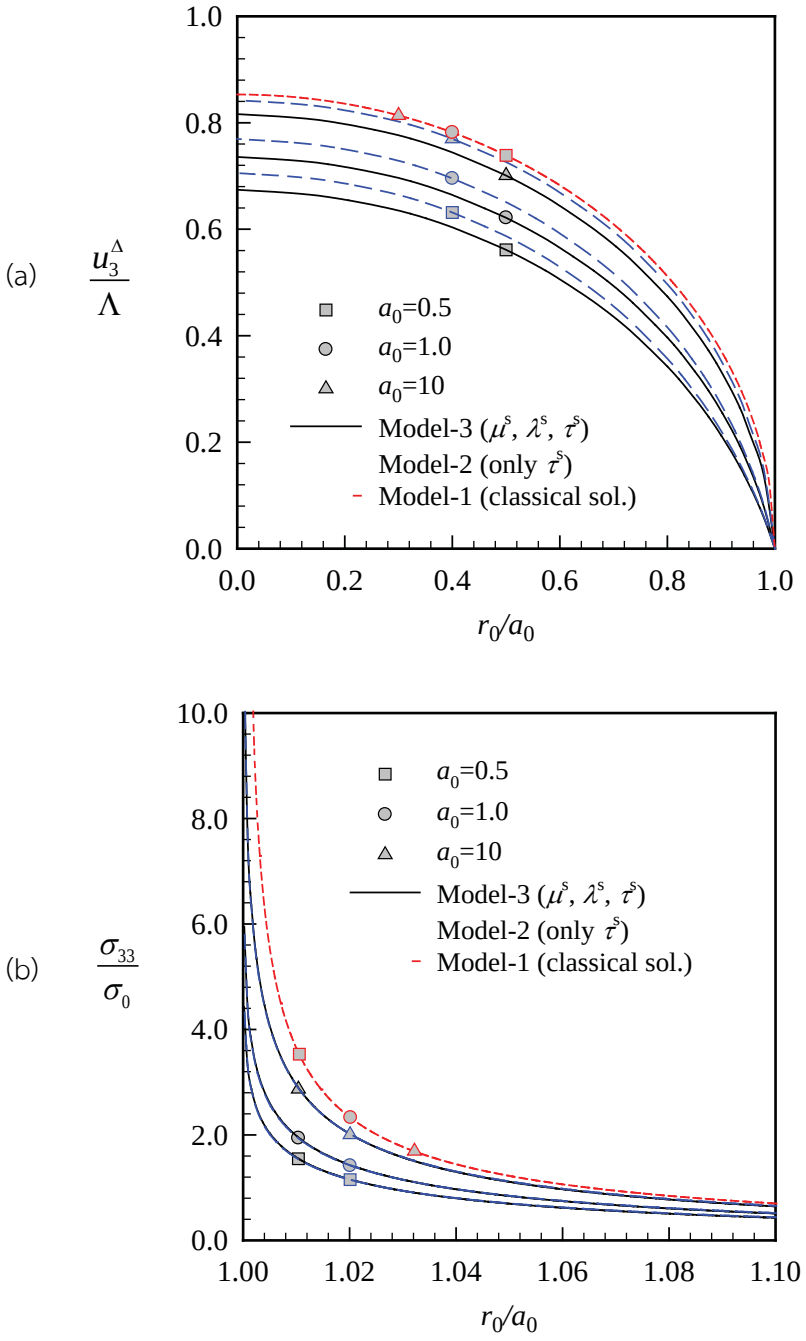

Figure 4.8 Penny-shaped crack under uniformly distributed normal traction, for three different crack radii $a_0 = a/\Lambda = 0.5, 1.0, 10$, and for $E = 107\,GPa$, $\nu = 0.33$, $\lambda^s = 4.4939\ N/m$, $\mu^s = 2.7779\ N/m$, $\tau^s = 0.6056\ N/m$: (a) normalized crack opening displacements and (b) normalized near-tip vertical stresses obtained by using mesh-3

Consider a penny-shaped crack of radius a embedded in an isotropic, linear elastic infinite medium as shown in Figure 4.9(a). The crack is subjected to the self-equilibrated, uniformly distributed shear traction $t_1^+ = -t_1^- = \tau_0$. Three meshes, adopted as depicted in Figure 4.9(b), are employed in the analysis.

Numerical results for the crack sliding displacements (CSD) and the stresses in the vicinity of the crack front along the x_1-direction (the direction of the applied shear traction) are presented in Figure 4.10. It is seen that numerical solutions exhibit very good convergence for both the CSD and the near-tip stresses. It can be pointed out from the results in Figure 4.10(a) that the CSD depend significantly on the surface stresses. In addition, the CSD, predicted by the model-2 and the model-3, are virtually the same. As a result, it can be concluded that the in-plane elastic constants prominently affect the CSD of cracks under in-plane loading conditions whereas the influence of the residual surface tension on the CSD is insignificant. It also can be argued from Figure 4.10(b) that the shear stress σ_{13} near the crack front is strongly influenced by the surface stresses. The magnitude of the predicted stresses near the crack front reduces considerably from the classical solution when the surface stresses are present. In particular, the in-plane elastic constants affect substantially the in-plane quantities for cracks under in-plane loadings in comparison with the residual surface tension.

To further understand the role of each parameter in the Gurtin-Murdoch model on the predicted solutions of mixed-mode crack problems, the following four cases obtained by varying the value of the in-plane elastic constants and the residual surface tension are considered:

- Case 1: Both the in-plane elastic constants (λ^s, μ^s) are varied from 0, 1, 5 and 10 times of their initial value ($\lambda^s = 4.4939\ N/m$, $\mu^s = 2.7779\ N/m$) whereas the residual surface tension remains fixed.
- Case 2: The residual surface tension (τ^s) is ranged from 0, 1, 5 and 10 times of its initial value ($\tau^s = 0.6056\ N/m$) whereas the in-plane elastic constants remain fixed.
- Case 3: Only the parameter λ^s is varied from 0, 1, 5 and 10 times of its initial value ($\lambda^s = 4.4939\ N/m$) whereas all remaining parameters remain fixed.
- Case 4: Only the parameter μ^s is varied from 0, 1, 5 and 10 times of its initial value ($\mu^s = 2.7779\ N/m$) whereas all remaining parameters remain fixed.

The normalized CSD and the normalized shear stresses in the vicinity of the crack front along the x_1-direction are reported in Figures 4.11-4.12 for all four cases. It can be seen that the surface elastic constants (λ^s, μ^s) in the Gurtin-Murdoch model significantly reduce the CSD and the shear stresses near the crack front, whereas the residual surface tension practically has no influence on the predicted solution of mixed-mode crack problems. It can be also pointed out that the parameter μ^s in the Gurtin-Murdoch model exhibits more prominent effect on the CSD and the near-tip shear stresses when compared to the parameter λ^s (see Figure 4.11(c)-(d) and Figure 4.12(c)-(d)). To investigate the size-dependent behavior of the solution of mixed-mode crack problems due to the presence of the surface stresses, the CSD and the shear stresses in the vicinity of the crack-front for different crack radii $a_0 = 0.5, 1.0, 10$ are considered. Results of the crack sliding displacement and the shear stresses along the x_1-direction are shown in Figure 4.13.

It can be seen from Figure 4.13 that the normalized CSD and the normalized shear stresses in the vicinity of the crack front along the x_1-direction obtained from the model-2 and model-3 are apparently size-dependent. This finding agrees with the case of mode-I loading conditions. When the crack-size decreases, the influence of the surface stresses on elastic responses of cracks subjected to mixed-mode loading conditions becomes more significant in the sense that the medium is stiffer.

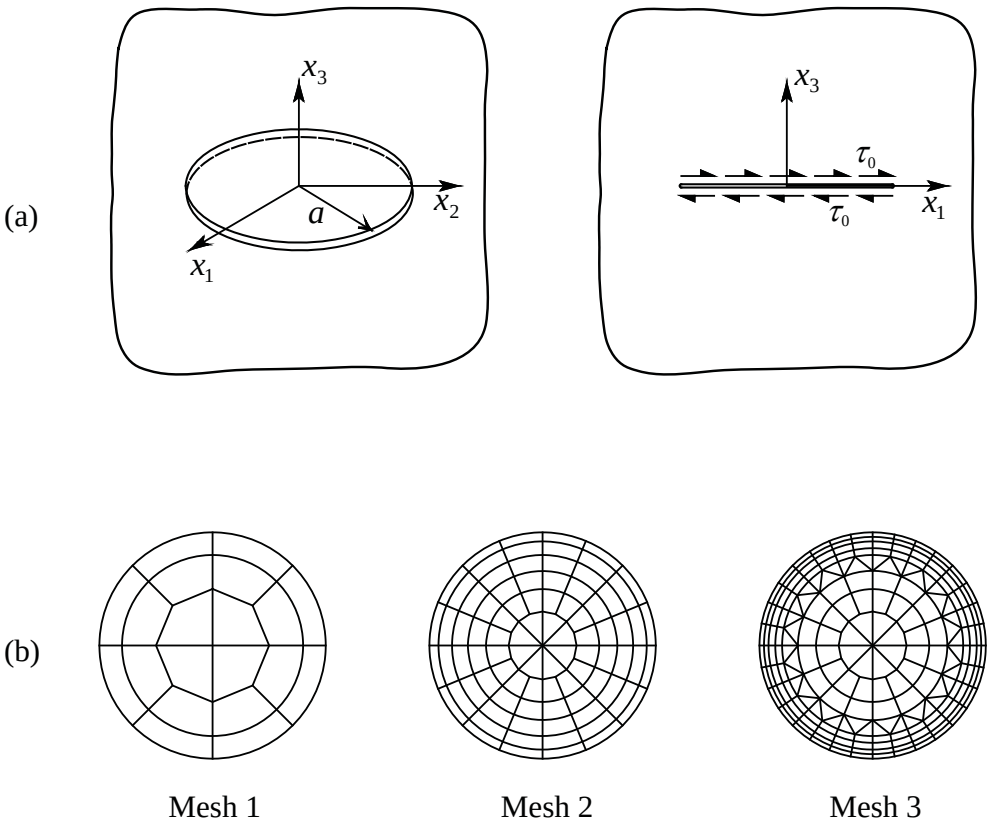

Figure 4.9: (a) Schematic of a penny-shaped crack of radius a embedded in an isotropic, linear elastic infinite medium subjected to uniformly distributed shear traction $t_1^+ = -t_1^- = \tau_0$; (b) meshes adopted in the analysis. Mesh 1: 20 elements and 77 nodes. Mesh 2: 88 elements and 297 nodes. Mesh 3: 216 elements and 665 nodes.

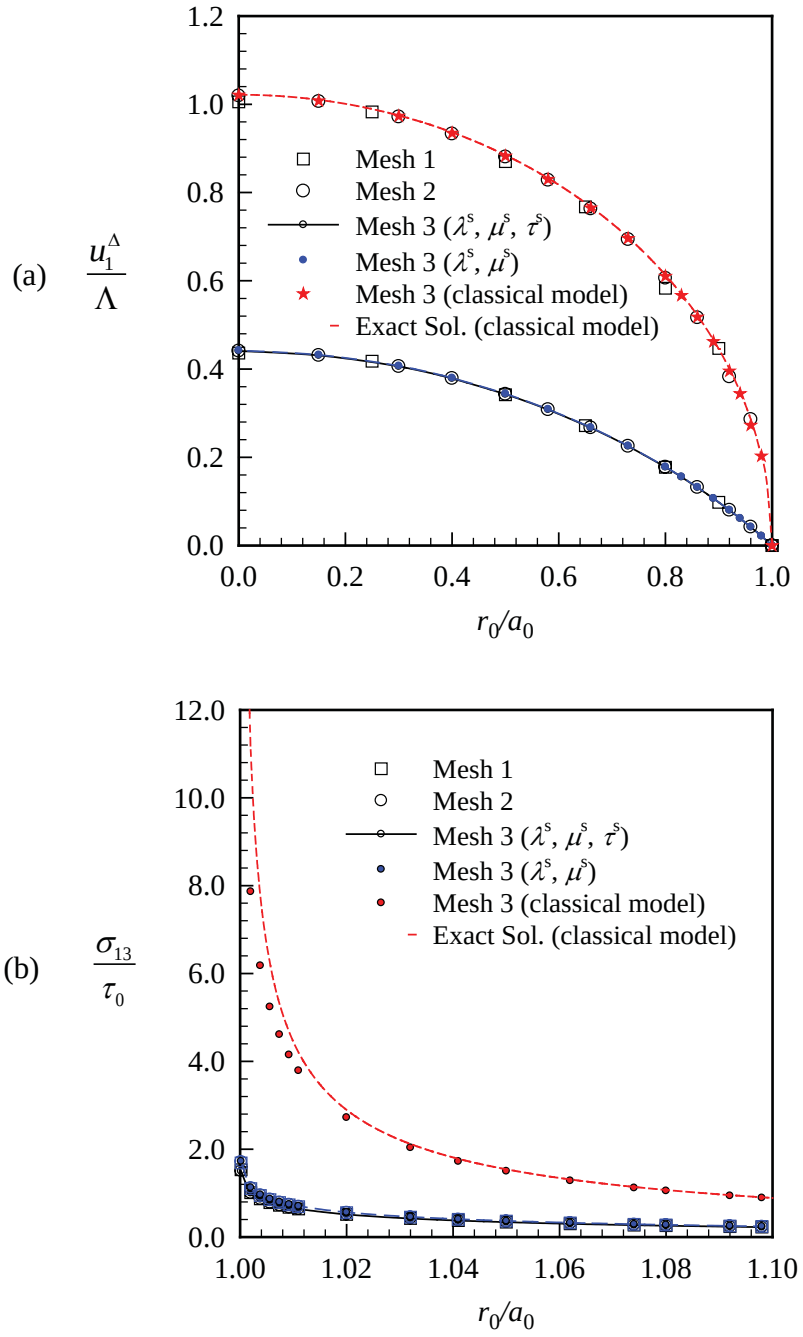

Figure 4.10: A penny-shaped crack under uniformly distributed shear traction, for $E = 107\,GPa$, $\nu = 0.33$, $\lambda^s = 4.4939\ N/m$, $\mu^s = 2.7779\ N/m$, $\tau^s = 0.6056\ N/m$: (a) normalized crack sliding displacements and (b) normalized near-tip shear stress along the x_1-direction.

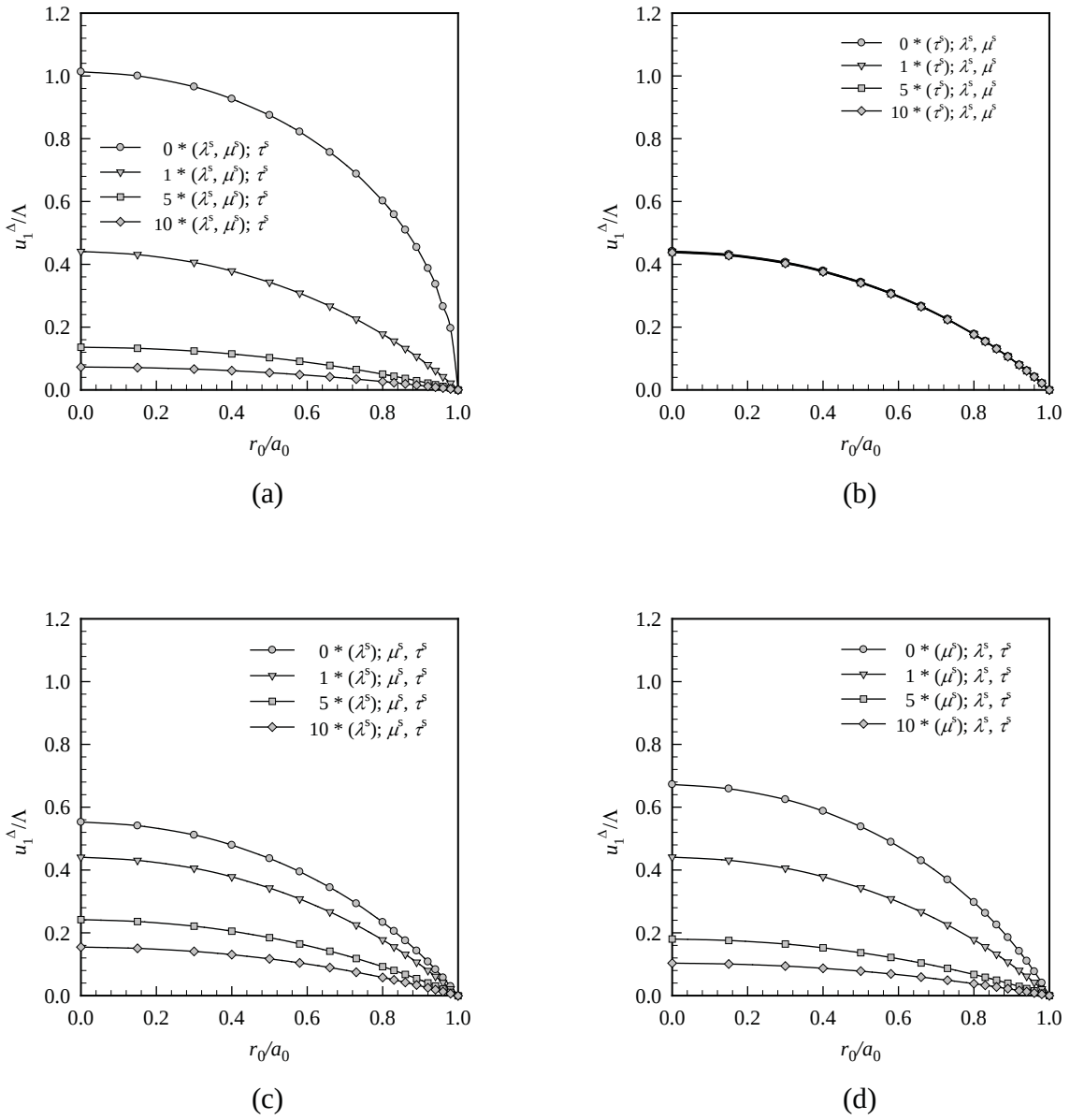

Figure 4.11 Normalized crack sliding displacements of a penny-shaped crack under uniformly distributed shear traction for $E = 107\,GPa$, $\nu = 0.33$ in four cases: (a) different values of (λ^s, μ^s) with $\tau^s = 0.6056\ N/m$; (b) different values of τ^s with $\lambda^s = 4.4939\ N/m$, $\mu^s = 2.7779\ N/m$; (c) different values of λ^s with $\mu^s = 2.7779\ N/m$, $\tau^s = 0.6056\ N/m$ and (d) different values of μ^s with $\lambda^s = 4.4939\ N/m$, $\tau^s = 0.6056\ N/m$ obtained by using mesh-3

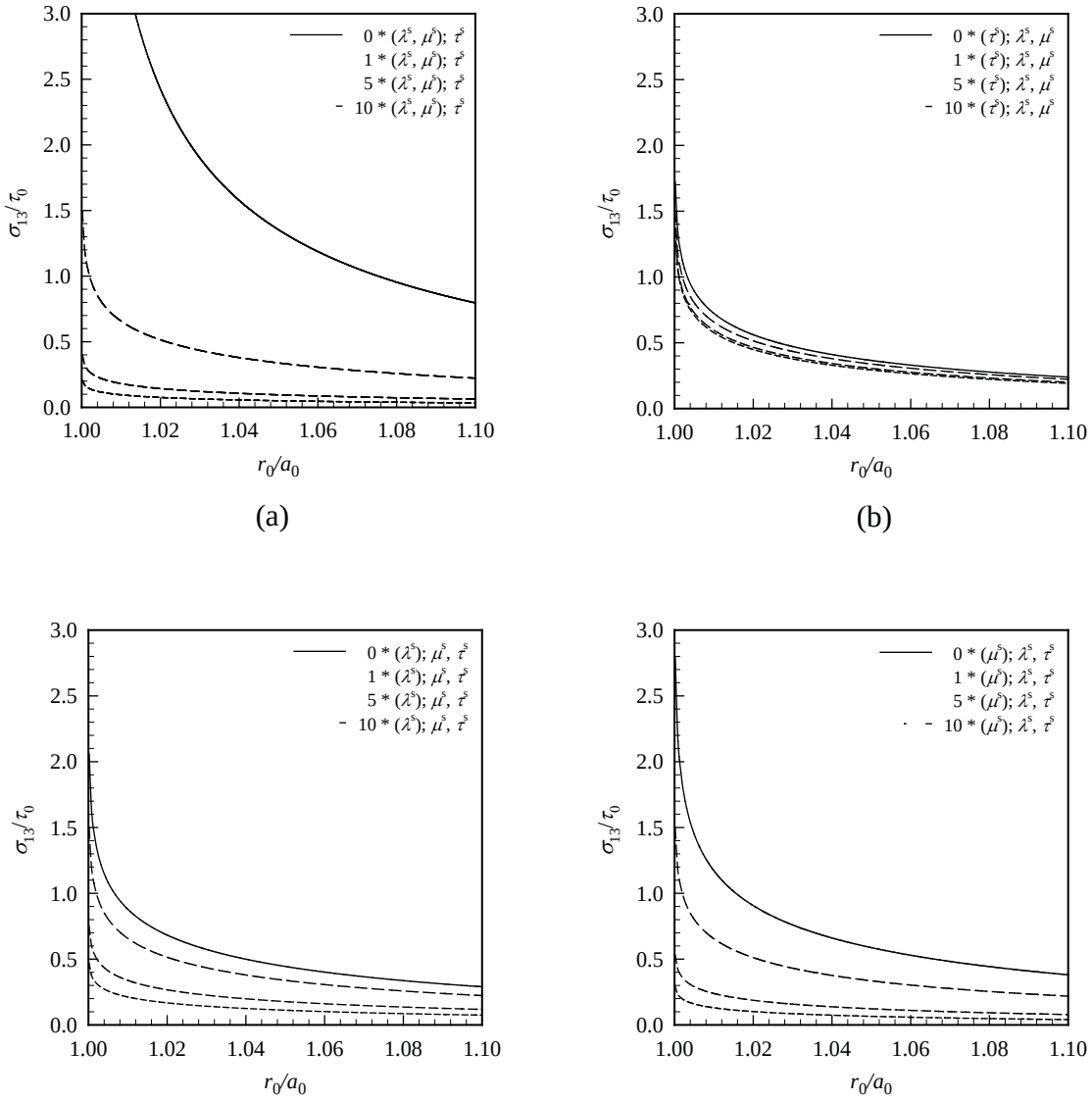

Figure 4.12 Normalized near-tip shear stresses of a penny-shaped crack under uniformly distributed shear traction for $E = 107\,GPa$, $\nu = 0.33$ in four cases: (a) different values of (λ^s, μ^s); (b) different values of τ^s; (c) different values of λ^s and (d) different values of μ^s obtained by using mesh-3

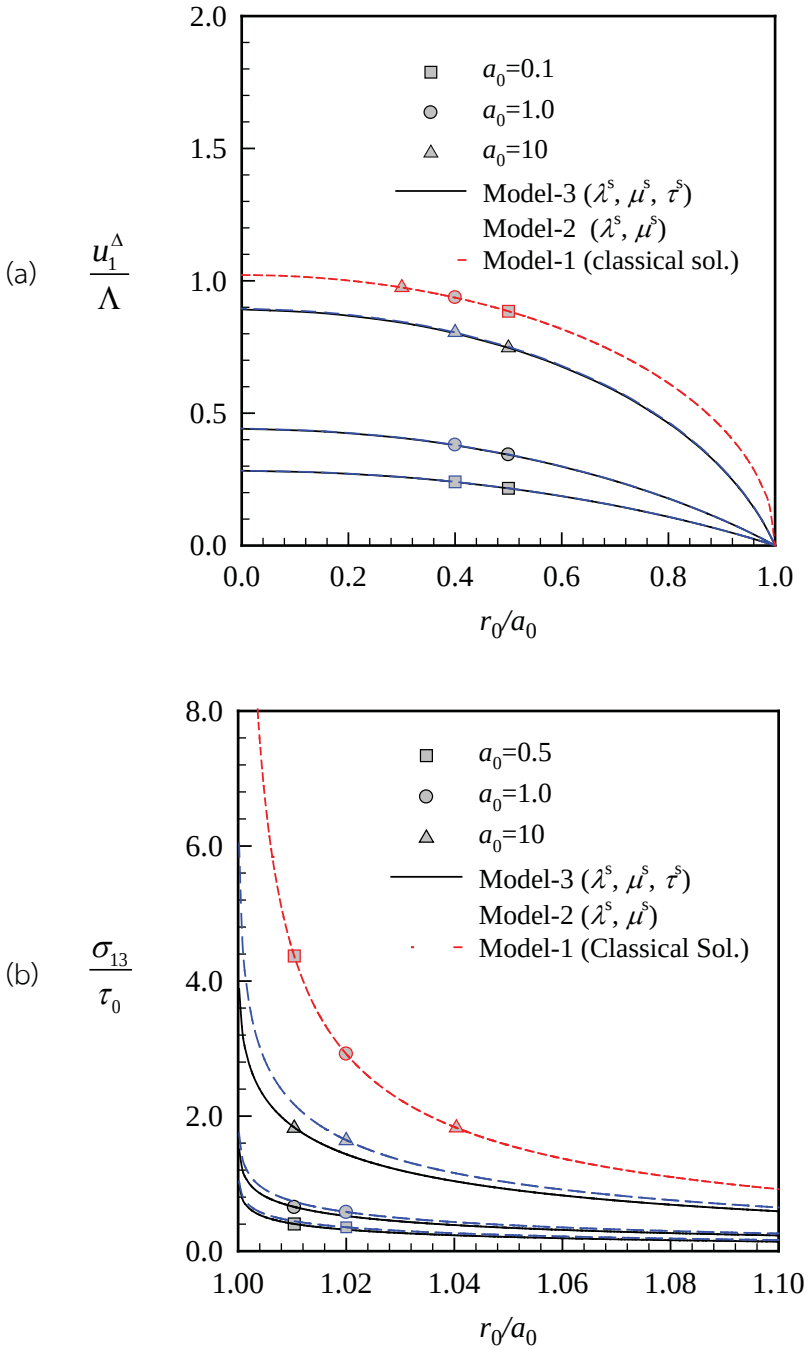

Figure 4.13 A penny-shaped crack under uniformly distributed shear traction, for different crack radii $a_0 = a/\Lambda = 0.5, 1.0, 10$, for $E = 107\,GPa$, $\nu = 0.33$, $\lambda^s = 4.4939\ N/m$, $\mu^s = 2.7779\ N/m$ and $\tau^s = 0.6056\ N/m$: (a) normalized crack sliding displacements and (b) normalized near-tip shear stresses obtained by using mesh-3.

4.3.3 Elliptical crack

To demonstrate the capability of the proposed FEM-SGBEM coupling technique for treating crack problems of arbitrary shapes with consideration of the surface stress effects, an elliptical crack embedded in an isotropic, linear elastic infinite domain is considered (see Figure 4.14(a)). The material in which the crack is embedded is Si [100] where properties of the bulk material are $E = 107\,GPa$, $\nu = 0.33$ and the surface elastic constants and the residual surface tension are obtained from Miller and Shenoy (2000). The crack-front is parameterized in terms the angle θ by

$$x_1 = a\cos\theta, \quad x_2 = b\sin\theta, \quad x_3 = 0; \quad \theta \in [0, 2\pi] \tag{4.78}$$

where a and b are the major and minor semi-axes of the crack, respectively. In this numerical example, two loading conditions are investigated. The first case is associated with the crack subjected to the self-equilibrated, uniformly distributed normal traction $t_3^+ = -t_3^- = \sigma_0$ (see Figure 4.14(b)) whereas the other case corresponds to the crack subjected to the self-equilibrated, uniformly distributed shear traction $t_2^+ = -t_2^- = \tau_0$ (see Figure 4.14(c)). Numerical results are presented for three different aspect ratios $a/b = 1, 2, 3$, and three meshes shown in Figure 4.14(d) are adopted to model the elliptical crack (Mesh 1 has 20 elements and 77 nodes; Mesh 2 has 88 elements and 297 nodes and Mesh 3 has 216 elements and 665 nodes).

4.3.3.1 Normal traction

For this particular loading condition, results obtained from three different models indicated below are presented and compared:

- Model-1 represents the classical model without the influence of the surface stresses. The classical solution of the crack opening displacements and the vertical stresses in the vicinity of crack front can be found in Zeng-shen (1982) and Kassir and Sih (1975), respectively.
- Model-2 is associated with the simplified version of Gurtin-Murdoch model without the contribution of surface elastic constants.
- Model-3 is the full version of Gurtin-Murdoch model where the surface elastic constants (λ^s, μ^s) and the residual surface tension (τ^s) are included.

The convergence study of the normalized crack opening displacement (COD) and the normalized vertical stress along the minor axis for the aspect ratio $a/b = 2$ using the model-2 and model-3 are reported in Figure 4.15. As observed from this figure, the predicted solutions for COD and the vertical stresses near the crack front show good convergence. The normalized CODs and the normalized vertical stresses σ_{33}/σ_0 along the minor axis of the crack are also presented in Figure 4.16 for the aspect ratios $a/b = 1, 2, 3$ and all three models. It can be seen from Figure 4.16 that the influence of the surface stresses on the CODs and the near-tip vertical stresses decreases when the aspect ratio a/b increases. It can also be remarked that for the mode-I crack problem, the difference between solutions predicted by the full version and simplified version of Gurtin-Murdoch model is insignificant. As a result, the simplified version of Gurtin-Murdoch model can be utilized to investigate the nano-scale influence of mode-I crack problems to simplify the calculation.

In order to investigate the role of the residual surface tension on responses of cracks under the mode-I loading conditions, the normalized CODs and the normalized vertical stresses σ_{33}/σ_0 are computed for different values of the residual surface tension τ^s ranging from 0.1 to 1.0 N/m. Solutions obtained from the model-3 are illustrated in Figure 4.17 for the aspect ratio $a/b=2$. It can be concluded from this set of results that the influence of the residual surface tension is also significant and the medium becomes much stiffer when τ^s increases.

To examine the size-dependent behavior of predicted results due to the presence of the residual surface tension, the CODs and the near-tip vertical stresses for $b_0 = 0.5, 1.0, 10$ and the aspect ratio $a/b=2$ are shown in Figure 4.18. As can be seen in Figure 4.18, the normalized CODs and normalized vertical stresses are clearly size-dependent. This is in contrast with the classical case (i.e. without the surface stress effects) where the solutions are size-independent. In particular, when the crack-size or the aspect ratio decreases, the influence of the surface stresses becomes more significant in the sense that the medium becomes stiffer.

4.3.3.2 Shear traction

Consider, next, an elliptical crack subjected to uniform shear traction τ_0 as shown in Figure 4.14(c). The direction of the applied shear traction is taken in the x_2-direction as shown schematically in Figure 4.14(c). As a consequence of the anti-symmetric nature of the applied load, only mode-II (sliding mode) and mode-III (tearing mode) responses are investigated. Once again, the following three different models are considered in the numerical study:

- Model-1 is associated with the classical model where the surface stresses are not included. It is remarked that the classical solution of the crack sliding displacement and the shear stresses in the vicinity of the crack front was given by Kassir and Sih (1975).
- Model-2 corresponds to the simplified version of Gurtin-Murdoch model where only the in-plane elastic constants are considered.
- Model-3 represents the full version of Gurtin-Murdoch model where both the in-plane elastic constants and the residual surface tension are considered.

The numerical results are obtained using the three meshes as indicated in Figure 4.14(d) to confirm the convergence of numerical solutions. The convergence study of the crack sliding displacement (CSD) and the shear stress σ_{23} in the vicinity of the crack front along the minor-axis are reported in Figure 4.19. It can be observed from these results that the proposed technique yields converged solutions for both the CSD and the shear stress.

The Normalized CSDs and the normalized shear stresses σ_{23}/τ_0 near the crack front along the minor-axis are presented in Figure 4.20 for three aspect ratios $a/b=1, 2, 3$ and for three models to show the influence of the surface stresses on responses of mixed-mode cracks. Numerical results shown in Figure 4.20(a) indicate that solutions of the CSDs predicted by model-2 and model-3 are almost identical, whereas solutions of shear stresses σ_{23} for this particular case (see Figure 4.20(b)) are slightly different. When compared to the classical solution (model-1), it can be easily recognized that the surface stresses (especially the in-plane elasticity constants) significantly reduce the CSDs and the shear stresses in the neighborhood of the crack front. This confirms that presence of the surface stresses renders the medium much stiffer. To further examine the influence of the in-plane elastic constants (λ^s, μ^s), these

parameters are varied from 0, 0.1, 0.5 and 1 times of their initial value ($\lambda^s = 4.4939\ N/m$, $\mu^s = 2.7779\ N/m$) while the residual surface tension remains the same. The numerical study is conducted only for two aspect ratios of $a/b = 2,\ 3$ and the model-3. The normalized CSDs and the shear stresses σ_{23} in the vicinity of the crack front along the minor-axis are presented in Figures 4.21. It can be seen that the surface elastic constants (λ^s, μ^s) in Gurtin-Murdoch surface elasticity theory significantly reduce the CSD and the near-tip shear stresses, whereas the residual surface tension virtually has no influence on the solution of mixed-mode crack problems. To investigate the size-dependent behavior of the solution of mixed-mode crack problems due to the presence of the surface stresses, the elliptical crack of the aspect ratio $a/b = 2$ is examined for different sizes of the minor semi-axis $b_0 = 0.5, 1.0, 10$. Results of the CSDs and the shear stresses in the vicinity of the crack-front along the minor-axis are shown in Figure 4.22. It can be seen that the normalized CSDs and the normalized shear stresses along the minor-axis predicted by model-2 and model-3 are size-dependent. Once again, this is in contrast with the classical case (i.e., without the surface stress effects) where the solutions are essentially size-independent upon proper normalization. When the crack-size decreases, the influence of surface stresses on the predicted responses becomes more significant.

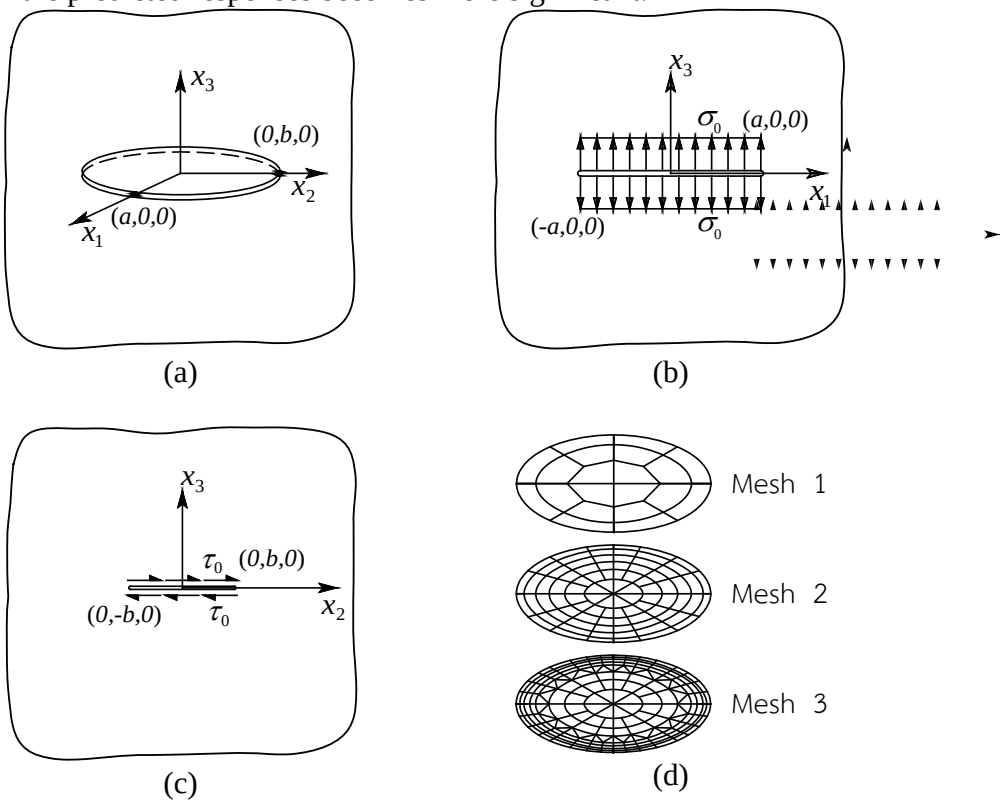

Figure 4.14 (a) Schematic of an elliptical crack embedded in an isotropic, linear elastic infinite medium; (b) both surfaces of the crack subjected to uniformly distributed normal traction $t_3^+ = -t_3^- = \sigma_0$; (c) both surfaces of the crack subjected to uniformly distributed shear traction $t_2^+ = -t_2^- = \tau_0$; (d) meshes used in the analysis

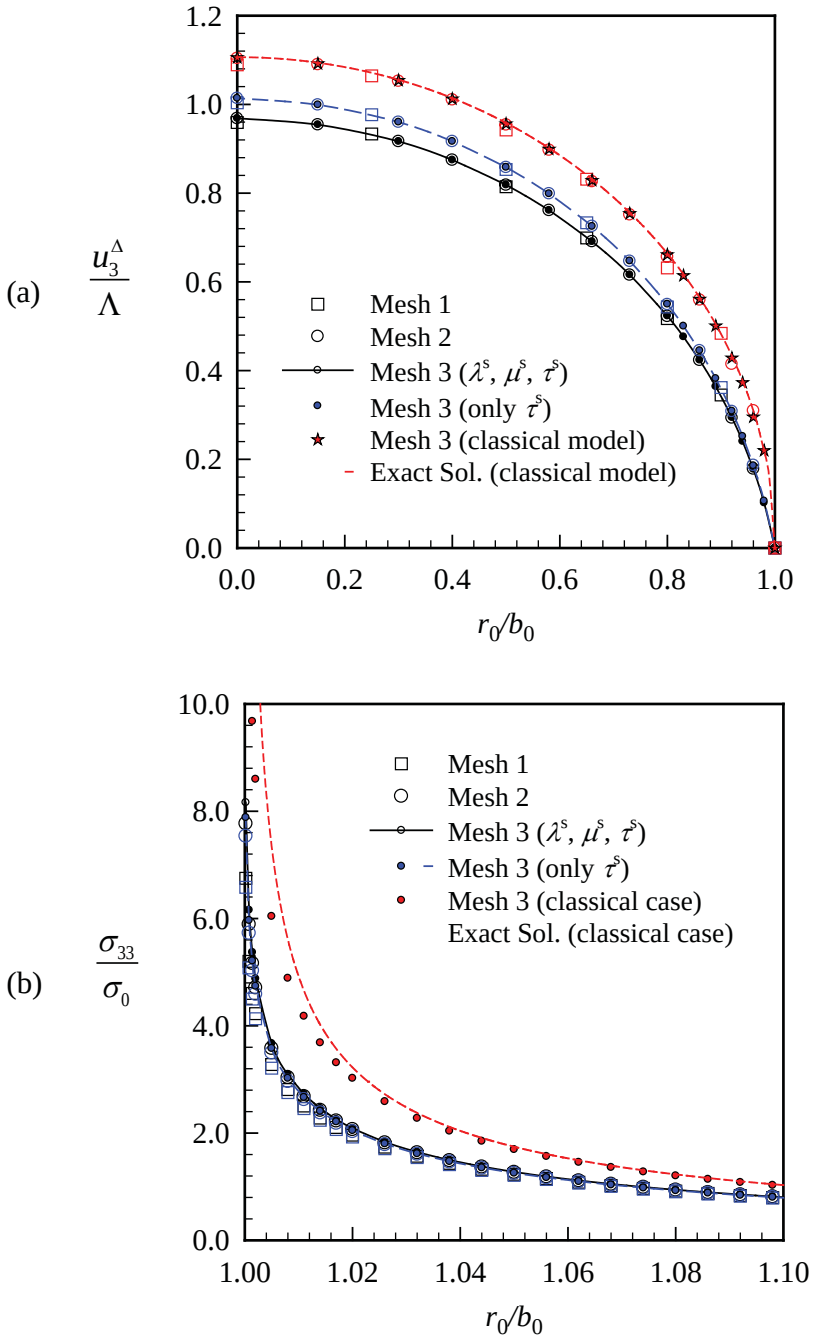

Figure 4.15 Convergence study of an elliptical crack under uniformly distributed normal traction for three different models and the aspect ratio $a/b=2$, for $E=107\,GPa$, $\nu=0.33$, $\lambda^s=4.4939\ N/m$, $\mu^s=2.7779\ N/m$ and $\tau^s=0.6056\ N/m$: (a) normalized crack opening displacements along minor-axis and (b) normalized near-tip vertical stresses along the minor-axis

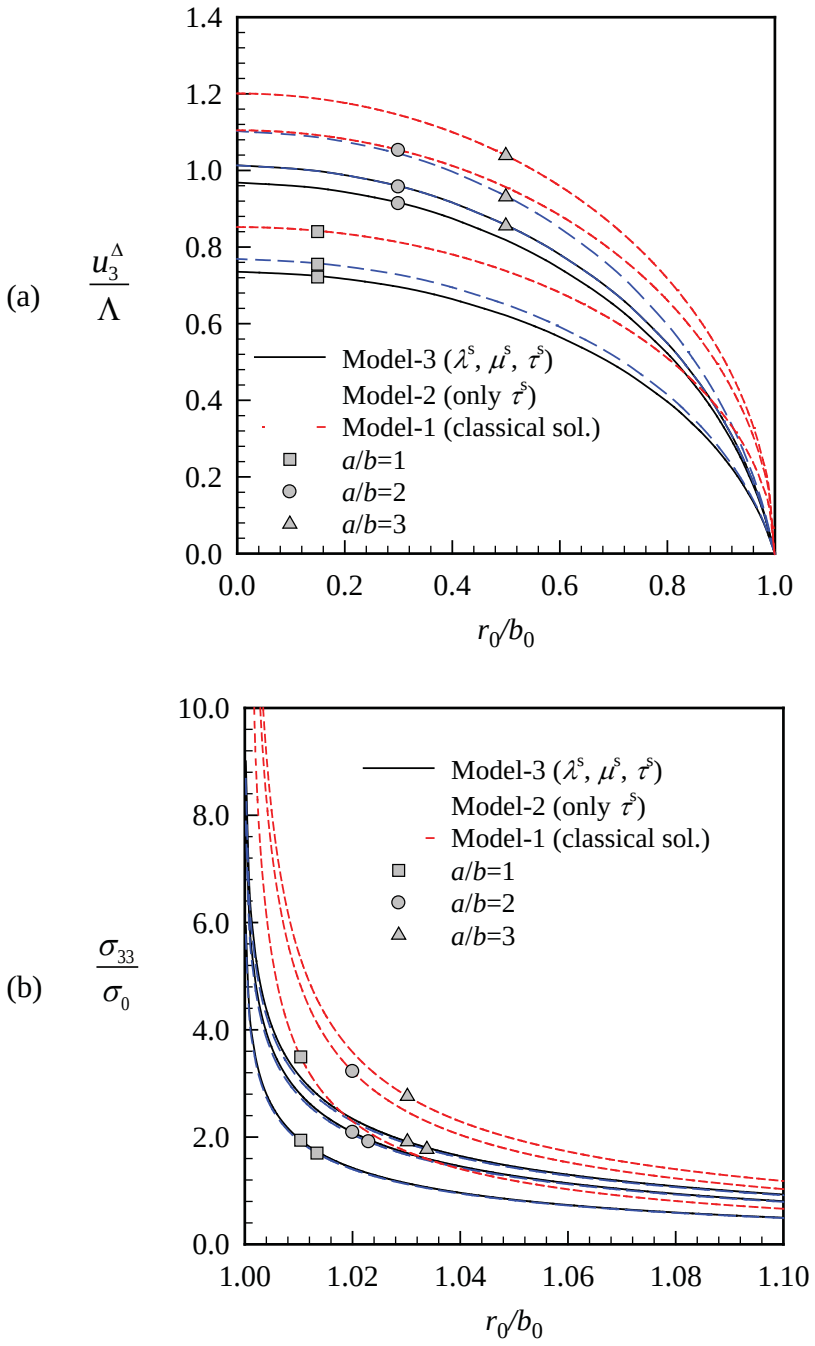

Figure 4.16 Comparison of results of an elliptical crack under uniformly distributed normal traction for three different models and three different aspect ratios $a/b = 1,\ 2,\ 3$, for $E = 107\,GPa$, $\nu = 0.33$, $\lambda^s = 4.4939\ N/m$, $\mu^s = 2.7779\ N/m$ and $\tau^s = 0.6056\ N/m$: (a) normalized CODs along minor-axis and (b) normalized near-tip vertical stresses along minor-axis obtained by using mesh-3

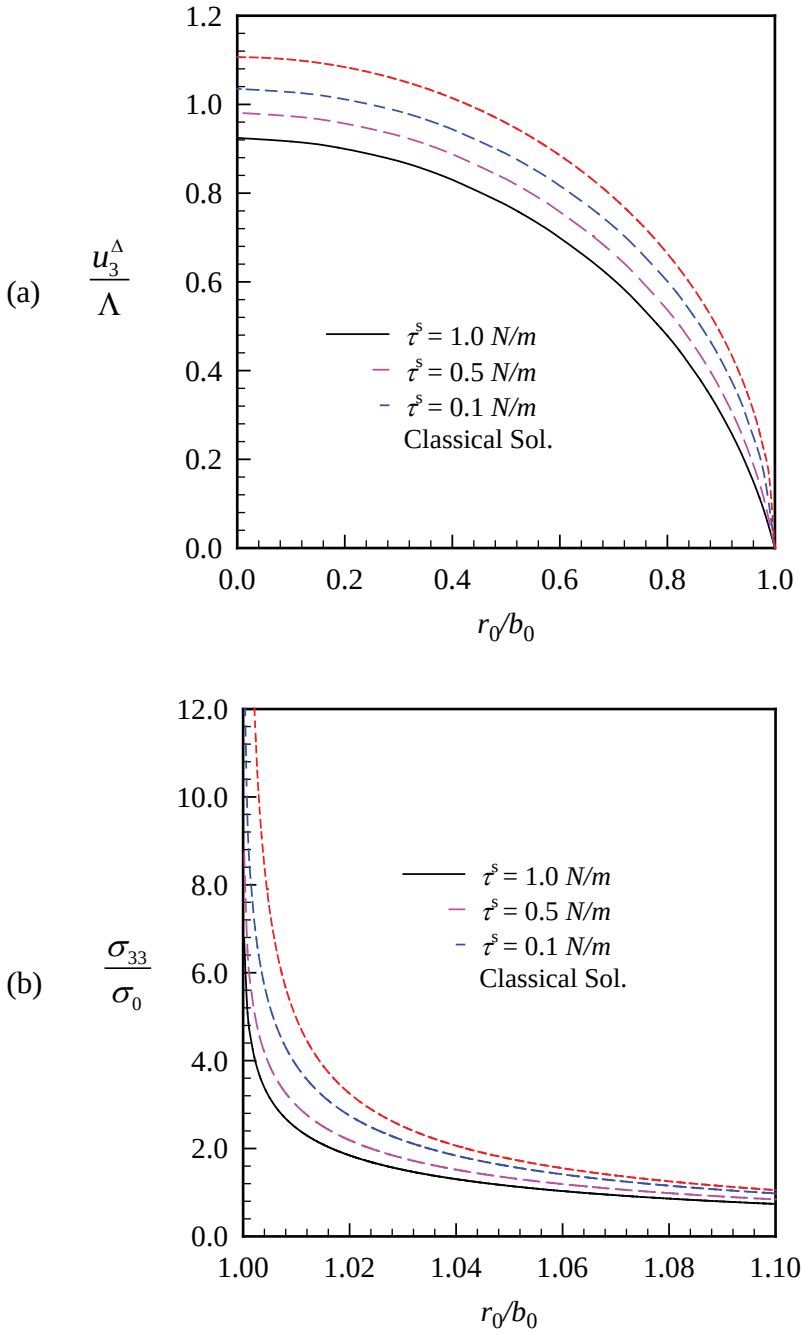

Figure 4.17 Elliptical crack under uniformly distributed normal traction for the model-3 with the aspect ratio $a/b = 2$ and different values of the residual surface tension τ^s, for $E = 107\,GPa$, $\nu = 0.33$, $\lambda^s = 4.4939\ N/m$, $\mu^s = 2.7779\ N/m$: (a) normalized CODs along the minor axis and (b) normalized near-tip vertical stresses along the minor axis obtained by using mesh-3

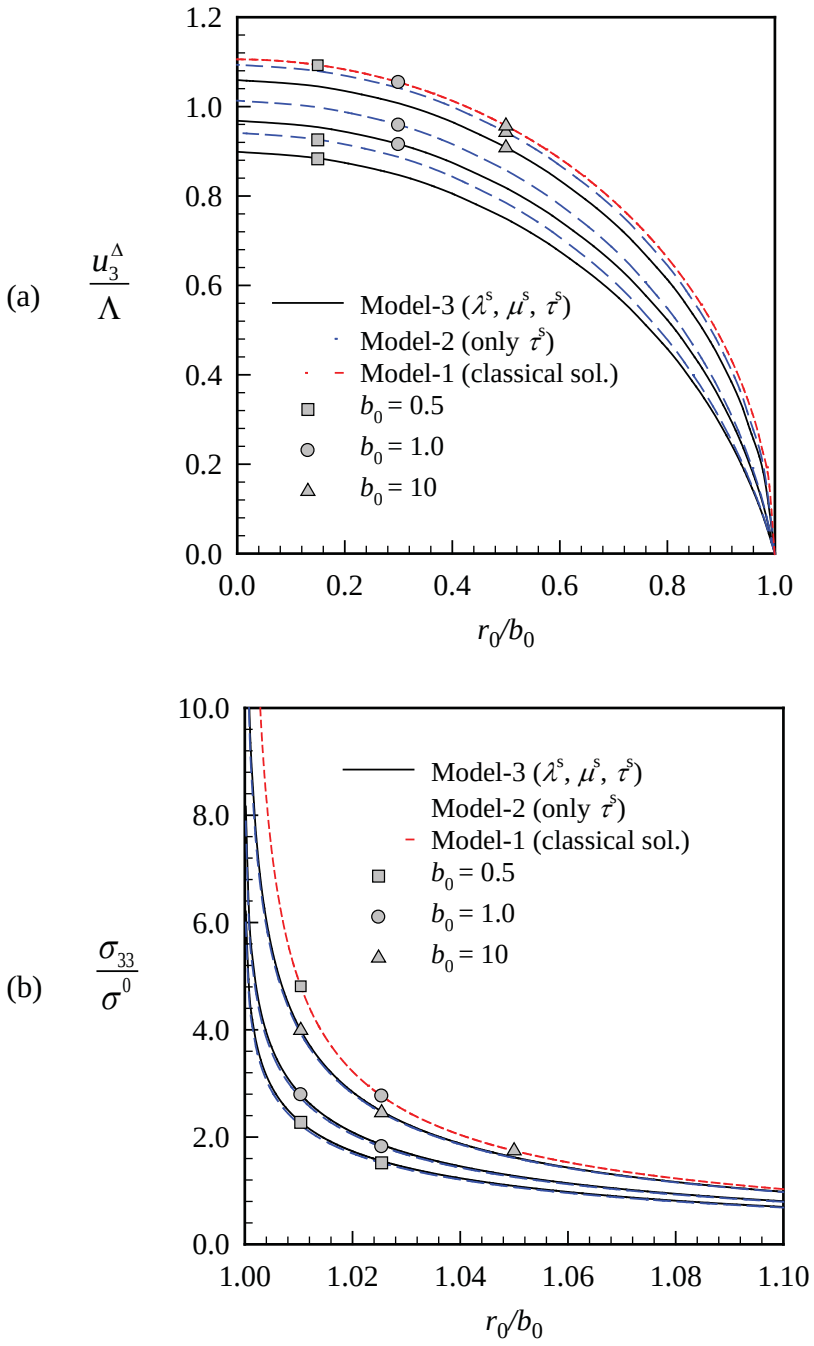

Figure 4.18 Elliptical crack under uniformly distributed normal traction for three different models with different minor semi-axes $b_0 = b/\Lambda = 0.5, 1.0, 10$ and the aspect ratio $a/b = 2$, for $E = 107\,GPa$, $\nu = 0.33$, $\lambda^s = 4.4939\ N/m$, $\mu^s = 2.7779\ N/m$ and $\tau^s = 0.6056\ N/m$: (a) normalized CODs along the minor axis and (b) normalized near-tip vertical stresses along the minor-axis obtained by using mesh-3

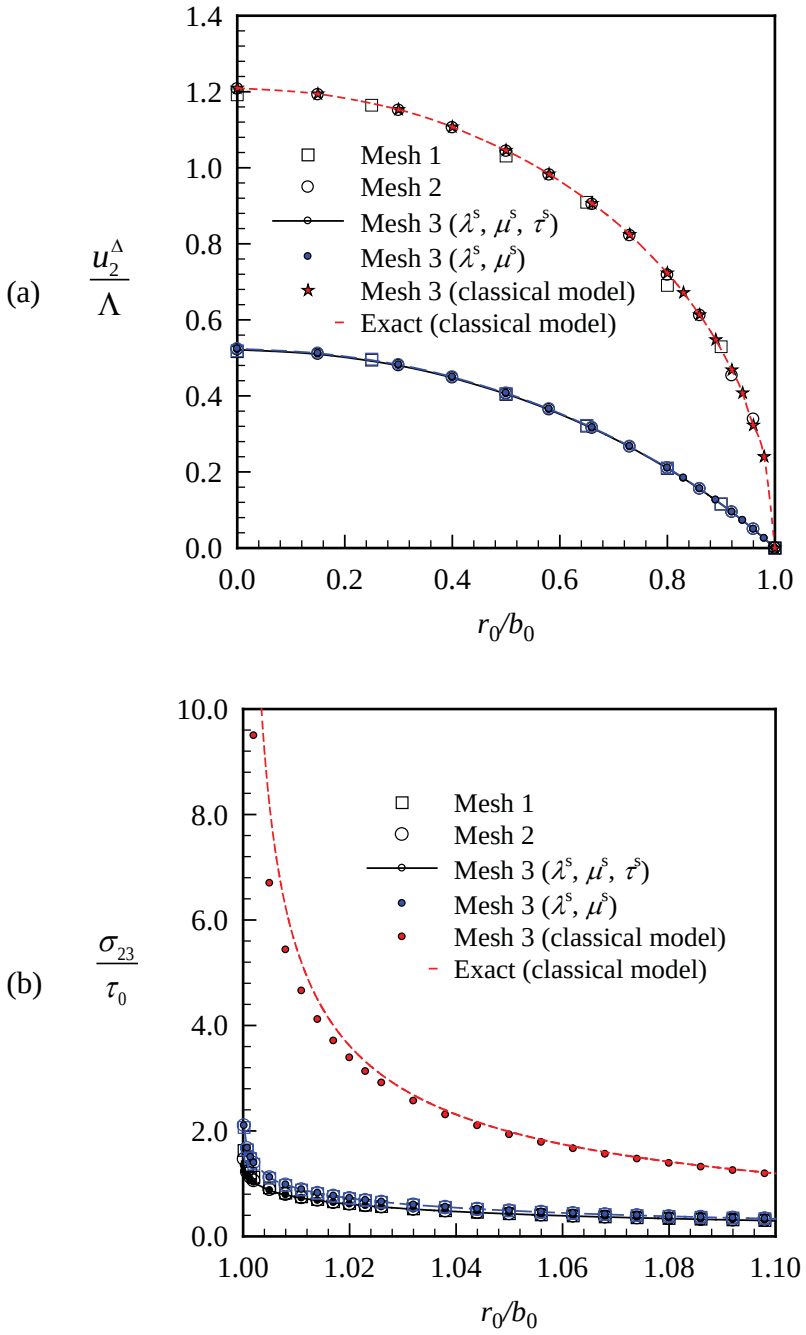

Figure 4.19 Convergence study of an elliptical crack under uniformly distributed shear traction in the x_2-direction with the aspect ratio $a/b = 2$, for $E = 107\,GPa$, $\nu = 0.33$, $\lambda^s = 4.4939\ N/m$, $\mu^s = 2.7779\ N/m$ and $\tau^s = 0.6056\ N/m$, for three different models: (a) normalized CSDs along the minor axis and (b) normalized near-tip shear stresses σ_{23} along the minor-axis

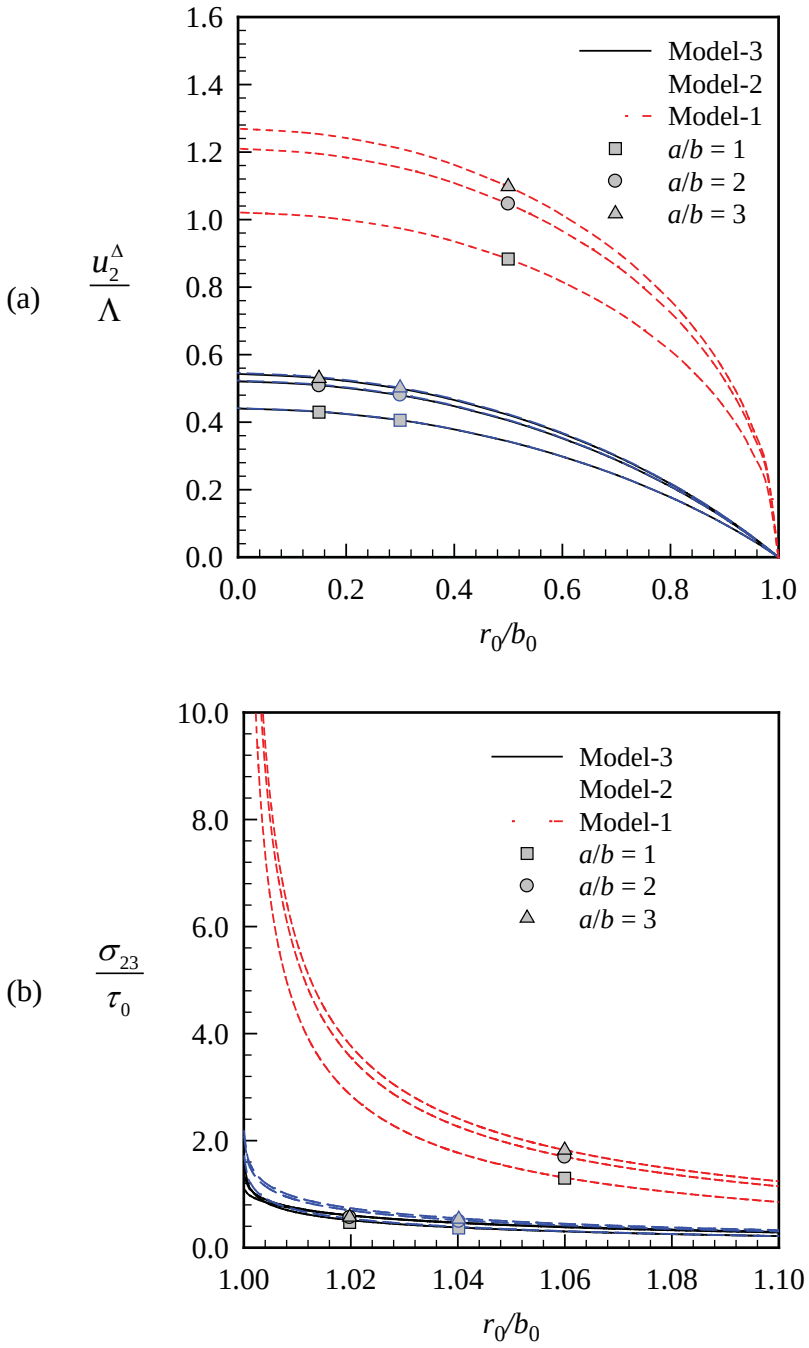

Figure 4.20 Elliptical crack under uniformly distributed shear traction in the x_2-direction with the aspect ratio $a/b = 1, 2, 3$, for $E = 107\,GPa$, $\nu = 0.33$, $\lambda^s = 4.4939\ N/m$, $\mu^s = 2.7779\ N/m$, $\tau^s = 0.6056\ N/m$ and for model-1, model-2, model-3: (a) normalized CSDs along the minor-axis and (b) normalized near-tip shear stresses σ_{23} along the minor-axis obtained by using mesh-3

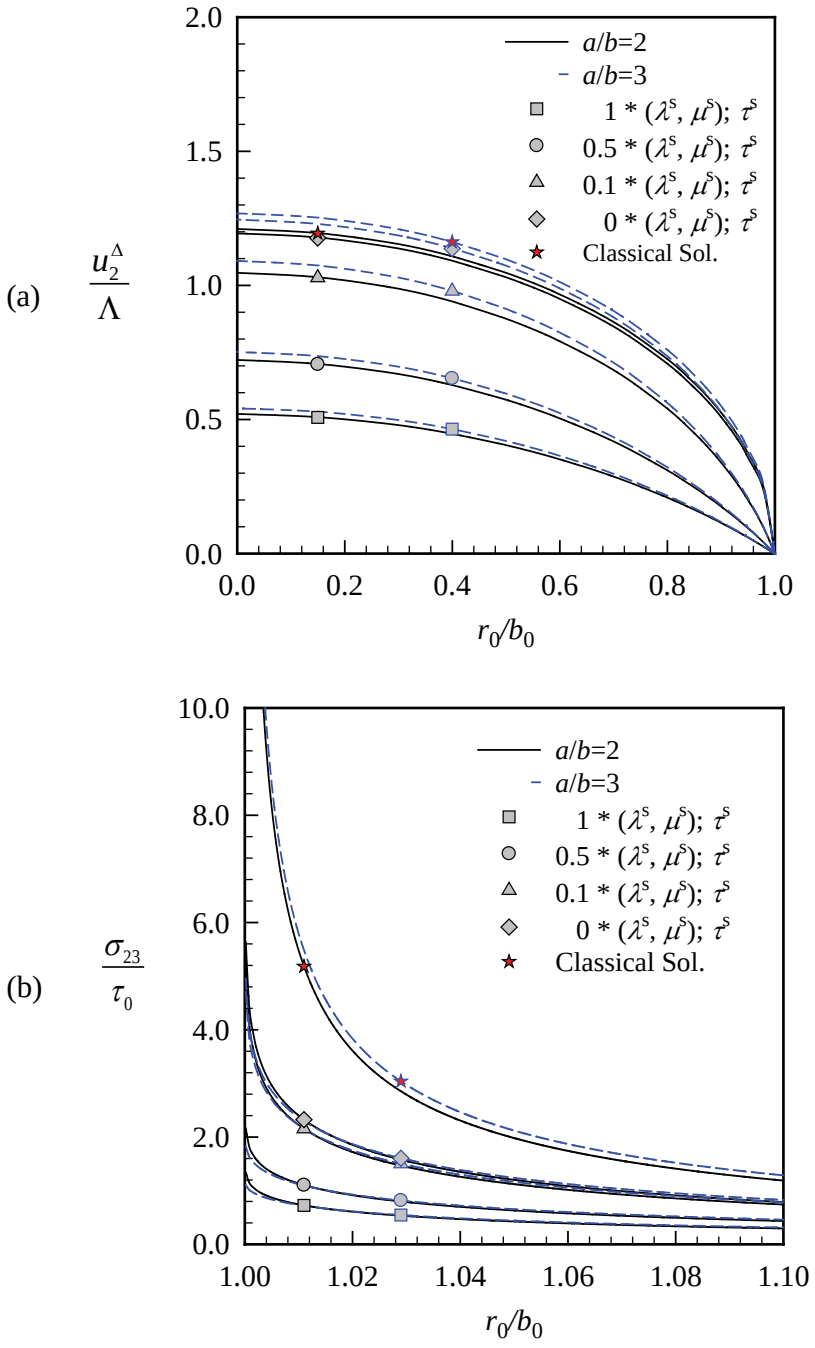

Figure 4.21 Elliptical crack under uniformly distributed shear traction in the x_2-direction for the model-3, the aspect ratios $a/b = 2,\ 3$ and different values of (λ^s, μ^s) ranging from 0 to 1 time their initial values $(\lambda^s = 4.4939\ N/m,\ \mu^s = 2.7779\ N/m)$, for $E = 107\,GPa$, $\nu = 0.33$, $\tau^s = 0.6056\ N/m$: (a) normalized CSDs along the minor-axis and (b) normalized near-tip shear stresses σ_{23} along the minor-axis obtained by using mesh-3

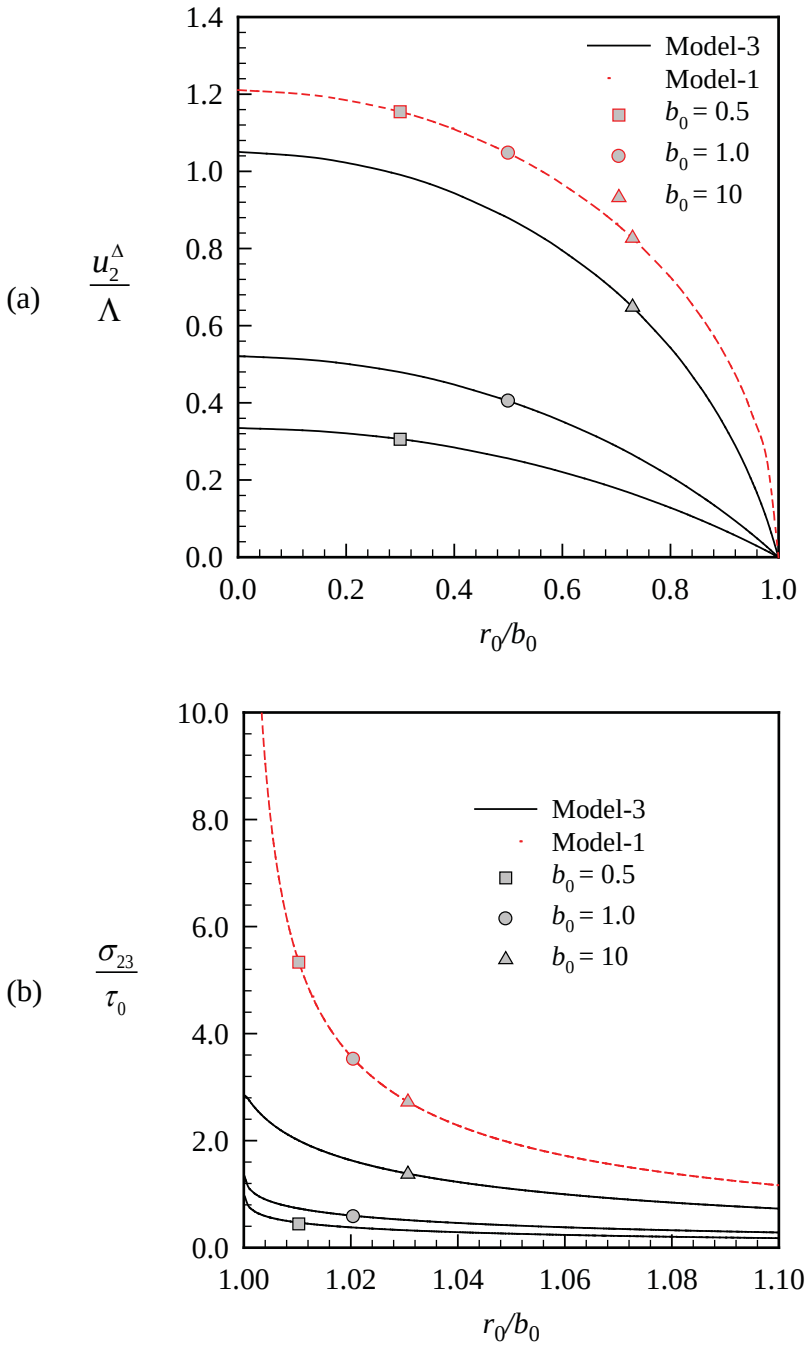

Figure 4.22 Elliptical crack under uniformly distributed shear traction in the x_2-direction for $a/b = 2$, $b_0 = b/\Lambda = 0.5,\ 1.0,\ 10$, for $E = 107\,GPa$, $\nu = 0.33$, $\lambda^s = 4.4939\ N/m$, $\mu^s = 2.7779\ N/m$, $\tau^s = 0.6056\ N/m$ and model-1, model-3: (a) normalized CSDs along the minor-axis and (b) normalized near-tip shear stresses σ_{23} along the minor-axis obtained by using mesh-3

4.3.4 Two co-planar penny-shaped cracks

Finally, to demonstrate another feature of the proposed FEM-SGBEM technique in modeling multiple cracks, a problem of two interacting penny-shaped cracks embedded in an unbounded domain with consideration of the surface stress effects is investigated in this section.

Consider a pair of co-planar, identical penny-shaped cracks of radius a embedded in an isotropic, linear elastic unbounded domain as shown in Figure 4.23(a). The distance between the centers of the two cracks is denoted by h. Both cracks are subjected to the self-equilibrated, uniformly distributed normal traction $t_3^+ = -t_3^- = \sigma_0$. Young's modulus and Poisson's ratio for the bulk material are taken as $E = 107\ GPa$ and $\nu = 0.33$ respectively. The influence of the interaction between the two cracks on the maximum crack opening displacement (COD) and on the stress in the vicinity of the crack front at a particular point A (see Figure 4.23(a)) is investigated. To investigate the size-dependent behavior, two values of the normalized radius of the crack, $a_0 = a/\Lambda = 1$ and 10 are considered. Three meshes shown in Figure 4.23(b) are used to test the convergence of numerical solutions. For this particular problem, the surface stress effects are modeled by the simplified version of Gurtin-Murdoch surface elasticity model with only the residual surface tension ($\tau^s = 0.6056\ N/m$) being treated.

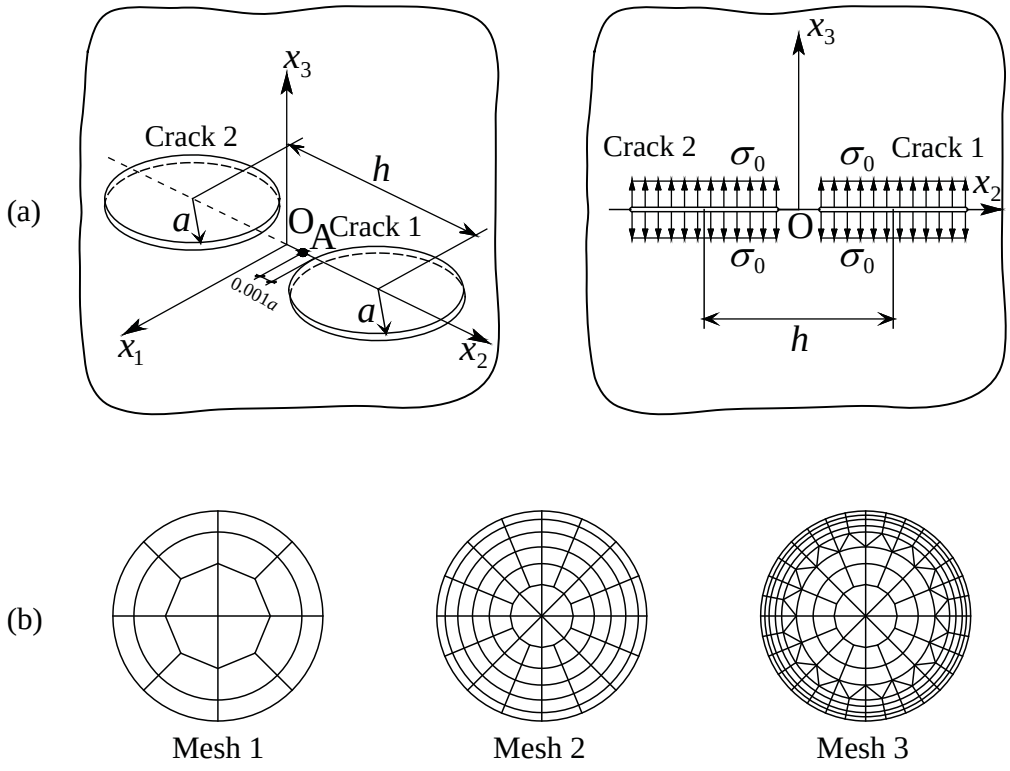

Figure 4.23 (a) Schematic of a pair of penny-shaped cracks of radius a embedded in an isotropic, linear elastic infinite medium subjected to uniformly distributed normal traction $t_3^+ = -t_3^- = \sigma_0$ and (b) meshes adopted for each crack. Mesh-1: 20 elements and 77 nodes. Mesh-2: 88 elements and 297 nodes. Mesh-3: 216 elements and 665 nodes.

To examine the convergence of the numerical solutions, the normalized CODs and the vertical stresses in the vicinity of the crack front of one of the penny shaped cracks (crack 1) with the normalized radius $a_0 = 1$ are obtained for the three meshes and results are reported in Figure 4.24 for $h/a = 2.2$. The results also are compared with classical solutions, which can be found in Fabrikant (1989). It is seen that converged results of the normalized CODs and the near-tip vertical stresses are obtained. The residual surface tension significantly lowers the crack opening displacement and the near-tip vertical stresses.

To study the interaction between the two coplanar cracks, the normalized maximum COD and the normalized vertical stress at the point A are plotted for different values of h/a in Figures 4.25-4.26 for two cases of radius $a_0 = a/\Lambda = 1$ and 10 with three values of the residual surface tension $\tau^s = 0$ (classical solution), $\tau^s = 0.6056\ N/m$, and $\tau^s = 1\ N/m$. It can be seen in Figure 4.25(a) that the maximum CODs and the vertical stresses in the neighborhood of the crack front decreases when the residual surface tension increases similar to what observed from other examples. The bulk medium becomes much stiffer with the presence of the residual surface tension for cracks under mode-I loading conditions. It can also be seen from Figures 4.25 and 4.26 that the interaction between the two cracks for the classical case is size-independent (i.e. solutions of the two cracks converge asymptotically to that of the single crack in the identical manner). On the contrary, when the residual surface tension is incorporated in the mathematical model, the size-dependent behavior can be clearly observed by comparing the results in Figures 4.25(a), (b) with the results in Figures 4.26(a), (b) respectively. The decrease in the crack size also reduces the interaction between the two cracks.

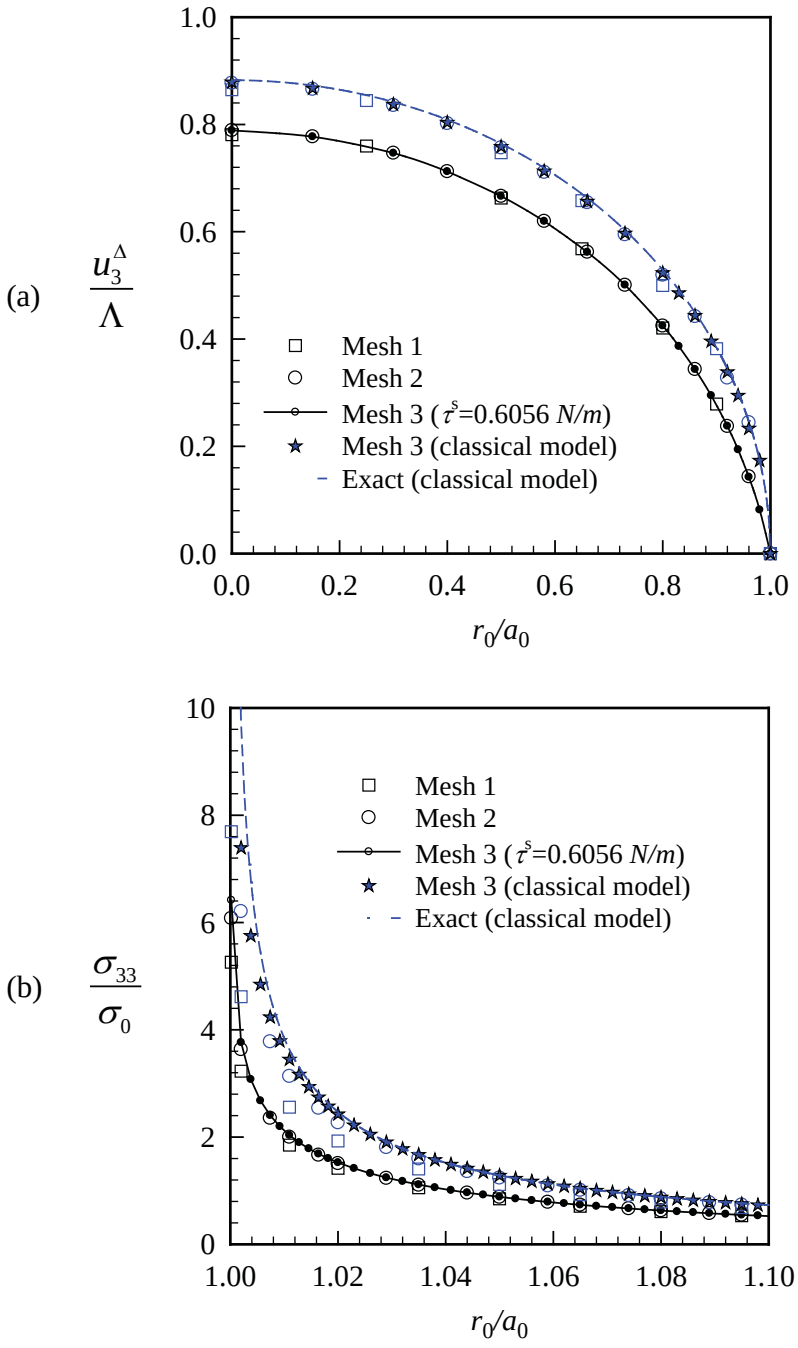

Figure 4.24 A pair of coplanar identical penny-shaped cracks with radius $a_0 = 1$ and $h/a = 2.2$ under uniformly distributed normal traction, for $E = 107\,GPa$, $\nu = 0.33$, $\lambda^s = 4.4939\ N/m$, and residual surface tension $\tau^s = 0.6056\ N/m$: (a) normalized CODs of crack 1 and (b) normalized near-tip vertical stresses of crack 1

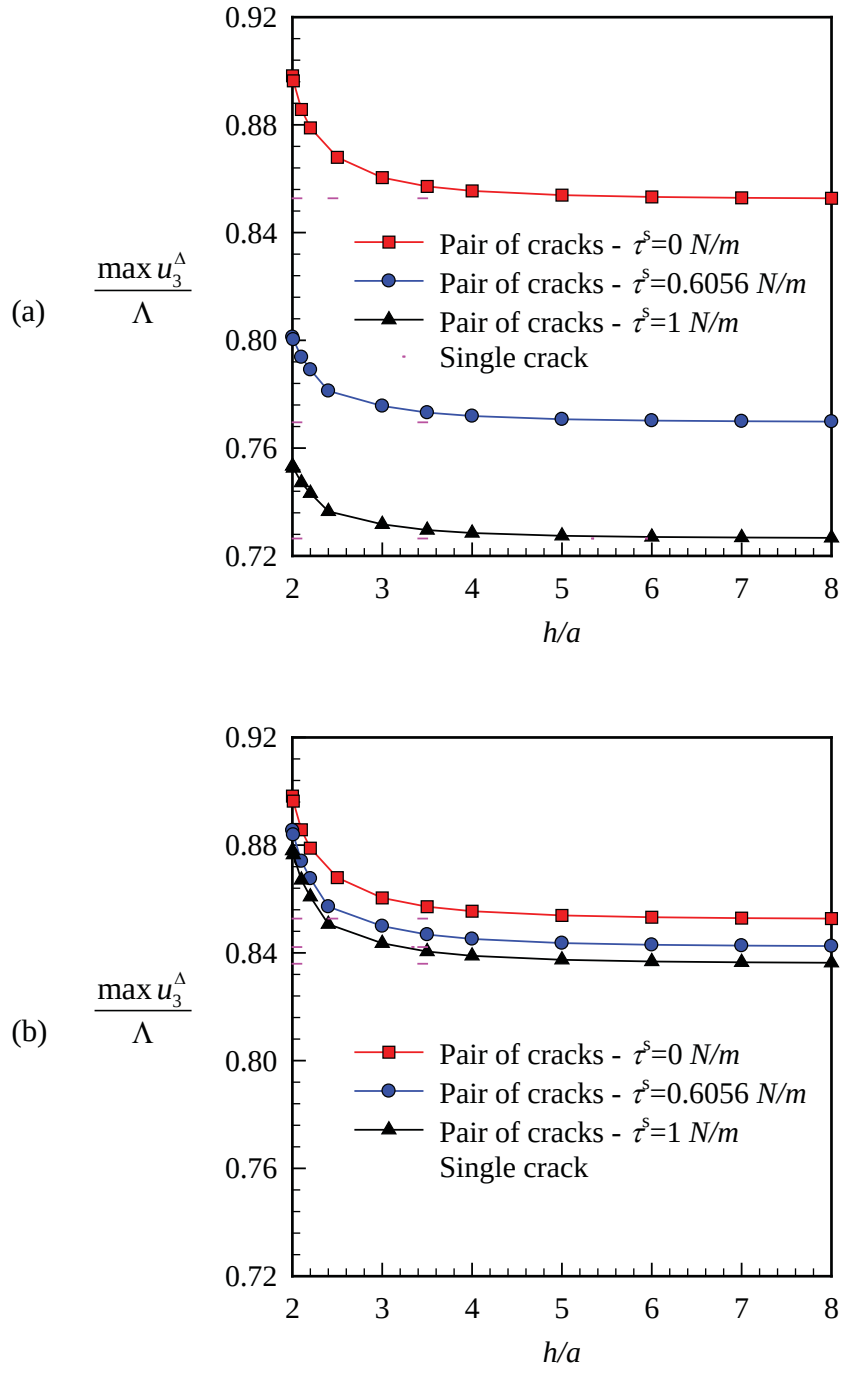

Figure 4.25 Normalized maximum crack opening displacements for a pair of coplanar identical penny-shaped cracks under uniformly distributed normal traction with different values of h/a, for $E=107\,GPa$, $\nu=0.33$, $\lambda^s=4.4939\ N/m$, and residual surface tension $\tau^s=0.6056\ N/m$: (a) $a_0=1$ and (b) $a_0=10$ obtained by using mesh-3

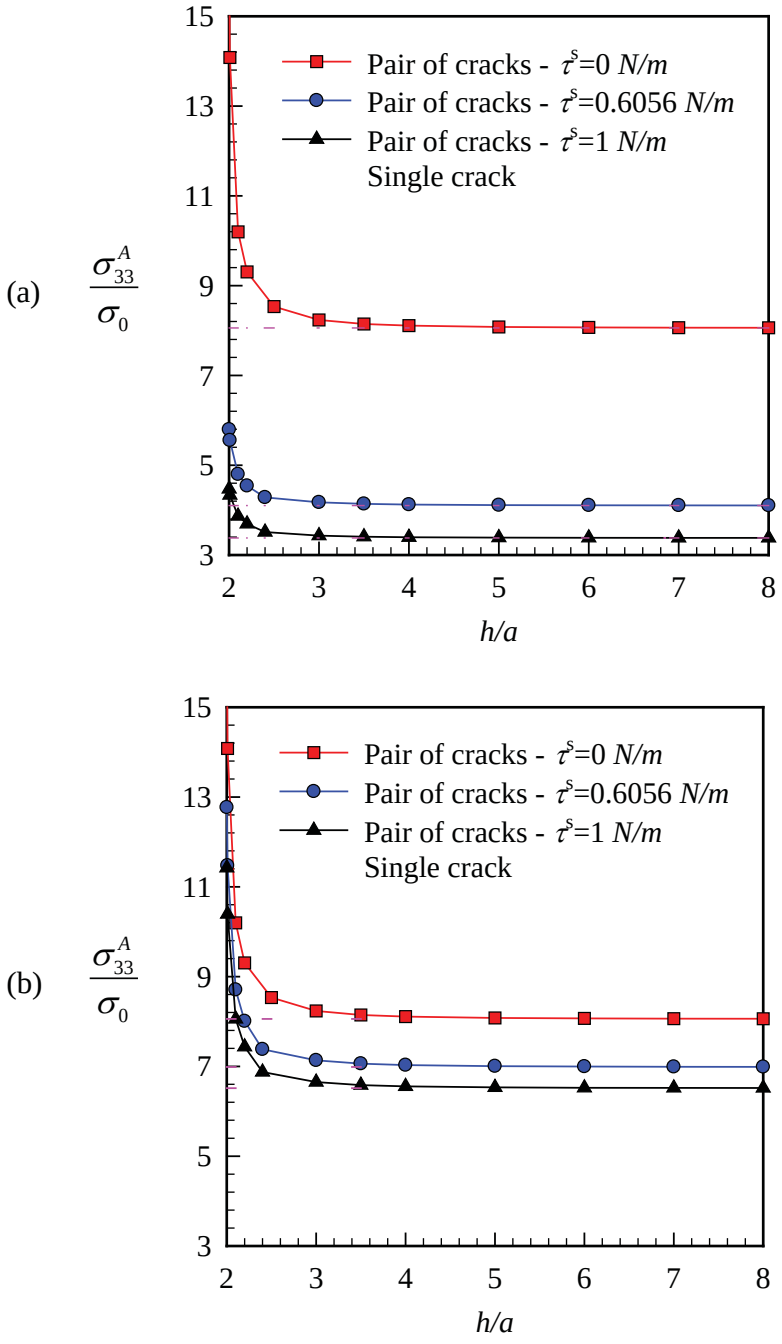

Figure 4.26 Normalized vertical stress at the point A for a pair of coplanar identical penny-shaped cracks under uniformly distributed normal traction with different values of h/a, for $E = 107\,GPa$, $\nu = 0.33$, $\lambda^s = 4.4939\ N/m$, and residual surface tension $\tau^s = 0.6056\ N/m$: (a) $a_0 = 1$ and (b) $a_0 = 10$ obtained by using mesh-3

CHAPTER V

CONCLUSIONS AND REMARKS

This chapter summarizes both analytical and numerical techniques established in the present investigation for solving fundamental problems in solid mechanics (e.g., elastic layers under surface loading, nano-indentations, and nano-sized cracks) with consideration of the nano-scale influence. Major findings regarding to both computational performance of the developed techniques and extensive parametric study on the influence of the surface stresses and size-dependency of the predicted solutions are presented. Limitations of the current development and the possible extensions for each particular problem are also indicated.

5.1 Elastic Layer under Surface Loading

A complete analytical solution of a three-dimensional, infinite elastic layer under the action of axisymmetric normal and tangential surface loadings with consideration of the surface energy effect has been derived. A novel feature of the present study is the use of a complete version of Gurtin-Murdoch constitutive relation to model the free surface of the layer. In solution procedure, Love's strain potential technique along with Hankel integral transform are applied to obtain the general solution for the bulk whereas the surface equations and conditions at the rigid base supply sufficient boundary conditions to determine all arbitrary constants. The displacement and stress fields within the bulk have been obtained via a selected efficient numerical quadrature. Once the obtained general solutions were verified by comparing with available benchmark solutions, extensive parametric study has been carried out to gain insights into the nano-scale influence and investigate the size dependency. Moreover, the three fundamental solutions corresponding to normal concentrated load, normal ring load, and tangential ring load, which constitute the basis for solving nano-indentations problems, have been constructed.

Results from extensive parametric studies have confirmed the significance of surface energy effects and the necessity to properly treat such influence in the continuum-based model. In the region close to the surface, the presence of the surface stresses exhibits very strong influence on both the displacement and stress fields. Magnitudes of field quantities obtained from models accounting for the surface energy effects are generally less than those obtained from the classical model. The presence of the surface energy renders the layer much stiffer than that of the classical case. This is due to the fact that not the entire loading that transfers directly into the bulk but part of it is carried by the surface through the equilibrium of the surface and the membrane-like action. Such influence also depends on the length scale of the problem, i.e. the influence of surface stresses becomes significant when the length scale is comparable to the intrinsic length of the surface. Moreover, it is worth pointing out that such behavior of the out-of-plane responses due to the normal traction are more apparent in the model that integrates the out-of-plane contribution of the residual surface tension into the analysis. This additionally confirms the necessity to treat such crucial contribution in the modeling of soft elastic solids and nano-scale problems.

In addition, the radial and vertical surface displacements of a layer under either a normal ring load or a tangential ring load, predicted by a model employed in the present study (i.e. the complete Gurtin-Murdoch surface elasticity model that includes the out-of-plane contribution of

the residual surface tension), are finite everywhere. If the out-of-plane term is neglected, the predicted vertical displacement due to the normal ring load is still singular at the location where the load is applied. For the case of a normal concentrated load acting to the origin, the vertical displacement obtained from both classical model and model incorporating the surface stress effects is singular at the applied load location whereas only the radial displacement obtained from a model accounting for the out-of-plane term is finite.

Due to the three fundamental solutions derived in the present study, frictionless indentation problems with arbitrary indentor profiles, axisymmetric frictionless indentation problems, axisymmetric indentation problems with the presence of friction, and axisymmetric, fully-bonded indentation problems can now be fully investigated. In addition, the formulation can further be generalized to treat the following two cases, namely, multiple layers under axisymmetric surface loading and a single layer under non-axisymmetric surface loading.

5.2 Nano-indentation Problem

The complete solutions of an axisymmetric rigid frictionless indentation acting on an isotropic, elastic half-space with consideration of surface energy effects by employing a complete version of Gurtin-Murdoch surface elasticity model have been fully investigated. Based on the axisymmetric solutions in term's of Love's strain potential together with the application of Hankel integral transform technique, the mixed boundary conditions on the surface of a half-space both inside and outside the contact region can be reduced to a set of dual integral equations, which can be further equivalently transformed into a single Fredholm integral equation of the second kind. To obtain the solution of this single integral equation, various numerical schemes have been employed in the present study to enhance both the accuracy and computational efficiency of the solutions. First, standard approximation of a solution form and a collocation technique are adopted to discretize the Fredholm integral equation. After a system of linear algebraic equations with non-symmetric, dense coeffient matrix is obtained from the discretization, either LU-decomposition or stabilized bi-conjugate gradient method has been applied to solve such a system. Finally, complete elastic fields within the half-space are obtained by applying the Hankel innversion along with employing standard Gaussian quadrature. For smooth-contact punches, a physically admissible condition associated with the continuity of vertical stress at the contact boundary is employed to determine the unknown contact radius for a given indentation depth.

The numerical procedures have been implemented as an in-house computer code to determine the complete elastic fields of both non-smooth contact and smooth contact punches. The validity of the current formulation and accuracy of the numerical implementations have been confirmed by comparing with the classical case in which exact solutions exist. As anticipated, obtained numerical results have demonstrated that the influence of surface energy effects becomes larger when the size of the punch is smaller especially in the region very near the punch. In addition, material behaves stiffer due to such effects. It is interestingly remarked that the distribution of contact pressure for two punch profiles (i.e. flat-ended and paraboloidal punches) obtained from the current model exhibits significant discrepancy. In particular, the contact pressure obtained from the current model for the flat-ended punch is considerable lower than the classical case and that by Zhao (2009) whereas, for the paraboloidal punch, the current model predicts much higher contact pressure than the other two models. However, for both types of contacts, elastic fields obtained from the current model indicate strong influence of the surface free energy for region relatively close to the punch. Such influence decays rapidly for the vertical

stresses but, for the vertical displacements, it exhibits slower decay as the depth increases. Still, the sigularity at the boundary has been observed for the case of a non-smooth contact. Size-dependent behavior has also been presented to confirm the essence of accounting surface energy effects on analysis of material properties at nanoscale and soft elastic solids due to their high surface to volume ratio.

The boundary value problem considered in the present study is restricted only to the axisymmetric indentation on an isotropic, elastic half-space. In addition, the punch is also assumed to be rigid with no friction. The generalization to alleviate all these limitations should be potentially useful to enhance the understanding of nano-mechanics and the mechanics of soft solids in a broader context. For instance,

(1) a punch profile can be generalized to non-axisymmetric one and an elastic half-space can also be replaced by a more general film/substrate system;
(2) A constitutive model for an elastic half-space can be generalized to treat both anisotropic linearly elastic and inelastic materials. The ability to treat material anisotropy and nonlinear material behavior will enhance the modeling capability for simulating more practical problems associated with characterization of material properties using nano-indentations.

A proper friction model can also be incorporated to treat the interaction between a punch and an elastic half-space. It is known that frictionless contact is very idealistic and can hardly be found in practices.

5.3 Nano-crack Problem

A computationally efficient numerical technique capable of modeling planar cracks in three-dimensional, linearly elastic media incorporating the influence of surface stresses has been established. In the formulation of the boundary value problem, the domain decomposition technique has been adopted to separate a cracked body into three parts: (i) an infinitesimally thin layer of materials on the upper crack surface, (ii) an infinitesimally thin layer of materials on the lower crack surface, and (iii) the remaining bulk medium with those two layers being removed. The classical theory of isotropic linear elasticity has been employed to form a system of governing equations of the bulk cracked medium in terms of weakly singular, weak-form boundary integral equations for the sum of the displacement and the jump of the traction across the crack surface of the bulk. Such governing equations possess several desirable features such as the weakly singular nature, simplicity to treat an infinite body and remote loading condition, and applicability to model cracks of arbitrary shapes and under general loading conditions. For both thin layers, they have been modeled as zero-thickness, two-sided surfaces with their behavior being described by Gurtin-Murdoch surface elasticity theory. In the present study the full version of Gurtin-Murdoch model including the in-plane surface elasticity, and the residual surface tension and its simplified versions without either the in-plane surface elasticity or the residual surface tension, are both considered. The weight residual technique has been applied to derive the final weak-form statement for the surface part in terms of the same types of primary unknowns as those appearing in the bulk equations. The strong continuity condition of the displacement and traction on the interface of the surface and the bulk medium has been enforced to obtain the fully-coupled system of equations governing the whole medium.

Standard FEM-SGBEM coupling procedure has been implemented to construct numerical solutions of the final coupled system of governing equations. In the discretization, continuous element-based interpolation functions have been employed everywhere in the

approximation of trial and test functions. In the present study, it has been postulated based on the physical evidence and previous investigations that the presence of surface stresses renders the stress along the crack front of the bulk medium finite. As the direct consequence, standard C^0-elements have been employed everywhere in the discretization of all primary unknowns on the crack surface when the full version of Gurtin-Murdoch model has been considered. For the special cases, when the simplified version of Gurtin-Murdoch model without either the residual surface tension or the in-plane surface elasticity has been applied, standard C^0-elements have been employed everywhere in the discretization except in a local region along the crack front where either the jump of the out-of-plane displacement or the jump of the in-plane displacement is discretized by special crack-tip elements respectively to enhance the capability of the technique to capture the near-tip field. In the construction of a coefficient matrix, standard Gaussian quadrature has been adopted to evaluate all involved regular integrals whereas such quadrature supplemented by a family of suitable transformation has been employed to efficiently compute both weakly singular and nearly singular integrals. The final system of linear algebraic equations has been solved by an efficient linear solver.

Extensive numerical experiments have been conducted and obtained results have been compared with available benchmark solutions to validate both formulation and numerical implementations of the proposed technique. From a convergence study of numerical solutions, it has been found that the FEM-SGBEM coupling technique yields converged solutions with only weak dependence on the mesh refinement. In addition, the capability and the robustness of the proposed method to model relatively complicated fracture problems with the treatment of the nano-scale influence have been confirmed via various examples involving mixed-mode loading conditions and interacting cracks.

From an extensive numerical study aiming to examine the influence of the surface stresses present at the crack surface on elastic responses of the bulk cracked medium, it has been found that the residual surface tension and the in-plane surface elasticity appearing in Gurtin-Murdoch model both play a vital role on the prediction of field responses, and can substantially deviate results from the classical solutions. In general, the results from the simulations using either the full or simplified version of Gurtin-Murdoch have indicated that the surface stresses tend to increase the local material stiffness in the vicinity of the crack, in particular, the predicted relative crack-face displacements and near-tip stresses are significantly lower than those obtained by the classical model without the contribution of the surface effects. In addition, the size-dependent behavior of the elastic responses predicted by models incorporating either the full or simplified version of Gurtin-Murdoch has been observed. In particular, as the characteristic size of the crack reduces to the intrinsic length scale of materials (in the range of nano-scale for metals), the influence of both the residual surface tension and the in-plane surface elasticity becomes more prominent.

Results from the investigation of pure mode-I crack problems have indicated that the residual surface tension plays an important role on the reduction of the crack-opening displacement and the vertical stress in the vicinity of the crack front from the classical solution whereas the in-plane surface elasticity exhibits insignificant effect on such quantities. This finding suggests that the simplified version of Gurtin-Murdoch model with only the residual surface tension being treated can be used sufficiently in the modeling of mode-I crack problems to simplify the calculations. On the contrary, for cracks subjected to pure in-plane loading conditions (i.e. mode-II and mode-III loading conditions), the influence of the in-plane surface elasticity on major in-plane quantities such as the crack sliding displacement and the mode-II and

mode-III shearing stresses is much more prominent than that of the residual surface tension. As a result, the simplified version of Gurtin-Murdoch model without the residual surface tension yields, in general, similar results to those predicted by a full model incorporating both the residual surface tension and the surface elastic constants. However, for cracks under full mixed-mode loadings, both the residual surface tension and the in-plane surface elasticity can play a crucial role on the predicted responses, and the full version of Gurtin-Murdoch model is required.

The present study has provided an alternative computational tool based primarily on an enhanced continuum-based model that can be used to explore the fundamental behavior of nano-scale fractures. Nevertheless, the proposed numerical technique has been developed within the context where the fractures must be modeled as isolated *planar* cracks embedded in a homogeneous, isotropic, linear elastic, infinite bulk medium. To further enhance the modeling capability of the developed technique for solving a wide range of problems and obtaining more interesting fracture data, the following potential extensions are suggested:

(1) the governing equations of the surface part can be extended to treat non-planar cracks;
(2) the formulation can be generalized to treat embedded, near-surface, and surface-breaking cracks in half-space or finite bodies; and
(3) the constitutive model for bulk materials can be extended to treat material anisotropy, non-uniformity, and multi-field material behavior such as piezoelectricity; and
(4) the computation of crucial fracture data such as the T-stress along the crack front can be added.

REFERENCES

Adnan, A., Sun, C.T. (2010). Evolution of nanoscale defects to planar cracks in a brittle solid. Journal of the Mechanics and Physics of Solids **58**(7): 983-1000.

Ahlvin, R.G., Ulery, H. H. (1962). Tabulated values for determining the complete pattern of stresses, strains, and deflections beneath a uniform load on a homogeneous half space. Highway Research Board, Bulletin **342**, 1-13

Armstrong, R.W., Shin, H., Ruff, A.W. (1995). Elastic/plastic effects during very low-load hardness testing of copper. Acta Metallurgica et Materialia **43**: 1037-1043.

Barber, J.R. (1992). Elasticity. The Netherlands: Kluwer Academic Publisher.

Bathe, K.J. (1990). Finite Element Procedures, Prentice-Hall, New Jersey.

Beegan, D., Chowdhury, S., Laugier, M.T. (2007). Comparison between nanoindentation and scratch test hardness (scratch hardness) values of copper thin films on oxidised silicon substrates. Surface and Coatings Technology **201**: 5804-5808.

Blandford, G.E., Ingraffea, A.R., Liggett, J.A. (1981). Two-dimensional stress intensity factor computations using the boundary element method. International Journal for Numerical Methods in Engineering **17**(3): 387-404.

Bonnet, M. (1995). Regularized direct and indirect symmetric variational BIE formulations for three-dimensional elasticity. Engineering Analysis with Boundary Elements **15**(1): 93-102.

Bonnet, M., Maier, G., Polizzotto, C. (1998). Symmetric Galerkin Boundary Element Methods. Applied Mechanics Reviews **51**(11): 669-704.

Booker, R., Boysen, E. (2005). Nanotechnology for dummies. New Jercy: Wiley.

Boussinesq, J. (1885). Applications des Potentiels à l' Étude de l' Équilibre et du Mouvement des Solides Élastiques. Paris: Gauthier-Villars.

Buehler, M.J., Abraham, F.F., Gao, H. (2003). Hyperelasticity governs dynamic fracture at a critical length scale. Nature **426**(6963): 141-146.

Buehler, M.J., Gao, H. (2006). Dynamical fracture instabilities due to local hyperelasticity at crack tips. Nature **439**(7074): 307-310.

Burmister, D.M. (1943). The theory of stresses and displacements in layered systems and applications to the design of airport runways. Proc.Highway Res.Board **23**: 127-148.

Burmister, D.M. (1945). The general theory of stresses and displacements in layered soil systems. Applied Physics **16**: 89-96, 126-127, 296-302.

Cammarata, R.C. (1994). Surface and interface stress effects in thin films. Progress in Surface Science **46**: 1-38.

Cammarata, R.C. (1997). Surface and interface stress effects on interfacial and nanostructured materials. Materials Science and Engineering A **237**: 180-184.

Chaudhuri, P.K., Ray, S. (2003). Effects of an axisymmetric rigid punch on a nonhomogeneous transversely isotropic half-space. Australian & New Zealand Industrial and Applied Mathematics Journal **44**: 461–474.

Chen, C.S., Wang, C.K., Chang, S.W. (2008). Atomistic simulation and investigation of nanoindentation, contact pressure and nanohardness. Interaction and Multiscale Mechanics **1**: 411-422.

Chen, Q., Chasiotis, I., Chen, C., Roy, A. (2008). Nanoscale and effective mechanical behavior and fracture of silica nanocomposites. Composites Science and Technology **68**(15–16): 3137-3144.

Chen, W. (2000). On piezoelastic contact problem for a smooth punch. International Journal of Solids and Structures **37**: 2331-2340.

Clements, D.L. (1971). The indentation of an anisotropic half space by a rigid punch. Journal of the Australian Mathematical Society **12**: 75-82.

Cruse, T.A. (1988). Boundary element analysis in computational fracture mechanics, Kluwer Academic Publishers, Dordrecht.

Dhaliwal, R.S., Rau, I.S. (1970). The axisymmetric boussinesq problem for a thick elastic layer under a punch of arbitrary profile. International Journal of Engineering Science **8**: 843-856.

Dingreville, R., Qu, J. (2007). A semi-analytical method to compute surface elastic properties. Acta Materialia **55**: 141-147.

Dingreville, R., Qu, J., Cherkaoui, M. (2005). Surface free energy and its effect on the elastic behavior of nano-sized particles, wires and films. Journal of the Mechanics and Physics of Solids **53**: 1827-1854.

Doerner, M.F., Nix, W.D. (1986). A method for interpreting the data from depth-sensing indentation instruments. Journal of Materials Research **1**: 601-609.

Duan, H.L., Wang, J., Huang, Z.P., Karihaloo, B.L. (2005). Eshelby formalism for nano-inhomogeneities. Proceedings of the Royal Society A **461**: 3335-3353.

Eshelby, J.D., Read, W.T., Shockley, W. (1953). Anisotropic elasticity with applications to dislocation theory. Acta Metallurgica **1**: 251-259.

Fabrikant, V.I. (1989). Applications of potential theory in mechanics: a selection of new results, Springer-Verlag New York, LLC.

Fang, Q.H., Liu, Y., Liu, Y.W., Huang, B.Y. (2009). Dislocation emission from an elliptically blunted crack tip with surface effects. Physica B: Condensed Matter **404**(20): 3421-3424.

Fang, Q. H., Liu, Y.W. (2006). Size-dependent elastic interaction between a screw dislocation and a circular nano-hole with surface stress. Physica status solidi (b) **243**(4): R28-R30.

Fang, Q.H., Liu , Y.W., Jin, B., Wen, P.H. (2009). Effect of interface stresses on the image force and stability of an edge dislocation inside a nanoscale cylindrical inclusion. International Journal of Solids and Structures **46**(6): 1413-1422.

Fischer, F.D., Waitz , T., Vollath, D., Simha, N.K. (2008). On the role of surface energy and surface stress in phase-transforming nanoparticles. Progress in Materials Science **53**(3): 481-527.

Frangi, A., Novati, G. (2003). BEM–FEM coupling for 3D fracture mechanics applications. Computational Mechanics **32**(4-6): 415-422.

Frangi, A., Novati, G., Springhetti, R., Rovizzi, M. (2002). 3D fracture analysis by the symmetric Galerkin BEM. Computational Mechanics **28**(3-4): 220-232.

Fu, X.L., Wang, G.F., Feng, X.Q. (2008). Surface effects on the near-tip stress fields of a mode-II crack. International Journal of Fracture **151**(2): 95-106.

Fu, X.L., Wang, G.F., Feng, X.Q. (2010). Surface effects on mode-I crack tip fields: A numerical study. Engineering Fracture Mechanics **77**(7): 1048-1057.

Gao, H., Ji, B. (2003). Modeling fracture in nanomaterials via a virtual internal bond method. Engineering Fracture Mechanics **70**(14): 1777-1791.

Gao, Y.F., Xu, H.T., Oliver, W.C., Pharr, G.M. (2008). Effective elastic modulus of film-on-substrate systems under normal and tangential contact. Journal of the Mechanics and Physics of Solids **56**: 402-416.

Giannakopoulos, A.E., Parmaklis, A.Z. (2007). The contact problem of a circular rigid punch on piezomagnetic materials. International Journal of Solids and Structures **44**: 4593–4612.

Gibbs, J.W. (1906). The scientific papers of J. Willard Gibbs. Vol. 1. London: Longmans Green.

Gray, L.J., Martha, L.F., Ingraffea, A.R. (1990). Hypersingular integrals in boundary element fracture analysis. International Journal for Numerical Methods in Engineering **29**(6): 1135-1158.

Gu, H., Yew, C.H. (1988). Finite element solution of a boundary integral equation for mode I embedded three-dimensional fractures. International Journal for Numerical Methods in Engineering **26**(7): 1525-1540.

Gurtin, M.E., Murdoch, A.I. (1975). A continuum theory of elastic material surfaces. Archive for Rational Mechanics and Analysis **57**: 291-323.

Gurtin, M.E., Murdoch, A.I. (1978). Surface stress in solids. International Journal of Solids and Structures **14**: 431-440.

Gurtin, M.E., Weissmüller, J., Larché, F. (1998). A general theory of curved deformable interfaces in solids at equilibrium. Philosophical Magazine A **78**: 1093-1109.

Hainsworth, S.V., Page, T.F. (1994). Nanoindentation studies of the chemomechanical effect in sapphire. Journal of Materials Science **29**: 5529-5540.

Harding, J.W., Sneddon, I.N. (1945). The elastic stresses produced by the indentation of the plane surface of a semi-infinite elastic solid by a rigid punch. Mathematical Proceedings of the Cambridge Philosophical Society **41**: 16-26.

Hasheminejad, B.S.M., Gheshlaghi, B., Mirzaei, Y., Abbasion, S. (2011). Free transverse vibrations of cracked nanobeams with surface effects. Thin Solid Films **519**(8): 2477-2482.

Hayami, K. (1992). A projection transformation method for nearly singular surface boundary element integrals. In: Brebbia, C. A., Orszag, S.A. (eds) Lecture notes in Engineering; **73**; 1-2. Springer-Verlag, Berlin.

Hayami, K., Brebbia, C.A. (1988). Quadrature methods for singular and nearly singular integrals in 3-D boundary element method, Boundary Element X, 237-264, Springer-Verlag, Berlin.

Hayami, K., Matsumoto, H. (1994). A numerical quadrature for nearly singular boundary element integrals. Engineering Analysis with Boundary Elements **13**(2): 143-154.

He, L.H., Lim, C.W. (2006). Surface green function for a soft elastic half-space: Influence of surface stress. International Journal of Solids and Structures **43**: 132–143.

He, L.H., Lim, C.W., Wu, B.S. (2004). A continuum model for size-dependent deformation of elastic films of nano-scale thickness. International Journal of Solids and Structures **41**: 847–857.

Huang, D.W. (2008). Size-dependent response of ultra-thin films with surface effects. International Journal of Solids and Structures **45**: 568-579.

Huang, G.Y., Yu, S.W. (2007). Effect of surface elasticity on the interaction between steps. Journal of Applied Mechanics **74**: 821.

Huang, S., Zhang, S., Belytschko, T., Terdalkar, S.S., Zhu, T. (2009). Mechanics of nanocrack: Fracture, dislocation emission, and amorphization. Journal of the Mechanics and Physics of Solids **57**(5): 840-850.

Hughes, T.J.R. (2000). The finite element method: Linear static and dynamic finite element analysis. New Jersey: Dover Publications.

Iijima, S. (1991). Helical microtubules of graphitic carbon. Nature **354**: 56-58.

Iijima, S., Ichihashi, T. (1993). Single-shell carbon nanotubes of 1-nm diameter. Nature **363**: 603-605.

Intarit, P. (2013). Solutions of elastic medium with surface stress effects, Ph.D. Dissertation, Chulalongkorn University, Thailand.

Intarit, P., Senjuntichai, T., Rajapakse, R.K.N.D., (2010). Dislocations and internal loading in a semi-infinite elastic medium with surface stresses. Engineering Fracture Mechanics, **77**: 3592-3603.

Intarit, P., Senjuntichai, T., Rungamornrat, J., Rajapakse, R.K.N.D. (2011). Surface Elasticity and Residual Stress Effect on the Elastic Field of a Nanoscale Elastic Layer. Interaction and Multiscale Mechanics, An Int't Journal, **4**: 85-105.

Intarit, P., Senjuntichai, T., Rungamornrat, J., Rajapakse, R.K.N.D. (2012). Stress analysis of penny-shaped crack considering the effects of surface elasticity. Proceedings of 20th Annual International Conference on Composites or Nano Engineering (ICCE-20), Ramada Beijing North Hotel, Beijing, P.R. China.

Jammes, M., Mogilevskaya, S.G., Crouch, S.L. (2009). Multiple circular nano-inhomogeneities and/or nano-pores in one of two joined isotropic elastic half-planes. Engineering Analysis with Boundary Elements **33**(2): 233-248.

Jing, G.Y., Duan, H.L., Sun, X.M., Zhang, Z.S., Xu, J., Li, y.d., et al. (2006). Surface effects on elastic properties of silver nanowires: Contact atomic-force microscopy. Physical Review B **73**: 235409.

Kachanov, M.L., Shafiro, B., Tsukrov, I. (2004). Handbook of Elasticity Solutions, Kluwer Academic Publishers.

Karimi, A., Wang, Y., Cselle, T., Morstein, M. (2002). Fracture mechanisms in nanoscale layered hard thin films. Thin Solid Films **420–421**(0): 275-280.

Kassir, M.K., Sih, G.C. (1975). Three-dimensional Crack Problems: A New Selection of Crack Solutions in Three-dimensional Elasticity, vol. 2, Noordhoff International Publishing, Leyden.

Kim, C., Ru, C.-Q., Schiavone, P. (2013). A clarification of the role of crack-tip conditions in linear elasticity with surface effects. Mathematics and Mechanics of Solids **18**(1): 59-66.

Kim, C.I., Schiavone, P., Ru, C.Q. (2010). Analysis of a mode-III crack in the presence of surface elasticity and a prescribed non-uniform surface traction. Zeitschrift für angewandte Mathematik und Physik **61**(3): 555-564.

Kim, C.I., Schiavone, P. Ru, C.Q. (2011). Analysis of Plane-Strain Crack Problems (Mode-I & Mode-II) in the Presence of Surface Elasticity. Journal of Elasticity **104**(1-2): 397-420.

Kim, C. I., Schiavone, P., Ru, C.Q. (2011). The effect of surface elasticity on a Mode-III interface crack. Archives of Mechanics **63**(3): pp. 267 - 286.

Lebedev, N.N., Ufliand, I.S. (1958). Axisymmetric contact problem for an elastic layer. Journal of Applied Mathematics and Mechanics **22**: 442-450.

Liao, F., Girshick, S.L., Mook, W.M., Gerberich, W.W., Zachariah, M.R. (2005). Superhard nanocrystalline silicon carbide films. Applied Physics Letters **86**: 171913.

Li, H.-B., Han, G.-M., Mang, H.A. (1985). A new method for evaluating singular integrals in stress analysis of solids by the direct boundary element method. International Journal for Numerical Methods in Engineering **21**(11): 2071-2098.

Li, S., Mear, M.E. (1998). Singularity-reduced integral equations for displacement discontinuities in three-dimensional linear elastic media. International Journal of Fracture **93**(1-4): 87-114.

Li, S., Mear, M.E., Xiao, L. (1998). Symmetric weak-form integral equation method for three-dimensional fracture analysis. Computer Methods in Applied Mechanics and Engineering **151**(3–4): 435-459.

Liu, C.L., Fang, T.H., Lin, J.F. (2007). Atomistic simulations of hard and soft films under nanoindentation. Materials Science and Engineering A **452-453**: 135-141.

Liu, Y.W., Fang, Q.H. (2007). Analysis of a screw dislocation inside an inhomogeneity with interface stress. Materials Science and Engineering: A **464**(1–2): 117-123.

Lu, C., Gao, Y., Michal, G., Huynh, N.N., Zhu, H.T., Tieu, A.K. (2009). Atomistic simulation of nanoindentation of iron with different indenter shapes. Proceedings of the Institution of Mechanical Engineers **223**: 997984.

Lu, P., He, L.H., Lee, H.P., Lu, C. (2006). Thin plate theory including surface effects. International Journal of Solids and Structures 43: 4631-4647.

Lucas, B.N., Hay, J.C., Oliver, W.C. (2003). Using multidimensional contact mechanics experiments to measure poisson's ratio. Journal of Materials Research **19**: 58-65.

Mandal, B.N. (1988). A note on Bessel function dual integral equation with weight function. International Journal of Mathematics and Mathematical Sciences **11**: 543-550.

Mao, S.X., Zhao, M., Wang, Z.L. (2003). Nanoscale mechanical behavior of individual semiconducting nanobelts. Applied Physics Letters **83**: 993-995.

Masuda-Jindo, K., Hung, V.V., Menon, M. (2009). Fracture and mechanical properties of nanotubes and nanowires. Procedia Engineering **1**(1): 163-166.

Miller, R.E., Shenoy, V.B. (2000). Size-dependent elastic properties of nanosized structural elements. Nanotechnology **11**: 139-147.

Mogilevskaya, S.G., Crouch, S.L., Stolarski, H.K. (2008). Multiple interacting circular nano-inhomogeneities with surface/interface effects. Journal of the Mechanics and Physics of Solids **56**(6): 2298-2327.

Nan, H., Wang, B. (2012). Effect of residual surface stress on the fracture of nanoscale materials. Mechanics Research Communications **44**(0): 30-34.

Nan, H.S., Wang, B.L. (2013). Effect of crack face residual surface stress on nanoscale fracture of piezoelectric materials. Engineering Fracture Mechanics **110**(0): 68-80.

Nix, W.D., Gao, H. (1998). Indentation size effects in crystalline materials: A law for strain gradient plasticity. Journal of the Mechanics and Physics of Solids **46**(3): 411-425.

Oh, E.-S., Walton, J.R., Slattery, J.C. (2005). A Theory of Fracture Based Upon an Extension of Continuum Mechanics to the Nanoscale. Journal of Applied Mechanics **73**(5): 792-798.

Oliver, W.C., Pharr, G.M. (1992). An improved technique for determining hardness and elastic modulus using load and displacement sensing indentation experiments. Journal of Materials Research **7**: 1564-1583.

Ou, Z.Y., Wang, G.F., Wang, T.J. (2008). Effect of residual surface tension on the stress concentration around a nanosized spheroidal cavity. International Journal of Engineering Science **46**(5): 475-485.

Pan, E., Yuan, F.G. (2000). Boundary element analysis of three-dimensional cracks in anisotropic solids. International Journal for Numerical Methods in Engineering **48**(2): 211-237.

Peng, B., Locascio, M., Zapol, P., Li, S., Mielke, S.L., Schatz, G.C., Espinosa, H.D. (2008). Measurements of near-ultimate strength for multiwalled carbon nanotubes and irradiation-induced crosslinking improvements. Nat Nano **3**(10): 626-631.

Phan, A.V., Tippur, H.V. (2009). Shape-sensitivity-based evaluation of the stress intensity factors at the nanoscale by means of quantized fracture mechanics. Mechanics Research Communications **36**(3): 336-342.

Pinyochotiwong, Y., Rungamornrat, J., Senjuntichai, T. (2010). Rigid frictionless indentation on half-space with surface stresses. Master's thesis, Chulalongkorn University. Thailand

Pinyochotiwong, Y., Rungamornrat, J., Senjuntichai, T. (2013). Rigid frictionless indentation on elastic half space with influence of surface stresses. International Journal of Engineering Science **71**(0): 15-35.

Poncharal, P., Wang, Z.L., Ugarte, D., de Heer, W.A. (1999). Electrostatic deflections and electromechanical resonances of carbon nanotubes. Science **283**: 1513-1516.

Poulos, H.G. (1974). Elastic solutions for soil and rock mechanics. The United States of America: John Wiley.

Povstenko, Y.Z. (1993). Theoretical investigation of phenomena caused by heterogeneous surface tension in solids, J. Mech. Phys. Solids, **41**: 1499-1514.

Pugno, N., Carpinteri, A., Ippolito, M., Mattoni, A., Colombo, L. (2008). Atomistic fracture: QFM vs. MD. Engineering Fracture Mechanics **75**(7): 1794-1803.

Qin, E.W., Lu, L., Tao, N.R., Tan, J., Lu, K. (2009). Enhanced fracture toughness and strength in bulk nanocrystalline Cu with nanoscale twin bundles. Acta Materialia **57**(20): 6215-6225.

Rafii-Tabar, H., Shodja, H.M., Darabi, M., Dahi, A. (2006). Molecular dynamics simulation of crack propagation in fcc materials containing clusters of impurities. Mechanics of Materials **38**(3): 243-252.

Ratner, M. A., Ratner, D. (2003). Nanotechnology: A Gentle Introduction to the Next Big Idea, Prentice Hall Professional.

Rau, I.S., Dhaliwal, R.S. (1972). Further considerations on the axisymmetric boussinesq problem. International Journal of Engineering Science **10**: 659-663.

Rungamornrat, J. (2006). Analysis of 3D cracks in anisotropic multi-material domain with weakly singular SGBEM. Engineering Analysis with Boundary Elements **30**(10): 834-846.

Rungamornrat, J., Mear, M.E. (2008). A weakly-singular SGBEM for analysis of cracks in 3D anisotropic media. Computer Methods in Applied Mechanics and Engineering **197**(49–50): 4319-4332.

Rungamornrat, J., Mear, M.E. (2008). Weakly-singular, weak-form integral equations for cracks in three-dimensional anisotropic media. International Journal of Solids and Structures **45**(5): 1283-1301.

Rungamornrat, J., Mear, M.E. (2011). SGBEM–FEM coupling for analysis of cracks in 3D anisotropic media. International Journal for Numerical Methods in Engineering **86**(2): 224-248.

Rungamornrat, J., Senjuntichai, T. (2009). Regularized boundary integral representations for dislocations and cracks in smart media. Smart Materials and Structures **18**(7): 074010.

Sáez, A., Ariza, M.P., Dominguez, J. (1997). Three-dimensional fracture analysis in transversely isotropic solids. Engineering Analysis with Boundary Elements **20**(4): 287-298.

Sakib, A.R.N., Adnan, A. (2012). On the size-dependent critical stress intensity factor of confined brittle nanofilms. Engineering Fracture Mechanics **86**(0): 13-22.

Sander, D. (2003). Surface stress: Implications and measurements. Current Opinion in Solid State and Materials Science **7**: 51-57.

Selvadurai, A.P.S. (2000). Partial differential equations in mechanics 2. Germany: Springer.

Sendova, T., Walton, J.R. (2010). A New Approach to the Modeling and Analysis of Fracture through Extension of Continuum Mechanics to the Nanoscale. Mathematics and Mechanics of Solids **15**(3): 368-413.

Sharma, P., Ganti, S. (2004). Size-Dependent Eshelby's Tensor for Embedded Nano-Inclusions Incorporating Surface/Interface Energies. Journal of Applied Mechanics **71**(5): 663-671.

Sharma, P., Wheeler, L.T. (2007). Size-dependent elastic state of ellipsoidal nano-inclusions incorporating surface/interface tension. Journal of Applied Mechanics - Transactions of the ASME **74**: 447-454.

Sharma, P., Ganti, S., Bhate, N. (2003). Effect of surfaces on the size-dependent elastic state of nano-inhomogeneities. Applied Physics Letters **82**: 535-537.

Shenoy, V.B. (2002). Size-dependent rigidities of nanosized torsional elements. International Journal of Solids and Structures **39**: 4039–4052.

Shenoy, V.B. (2005). Atomistic calculations of elastic properties of metallic fcc crystal surfaces. Physical Review B **71**: 094104.

Shuttleworth, R. (1950). The surface tension of solids. Proceedings of the Physical Society Section A **63**: 444-457.

Sinnott, S.B., Colton, R.J., White, C.T., Shenderova, O.A., Brenner, D.W., Harrison, J.A. (1997). Atomistic simulations of the nanometer-scale indentation of amorphous-carbon thin films. Journal of Vacuum Science and Technology A 15: 936-940.

Sneddon, I.N. (1951). Fourier transform. New York: McGraw-Hill.

Sneddon, I.N. (1965). The relation between load and penetration in the axisymmetric boussinesq problem for a punch of arbitrary profile. International Journal of Engineering Science **3**: 47-57.

Sneddon, I.N. (1966). Mixed boundary value problems in potential theory. New York: John Wiley & Sons.

Song, F., Huang, G.L., Park, H.S., Liu, X.N. (2011). A continuum model for the mechanical behavior of nanowires including surface and surface-induced initial stresses. International Journal of Solids and Structures **48**(14–15): 2154-2163.

Stroh, A.N. (1958). Dislocations and cracks in anisotropic elasticity. Philosophical Magazine 3: 625-646.

Sumomogi, T., Nakamura, M., Endo, T., Goto, T., Kaji, S. (2002). Evaluation of surface and subsurface cracks in nanoscale-machined single-crystal silicon by scanning force

microscope and scanning laser microscope. Materials Characterization **48**(2–3): 141-145.
Sundararajan, S., Bhushan, B. (2002). Development of AFM-based techniques to measure mechanical properties of nanoscale structures. Sensors and Actuators A: Physical **101**(3): 338-351.
Sutradhar, A., Paulino, G.H. (2004). Symmetric Galerkin boundary element computation of T-stress and stress intensity factors for mixed-mode cracks by the interaction integral method. Engineering Analysis with Boundary Elements **28**(11): 1335-1350.
Tada, H., Paris, P.C., Irwin, G.R. (2000). The Stress Analysis of Cracks Handbook, American Society of Mechanical Engineers.
Tian, L., Rajapakse, R.K.N.D. (2006). Analytical Solution for Size-Dependent Elastic Field of a Nanoscale Circular Inhomogeneity. Journal of Applied Mechanics **74**(3): 568-574.
Tian, L., Rajapakse, R.K.N.D. (2007). Elastic field of an isotropic matrix with a nanoscale elliptical inhomogeneity. International Journal of Solids and Structures **44**: 7988-8005.
Timoshenko, S., Goodier, J.N. (1951). Theory of Elasticity. New York: McGraw-Hill.
Wang, G.-F., Feng, X.-Q., Wang, T.-J., Gao, W. (2007). Surface Effects on the Near-Tip Stresses for Mode-I and Mode-III Cracks. Journal of Applied Mechanics **75**(1): 011001-011001.
Wang, G. F., Wang, T.J. (2006). Deformation around a nanosized elliptical hole with surface effect. Applied Physics Letters **89**(16): -.
Wang, J.-S., Feng, X.-Q., Wang, G.-F., Yu, S.-W. (2008). Twisting of nanowires induced by anisotropic surface stresses. Applied Physics Letters **92**(19): -.
Wang, W., Zeng, X., Ding, J. (2010). Finite element modeling of two-dimensional nanoscale structures with surface effects. World Academy of Science, Engineering and Technology **72**: 867-872.
Wong, E.W., Sheehan, P.E., and Lieber, C.M. (1997). Nanobeam mechanics: Elasticity, strength, and toughness of nanorods and nanotubes. Science **277**: 1971-1975.
Wu, C.H. (1999). The effect of surface stress on the configurational equilibrium of voids and cracks. Journal of the Mechanics and Physics of Solids **47**(12): 2469-2492.
Wu, C.H., Wang, M.L. (2000). The effect of crack-tip point loads on fracture. Journal of the Mechanics and Physics of Solids **48**(11): 2283-2296.
Wu, C. H., Wang, M.L. (2001). Configurational equilibrium of circular-arc cracks with surface stress. International Journal of Solids and Structures **38**(24–25): 4279-4292.
Xiao, L. (1998). Symmetric weak-form integral equation method for three-dimensional fracture analysis. Ph.D. Dissertation, The University of Texas at Austin. USA
Xu, G. (1999). A Variational Boundary Integral Method for the Analysis of Three-Dimensional Cracks of Arbitrary Geometry in Anisotropic Elastic Solids. Journal of Applied Mechanics **67**(2): 403-408.
Xu, G., Ortiz, M. (1993). A variational boundary integral method for the analysis of 3-D cracks of arbitrary geometry modelled as continuous distributions of dislocation loops. International Journal for Numerical Methods in Engineering **36**(21): 3675-3701.

Yakobson, B. I. (2003). Nanomechanics. In W. A. Goddard; D. W. Brenner; S. E. Lyshevski; and G. J. Iafrate (eds.), Handbook of nanoscience, engineering, and technology, chapter 17. Florida: CRC Press.

Yan, Y., Sumigawa, T., Shang, F., Kitamura, T. (2011). Cohesive zone criterion for cracking along the Cu/Si interface in nanoscale components. Engineering Fracture Mechanics **78**(17): 2935-2946.

Yang, F. (1998). Indentation of an incompressible elastic film. Mechanics of Materials **30**: 275-286.

Yang, F., Li, J.C.M. (1995). Impression test of 63Sn-37Pb eutectic alloy. Materials Science and Engineering A **201**: 40-49.

Yang, F., Li, J.C.M. (1997). Viscosity of selenium measured by impression test. Journal of Non-Crystalline Solids **212**: 136-142.

Yang, Y.T., et al. 2001. Monocrystalline silicon carbide nanoelectromechanical systems. Applied Physics Letters **78**: 162-164.

Yu, H.Y., Sanday, S.C., Rath, B.B. (1990). The effect of substrate on the elastic properties of films determined by the indentation test-axisymmetric boussinesq problem. Journal of the Mechanics and Physics of Solids **38**: 745-764.

Zeng-shen, C. (1982). Discussion on the SIF for points on border of elliptical flat crack inside infinite solid under uniform tension. Applied Mathematics and Mechanics **3**(4): 521-526.

Zhang, S., Mielke, S.L., Khare, R., Troya, D., Ruoff, R.S., Schatz, G.C., Belytschko, T. (2005). Mechanics of defects in carbon nanotubes: Atomistic and multiscale simulations. Physical Review B **71**(11): 115403.

Zhao, C.W., Xing, Y.M. (2008). Nanoscale experimental study of a micro-crack in silicon. Physica B: Condensed Matter **403**(23–24): 4202-4204.

Zhao, C.W., Xing, Y.M. (2010). Nanoscale deformation analysis of a crack-tip in silicon by geometric phase analysis and numerical moiré method. Optics and Lasers in Engineering **48**(11): 1104-1107.

Zhao, X.J. (2009). Surface loading and rigid indentation of an elastic layer with surface energy effects. Master's thesis, The University of British Columbia (Vancouver). Canada

Zhao, X.J., Rajapakse, R.K.N.D. (2009). Analytical solutions for a surface-loaded isotropic elastic layer with surface energy effects. International Journal of Engineering Science **47**(11–12): 1433-1444.

Zienkiewicz, O.C., Taylor, R.L. (2000). The finite element method: Solid mechanics, volume 2, Butterworth-Heinemann, Oxford.

Appendix A: OUTPUT

Articles in International Journals:

[1] Pinyochotiwong Y., Rungamornrat J., Senjuntichai T., "Rigid frictionless indentation on elastic half space with influence of surface stresses". *International Journal of Engineering Science*, 2013, 71, pp. 15-35.

[2] Intarit P., Senjuntichai T., Rungamornrat J., Rajapakse R.K.N.D. "Surface Elasticity and Residual Stress Effect on the Elastic Field of a Nanoscale Elastic Layer". *Interaction and Multiscale Mechanics*, 2011, 4(2), pp.85-105.

[3] Nguyen T.B., Rungamornrat J., Senjuntichai T., Wijeyewickrema A.C. "FEM-SGBEM coupling for modeling of mode-I planar cracks in three-dimensional elastic media with residual surface tension effects". *Engineering Analysis with Boundary Elements*, **accepted for publication**.

[4] Nguyen T.B., Rungamornrat J., Senjuntichai T., Wijeyewickrema A.C. "Analysis of 3D planar cracks with consideration of surface stress effects". *ASEAN Engineering Journal Part C*, **accepted for publication**.

[5] Tuttipongsawat P., Rungamornrat J., Senjuntichai T. "Elastic layer under axisymmetric surface loads and influence of surface stresses". *Applied Mathematical Modeling*, **under review**.

Articles in Conference Proceedings:

[1] Nguyen BT, Rungamornrat J, Senjuntichai T, Wijeyewickrema AC, "Analysis of 3D planar cracks with consideration of surface stress effects". Proceedings of the 6th Asian Civil Engineering Conference (ACEC) and the 6th Asian Environmental Engineering Conference (AEEC), Pathumwan Princess Hotel, Bangkok, Thailand, November 21-22, 2013.

[2] Nguyen BT, Rungamornrat J, Senjuntichai T, Wijeyewickrema AC, "FEM-SGBEM coupling for modeling of cracks in three-dimensional elastic media with influence of surface stresses". Proceedings of 13th International Conference on Fracture (ICF13), Beijing, China, June 16-21, 2013.

[3] Intarit P, Senjuntichai T, Rungamornrat J, Rajapakse RKND, “Stress Analysis of Penny-shaped Crack Considering the Effects of Surface Elasticity”. Proceedings of 20th Annual International Conference on Composites or Nano Engineering (ICCE-20), Ramada Beijing North Hotel, Beijing, P.R. China, July 22-28, 2012.

[4] Tuttipongsawat P, Rungamornrat J, Senjuntichai T. Infinite elastic layer under surface loads and influence of surface stresses. The 17th National Convention on Civil Engineering, Udonthani, May 9-11, 2012.

Appendix B: REPRINTS/MANUSCRIPTS

International Journal of Engineering Science 71 (2013) 15–35

Contents lists available at SciVerse ScienceDirect

International Journal of Engineering Science

journal homepage: www.elsevier.com/locate/ijengsci

Rigid frictionless indentation on elastic half space with influence of surface stresses

Yutiwadee Pinyochotiwong, Jaroon Rungamornrat *, Teerapong Senjuntichai

Department of Civil Engineering, Faculty of Engineering, Chulalongkorn University, Bangkok 10330, Thailand

ARTICLE INFO

Article history:
Received 13 January 2013
Received in revised form 26 April 2013
Accepted 30 April 2013

Keywords:
Indentations
Surface elasticity
Surface stresses
Half-space
Gurtin–Murdoch

ABSTRACT

This paper proposes an application of continuum-based concepts in the analysis of an axisymmetric rigid frictionless indentor acting on an isotropic, linearly elastic half-space accounted for surface energy effects. The influence of surface stresses is considered by employing a complete Gurtin–Murdoch continuum model for surface elasticity. With use of standard Love's representation and Hankel integral transform, such boundary value problem is reduced to a set of dual integral equations that can be further transformed into an equivalent Fredholm integral equation of the second kind. Selected numerical procedures based on the solution discretization and standard collocation technique are then implemented to construct its solution numerically. Obtained numerical results for elastic fields within the bulk are shown and compared for indentors of different profiles and contact radii at various depths. It is found that the influence of surface free energy on bulk stresses and displacements and the size-dependency of solutions become more apparent in a region very near the free surface. The significant contribution of the residual surface tension on predicted responses is obviously observed in comparison with existing results. The proposed mathematical model not only offers an alternative for specifically studying both mechanical properties and elastic fields for indentors of arbitrary axisymmetric profiles but also provides, in general, a crucial basis for further investigations in the area of nano-mechanics.

1. Introduction

Nowadays, it is undeniable that a wide range of engineering and industrial sectors has benefited greatly from vast applications of nanotechnology. Many new nano-materials have been developed by utilizing the fact that, at a nano-scale, materials begin to exhibit unique properties (i.e., optical, electrical, chemical and mechanical properties), which significantly differ from those at a larger scale. To take most advantages of these novel properties on the development of powerful nano-devices, profound understanding on their behavior and characterization of material properties at such very small scale is essential for various researchers.

Mechanical behavior of nano-structured materials and nano-sized elements can be investigated by two basic approaches, namely, experimental methods and theoretical simulations. The former approach basically yields results reflecting the real behaviors but it has been found highly dependent on experimental settings and, generally, expensive due to the requirement of high precision testing devices and procedures. For the latter approach, though existing molecular simulations offer advantages in precise response prediction according to proper underlying governing physics, they require simultaneously

* Corresponding author. Tel.: +66 22186460; fax: +66 22517304.
E-mail addresses: yutiwadee_p@yahoo.com (Y. Pinyochotiwong), jaroon.r@chula.ac.th (J. Rungamornrat), teerapong.s@chula.ac.th (T. Senjuntichai).

0020-7225/$ - see front matter © 2013 Elsevier Ltd. All rights reserved.
http://dx.doi.org/10.1016/j.ijengsci.2013.04.005

intensive computational resources associated with the modeling of a large number of degrees of freedom at a nano-scale. Due to such highly demanding requirement, applications of those techniques to modeling practical problems have been quite limited. The continuum-based approach is therefore considered as an attractive alternative since the use of simplified governing physics dramatically reduces the computational cost. Nevertheless, the classical continuum theory generally neglects the presence of intrinsic size and thus seems incapable of demonstrating the size-dependent behavior which truly exists in nano-materials and soft elastic solids, e.g., polymer gels. The size dependency of material behaviors at a nano-scale has been well recognized due to their relatively high surface-to-volume ratio whereas, in the case of soft elastic materials, the intrinsic length scale, which is defined as the ratio of surface free energy and Young's modulus (Yakobson, 2003), is much larger than that of conventional solids and becomes comparable to the characteristic length of the material element in practical situations (He & Lim, 2006). As a consequence, the influence of free surfaces should be properly incorporated into classical continuum-based models in order to obtain ones that are capable of capturing real responses to the level of complexity involved with predicted results of sufficiently high accuracy.

The concept of surface phenomena (i.e., the thermodynamics of solid surfaces) was noticed for more than a century ago by Gibbs (1906). Comprehensive literature review on the surface energy effects and the Gibbsian formulation of the thermodynamics of surfaces can be found in many researches on surface and interface stresses (Cammarata, 1994; Cammarata, 1997; Fischer, Waitz, Vollath, & Simha, 2008). To study the mechanical behavior of an immediate neighborhood of material surfaces through a continuum-based model, Gurtin and his co-workers (Gurtin & Murdoch, 1975; Gurtin & Murdoch, 1978; Gurtin, Weissmüller, & Larché, 1998) developed a mathematical framework, known as the theory of surface elasticity, to account for the influence of surface free energy. In their model, the existing surface is simply represented by an infinitesimally thin layer (or, mathematically, a layer of zero thickness) bonded perfectly to the bulk (i.e., an interior of the body) and its behavior is governed by a constitutive law different from that of the bulk. In the study of nano-scale problems, all material constants appearing in that constitutive model were commonly calibrated with data obtained from either experimental measurements (Jing et al., 2006) or atomistic simulations (Miller & Shenoy, 2000; Shenoy, 2005). Upon various verifications and comparisons with results predicted by atomistic and molecular static simulations (Dingreville, Qu, & Cherkaoui, 2005; Miller & Shenoy, 2000; Shenoy, 2005), Gurtin–Murdoch surface elasticity model has proven promising and attractive for modeling a variety of nano-scale problems to account for the influence of free surfaces. The model has gained rapid recognition from various researchers and been widely used in the investigation of mechanical responses of nano-structures, e.g. ultra-thin elastic films (He, Lim, & Wu, 2004; Huang, 2008), thin plates (Lu, He, Lee, & Lu, 2006), nano-scale inhomogeneities (Sharma, Ganti, & Bhate, 2003; Duan, Wang, Huang, & Karihaloo, 2005; Sharma & Wheeler, 2007; Tian & Rajapakse, 2007), dislocations (Intarit, Senjuntichai, & Rajapakse, 2010) and nano-scale elastic layers (Intarit, Senjuntichai, Rungamornrat, & Rajapakse, 2011; Zhao & Rajapakse, 2009). This should additionally confirm the benefit of employing such alternative continuum-based model to save the computational resources with an acceptable level of accuracy gained.

Indentation techniques have been extensively employed by many researchers in the study of material properties such as hardness and elastic modulus. For instance, by using depth-sensing indentation tests with either spherical or conical indentors, Young's modulus can be calculated from the slope of the linear regime of the unloading curve in the load versus penetration depth while hardness can be obtained from data along the loading curve (Doerner & Nix, 1986; Oliver & Pharr, 1992). In nano-applications, such techniques were also applied to measure the mechanical properties of ceramics (Hainsworth & Page, 1994), metals (Armstrong, Shin, & Ruff, 1995; Beegan, Chowdhury, & Laugier, 2007) and polymers (Yang & Li, 1995; Yang & Li, 1997). Besides those experimental studies, modeling of indentation problems via the use of suitable mathematical models has been also of interest for more than a century and offered an attractive candidate for investigating various aspects and gaining fundamental insight of material properties. The classical problem of an axisymmetric rigid punch indenting on an elastic half-space seems to be first considered by Boussinesq (1885) and, in that work, results were presented only for flat-ended cylindrical and conical punches. Harding and Sneddon (1945) and Sneddon (1965) resolved Boussinesq's problem for a punch of an arbitrary profile by applying the Hankel integral transform technique. The indentation problems associated with an elastic layer perfectly bonded to an elastic half-space have also been investigated. For instance, Lebedev and Ufliand (1958) studied a problem of a flat-ended rigid cylindrical indentor on an elastic layer resting on a rigid foundation by using Papkovich–Neuber's representation for the displacement vector. After reducing mixed boundary conditions to a pair of integral equations, a Fredholm integral equation was obtained and solved numerically. By applying the Hankel integral transform technique, Dhaliwal and Rau (1970) derived a Fredholm integral equation governing a problem of an elastic layer lying over an elastic half-space under an axisymmetric rigid punch of arbitrary profile. Subsequently, Rau and Dhaliwal (1972) developed a numerical technique to solve the integral equation developed by Dhaliwal and Rau (1970) and obtained the complete elastic field. Yu, Sanday, and Rath (1990) presented numerical results obtained from solving Fredholm integral equation of the second kind to demonstrate the effect of a substrate on the elastic properties of films and provided useful guidelines for the proper choice of an approximate layer thickness and substrate elastic properties to determine the elastic constants of the layer. Motivated by a recently developed multi-dimensional nano-contact system (Lucas, Hay, & Oliver, 2003), Gao, Xu, Oliver, and Pharr (2008) gave an analytical formulation by applying Green's function in Fourier space to predict the effective elastic modulus of film-on-substrate systems under normal and tangential contacts. In addition, Yang (1998) applied the Hankel integral transform to investigate the problem of compressing an incompressible elastic film by a rigid flat-ended cylindrical indentor. While analysis of indentation problems have been carried out extensively within the context of classical linear elasticity, on the basis of a careful literature survey, works towards the treatment of surface stresses to model nano-scale influences are still relatively few. Recently, Zhao (2009) proposed a continuum-based

model to study the influence of surface stresses on mechanical responses of an elastic half-space compressed by an axisymmetric, rigid, frictionless nano-indentor. In the analysis, a method of Hankel integral transform was utilized to construct an analytical solution and results were reported for certain indentor profiles. Although Zhao's model can successfully capture the size-dependency behavior of solutions and contribution of the surface stresses, Gurtin–Murdoch constitutive relation used in his formulation is still not complete (i.e., the out-of-plane contribution of the residual surface tension was ignored). Lack of such term can significantly alter predicted responses such as the pressure profile beneath the indentor and normal components of elastic fields in the vicinity of the indentor.

The primary objective of the present study is to generalize the work of Zhao (2009) to investigate mechanical responses of an elastic half-space compressed by an axisymmetric, rigid, frictionless indentor by using a complete Gurtin–Murdoch surface elasticity model to account for the influence of surface stresses. It is vital to emphasize here that the generalization to include the out-of-plane contribution of the residual surface tension becomes theoretically and computationally non-trivial since presence of such extra term requires very distinct solution procedure from that employed by Zhao (2009). In the following sections, a problem description is addressed first and a formulation of the boundary value problem using Love' strain representation and Hankel integral transform is then outlined. A technique to form the final, single governing equation in terms of Fredholm integral equation of the second kind is clearly demonstrated. Next, a selected numerical procedure to determine the primary unknown and all related field quantities is fully discussed. Finally, selected numerical results and findings from extensive parametric studies are reported to demonstrate the size-dependency and influence of surface stresses for different indentor profiles and indentation depths.

2. Problem description

Consider a half-space Ω compressed by an axisymmetric, frictionless, rigid indentor as shown schematically in Fig. 1. A top surface of the half-space possesses a constant residual surface tension τ^s under unstrained conditions and surface Lame's constants μ^s and λ^s whereas the remaining majority of the medium is made of a homogeneous, isotropic, linearly elastic material with Lame's constants μ and λ. For convenience, a reference Cartesian coordinate system (x,y,z) is chosen such that its origin is located at the center of the indentor and the z-axis directs downward, and the corresponding cylindrical coordinate system used in the formulation presented further below is denoted by (r,θ,z). A profile of the indentor is completely described by a function $\delta = \delta(r)$ which represents the distance from the reference datum at the center of the indentor to its surface, i.e., $\delta(0) = 0$. The radius of a contact region and the indentation depth resulting from a resultant force P at the center

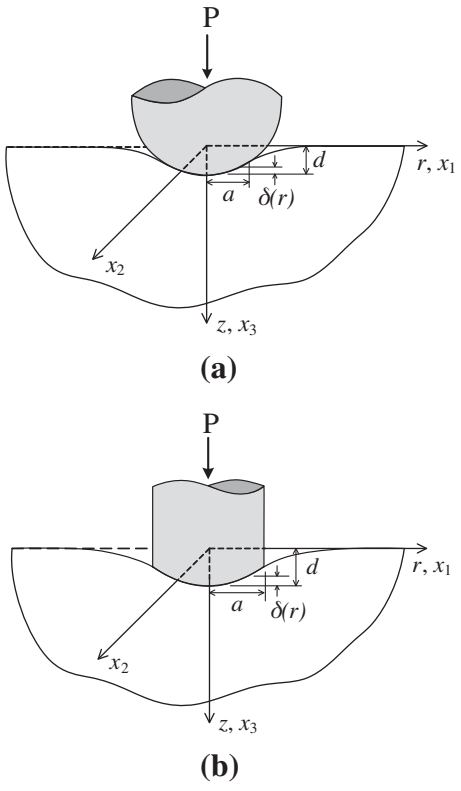

Fig. 1. Elastic half-space compressed by axisymmetric rigid frictionless indentor: (a) smooth contact profile and (b) non-smooth contact profile.

of the indentor are denoted by a and d, respectively. In the present study, the profile of the indentor is assumed to be smooth at any interior point of the contact region (i.e., the unit normal vector to the surface of the indentor or, equivalently, $d\delta/dr$ is well-defined for $r < a$) whereas, along the boundary $r = a$, the profile is allowed to be non-smooth. For brevity in further reference, an indentor with the well-defined $d\delta/dr$ for $r \leqslant a$ is termed here a *smooth-contact* indentor (see Fig. 1(a)) whereas that possessing the well-defined $d\delta/dr$ only for $r < a$ is termed a *non-smooth-contact* indentor (see Fig. 1(b)).

The problem statement is to determine the pressure distribution exerted by the indentor and the complete elastic fields (e.g., displacements and stresses) within the half-space accounted for the influence of surface stresses. The size-dependency behavior of the predicted solutions and the contribution of the surface stresses to those solutions are to be fully investigated.

3. Formulation of indentation problem

In the formulation of a boundary value problem, the given half-space Ω is first decomposed into two parts: a bulk denoted by Ω^b and a surface denoted by S. A surface S is defined as a layer of zero thickness located at the top boundary of Ω and the bulk Ω^b is simply the original half-space Ω with the surface S being removed. Since the surface S is modeled as a zero-thickness layer, the geometry of the bulk Ω^b (which is treated as a homogeneous half-space) is identical to that of Ω. The boundary of the bulk is subjected to the unknown traction $\mathbf{t}^b$ exerted directly by the surface S whereas S is treated as a two-sided surface with the top side compressed by the indentor and the bottom side subjected to the traction $\mathbf{t}^s$ exerted by the bulk.

3.1. Basic equations

In the present study, behavior of the bulk Ω^b is modeled by a classical theory of linear elasticity. In the absence of a body force, the governing field equations (i.e., equilibrium equations, constitutive laws and strain–displacement relations) can be expressed in a standard indicial form as

$$\sigma_{ij,j} = 0 \tag{1}$$

$$\sigma_{ij} = 2\mu\varepsilon_{ij} + \lambda\delta_{ij}\varepsilon_{kk} \tag{2}$$

$$\varepsilon_{ij} = \frac{1}{2}(u_{i,j} + u_{j,i}) \tag{3}$$

where u_i, σ_{ij} and ε_{ij} denote components of the displacement vector, stress and strain tensors, respectively, and δ_{ij} is a Kronecker-delta symbol. Note that lower-case indices range from 1 to 3 and repeated indices imply the summation over their range.

Behavior of the surface S is treated differently by Gurtin–Murdoch surface elasticity model. The equilibrium conditions on the surface, surface constitutive relations and strain–displacement relationship, when specialized to the flat surface, are given by Gurtin and Murdoch (1975), Gurtin and Murdoch (1978), Gurtin et al. (1998)

$$\sigma^s_{i\alpha,\alpha} + t^s_i + t^0_i = 0 \tag{4}$$

$$\sigma^s_{\beta\alpha} = \tau^s\delta_{\beta\alpha} + 2(\mu^s - \tau^s)\varepsilon^s_{\beta\alpha} + (\lambda^s + \tau^s)\varepsilon^s_{\gamma\gamma}\delta_{\beta\alpha} + \tau^s u^s_{\beta,\alpha}, \quad \sigma^s_{3\alpha} = \tau^s u^s_{3,\alpha} \tag{5}$$

$$\varepsilon^s_{\alpha\beta} = \frac{1}{2}\left(u^s_{\alpha,\beta} + u^s_{\beta,\alpha}\right) \tag{6}$$

where the superscript 's' is used to denote the quantities corresponding to the surface and $\mathbf{t}^0$ denotes the traction exerted on the top side of the surface. It is important to emphasize here that appearing Greek indices range from 1 to 2 and, again, repeated indices imply the summation over their range. By substituting (5) and (6) into (4), it leads to the in-plane and out-of-plane equilibrium equations of the surface in terms of the surface displacement as shown below

$$\mu^s u^s_{\beta,\alpha\alpha} + (\mu^s + \lambda^s)u^s_{\alpha,\alpha\beta} + t^s_\beta + t^0_\beta = 0 \tag{7}$$

$$\tau^s u^s_{3,\alpha\alpha} + t^s_3 + t^0_3 = 0 \tag{8}$$

3.2. Boundary and continuity conditions

Since the surface S is adhered perfectly to the bulk Ω^b without slipping, the displacement and traction along the interface of the surface and the bulk must be continuous. This renders the following continuity conditions:

$$u^s_i = u_i|_{z=0}, \quad t^s_i + t^b_i = 0 \tag{9}$$

The traction $\mathbf{t}^b$ can be related to the stress components within the bulk by

$$t^b_i = -\sigma_{i3}|_{z=0} \tag{10}$$

From the frictionless condition of the indentor and its prescribed profile, the traction $\mathbf{t}^0$ on the top side of the surface S identically vanishes outside the contact region whereas, within the contact region, the tangential components of $\mathbf{t}^0$ vanish and the normal displacement is prescribed in terms of the indentation depth d and the indentor profile $\delta(r)$, i.e.,

$$\begin{aligned} &t_i^0 = 0 && \text{for } r > a \\ &t_\alpha^0 = 0, u_3^s = d - \delta(r) && \text{for } r \leqslant a \end{aligned} \tag{11}$$

3.3. General solution for bulk

A general solution for stress and displacement fields within the bulk Ω^b, for an axisymmetric case, can readily be obtained in terms of the Love's strain potential $\Phi = \Phi(r,z)$ in the cylindrical coordinate system (r,θ,z) as follows (Sneddon, 1951; Selvadurai, 2000)

$$\sigma_{rr} = \lambda\nabla^2\left(\frac{\partial\Phi}{\partial z}\right) - 2(\lambda+\mu)\frac{\partial^3\Phi}{\partial r^2\partial z} \tag{12a}$$

$$\sigma_{\theta\theta} = \lambda\nabla^2\left(\frac{\partial\Phi}{\partial z}\right) - \frac{2(\lambda+\mu)}{r}\frac{\partial^2\Phi}{\partial r\partial z} \tag{12b}$$

$$\sigma_{zz} = (3\lambda+4\mu)\nabla^2\left(\frac{\partial\Phi}{\partial z}\right) - 2(\lambda+\mu)\frac{\partial^3\Phi}{\partial z^3} \tag{12c}$$

$$\sigma_{rz} = (\lambda+2\mu)\frac{\partial}{\partial r}(\nabla^2\Phi) - 2(\lambda+\mu)\frac{\partial^3\Phi}{\partial z^2\partial r} \tag{12d}$$

$$u_r = -\frac{\lambda+\mu}{\mu}\frac{\partial^2\Phi}{\partial r\partial z} \tag{12e}$$

$$u_z = \frac{\lambda+2\mu}{\mu}\nabla^2\Phi - \frac{\lambda+\mu}{\mu}\frac{\partial^2\Phi}{\partial z^2} \tag{12f}$$

where Φ is governed by a bi-harmonic equation $\nabla^2(\nabla^2\Phi) = 0$ with $\nabla^2 = \frac{\partial^2}{\partial r^2} + \frac{1}{r}\frac{\partial}{\partial r} + \frac{\partial^2}{\partial z^2}$ denoting an axisymmetric Laplace operator. By applying Hankel integral transforms, the bi-harmonic equation can be reduced to

$$\left(\frac{d^2}{dz^2} - \xi^2\right)^2 G(\xi,z) = 0 \tag{13}$$

where $G(\xi,z) = \int_0^\infty r\Phi J_0(\xi r)dr$ and $J_n(\xi)$ denotes the first order Bessel functions of order n. The general solution of (13) is given by

$$G(\xi,z) = (A+Bz)e^{-\xi z} + (C+Dz)e^{\xi z} \tag{14}$$

where A, B, C and D are arbitrary functions of ξ that can be determined from boundary conditions.

The general solution for the displacements and stresses can be subsequently transformed into relations involving $G(\xi,z)$ and its derivatives with respect to z by using Hankel transform inversion and the relations (12a)–(12f). Final results are given by

$$\sigma_{rr} = \int_0^\infty \xi\left[\lambda\frac{d^3G}{dz^3} + (\lambda+2\mu)\xi^2\frac{dG}{dz}\right]J_0(\xi r)d\xi - \frac{2(\lambda+\mu)}{r}\int_0^\infty \xi^2\frac{dG}{dz}J_1(\xi r)d\xi \tag{15a}$$

$$\sigma_{\theta\theta} = \lambda\int_0^\infty \xi\left[\frac{d^3G}{dz^3} - \xi^2\frac{dG}{dz}\right]J_0(\xi r)d\xi + \frac{2(\lambda+\mu)}{r}\int_0^\infty \xi^2\frac{dG}{dz}J_1(\xi r)d\xi \tag{15b}$$

$$\sigma_{zz} = \int_0^\infty \xi\left[(\lambda+2\mu)\frac{d^3G}{dz^3} - (3\lambda+4\mu)\xi^2\frac{dG}{dz}\right]J_0(\xi r)d\xi \tag{15c}$$

$$\sigma_{rz} = \int_0^\infty \xi^2\left[\lambda\frac{d^2G}{dz^2} + (\lambda+2\mu)\xi^2 G\right]J_1(\xi r)d\xi \tag{15d}$$

$$u_r = \frac{\lambda+\mu}{\mu}\int_0^\infty \xi^2\frac{dG}{dz}J_1(\xi r)d\xi \tag{15e}$$

$$u_z = \int_0^\infty \xi\left[\frac{d^2G}{dz^2} - \frac{\lambda+2\mu}{\mu}\xi^2 G\right]J_0(\xi r)d\xi \tag{15f}$$

Note that u_θ, $\sigma_{r\theta}$ and $\sigma_{z\theta}$ vanish due to the symmetry and all non-zero field variables are obviously independent of θ. By invoking the remote condition that the displacements and stresses approach zero as $z \to \infty$, C and D must vanish and the function $G(\xi,z)$ therefore reduces to

$$G(\xi,z)=(A+Bz)e^{-\xi z} \tag{16}$$

Upon substituting (16) into (15), components of stresses and displacements can be expressed in terms of A and B by

$$\frac{\sigma_{rr}}{2(\lambda+\mu)}=\int_0^\infty \xi^3\left[-\xi A+\left(\frac{2\lambda+\mu}{\lambda+\mu}-\xi z\right)B\right]e^{-\xi z}J_0(\xi r)d\xi-\frac{1}{r}\int_0^\infty \xi^2[-\xi A+(1-\xi z)B]e^{-\xi z}J_1(\xi r)d\xi \tag{17}$$

$$\frac{\sigma_{\theta\theta}}{2(\lambda+\mu)}=\frac{\lambda}{\lambda+\mu}\int_0^\infty \xi^3 Be^{-\xi z}J_0(\xi r)d\xi+\frac{1}{r}\int_0^\infty \xi^2[-\xi A+(1-\xi z)B]e^{-\xi z}J_1(\xi r)d\xi \tag{18}$$

$$\frac{\sigma_{zz}}{2(\lambda+\mu)}=\int_0^\infty \xi^3\left[\xi A+\left(\frac{\mu}{\lambda+\mu}+\xi z\right)B\right]e^{-\xi z}J_0(\xi r)d\xi \tag{19}$$

$$\frac{\sigma_{rz}}{2(\lambda+\mu)}=\int_0^\infty \xi^3\left[\xi A-\left(\frac{\lambda}{\lambda+\mu}-\xi z\right)B\right]e^{-\xi z}J_1(\xi r)d\xi \tag{20}$$

$$u_r=\frac{\lambda+\mu}{\mu}\int_0^\infty \xi^2[-\xi A+(1-\xi z)B]e^{-\xi z}J_1(\xi r)d\xi \tag{21}$$

$$u_z=-\frac{\lambda+\mu}{\mu}\int_0^\infty \xi^2\left[\xi A+\left(\frac{2\mu}{\lambda+\mu}+\xi z\right)B\right]e^{-\xi z}J_0(\xi r)d\xi \tag{22}$$

3.4. Governing equation for A and B

For an axisymmetric case, the in-plane equilibrium equations (7) and the out-of-plane equilibrium equation (8) simply reduce to the following equilibrium equations in the radial direction and z-direction, respectively:

$$\kappa^s\left(\frac{d^2u_r^s}{dr^2}+\frac{1}{r}\frac{du_r^s}{dr}-\frac{u_r^s}{r^2}\right)+t_r^s+t_r^0=0 \tag{23}$$

$$\tau^s\left(\frac{d^2u_z^s}{dr^2}+\frac{1}{r}\frac{du_z^s}{dr}\right)+t_z^s+t_z^0=0 \tag{24}$$

where κ^s is a material constant defined by $\kappa^s=2\mu^s+\lambda^s$; u_r^s and u_z^s denote the displacement of the surface in the radial and z-directions; t_r^s and t_z^s denote components of the traction $\mathbf{t}^s$ in the radial and z-directions; and t_r^0 and t_z^0 denote components of the traction $\mathbf{t}^0$ in the radial and z-directions. By using the continuity conditions (9) and the relation (10) for the axisymmetric case (i.e., $u_r^s=u_r|_{z=0}$, $u_z^s=u_z|_{z=0}$, $t_r^s=-t_r^b=\sigma_{rz}|_{z=0}$, $t_z^s=-t_z^b=\sigma_{zz}|_{z=0}$), Eqs. (23) and (24) can be rewritten in terms of the displacement and traction on the surface of the bulk as

$$\kappa^s\left(\frac{d^2u_r}{dr^2}+\frac{1}{r}\frac{du_r}{dr}-\frac{u_r}{r^2}\right)\Bigg|_{z=0}+\sigma_{rz}|_{z=0}+t_r^0=0 \tag{25}$$

$$\tau^s\left(\frac{d^2u_z}{dr^2}+\frac{1}{r}\frac{du_z}{dr}\right)\Bigg|_{z=0}+\sigma_{zz}|_{z=0}+t_z^0=0 \tag{26}$$

By enforcing the boundary conditions (11) along with the continuity condition $u_z^s=u_z|_{z=0}$ and the relations (25) and (26), it leads to a set of mixed boundary conditions for the bulk Ω^b as

$$u_z|_{z=0}=d-\delta(r),\quad 0\leqslant r\leqslant a \tag{27}$$

$$\sigma_{zz}|_{z=0}+\tau^s\left(\frac{d^2u_z}{dr^2}+\frac{1}{r}\frac{du_z}{dr}\right)\Bigg|_{z=0}=0,\quad a<r<\infty \tag{28}$$

$$\sigma_{rz}|_{z=0}+\kappa^s\left(\frac{d^2u_r}{dr^2}+\frac{1}{r}\frac{du_r}{dr}-\frac{u_r}{r^2}\right)\Bigg|_{z=0}=0,\quad 0\leqslant r<\infty \tag{29}$$

Upon substituting (20) and (21) into the boundary condition (29), it yields a relation between A and B:

$$A\xi(1+\Lambda_0\xi)=\left(\frac{\lambda}{\lambda+\mu}+\Lambda_0\xi\right)B \tag{30}$$

where $\Lambda_0=\kappa^s/2\mu$. By enforcing the mixed boundary conditions (27) and (28) along with the relation (30), we obtain a pair of integral equations:

$$-\int_0^\infty \xi^2\left[\frac{(\lambda+2\mu)+(\lambda+3\mu)\Lambda_0\xi}{\mu(1+\Lambda_0\xi)}\right]BJ_0(\xi r)d\xi = d-\delta(r), \quad 0\leqslant r\leqslant a \tag{31}$$

$$\int_0^\infty \xi^3\left\{\frac{2\mu[(\lambda+\mu)+(\lambda+2\mu)\Lambda_0\xi]+\tau^s\xi[(\lambda+2\mu)+(\lambda+3\mu)\Lambda_0\xi]}{\mu^2(1+\Lambda_0\xi)}\right\}BJ_0(\xi r)d\xi = 0, \quad a<r<\infty \tag{32}$$

The dual integral equations (31) and (32) constitute a complete set of equations for determining the unknown function $B = B(\xi)$ for $\xi\in[0,\infty)$. By introducing two functions $\phi = \phi(\xi)$ and $w = w(\xi)$ such that

$$\phi(\xi) = \xi^3\left\{\frac{2\mu[(\lambda+\mu)+(\lambda+2\mu)\Lambda_0\xi]+\tau^s\xi[(\lambda+2\mu)+(\lambda+3\mu)\Lambda_0\xi]}{\mu^2(1+\Lambda_0\xi)}\right\}B \tag{33}$$

$$\xi^{-1}\phi(\xi)[1+w(\xi)] = \xi^2\left[\frac{(\lambda+2\mu)+(\lambda+3\mu)\Lambda_0\xi}{\mu(1+\Lambda_0\xi)}\right]B \tag{34}$$

the integral equations (31) and (32) can be further simplified to

$$\int_0^\infty \bar{\xi}^{-1}\bar{\phi}(\bar{\xi})[1+w(\bar{\xi})]J_0(\bar{\xi}\bar{r})d\bar{\xi} = \bar{f}(\bar{r}), \quad 0\leqslant\bar{r}\leqslant 1 \tag{35}$$

$$\int_0^\infty \bar{\phi}(\bar{\xi})J_0(\bar{\xi}\bar{r})d\bar{\xi} = 0, \quad 1<\bar{r}<\infty \tag{36}$$

where $\bar{f}(\bar{r}) = f(\bar{r})/a = -[\bar{d}-\bar{\delta}(\bar{r})]$, $\bar{\delta}(\bar{r}) = \delta(\bar{r})/a$, $\bar{d} = d/a$, $\bar{\xi} = \xi a$, $\bar{r} = r/a$, and $\bar{\phi} = \bar{\phi}(\bar{\xi}) = \phi(\bar{\xi})/a$. The function $\bar{\phi} = \bar{\phi}(\bar{\xi})$ becomes the primary unknown of the dual integrals (35) and (36) while the function $w = w(\bar{\xi})$ can be obtained directly from (33) and (34) as

$$w(\bar{\xi}) = \frac{(\bar{\lambda}+2)+(\bar{\lambda}+3)\overline{\Lambda}_0\bar{\xi}}{2[(\bar{\lambda}+1)+(\bar{\lambda}+2)\overline{\Lambda}_0\bar{\xi}]+\overline{\tau}^s\bar{\xi}[(\bar{\lambda}+2)+(\bar{\lambda}+3)\overline{\Lambda}_0\bar{\xi}]}-1 \tag{37}$$

where $\bar{\lambda} = \lambda/\mu$, $\overline{\Lambda}_0 = \Lambda_0/a$ and $\overline{\tau}^s = \tau^s/(\mu a)$. It is evident from (37) that the function $w = w(\bar{\xi})$ possesses a limit equal to –1 as $\bar{\xi}\to\infty$. This condition renders the technique employed by Zhao (2009) inapplicable to determine the unknown function $\bar{\phi} = \bar{\phi}(\bar{\xi})$.

To construct a solution of the dual integral equations of the type (35) and (36), a technique proposed by Sneddon (1966) and Mandal (1988) is adopted. By following their procedures, the dual integral equations (35) and (36) can be reduced to a Fredholm integral equation of the second kind of the form

$$\bar{\phi}(\bar{\xi}) = \frac{2\bar{\xi}}{\pi}\int_0^1 \cos(\bar{\xi}t)dt\frac{d}{dt}\int_0^t \frac{u\bar{f}(u)du}{\sqrt{t^2-u^2}} - \frac{\bar{\xi}}{\pi}\int_0^\infty \frac{w(u)\bar{\phi}(u)}{u}\left\{\frac{\sin(u+\bar{\xi})}{u+\bar{\xi}}+\frac{\sin(u-\bar{\xi})}{u-\bar{\xi}}\right\}du \tag{38}$$

It can be seen from (38) that the function $\bar{f}(u)$ is merely related to the indentor profile and the function $w(u)$ is related to the boundary conditions involving the surface stress parameters. This single integral equation (38) is in a form well-suited for constructing the numerical solution for $\bar{\phi} = \bar{\phi}(\bar{\xi})$. Once the function $\bar{\phi} = \bar{\phi}(\bar{\xi})$ is solved, the functions A and B can be subsequently determined from (30) and (33), respectively, and the complete elastic fields within the half-space can also be obtained from (17)–(22). In addition, the magnitude of the total indentation force P producing the indentation depth d can be obtained by integrating the contact pressure, i.e., the same quantity as that appears on left hand side of Eq. (28) with the negative sign, over the area of the contact region.

It is worth noting that in the absence of surface energy effects, the above formulation can be readily specialized to a classical indentation problem by setting $\overline{\Lambda}_0 = 0$ and $\overline{\tau}^s = 0$. The function $w = w(\bar{\xi})$ in (37) simply reduces to a constant w^* given below:

$$w^* = \frac{\bar{\lambda}+2}{2(\bar{\lambda}+1)}-1 \tag{39}$$

The dual integral equations (35) and (36) for this special case become

$$\int_0^\infty \bar{\xi}^{-1}\bar{\phi}(\bar{\xi})J_0(\bar{\xi}\bar{r})d\bar{\xi} = f^*(\bar{r}), \quad 0\leqslant\bar{r}\leqslant 1 \tag{40}$$

$$\int_0^\infty \bar{\phi}(\bar{\xi})J_0(\bar{\xi}\bar{r})d\bar{\xi} = 0, \quad 1<\bar{r}<\infty \tag{41}$$

where $f^*(\bar{r}) = \bar{f}(\bar{r})/(1+w^*)$. A set of dual integral equations (40) and (41) was solved analytically by Sneddon (1965).

4. Numerical implementation

Due to the complexity of the Fredholm integral equation of the second kind formulated in the previous section, a numerical procedure must be employed to construct an approximate solution for $\bar{\phi} = \bar{\phi}(\bar{\xi})$. Essential ingredients for such numerical implementation including the convergence study are briefly summarized below.

4.1. Solution approximation

It is evident that the second integral of the Fredholm integral equation (38) is an improper integral with an infinite upper limit and the involved primary unknown function $\bar{\phi} = \bar{\phi}(\bar{\xi})$ is defined on a semi-infinite interval $[0,\infty)$. Before constructing an approximate solution for $\bar{\phi} = \bar{\phi}(\bar{\xi})$, the domain of integration of the improper integral is first truncated from $[0,\infty)$ to $[0,\bar{\xi}_R]$ where $\bar{\xi}_R$ is a finite real number. The truncated Fredholm integral equation is given by

$$\bar{\phi}(\bar{\xi}) = \frac{2\bar{\xi}}{\pi}\int_0^1 \cos(\bar{\xi}t)dt\frac{d}{dt}\int_0^t \frac{u\bar{f}(u)du}{\sqrt{t^2-u^2}} - \frac{\bar{\xi}}{\pi}\int_0^{\bar{\xi}_R} \frac{w(u)\bar{\phi}(u)}{u}\left\{\frac{\sin(u+\bar{\xi})}{u+\bar{\xi}} + \frac{\sin(u-\bar{\xi})}{u-\bar{\xi}}\right\}du \tag{42}$$

The unknown function $\bar{\phi} = \bar{\phi}(\bar{\xi})$ over the entire truncated domain $[0,\bar{\xi}_R]$ can be approximated by

$$\bar{\phi}(\bar{\xi}) = \bar{\xi}\sum_{j=1}^{n}\alpha_j\psi_j(\bar{\xi}) \tag{43}$$

where α_j are unknown nodal quantities to be determined, $\psi_j(\bar{\xi})$ are nodal basis functions, and n is the number of nodes resulting from the discretization. It is worth noting that the approximation (43) results from a special property of the function $\bar{\phi}$ at the origin, more specifically, this function vanishes at the origin of order $\mathcal{O}(\bar{\xi})$. In addition, in the present study, the nodal basis functions $\psi_j(\bar{\xi})$ are constructed systematically in an element-wise fashion based on standard isoparametric, quadratic elements.

Upon inserting the approximation (43) into (42) and then dividing the entire equation by $\bar{\xi}$, it leads to a discretized integral equation

$$\sum_{j=1}^{n}\mathcal{M}_j(\bar{\xi})\alpha_j = \mathcal{F}(\bar{\xi}) \tag{44}$$

where the integrals $\mathcal{M}_j(\bar{\xi})$ and $\mathcal{F}(\bar{\xi})$ are defined on the truncated domain $[0,\bar{\xi}_R]$ by

$$\mathcal{M}_j(\bar{\xi}) = \psi_j(\bar{\xi}) + \int_0^{\bar{\xi}_R}\psi_j(u)K(\bar{\xi},u)du \tag{45}$$

$$\mathcal{F}(\bar{\xi}) = \frac{2}{\pi}\int_0^1 \cos(\bar{\xi}t)dt\frac{d}{dt}\int_0^t \frac{u\bar{f}(u)du}{\sqrt{t^2-u^2}} \tag{46}$$

$$K(\bar{\xi},u) = \frac{w(u)}{\pi}\left\{\frac{\sin(u+\bar{\xi})}{u+\bar{\xi}} + \frac{\sin(u-\bar{\xi})}{u-\bar{\xi}}\right\} \tag{47}$$

It can readily be verified that the kernel $K(\bar{\xi},u)$ is regular for any pair of points $(\bar{\xi},u)$ and, as a result, $\mathcal{M}_j(\bar{\xi})$ involves only an regular integral for all $\bar{\xi}\in[0,\bar{\xi}_R]$. The integral $\mathcal{F}(\bar{\xi})$ is given in terms of a double line integral whose inner integrand involves the prescribed profile of the indentor and is only weakly singular at $u = t$. To obtain a better form well-suited for numerical integration, an integration by parts is performed along with applying a special variable transformation (i.e., $u = t\sin\theta$) to remove such singularity and this, finally, leads to

$$\mathcal{F}(\bar{\xi}) = \frac{2\bar{\xi}}{\pi}\int_0^1 \sin(\bar{\xi}t)\int_0^{\pi/2} u\bar{f}(u)|_{u=t\sin\theta}d\theta dt + \frac{2\cos(\bar{\xi})}{\pi}\int_0^{\pi/2} u\bar{f}(u)|_{u=\sin\theta}d\theta \tag{48}$$

To obtain a sufficient number of equations to solve for the unknown constants α_j, a collocation-based technique is utilized. In particular, the discretized integral equation (44) is collocated (or, equivalently, forced to be satisfied) at all nodes $\bar{\xi} = \bar{\xi}_i$ (for $i = 1,2,3,\ldots,n$) and this leads to a set of n linear algebraic equations governing the nodal quantities α_j as follows

$$\mathbf{M}\boldsymbol{\alpha} = \mathbf{F} \tag{49}$$

where $\boldsymbol{\alpha} = \{\alpha_1,\alpha_2,\ldots,\alpha_n\}^T$ is vector of nodal quantities and entries of the coefficient matrix $\mathbf{M}$ and the prescribed vector $\mathbf{F}$ are given by

$$[\mathbf{M}]_{ij} = \mathcal{M}_j(\bar{\xi}_i) = \psi_j(\bar{\xi}_i) + \int_0^{\bar{\xi}_R}\psi_j(u)K(\bar{\xi}_i,u)du \tag{50}$$

$$[\mathbf{F}]_i = \mathcal{F}(\bar{\xi}_i) = \frac{2\bar{\xi}_i}{\pi}\int_0^1 \sin(\bar{\xi}_i t)\int_0^{\pi/2} u\bar{f}(u)|_{u=t\sin\theta}d\theta dt + \frac{2\cos(\bar{\xi}_i)}{\pi}\int_0^{\pi/2} u\bar{f}(u)|_{u=\sin\theta}d\theta \tag{51}$$

It is evident from (50) and (51) that entries of the matrix $\mathbf{M}$ and the prescribed vector $\mathbf{F}$ involve only regular integrals. Thus, a standard Gaussian quadrature can be applied to efficiently and accurately evaluate such integrals. Note also that, for some special indentor profiles, the integral $\mathcal{F}(\bar{\xi})$ admits an explicit expression and, as a result, construction of the corresponding vector $\mathbf{F}$ requires no numerical integration. For instance, the integral $F(\bar{\xi})$ can be obtained for a flat-ended cylindrical indentor (i.e., $\bar{\delta}(\bar{r}) = 0$) and a paraboloidal indentor (i.e., $\bar{\delta}(\bar{r}) = \alpha a\bar{r}^2$ where α is a constant representing the slenderness of the indentor profile) as

$$\text{Flat-ended cylindrical indentor}: \mathcal{F}(\bar{\xi}) = -\frac{2\bar{d}}{\pi\bar{\xi}}\sin(\bar{\xi}) \tag{52}$$

$$\text{Paraboloidal indentor}: F(\bar{\xi}) = -\frac{2\bar{d}}{\pi\bar{\xi}}\sin(\bar{\xi}) + \frac{4\alpha a}{\pi\bar{\xi}^3}\{2\bar{\xi}\cos(\bar{\xi}) + (-2+\bar{\xi}^2)\sin(\bar{\xi})\} \tag{53}$$

Once the nodal quantities α_j are obtained by solving a system of linear equations (49), the approximate solution for $\bar{\phi} = \bar{\phi}(\bar{\xi})$ can readily be computed from (43) for any $\bar{\xi}$ in the truncated domain $[0, \bar{\xi}_R]$ and then functions $\overline{A} = \overline{A}(\bar{\xi}) = A(\bar{\xi})/a^5$ and $\overline{B} = \overline{B}(\bar{\xi}) = B(\bar{\xi})/a^4$ can be determined at any $\bar{\xi} \in [0, \bar{\xi}_R]$ by directly solving the relations (30) and (33) with the proper normalization. The explicit formulae for $\overline{A} = \overline{A}(\bar{\xi})$ and $\overline{B} = \overline{B}(\bar{\xi})$ in terms of $\bar{\phi} = \bar{\phi}(\bar{\xi})$ are given respectively by

$$A(\bar{\xi}) = \frac{\left(\frac{\bar{\lambda}}{\bar{\lambda}+1} + \overline{\Lambda}_0\bar{\xi}\right)\bar{\phi}(\bar{\xi})}{\bar{\xi}^4\left\{2[(\bar{\lambda}+1) + (\bar{\lambda}+2)\overline{\Lambda}_0\bar{\xi}] + \overline{\tau}^s\bar{\xi}[(\bar{\lambda}+2) + (\bar{\lambda}+3)\overline{\Lambda}_0\bar{\xi}]\right\}} \tag{54}$$

$$B(\bar{\xi}) = \frac{(1 + \overline{\Lambda}_0\bar{\xi})\bar{\phi}(\bar{\xi})}{\bar{\xi}^3\left\{2\left[(\bar{\lambda}+1) + (\bar{\lambda}+2)\overline{\Lambda}_0\bar{\xi}\right] + \overline{\tau}^s\bar{\xi}[(\bar{\lambda}+2) + (\bar{\lambda}+3)\overline{\Lambda}_0\bar{\xi}]\right\}} \tag{55}$$

The normalized stress and displacement fields within the bulk can then be approximated by the integral relations (17)–(22) with their upper limit being replaced by $\bar{\xi}_R$, i.e.,

$$\bar{\sigma}_{rr}(\bar{r},\bar{z}) = \frac{\sigma_{rr}}{2(\lambda+\mu)} = \int_0^{\bar{\xi}_R}\bar{\xi}^3\left[-\bar{\xi}\overline{A} + \left(\frac{2\bar{\lambda}+1}{\bar{\lambda}+1} - \bar{\xi}\bar{z}\right)\overline{B}\right]e^{-\bar{\xi}\bar{z}}J_0(\bar{\xi}\bar{r})d\bar{\xi} - \frac{1}{\bar{r}}\int_0^{\bar{\xi}_R}\bar{\xi}^2[-\bar{\xi}\overline{A} + (1-\bar{\xi}\bar{z})\overline{B}]e^{-\bar{\xi}\bar{z}}J_1(\bar{\xi}\bar{r})d\bar{\xi} \tag{56}$$

$$\bar{\sigma}_{\theta\theta}(\bar{r},\bar{z}) = \frac{\sigma_{\theta\theta}}{2(\lambda+\mu)} = \frac{\bar{\lambda}}{\bar{\lambda}+1}\int_0^{\bar{\xi}_R}\bar{\xi}^3\overline{B}e^{-\bar{\xi}\bar{z}}J_0(\bar{\xi}\bar{r})d\bar{\xi} + \frac{1}{\bar{r}}\int_0^{\bar{\xi}_R}\bar{\xi}^2[-\bar{\xi}\overline{A} + (1-\bar{\xi}\bar{z})\overline{B}]e^{-\bar{\xi}\bar{z}}J_1(\bar{\xi}\bar{r})d\bar{\xi} \tag{57}$$

$$\bar{\sigma}_{zz}(\bar{r},\bar{z}) = \frac{\sigma_{zz}}{2(\lambda+\mu)} = \int_0^{\bar{\xi}_R}\bar{\xi}^3\left[\bar{\xi}\overline{A} + \left(\frac{1}{\bar{\lambda}+1} + \bar{\xi}\bar{z}\right)\overline{B}\right]e^{-\bar{\xi}\bar{z}}J_0(\bar{\xi}\bar{r})d\bar{\xi} \tag{58}$$

$$\bar{\sigma}_{rz}(\bar{r},\bar{z}) = \frac{\sigma_{rz}}{2(\lambda+\mu)} = \int_0^{\bar{\xi}_R}\bar{\xi}^3\left[\bar{\xi}\overline{A} - \left(\frac{\bar{\lambda}}{\bar{\lambda}+1} - \bar{\xi}\bar{z}\right)\overline{B}\right]e^{-\bar{\xi}\bar{z}}J_1(\bar{\xi}\bar{r})d\bar{\xi} \tag{59}$$

$$\bar{u}_r(\bar{r},\bar{z}) = \frac{u_r}{a} = (\bar{\lambda}+1)\int_0^{\bar{\xi}_R}\bar{\xi}^2\left[-\bar{\xi}\overline{A} + (1-\bar{\xi}\bar{z})\overline{B}\right]e^{-\bar{\xi}\bar{z}}J_1(\bar{\xi}\bar{r})d\bar{\xi} \tag{60}$$

$$\bar{u}_z(\bar{r},\bar{z}) = \frac{u_z}{a} = -(\bar{\lambda}+1)\int_0^{\bar{\xi}_R}\bar{\xi}^2\left[\bar{\xi}\overline{A} + \left(\frac{2}{\bar{\lambda}+1} + \bar{\xi}\bar{z}\right)\overline{B}\right]e^{-\bar{\xi}\bar{z}}J_0(\bar{\xi}\bar{r})d\bar{\xi} \tag{61}$$

where $\bar{z} = z/a$. To evaluate truncated Hankel transform inversions appearing in (56)–(61) for any pair of points $(\bar{r},\bar{z})$, standard Gaussian quadrature is again employed. It is important to point out that presence of the exponential term $e^{-\bar{\xi}\bar{z}}$ in the integrand significantly increases the rate of decay of the unfavorable oscillated behavior arising from the Bessel functions $J_n(\bar{\xi})$ for $\bar{z} > 0$ and, as a result, the associated integrals converges very rapidly with a relatively low $\bar{\xi}_R$. On the contrary, such exponential term becomes unity on a surface of the bulk (i.e., $\bar{z} = 0$) and, due to the slow rate of decay of the Bessel functions, it generally requires a sufficiently large $\bar{\xi}_R$ for those integrals associated with $\bar{z} = 0$ to achieve their converged value.

Once the elastic fields within the bulk are obtained, other interesting quantities can also be computed. For instance, the normalized contact pressure under the indentor, denoted by $\bar{p} = \bar{p}(\bar{r})$, can readily be obtained from

$$\bar{p}(\bar{r}) = \frac{p}{2(\lambda+\mu)} = -\left[\bar{\sigma}_{zz}(\bar{r},\bar{z}=0) + \frac{\overline{\tau}^s\hat{\nabla}^2\bar{u}_z(\bar{r},\bar{z}=0)}{2(\bar{\lambda}+1)}\right], \quad 0 \leqslant \bar{r} \leqslant 1 \tag{62}$$

where $\hat{\nabla}^2 = \frac{d^2}{d\bar{r}^2} + \frac{1}{\bar{r}}\frac{d}{d\bar{r}}$. It is remarked that the Laplacian of the normal displacement appearing on the right hand side of (62) can directly be evaluated using the prescribed boundary condition (27). The normalized indentation force $\overline{P}$ can further be computed by integrating the contact pressure $\bar{p} = \bar{p}(\bar{r})$ over the contact region as follows

$$\bar{P} = \frac{P}{2a^2(\lambda+\mu)} = \int_0^{2\pi}\int_0^1 \bar{p}(\bar{r})\bar{r}d\bar{r}d\theta = 2\pi\int_0^1 \bar{p}(\bar{r})\bar{r}d\bar{r} \tag{63}$$

4.2. Determination of contact radius for smooth-contact indentor

For a smooth-contact indentor, the contact radius a is unknown a priori and must be determined first before other quantities of interest can be obtained. It is remarked that once the contact radius a is known, there is no difference between a

solution procedure for both smooth-contact and nonsmooth-contact indentors. To solve for a final contact radius a that corresponds to a given indentation depth d, a physically admissible condition associated with the continuity of the vertical stress at $r = a$ is utilized. However, the explicit or closed-form relationship between those two parameters (a and d) cannot be obtained due to the complexity of the boundary value problem accounted for the surface energy effects.

4.3. Convergence study

For the proposed numerical technique, three key factors that affect the accuracy of the approximate solutions are the truncated parameter $\bar{\xi}_R$, the number of elements employed in the discretization, and the number of integration points used in standard Gaussian quadrature. Extensive numerical experiments have been performed to choose a proper truncated domain, the level of mesh refinement and optimal quadrature to ensure the convergence and accuracy of numerical results. Such investigation is briefly discussed below.

The number of Gauss points required in the numerical integration can be significant to accurately integrate oscillating and complex integrands (resulting from the Bessel functions, $\bar{\phi} = \bar{\phi}(\bar{\xi})$, and the kernel $K(\bar{\xi}, u)$). From numerical experiments, it is found that as the size of elements decreases (i.e., the number of elements in the discretization increases), it only requires few Gauss points to achieve highly accurate results since the integrand on each element exhibits milder variation without oscillating behavior.

To investigate the level of mesh refinement required to obtain the converged results, we perform experiments for a given truncated domain $[0, \bar{\xi}_R]$. A series of meshes for the fixed interval $[0, \bar{\xi}_R]$ is constructed and then used in the analysis. The number of elements in the discretization (N) is increased until a converged solution (for a specified tolerance) is attained for a fixed $\bar{\xi}_R$. By repeating the analysis for various values of $\bar{\xi}_R$, a ratio $N/\bar{\xi}_R$ (representing the level of mesh refinement) greater than or equal to 1 is found to yield sufficiently fine meshes.

To obtain a proper truncated domain that optimizes the computational cost but, at the same time, yields accurate results, we next investigate the convergence of approximate solutions with respect to the truncated parameter $\bar{\xi}_R$. From such study, it can be concluded that the truncated parameter $\bar{\xi}_R$ to obtain converged results for the non-smooth contact indentor is much larger than that for the smooth contact one. This is due primarily to the singularity induced at the boundary of the contact region of the non-smooth contact indentor. On the basis of extensive numerical experiments, the suggested values of the truncated parameter $\bar{\xi}_R$ in the analysis of non-smooth contact and smooth contact indentors are approximately equal to 10,000 and 1,000, respectively. These values of $\bar{\xi}_R$ are therefore employed along with $N/\bar{\xi}_R = 1$ to obtain all numerical results presented further below.

5. Numerical results and discussion

Accuracy of the proposed numerical scheme is first verified by comparing computed results with available analytical solutions of the classical case (without the influence of surface stresses) for both smooth-contact and non-smooth-contact indentors. In the analysis, indentors with flat-ended and paraboloidal profiles are chosen to represent the non-smooth and smooth contacts, respectively. Results for both elastic fields and pressure beneath the indentor predicted by three different models (i.e., a model based on classical linear elasticity and two models accounted for surface stress effects with and without the out-of-plane contribution of the residual surface tension) are fully investigated and compared. In addition, some crucial findings are addressed.

5.1. Verification with analytical solutions

Consider an elastic half-space compressed by a rigid frictionless indentor with either a flat-ended cylindrical profile described by $\delta(r) = 0$ or a paraboloidal profile described by $\delta(r) = \alpha r^2$ where α is a constant. It is remarked that for both cases, the indentation depth d and the final radius of contact a are associated with the indentation force P. Without the influence of surface stresses, the analytical solutions derived by Sneddon (1965) are employed to validate the proposed formulation and numerical implementations.

In numerical experiments, the proposed solution scheme is specialized to treat the classical case by setting $\overline{\Lambda}_0 = 0$ and $\overline{\tau^s} = 0$. Though the properties of elastic materials in the current formulation can be chosen arbitrarily, to allow the comparison with results obtained by Zhao (2009) when the influence of surface stresses is considered, the same set of material properties is uitilized. Aluminum is used for the bulk material (Meyers & Chawla, 2009) whereas Al [1 1 1] is employed for the surface (Miller & Shenoy, 2000). The corresponding material constants are given by $\lambda = 58.17 \times 10^9$ N/m^2, $\mu = 26.13 \times 10^9$ N/m^2, $\Lambda_0 = 0.16707$ nm, $\lambda^s = 6.8511$ N/m, $\mu^s = -0.376$ N/m, $\tau^s = 1$ N/m. For convenience in the numerical study, following non-dimensional quantities: $r_0 = r/\Lambda_0$, $z_0 = z/\Lambda_0$, $a_0 = a/\Lambda_0$, $d_0 = d/\Lambda_0$ and $\alpha_0 = \alpha\Lambda_0$ are introduced. It is worth noting that although the classical solution is independent of Λ_0, use of this parameter in the normalization allows a direct comparison between non-classical and classical solutions.

In the case of a flat-ended cylindrical indentor with the contact radius $a_0 = 0.5$, comparisons between numerical solutions for the contact pressure and vertical displacement and the benchmark solutions are reported in Fig. 2(a) and (b), respectively. It is evidently found that results obtained from the present study are nearly indistinguishable from the analytical solutions

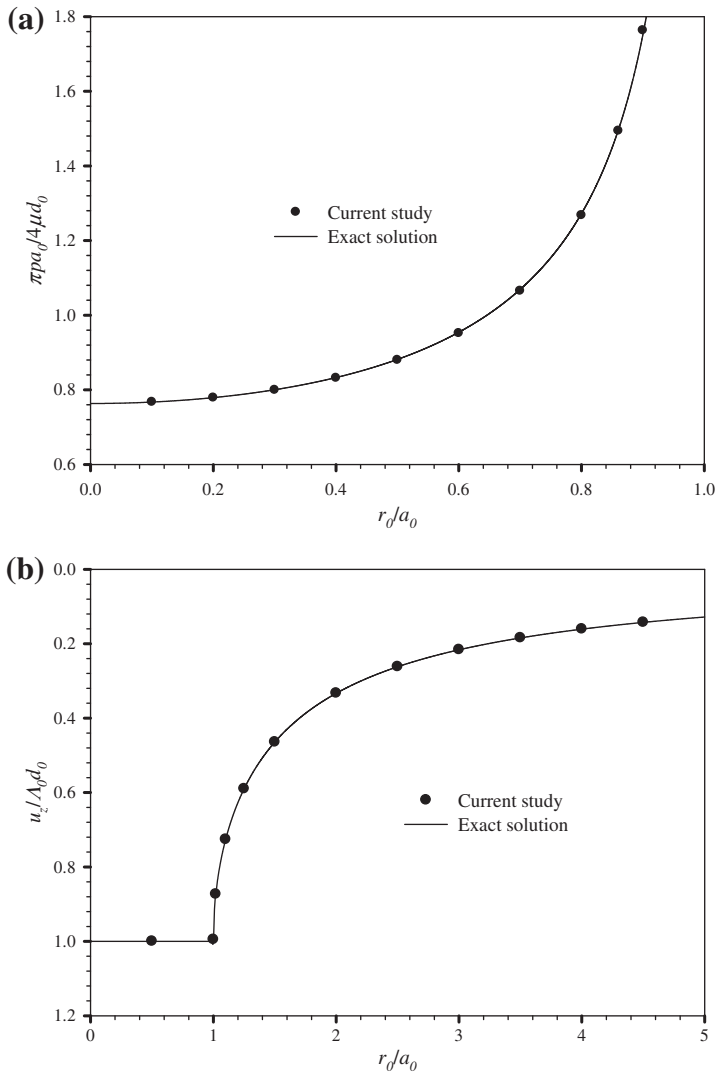

Fig. 2. Comparisons of classical numerical solutions with analytical solutions for flat-ended cylindrical indentor: (a) normalized contact pressure and (b) normalized vertical displacement.

proposed by Sneddon (1965). Another comparison is performed for the case of a paraboloidal indentor with $\alpha_0 = 0.5$. It can be obviously seen from Fig. 3(a) and (b) that two numerical solutions obtained from the present scheme, one is the contact pressure and the other is the vertical displacement at the free surface, again exhibit excellent agreement with the corresponding reference solutions. This additionally confirms the accuracy of the proposed technique.

5.2. Results of indentor with surface stress effects

From the high accuracy of numerical solutions obtained in the classical case, the proposed scheme is now convincingly applied to investigate the indentation problems with the influence of surface stress being incorporated. To allow comparisons with results obtained from Zhao (2009) and demonstrate the significant role of the residual surface tension τ^s, Gurtin–Murdoch model without the out-of-plane contribution of τ^s is also considered. Selected numerical results are reported and dicussed for both indentor profiles as follows.

5.2.1. Flat-ended cylindrical indentor

The case of an elastic half-space indented by a flat-ended cylindrical indentor with a specified contact radius a and indentation depth d is first examined. Note that this particular indentor is an example of a non-smooth-contact indentor since $d\delta/dr$ is not well-defined at $r = a$. Numerical results for elastic fields within the bulk are reported in Figs. 4–7.

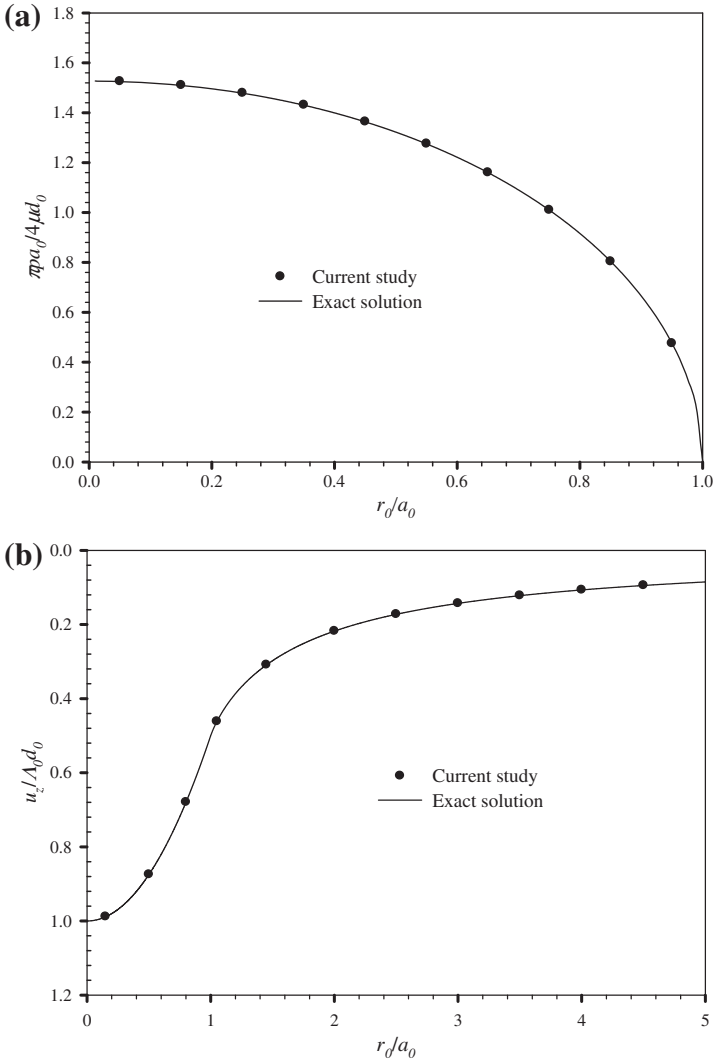

Fig. 3. Comparisons of classical numerical solutions with analytical solutions for paraboloidal indentor: (a) normalized contact pressure and (b) normalized vertical displacement.

It can be apparently seen from Fig. 4 that the distribution of the contact pressure under the indentor accounted for the surface stress effects possesses the same trend as that for the classical solution in which the singularity still exists at the edge of the indentor. Due to the integration of the out-of-plane contribution of the residual surface tension, the predicted contact pressure for this particular model is considerably less than those obtained from the other two models (i.e., the classical model and Gurtin–Murdoch model without the out-of-plane contribution of τ^s). In the analysis, three values of the normalized contact radius, $a_0 = 0.5$, 1.0 and 1.5, are considered to study the size-dependent behavior. It is found that when the radius of the indentor becomes smaller, the influence of surface stresses is comparatively larger. It is interesting to point out that when the contact pressure p has been normalized in a proper manner (e.g., normalized as $\pi p a_0/4\mu d_0$), size-dependent behavior due to the influence of surface stresses is significantly apparent and this phenomenon cannot be certainly observed from the solution predicted by the classical model (only one single dotted line is shown in spite of changing the contact radius a_0). It implies that the classical model completely ignores an inevitable material parameter (i.e., the intrinsic length Λ_0) and, as a result, it cannot capture the size-dependent behvior and yields a solution significantly different from those predicated by the other two models when the radius of the indentor becomes relatively small. However, the contact pressure under the larger indentor (i.e., larger contact radius a_0) for both models accounted for the surface stress effects converges monotonically to the classical solution.

The variations of the normalized vertical stress, $\pi\sigma_{zz}/4\mu\, d_0$, along the radial direction at four depths $z_0 = 0.1$, 0.5, 1.0 and 1.5 and for the contact radius $a_0 = 0.5$ are shown in Fig. 5. The vertical stress profiles indicate the strong influence of the surface stresses for a region relatively close to the indentor. In particular, at very small depth (i.e., $z_0 = 0.1$), the vertical stress

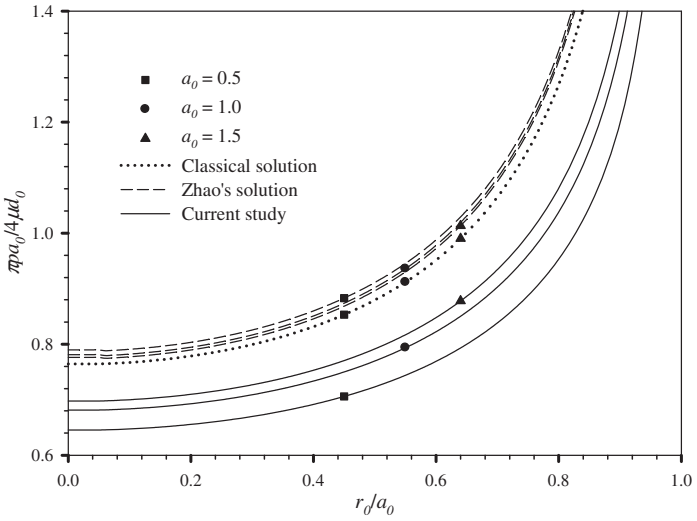

Fig. 4. Distribution of normalized contact pressure under flat-ended cylindrical indentor with various contact radii.

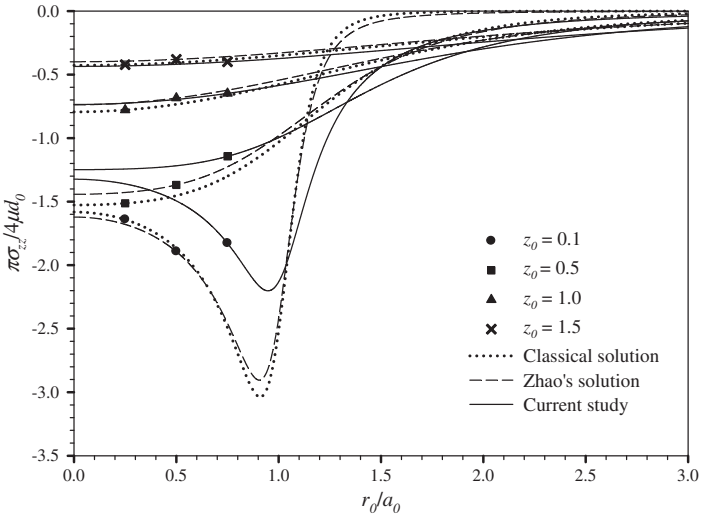

Fig. 5. Normalized vertical stress profiles for flat-ended cylindrical indentor with contact radius $a_0 = 0.5$ at various depths.

increases monotonically and reaches their peak values near $r_0/a_0 = 1$ and then starts to drop rapidly when r_0 increases. At larger depths, the vertical stress reaches its maximum at $r_0 = 0$ and decreases monotonically to zero as r_0 increases. It is evident that an ideal surface attached to the bulk of the current model distributes the localized indentation force to an area outside the contact region. As a direct consequence, the current model (i.e., Gurtin–Murdoch model with the out-of-plane contribution of τ^s) predicts the lower vertical stress under the indentor and higher vertical stress outside the contact region than those obtained from the other two models. However, such discrepancy becomes insignificant in the region far away from the indentor.

Numerical results for the normalized shear stress, $\pi\sigma_{rz}/4\mu d_0$, and the radial stress, $\pi\sigma_{rr}/4\mu d_0$, at various depths and for the contact radius $a_0 = 0.5$ are also presented in Fig. 6(a) and (b), respectively. Similar to the vertical stress, the magnitude of shear stresses along the radial direction predicted by the current model is generally lower than and higher than those obtained from the other two models for regions inside and outside the contact, respectively. The shear stress at any depth vanishes at $r_0 = 0$ due to the axisymmetry, reaches its peak value near the edge of the indentor ($r_0/a_0 = 1$), and starts to decay to zero for sufficiently large r_0. Nevertheless, such behavior is significantly different from that of the radial stress; for instance, the magnitude of the radial stress at $z_0 = 0.5$ obtained from the current model lies between those predicted by the other two models for a region inside the contact. As anticipated, the shear and radial stresses obtained from all three models for relatively large r_0 possess the same trend and decay monotonically to zero. The inflence of surface stresses is extremely small

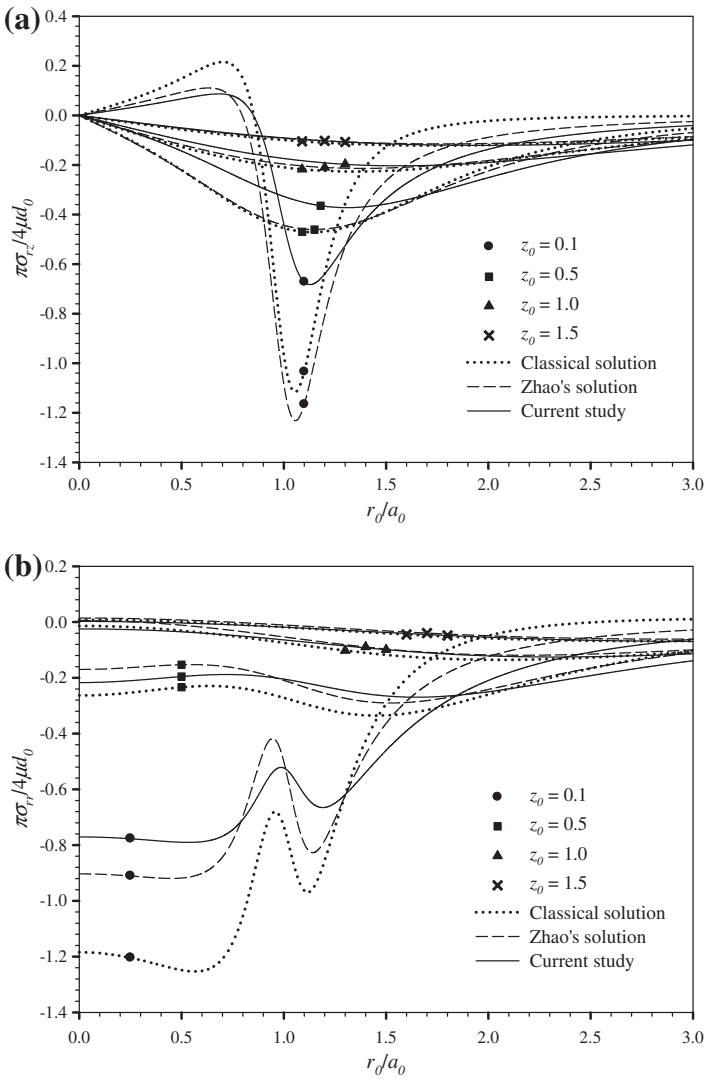

Fig. 6. Normalized stress profiles for flat-ended cylindrical indentor with contact radius $a_0 = 0.5$ at various depths: (a) shear stress and (b) radial stress.

for $z_0 \geqslant 1.5$ as clearly demonstrated by insignificant discrepancy between solutions obtained from the current and classical models.

According to results shown in Fig. 7(a) for the normalized vertical displacement, $u_z/\Lambda_0 d_0$, along the radial direction at five different depths, $z_0 = 0.0$, 0.1, 0.5, 1.0 and 1.5, and for contact radius $a_0 = 0.5$, the one predicted by the current model is comparatively higher than those obtained from the other two models due to the fact that higher indentation force is required to produce the same indentation depth resulting in the half-space Ω^b in the current model subjected to larger surface traction than the other two half-spaces. Unlike the solution for stresses, the vertical displacement from the present study exhibits a slower rate of decay for larger value of z_0, and it gradually converges to the other two solutions as r_0 increases. As a final set of results for this particular indentor, the normalized radial displacement, $u_r/\Lambda_0 d_0$, at four dfifferent depths, $z_0 = 0.1$, 0.5, 1.0 and 1.5, and for the same contact radius $a_0 = 0.5$ is reported in Fig. 7(b). Clearly, the radial displacement increases rapidly from zero at $r_0 = 0$ to its peak value at relatively small r_0, and then gradually decreases as r_0 increases. It should be noted that the surface stresses only influence the magnitude of the radial displacement while its distribution along the radial direction predicted by all three models is quite similar.

5.2.2. Paraboloidal indentor

Consider, next, a paraboloidal indentor with $\alpha_0 = 0.5$ acting on the elastic half-space with the indentation depth d and final contact radius a. This particular indentor belongs to a class of smooth-contact indentors since $d\delta/dr$ is well-defined at $r = a$ where a is unknown a priori. Note again that the final contact radius a is determined by enforcing the continuity

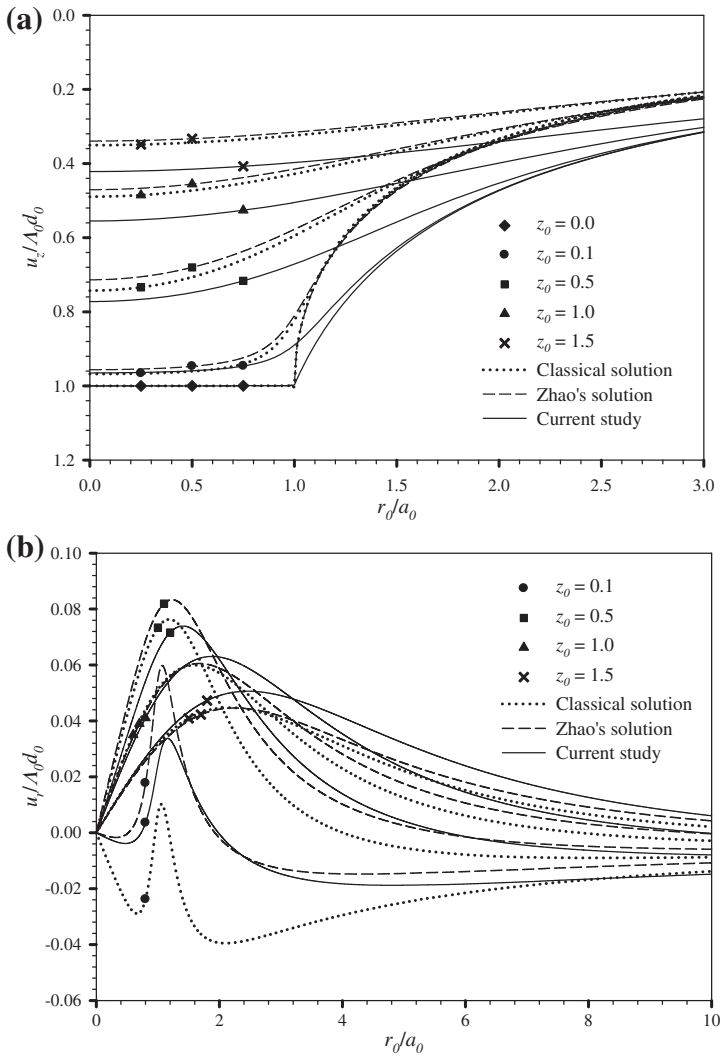

Fig. 7. Normalized displacement profiles for flat-ended cylindrical indentor with contact radius $a_0 = 0.5$ at various depths: (a) vertical displacement and (b) radial displacement.

condition of the vertical stress beneath the indentor at $r = a$. Numerical results for elastic fields of this particular case are reported in Figs. 8–11 and those demonstrating the size-dependent behavior and increase of material stiffness due to the presence of surface stresses are shown in Figs. 12–14. All crucial findings and remarks are summarized as follows.

To demonstrate the size-dependency resulting from the influence of surface stresses, the distribution of the normalized contact pressure under a paraboloidal indentor, $\pi p a_0/4\mu d_0$, is first presented in Fig. 8 for three different values of the contact radius, $a_0 = 0.5$, 0.8 and 1.0. Interestingly, the contact pressure predicted by the current model becomes finite at the boundary of the contact region while that obtained from the classical case and Zhao's model vanishes at that boundary. Unlike the results for the flat-ended cylindrical indentor, the contact pressure obtained from the current model is significantly larger than those obtained from the other two models. However, such discrepancy becomes smaller when the contact radius increases. Note in addition that, upon the proper normalization, the distribution of the contact pressure for the classical case is obviously independent of the contact radius and exhibits no size-dependency.

Normalized vertical stress profiles for the paraboloidal indentor for a fixed contact radius $a_0 = 0.5$ and five different depths, $z_0 = 0.0$, 0.1, 0.5, 1.0 and 1.5, are reported in Fig. 9. It is important to emphasize that due to the enforcement of continuity of the vertical stress at $r = a$, the singularity behavior at the boundary of the contact region observed in the case of the flat-ended indentor disappears for this particular indentor profile. The maximum value of the vertical stress occurs at $r = 0$ and rapidly decays to zero as r_0 increases. Clearly, the distribution of the vertical stress along the radial direction at a very small depth exhibits significant difference from the case of the flat-ended indentor. Again, the vertical stress in a region very near the free surface predicted by the current model deviates from those obtained from the classical and Zhao's models

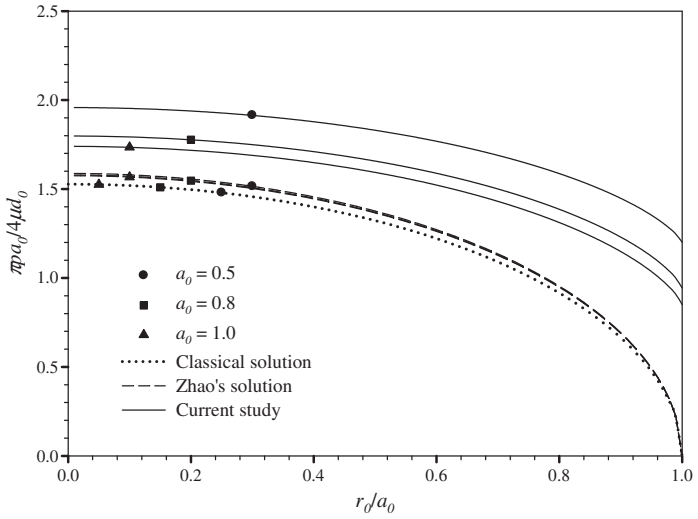

Fig. 8. Distribution of normalized contact pressure under paraboloidal indentor with various contact radii.

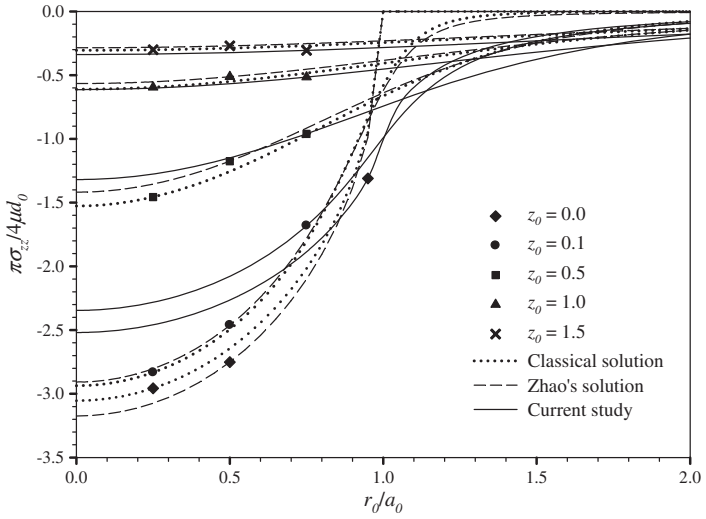

Fig. 9. Normalized vertical stress profiles for paraboloidal indentor with contact radius $a_0 = 0.5$ at various depths.

indicating the significant influence of the surface stresses and the out-of-plane contribution of the residual surface tension. It is also worth pointing out that the contact pressure shown in Fig. 8 is clearly identical to the negative value of the vertical stress at $z_0 = 0$ shown in Fig. 9 for both classical and Zhao's models (when $a_0 = 0.5$ is brought into the normalization) whereas the significant discrepancy of those two quantities is observed in the current model. This is due primarily to the out-of-plane contribution of the residual surface tension as indicated by the relation (62).

Fig. 10(a) and (b) show the normalized shear and radial stresses along the radial direction for the contact radius $a_0 = 0.5$ and four different depths $z_0 = 0.1, 0.5, 1.0$ and 1.5. Similar to the case of the flat-ended indentor, the shear stress at each depth increases from zero at $r_0 = 0$ to its peak value near the indentor boundary ($r_0/a_0 = 1$) and then decays rapidly as r_0 increases whereas the radial stress decreases monotonically from its maximum value at $r_0 = 0$ as r_0 increases. Again, the surface stresses exhibits significant influence on both shear and radial stresses only in a local region very close to the indentor, and its contribution becomes negligible at a region very far from the indentor. The influence of surface stresses on the vertical and radial displacements is also clearly demonstrated by the results shown in Fig. 11(a) and (b) respectively. The vertical displacement predicted by the current model is comparatively higher with a slower decay rate when compared to those obtained from the other two models. In addition, the magnitude of the radial displacement depends significantly on the

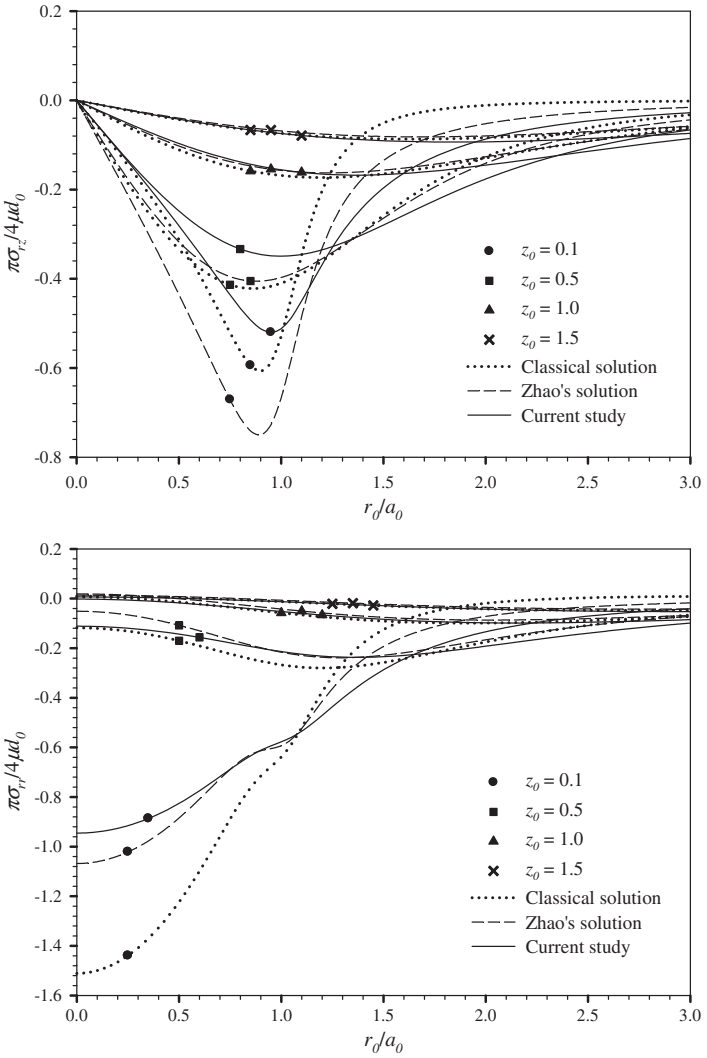

Fig. 10. Normalized stress profiles for paraboloidal indentor with contact radius $a_0 = 0.5$ at various depths: (a) shear stress and (b) radial stress.

surface stresses whereas the radial distributions predicted by all three models are rather similar. These behaviors are similar to what observed in the case of the flat-ended indentor.

To further demonstrate the size-dependent behavior, the relationship between the ratio a_0/a_c (where a_c denotes the contact radius for the classical case) and the contact radius a_0 of the paraboloidal indentor is investigated and results are reported in Fig. 12. Due to the influence of surface stresses, it is evident that the contact radius is smaller than that obtained from the classical case for the same indentation depth. This implies that presence of the surface stress render the material stiffer. In particular, the difference in comparison with the classical solution is less than 1% for Zhao's model and up to 30% for the current model. It appears that the out-of-plane contribution of the residual surface tension strongly affects the material stiffness and the surface stresses play a prominent role in mechanical responses and properties of materials in the nano-scale.

Another set of results that confirms the size-dependent behavior of predicted solutions, when the influence of surface stresses is incorporated, is associated with the relationship between the normalized indentation force, P/P_c (where P_c denotes the indentation force for the classical case), and the contact radius a_0 for the flat-ended cylindrical and paraboloidal indentors as shown in Fig. 13. It is obviously seen that, when the radius of the indentor becomes smaller, the indentation force required to produce the same indentation depth is relatively higher due to the surface stresses effect. The discrepancy is more pronounced for the results predicted by the current model when compared with Zhao's solutions. This implies that the stiffness of materials characterized by the indentation experiment depends not only on the penetration depth but also on the contact radius of the indentor. In particular, at the contact radius $a_0 = 0.1$, results obtained from Zhao's model are approximately 5% higher than the classical solution for both indentor profiles whereas those predicted by the current model

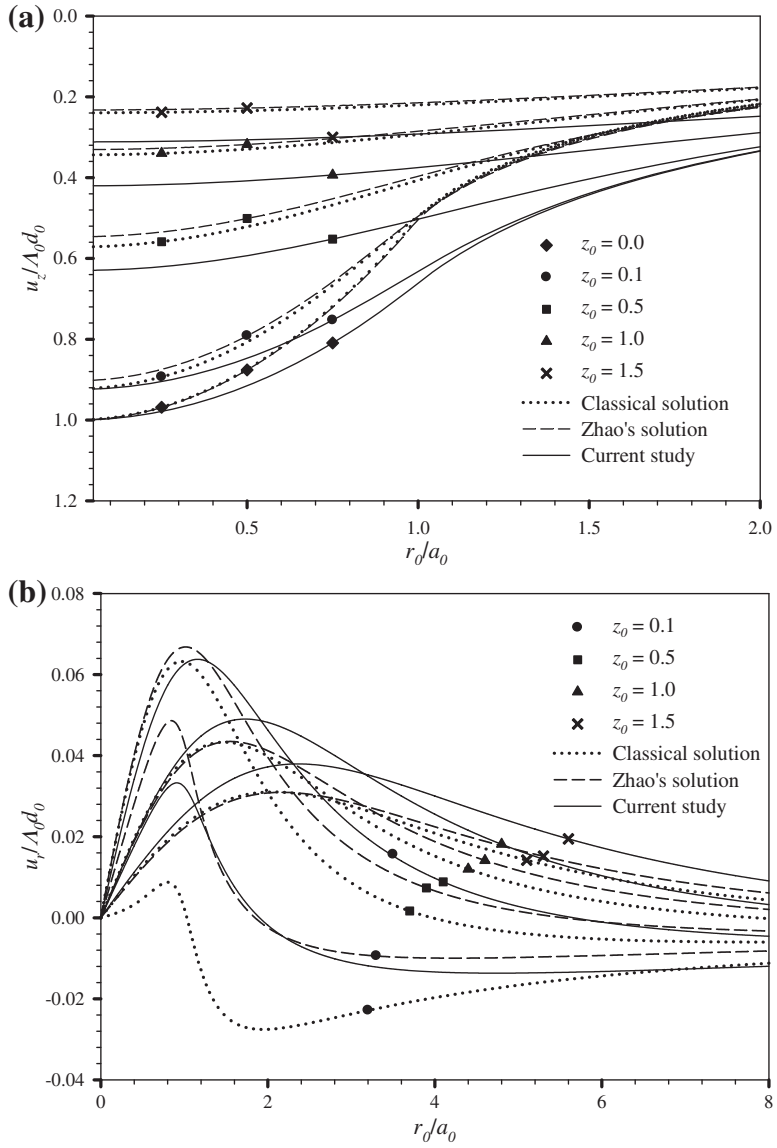

Fig. 11. Normalized displacement profiles for paraboloidal indentor with contact radius $a_0 = 0.5$ at various depths: (a) vertical displacement and (b) radial displacement.

accounted for the out-of-plane contribution of the residual surface tension are up to 120% and 160% higher than that obtained from the classical model for paraboloidal and flat-ended indentors, respectively.

To clearly demonstrate the influence of surface stresses on the material stiffness, the relationship between the normalized indentation force, $P/4\mu\Lambda_0^2$, and the indentation depth d_0 for both indentor profiles is presented in Fig. 14(a) and (b). It can be concluded from this set of results that the indentation force for both indentors predicted by the current model is significantly higher than that obtained from the classical and Zhao's models. This additionally confirms that materials become stiffer due to the presence of the surface stresses and the out-of-plane contribution of the residual surface tension amplifies such influence. It is also important to emphasize that the discrepancy of results for the flat-ended cylindrical indentor is more pronounced than that for the paraboloidal indentor due to the non-smoothness of the indentor profile and the singularity of stress field introduced at the boundary of the contact region.

6. Conclusion and remark

The complete solutions of elastic fields and related quantities for a linear elastic half-space compressed by an axisymmetric, rigid, frictionless indentor with integration of the influence of surface stresses have been fully investigated. In the

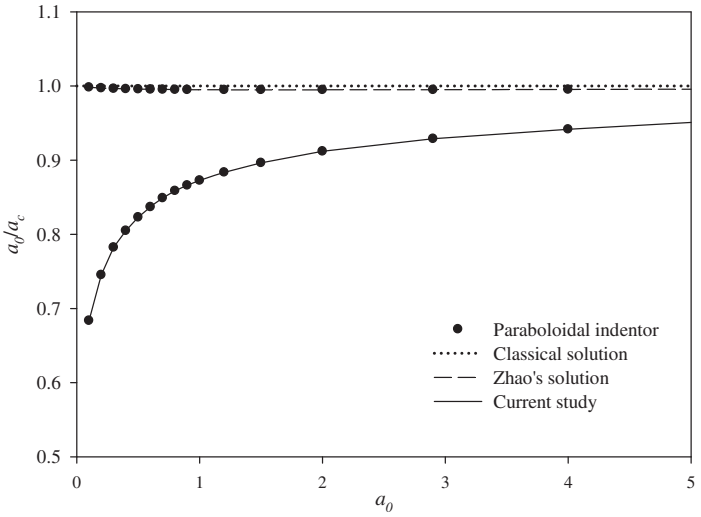

Fig. 12. Variation of a_0/a_c versus contact radius a_0.

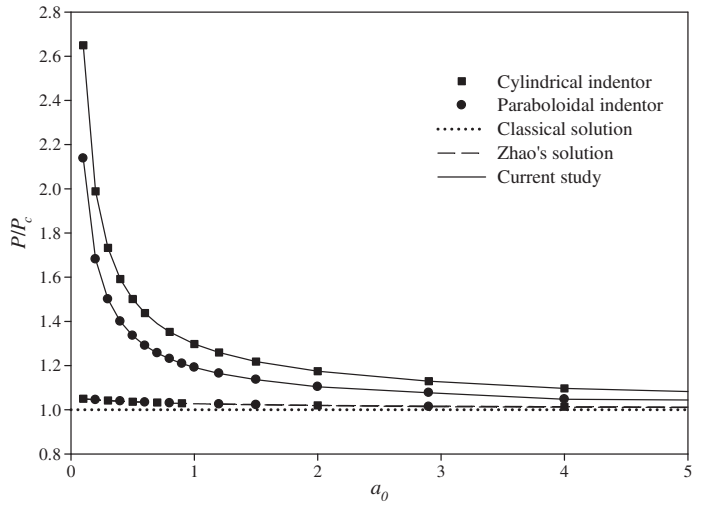

Fig. 13. Variation of normalized indentation force versus contact radius a_0.

modeling of surface behavior, a complete version of Gurtin–Murdoch surface elasticity model has been used. By employing the solution representation in terms of Love's strain potential together with the application of Hankel integral transform technique, the associated boundary value problem has been reduced to a set of dual integral equations which can be further transformed into an equivalent Fredholm integral equation of the second kind. Various numerical schemes have been applied to enhance both the solution accuracy and computational efficiency of the proposed technique. For smooth-contact indentors, a physically admissible condition associated with the continuity of the vertical stress at the boundary of the contact region is enforced to determine the unknown contact radius for a given indentation depth. The validity of the current formulation and accuracy of the numerical implementations have been confirmed by comparing computed results with existing analytical solutions in the classical case for both smooth and non-smooth contacts.

As anticipated, obtained numerical results from extensive numerical experiments have demonstrated that the influence of surface stresses becomes more significant when the size of the indentor is smaller especially in the region very near the indentor. In addition, material behaves stiffer due to the presence of such effect. It is interesting to remark that the distribution of the contact pressure for two indentor profiles (i.e., flat-ended and paraboloidal indentors) predicted by the current model exhibits significant discrepancy from those obtained from the classical model and the model accounted for the surface stresses but without out-of-plane contribution of the residual surface tension. The singularity of the contact pressure and vertical stress at the boundary of the contact region is still observed in the current model for the case of non-smooth-contact

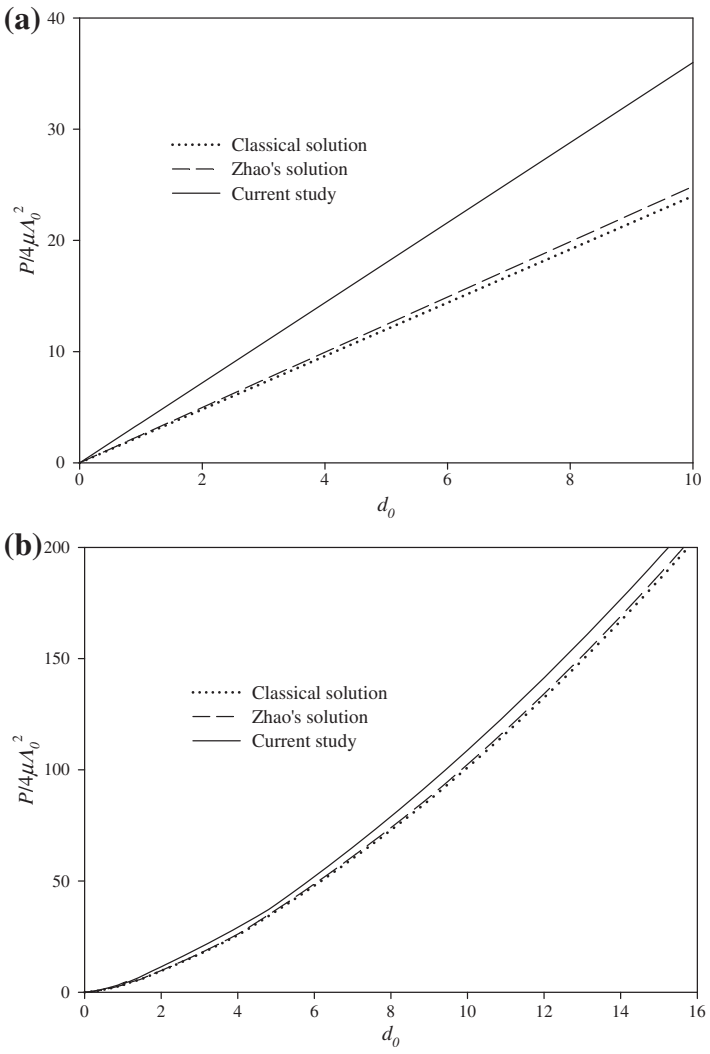

Fig. 14. Relationship between normalized indentation force and indentation depth d_0: (a) flat-ended cylindrical indentor and (b) paraboloidal indentor.

indentors whereas such blow-up behavior completely disappears in the case of smooth-contact indentors. Size-dependent behavior has been also presented to confirm the essence of integrating the influence of surface stresses into the mathematical model in order to accurately capture mechanical responses and properties of materials at a nano-scale and soft elastic solids.

It is important to emphasize that the boundary value problem considered in the present study is restricted mainly to an indentation problem with axisymmetric data and rigid, frictionless indentors. The generalization of the current work to alleviate all those limitations (e.g., treatment of indentors of non-axisymmetric profiles and non-frictionless contact) should be potentially useful to enhance understanding of nano-mechanics and mechanics of soft solids in a broader context.

Acknowledgement

The work presented in this paper was supported by Thailand Research Fund (Grant No. BRG5480006). This support is gratefully acknowledged.

References

Armstrong, R. W., Shin, H., & Ruff, A. W. (1995). Elastic/plastic effects during very low-load hardness testing of copper. *Acta Metallurgica Materials, 43*, 1037–1043.

Beegan, D., Chowdhury, S., & Laugier, M. T. (2007). Comparison between nanoindentation and scratch test hardness (scratch hardness) values of copper thin films on oxidised silicon substrates. *Surface and Coatings Technology, 201*, 5804–5808.

Boussinesq, J. (1885). *Applications des Potentiels à l' Étude de l' Équilibre et du Mouvement des Solides Élastiques*. Paris: Gauthier-Villars.
Cammarata, R. C. (1994). Surface and interface stress effects in thin films. *Progress in Surface Science, 46*, 1–38.
Cammarata, R. C. (1997). Surface and interface stress effects on interfacial and nanostructured materials. *Materials Science and Engineering A, 237*, 180–184.
Dhaliwal, R. S., & Rau, I. S. (1970). The axisymmetric boussinesq problem for a thick elastic layer under a punch of arbitrary profile. *International Journal of Engineering Science, 8*, 843–856.
Dingreville, R., Qu, J., & Cherkaoui, M. (2005). Surface free energy and its effect on the elastic behavior of nano-sized particles, wires and films. *Journal of the Mechanics and Physics of Solids, 53*, 1827–1854.
Doerner, M. F., & Nix, W. D. (1986). A method for interpreting the data from depth-sensing indentation instruments. *Journal of Materials Research, 1*, 601–609.
Duan, H. L., Wang, J., Huang, Z. P., & Karihaloo, B. L. (2005). Eshelby formalism for nano-inhomogeneities. *Proceedings of Royal Society A, 461*, 3335–3353.
Fischer, F. D., Waitz, T., Vollath, D., & Simha, N. K. (2008). On the role of surface energy and surface stress in phase-transforming nanoparticles. *Progress in Materials Science, 53*, 481–527.
Gao, Y. F., Xu, H. T., Oliver, W. C., & Pharr, G. M. (2008). Effective elastic modulus of film-on-substrate systems under normal and tangential contact. *Journal of the Mechanics and Physics of Solids, 56*, 402–416.
Gibbs, J. W. (1906). *The Scientific Papers of J. Willard Gibbs* (Vol. 1). London: Longmans Green.
Gurtin, M. E., & Murdoch, A. I. (1975). A continuum theory of elastic material surfaces. *Archive for Rational Mechanics and Analysis, 57*, 291–323.
Gurtin, M. E., & Murdoch, A. I. (1978). Surface stress in solids. *International Journal of Solids and Structures, 14*, 431–440.
Gurtin, M. E., Weissmüller, J., & Larché, F. (1998). A general theory of curved deformable interfaces in solids at equilibrium. *Philosophical Magazine A, 78*, 1093–1109.
Hainsworth, S. V., & Page, T. F. (1994). Nanoindentation studies of the chemomechanical effect in sapphire. *Journal of Materials Science, 29*, 5529–5540.
Harding, J. W., & Sneddon, I. N. (1945). The elastic stresses produced by the indentation of the plane surface of a semi-infinite elastic solid by a rigid punch. *Mathematical Proceedings of the Cambridge Philosophical Society, 41*, 16–26.
He, L. H., & Lim, C. W. (2006). Surface green function for a soft elastic half-space: Influence of surface stress. *International Journal of Solids and Structures, 43*, 132–143.
He, L. H., Lim, C. W., & Wu, B. S. (2004). A continuum model for size-dependent deformation of elastic films of nano-scale thickness. *International Journal of Solids and Structures, 41*, 847–857.
Huang, D. W. (2008). Size-dependent response of ultra-thin films with surface effects. *International Journal of Solids and Structures, 45*, 568–579.
Intarit, P., Senjuntichai, T., & Rajapakse, R. K. N. D. (2010). Dislocations and internal loading in a semi-infinite elastic medium with surface stresses. *Engineering Fracture Mechanics, 77*, 3592–3603.
Intarit, P., Senjuntichai, T., Rungamornrat, J., & Rajapakse, R. K. N. D. (2011). Surface elasticity and residual stress effect on the elastic field of a nanoscale elastic layer. *Interaction and Multiscale Mechanics, 4*, 85–105.
Jing, G. Y., Duan, H. L., Sun, X. M., Zhang, Z. S., Xu, J., Li, Y. D., et al (2006). Surface effects on elastic properties of silver nanowires: Contact atomic-force microscopy. *Physical Review B, 73*, 235409.
Lebedev, N. N., & Ufliand, I. S. (1958). Axisymmetric contact problem for an elastic layer. *Journal of Applied Mathematics and Mechanics, 22*, 442–450.
Lucas, B. N., Hay, J. C., & Oliver, W. C. (2003). Using multidimensional contact mechanics experiments to measure Poisson's ratio of porous low-k films. *Materials Research Society Symposium Proceedings, 766*, E9.5.1–E9.5.6.
Lu, P., He, L. H., Lee, H. P., & Lu, C. (2006). Thin plate theory including surface effects. *International Journal of Solids and Structures, 43*, 4631–4647.
Mandal, B. N. (1988). A note on Bessel function dual integral equation with weight function. *International Journal of Mathematics and Mathematical Sciences, 11*, 543–550.
Meyers, M. A., & Chawla, K. K. (2009). *Mechanical behavior of materials*. New York: Cambridge University Press.
Miller, R. E., & Shenoy, V. B. (2000). Size-dependent elastic properties of nanosized structural elements. *Nanotechnology, 11*, 139–147.
Oliver, W. C., & Pharr, G. M. (1992). An improved technique for determining hardness and elastic modulus using load and displacement sensing indentation experiments. *Journal of Materials Research, 7*, 1564–1583.
Rau, I. S., & Dhaliwal, R. S. (1972). Further considerations on the axisymmetric boussinesq problem. *International Journal of Engineering Science, 10*, 659–663.
Selvadurai, A. P. S. (2000). *Partial differential equations in mechanics 2*. Germany: Springer.
Sharma, P., Ganti, S., & Bhate, N. (2003). Effect of surfaces on the size-dependent elastic state of nano-inhomogeneities. *Applied Physics Letters, 82*, 535–537.
Sharma, P., & Wheeler, L. T. (2007). Size-dependent elastic state of ellipsoidal nano-inclusions incorporating surface/interface tension. *Journal of Applied Mechanics, 74*, 447–454.
Shenoy, V. B. (2005). Atomistic calculations of elastic properties of metallic fcc crystal surfaces. *Physical Review B, 71*, 094104.
Sneddon, I. N. (1951). *Fourier transform*. New York: McGraw-Hill.
Sneddon, I. N. (1965). The relation between load and penetration in the axisymmetric boussinesq problem for a punch of arbitrary profile. *International Journal of Engineering Science, 3*, 47–57.
Sneddon, I. N. (1966). *Mixed boundary value problems in potential theory*. New York: John Wiley & Sons.
Tian, L., & Rajapakse, R. K. N. D. (2007). Elastic field of an isotropic matrix with a nanoscale elliptical inhomogeneity. *International Journal of Solids and Structures, 44*, 7988–8005.
Yakobson, B. I. (2003). Nanomechanics. In W. A. Goddard, D. W. Brenner, S. E. Lyshevski, & G. J. Iafrate (Eds.), *Handbook of Nanoscience, Engineering and Technology* (pp. 17.1–17.18). Florida: CRC Press.
Yang, F. (1998). Indentation of an incompressible elastic film. *Mechanics of Materials, 30*, 275–286.
Yang, F., & Li, J. C. M. (1995). Impression test of 63Sn-37Pb eutectic alloy. *Materials Science and Engineering A, 201*, 40–49.
Yang, F., & Li, J. C. M. (1997). Viscosity of selenium measured by impression test. *Journal of Non-Crystalline Solids, 212*, 136–142.
Yu, H. Y., Sanday, S. C., & Rath, B. B. (1990). The effect of substrate on the elastic properties of films determined by the indentation test – axisymmetric boussinesq problem. *Journal of the Mechanics and Physics of Solids, 38*, 745–764.
Zhao, X. J. (2009). Surface loading and rigid indentation of an elastic layer with surface energy effects, Master thesis, The University of British Columbia, Vancouver, Canada.
Zhao, X. J., & Rajapakse, R. K. N. D. (2009). Analytical solutions for a surface-loaded isotropic elastic layer with surface energy effects. *International Journal of Engineering Science, 47*, 1433–1444.

Surface elasticity and residual stress effect on the elastic field of a nanoscale elastic layer

P. Intarit[1], T. Senjuntichai*[1], J. Rungamornrat[1] and R.K.N.D. Rajapakse[2]

[1]*Department of Civil Engineering, Faculty of Engineering, Chulalongkorn University Bangkok 10330, Thailand*
[2]*Faculty of Applied Sciences, Simon Fraser University, Burnaby, Canada V5A 1S6*

(Received November 19, 2010, Accepted February 26, 2011)

Abstract. The influence of surface elasticity and surface residual stress on the elastic field of an isotropic nanoscale elastic layer of finite thickness bonded to a rigid material base is considered by employing the Gurtin-Murdoch continuum theory of elastic material surfaces. The fundamental solutions corresponding to buried vertical and horizontal line loads are obtained by using Fourier integral transform techniques. Selected numerical results are presented for the cases of a finite elastic layer and a semi-infinite elastic medium to portray the influence of surface elasticity and residual surface stress on the bulk stress field. It is found that the bulk stress field depends significantly on both surface elastic constants and residual surface stress. The consideration of out-of-plane terms of the surface stress yields significantly different solutions compared to previous studies. The solutions presented in this study can be used to examine a variety of practical problems involving nanoscale/soft material systems and to develop boundary integral equations methods for such systems.

Keywords: continuum mechanics; elasticity; nanomechanics; residual stress; surface energy; surface stress; thin films.

1. Introduction

Nanomaterials and nanostructures are increasingly used in advanced engineering applications due to their superior mechanical, electronic and optical properties (Wong *et al.* 1997). In nanoscale systems, the surface-to-volume ratio is relatively high compared to macroscale systems and the influence of surface/interface free energy becomes an important factor in their mechanical properties and behavior (Yakobson 2003). Surface energy effects are also important in soft materials such as polymer gels and biomaterials (Peter *et al.* 2000, Srinivasan *et al.* 2001). Although atomistic methods (e.g. Chen *et al.* 2008, Chen and Lee 2010) are considered very accurate for nanoscale systems, the associated computational resources are significantly large. Modified continuum methods are therefore considered very efficient in obtaining a first-approximation to nanoscale systems. Gurtin and Murdoch (1975, 1978) developed a rigorous theory based on continuum mechanics concepts to incorporate the surface and interfacial energy effects. The surface is modeled

* Corresponding author, Professor, E-mail: Teerapong.S@eng.chula.ac.th

as a layer with zero thickness perfectly bonded to the underlying bulk material. The surface elastic constants can be obtained from atomistic simulations (Miller and Shenoy 2000, Shenoy 2005, Dingreville and Qu 2007).

Over the past decade, Gurtin-Murdoch theory of deformable material surfaces has been extensively applied to study problems in nanotechnology and soft materials. He and Lim (2006) derived the surface Green's function for a soft incompressible isotropic elastic half-space by assuming that the surface elastic properties are the same as bulk properties. The elastic field of a half-plane subjected to surface loading in the presence of surface stresses was considered by Huang and Yu (2007). Zhao and Rajapakse (2009) studied the plane-strain and axisymmetric response of an isotropic elastic layer bonded to a rigid base under vertical and horizontal surface loads. Recently, Intarit *et al.* (2010) derived the fundamental solutions of an elastic half-plane with surface effects under internal loading and dislocations.

In the above studies, the surface stress tensor is considered a 2D quantity and its out-of-plane components are excluded. A recent study by Wang *et al.* (2010), who formulated the surface elasticity theory in the Lagrangian and Eulerian frameworks, indicated that the deformed and undeformed configurations should be discriminated even in the case of small deformations. The out-of-plane terms of the surface displacement gradient could be significant particularly for curved and rotated surfaces. Povstenko (1993) studied the influence of residual surface stress gradient on the elastic field of a half-space that has a jump in residual surface stress over a circular area.

This paper examines the elastic field of an isotropic nanoscale or soft elastic material layer of finite thickness bonded to a rigid material base and subjected to internal and surface loading. The surface elasticity and residual surface stresses are considered in the formulation. This class of problems has extensive applications in the study of nanocoatings and nanoscale surface layers that are used in electronic devices, tribological and biomaterial applications, advanced industrial materials, communication devices, etc. The boundary-value problems involve non-classical boundary conditions due to surface stresses are solved by using Fourier integral transforms. Selected numerical results are presented to demonstrate the influence of surface elasticity and residual surface stress on the elastic field.

2. Governing equations and general solutions

Consider a finite elastic layer of thickness t bonded to a rigid material base, and subjected to vertical and horizontal loading at a depth h below the free surface as shown in Fig. 1. In the absence of body forces, the equilibrium equations, constitutive laws and strain-displacement relations of an isotropic bulk material are given by

$$\sigma_{ij,j} = 0 \tag{1}$$

$$\sigma_{ij} = 2\mu\varepsilon_{ij} + \lambda\delta_{ij}\varepsilon_{kk} \tag{2}$$

$$\varepsilon_{ij} = \frac{1}{2}(u_{i,j} + u_{j,i}) \tag{3}$$

where u_i, σ_{ij} and ε_{ij} denote respectively the components of displacement, stress and strain tensors. In addition, μ and λ are Lamé constants of the bulk material.

For the surface, the equilibrium equation, constitutive laws and strain-displacement relations can

be expressed as (Gurtin and Murdoch 1975, 1978).

$$\sigma^s_{i\alpha,\alpha} + \sigma_{ij} n_j = 0 \tag{4}$$

$$\sigma^s_{\beta\alpha} = \tau^s \delta_{\beta\alpha} + 2(\mu^s - \tau^s)\varepsilon_{\beta\alpha} + (\lambda^s + \tau^s)\varepsilon_{\gamma\gamma}\delta_{\beta\alpha} + \tau^s u^s_{\beta,\alpha}, \quad \sigma^s_{3\alpha} = \tau^s u_{3,\alpha} \tag{5}$$

$$\varepsilon^s_{\alpha\beta} = \frac{1}{2}(u^s_{\alpha,\beta} + u^s_{\beta,\alpha}) \tag{6}$$

where the superscript 's' is used to denote the quantities corresponding to the surface; μ^s and λ^s are surface Lamé constants; τ^s is the surface residual stress (or surface tension) under unstrained conditions; and n_i denotes the components of the unit normal vector of the surface. It is noted that the value of τ^s is constant for a given surface orientation of a pure metal/semiconductor at a specific temperature (Zhao and Rajapakse 2009).

In the above equations, Greek subscripts denote the field quantities associated with the surface and take the value of 1 or 2, while the Latin subscripts adopt values from 1 to 3. A majority of existing studies based on the Gurtin-Murdoch theory has formulated the problems in undeformed configuration due to the assumption of infinitesimal deformations thus the out-of-plane component of surface stresses given by the second equation in Eq. (5) is normally ignored. The term $\tau^s u_{3,\alpha}$ can simply be viewed as the out-of-plane component of the pre-existing surface tension τ^s in the deformed configuration whereas the surface gradient of the displacement $u_{3,\alpha}$ act as the out-of-plane component of the unit vector tangent to the surface in the deformed state. While the component $\tau^s u_{3,\alpha}$ has physical meaning only in the deformed state and identically vanishes in the undeformed configuration, its contribution to the constitutive Eq. (5) is of the same order as other terms. As recently pointed out by Wang *et al.* (2010), these out-of-plane terms could become significant even in the case of small deformations.

It is assumed that the deformations under consideration are plane-strain in the xz-plane, i.e. $\varepsilon_{xy} = \varepsilon_{yy} = \varepsilon_{yz} = 0$. The general solutions for the bulk stresses and displacements can be expressed with respect to a Cartesian coordinate system (Fig. 1) by using Fourier integral transforms as (Sneddon 1951)

$$\sigma_{zz} = -\frac{1}{2\pi}\int_{-\infty}^{+\infty} \xi^2 \Phi e^{-i\xi x} d\xi \tag{7}$$

$$\sigma_{xx} = \frac{1}{2\pi}\int_{-\infty}^{+\infty} \frac{d^2\Phi}{dz^2} e^{-i\xi x} d\xi \tag{8}$$

$$\sigma_{xz} = \frac{1}{2\pi}\int_{-\infty}^{+\infty} i\xi \frac{d\Phi}{dz} e^{-i\xi x} d\xi \tag{9}$$

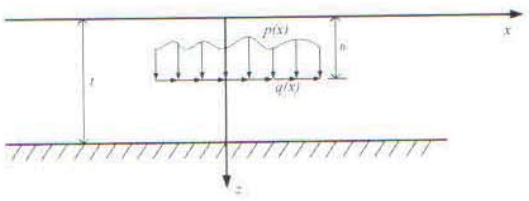

Fig. 1 An isotropic elastic layer subjected to internal vertical and horizontal loading

$$u_z = \frac{1}{8\pi\mu(\lambda+\mu)}\int_{-\infty}^{\infty}\left[(\lambda+2\mu)\frac{d^3\Phi}{dz^3} - (3\lambda+4\mu)\xi^2\frac{d\Phi}{dz}\right]e^{-i\xi x}\frac{d\xi}{\xi^2} \tag{10}$$

$$u_x = \frac{1}{8\pi\mu(\lambda+\mu)}\int_{-\infty}^{\infty}\left[(\lambda+2\mu)\frac{d^2\Phi}{dz^2} + \lambda\xi^2\Phi\right]ie^{-i\xi x}\frac{d\xi}{\xi} \tag{11}$$

where

$$\Phi(\xi, z) = (A+Bz)e^{-|\xi|z} + (C+Dz)e^{|\xi|z} \tag{12}$$

Note that Φ is the Fourier transform of Airy stress function that satisfies the two-dimensional biharmonic equation. In addition, the arbitrary functions A, B, C and D are determined from the appropriate boundary conditions.

3. Solutions of boundary-value problems

The solution to the elastic layer problem shown in Fig. 1 can be derived by dividing the elastic layer into two sub-domains. The sub-domain '1' corresponds to the region where $0 \le z \le h$ and the sub-domain '2' corresponds to the region where $h \le z \le t$. The general solution of the sub-domain '1' is given by Eqs. (7) - (12) whereas the general solution of the sub-domain '2' is also given by Eqs. (7) - (12) with the arbitrary functions A to D being replaced by E to H respectively. A superscript 'i' ($i = 1, 2$) is used hereafter to denote quantities associated with each sub-domain. The arbitrary functions A to H corresponding to each sub-domain can be obtained by solving the following boundary value problem.

$$\sigma_{zz}^{(1)}\Big|_{z=0} + \left(\frac{d\tau^s}{dx}\frac{du_z}{dx} + \tau^s\frac{d^2u_z}{dx^2}\right)_{z=0} = 0 \tag{13}$$

$$\sigma_{zx}^{(1)}\Big|_{z=0} + \left(\frac{d\tau^s}{dx} + \kappa^s\frac{d^2u_x}{dx^2}\right)_{z=0} = 0 \tag{14}$$

$$\sigma_{zz}^{(1)}\Big|_{z=h^-} - \sigma_{zz}^{(2)}\Big|_{z=h^+} = p(x) \tag{15}$$

$$\sigma_{zx}^{(1)}\Big|_{z=h^-} - \sigma_{zx}^{(2)}\Big|_{z=h^+} = q(x) \tag{16}$$

$$u_z^{(1)}\Big|_{z=h^-} = u_z^{(2)}\Big|_{z=h^+} \tag{17}$$

$$u_x^{(1)}\Big|_{z=h^-} = u_x^{(2)}\Big|_{z=h^+} \tag{18}$$

$$u_z^{(2)}\Big|_{z=t} = 0 \tag{19}$$

$$u_x^{(2)}\Big|_{z=t} = 0 \tag{20}$$

where $\kappa^s = 2\mu^s + \lambda^s$ is a surface material constant. In addition, $p(x)$ and $q(x)$ denote the jump of

the normal traction and shear traction across the line $z = h$ due to the applied internal vertical and horizontal loads respectively (see Fig. 1). The Fourier transforms of $p(x)$ and $q(x)$ are given respectively by

$$\bar{p}(\xi) = \int_{-\infty}^{+\infty} p(x) e^{i\xi x} dx \tag{21}$$

$$\bar{q}(\xi) = \int_{-\infty}^{+\infty} q(x) e^{i\xi x} dx \tag{22}$$

It should be noted that both Eqs. (13) and (14) are non-classical boundary conditions obtained from Eqs. (4) and (5). In addition, Eq. (13) contains the out-of-plane component of surface stresses associated with residual surface stress, which has generally been ignored in most previous studies. For a flat surface, it can be seen from Eqs. (13) and (14) that the influence of residual surface stress τ^s will be neglected if the out-of-plane component of surface stresses is disregarded (the second term on the left-hand side of Eq. (13) vanishes) and the residual surface stress is assumed to be constant. In view of Eqs. (7) - (11), a set of linear simultaneous equations for determining the arbitrary functions can be constituted by applying Fourier integral transforms to Eqs. (13) - (20) together with the assumption that the surface residual stress is constant. The following solutions are obtained for the arbitrary functions A to H.

$$A = \frac{(A_p + iA_q)}{I}; \quad B = \frac{(B_p + iB_q)}{I} \tag{23}$$

$$C = \frac{(C_p + iC_q)}{I}; \quad D = \frac{(D_p + iD_q)}{I} \tag{24}$$

$$E = \frac{(E_p + iE_q)}{I}; \quad F = \frac{(F_p + iF_q)}{I} \tag{25}$$

$$G = \frac{(G_p + iG_q)}{I}; \quad H = \frac{(H_p + iH_q)}{I} \tag{26}$$

where the explicit expressions of A_p, A_q, B_p, B_q, C_p, C_q, D_p, D_q, E_p, E_q, F_p, F_q, G_p, G_q, H_p, H_q and I are given in Appendix.

In the following subsections, the explicit expressions of the arbitrary functions for the special cases of surface loading $h \to 0$ and a semi-infinite medium $t \to \infty$ are presented.

3.1 Surface loading on a finite layer

The surface loading of a nanoscale layer has many practical applications. The elastic field corresponding to this case can be obtained by taking the limit of $h \to 0$ in Eqs. (23)-(26). The corresponding arbitrary functions are given by Eqs. (23) and (24) with A_i to D_i ($i = p, q$) defined as follows

$$A_i = \frac{\bar{p}(\xi)}{2\xi^2}\left\{(\lambda+3\mu)[(1+\Lambda|\xi|)e^{2|\xi|t} - \Lambda|\xi|] + 2t\xi^2(\lambda+\mu)(\Lambda+t) - \frac{2(\lambda+\mu)^2}{(\lambda+2\mu)}\Lambda t^2|\xi|^3 - 2(\lambda+\mu)t|\xi| + \frac{\lambda^2+4\lambda\mu+5\mu^2}{\lambda+\mu}\right\} \tag{27}$$

$$B_p = \frac{\bar{p}(\xi)}{2|\xi|}\left\{(\lambda+3\mu)\left[\left(1+\frac{\lambda+\mu}{\lambda+2\mu}\Lambda|\xi|\right)e^{2|\xi|t}-\frac{\lambda+\mu}{\lambda+2\mu}\Lambda|\xi|\right]+\frac{2(\lambda+\mu)^2}{(\lambda+2\mu)}\Lambda t\xi^2+(\lambda+\mu)(1-2t|\xi|)\right\} \quad (28)$$

$$C_p = \frac{\bar{p}(\xi)}{2\xi^2}\left\{(\lambda+3\mu)[(1-\Lambda|\xi|)e^{-2|\xi|t}+\Lambda|\xi|]+2t\xi^2(\lambda+\mu)(\Lambda+t)+\frac{2(\lambda+\mu)^2}{(\lambda+2\mu)}\Lambda t^2|\xi|^3+2(\lambda+\mu)t|\xi|+\frac{\lambda^2+4\lambda\mu+5\mu^2}{\lambda+\mu}\right\} \quad (29)$$

$$D_p = -\frac{\bar{p}(\xi)}{2|\xi|}\left\{(\lambda+3\mu)\left[\left(1-\frac{\lambda+\mu}{\lambda+2\mu}\Lambda|\xi|\right)e^{-2|\xi|t}+\frac{\lambda+\mu}{\lambda+2\mu}\Lambda|\xi|\right]+\frac{2(\lambda+\mu)^2}{(\lambda+2\mu)}\Lambda t\xi^2+(\lambda+\mu)(1+2t|\xi|)\right\} \quad (30)$$

$$A_q = -\frac{\bar{q}(\xi)}{|\xi|\xi}\left\{(\lambda+3\mu)\left[\frac{\tau^s|\xi|}{4(\lambda+\mu)}e^{2|\xi|t}-\frac{\tau^s|\xi|}{4(\lambda+\mu)}\right]+\frac{\mu(\lambda+2\mu)}{\lambda+\mu}+(\lambda+\mu)t^2\xi^2-\frac{\tau^s t\xi^2}{2}-\frac{(\lambda+\mu)}{2\mu}\tau^s t^2|\xi|^3\right\} \quad (31)$$

$$B_q = \frac{\bar{q}(\xi)}{2\xi}\left\{(\lambda+3\mu)\left[\left(1+\frac{\tau^s|\xi|}{2\mu}\right)e^{2|\xi|t}-\frac{\tau^s|\xi|}{2\mu}\right]+(\lambda+\mu)(1+2t|\xi|)-\frac{(\lambda+\mu)}{\mu}\tau^s t\xi^2\right\} \quad (32)$$

$$C_q = \frac{\bar{q}(\xi)}{|\xi|\xi}\left\{(\lambda+3\mu)\left[-\frac{\tau^s|\xi|}{4(\lambda+\mu)}e^{-2|\xi|t}+\frac{\tau^s|\xi|}{4(\lambda+\mu)}\right]+\frac{\mu(\lambda+2\mu)}{\lambda+\mu}+(\lambda+\mu)t^2\xi^2-\frac{\tau^s t\xi^2}{2}+\frac{(\lambda+\mu)}{2\mu}\tau^s t^2|\xi|^3\right\} \quad (33)$$

$$D_q = \frac{\bar{q}(\xi)}{2\xi}\left\{(\lambda+3\mu)\left[\left(1-\frac{\tau^s|\xi|}{2\mu}\right)e^{-2|\xi|t}+\frac{\tau^s|\xi|}{2\mu}\right]+(\lambda+\mu)(1-2t|\xi|)-\frac{(\lambda+\mu)}{\mu}\tau^s t\xi^2\right\} \quad (34)$$

The fundamental solutions corresponding to an elastic layer subjected to a vertical line load P_0 and a horizontal line load Q_0 can be obtained by substituting $\bar{p}(\xi) = P_0$ and $\bar{q}(\xi) = Q_0$ in the above solutions.

For the cases of vertical strip load of constant magnitude p_0 and horizontal strip load of constant magnitude q_0 over the region $-a \le x \le a$

$$\bar{p}(\xi) = \frac{2\sin(\xi a)}{\xi}p_0 \quad (35)$$

$$\bar{q}(\xi) = \frac{2\sin(\xi a)}{\xi}q_0 \quad (36)$$

Note that $\Lambda = \kappa^s(\lambda+2\mu)/2\mu(\lambda+\mu)$ is a parameter with a dimension of length. This parameter can be viewed as a material characteristic length that represents the influence of surface stress. It is clear from the above solutions that the influence from surface stresses does not only come from the surface material constant κ^s (or Λ) but also from the residual surface stress τ^s. In the absence of surface stress effects, Λ and τ^s vanish and the above solutions reduce to the classical elasticity solutions.

The elastic field of a semi-infinite medium under surface loading can readily be obtained from the solutions in Eqs. (23) and (24), with A_i to D_i $(i = p, q)$ given by Eqs. (27) to (34), by taking the limit of $t \to \infty$. Note that the arbitrary functions C and $D \equiv 0$ to ensure the regularity of the solutions at infinity. In the case of the vertical load, the arbitrary functions A and B take the form,

$$A = \frac{\bar{p}(\xi)}{\eta\xi^2}(1+\Lambda|\xi|) \tag{37}$$

$$B = \frac{\bar{p}(\xi)}{\eta|\xi|}\left[1+\frac{(\lambda+\mu)}{(\lambda+2\mu)}\Lambda|\xi|\right] \tag{38}$$

where

$$\eta = (1+\Lambda|\xi|)+\tau^*\left[\frac{(\lambda+2\mu)}{2\mu(\lambda+\mu)}|\xi|+\frac{(\lambda+3\mu)}{2\mu(\lambda+2\mu)}\Lambda\xi^2\right] \tag{39}$$

In the case of the horizontal loading

$$A = -i\frac{\bar{q}(\xi)}{\eta\xi}\left[\frac{\tau^*}{2(\lambda+\mu)}\right] \tag{40}$$

$$B = i\frac{\bar{q}(\xi)}{\eta\xi}\left(1+\frac{\tau^*|\xi|}{2\mu}\right) \tag{41}$$

3.2 Internal loading in a semi-infinite medium

The stress and displacement fields of a semi-infinite medium under vertical and horizontal loads applied at a depth h below free surface can also be obtained from the solutions in Eqs. (23)-(26) by taking the limit of $t \to \infty$. Note that the arbitrary functions G and $H \equiv 0$ to ensure the regularity of the solutions at infinity and the arbitrary functions A to F can be specialized to the case of a half-plane as follows.

3.2.1 Arbitrary functions for internal vertical loading

$$A = \frac{\bar{p}(\xi)}{2\eta\xi^2}e^{-|\xi|h}\left\{(1+\Lambda|\xi|)\left(1+\frac{\lambda+\mu}{\lambda+2\mu}h|\xi|\right)-\frac{\tau^*}{2\mu}|\xi|\left[\frac{\lambda+2\mu}{\lambda+\mu}+h|\xi|+\frac{\lambda+3\mu}{\lambda+2\mu}\Lambda|\xi|+\frac{(\lambda+\mu)^2}{(\lambda+2\mu)^2}\Lambda h\xi^2\right]\right\} \tag{42}$$

$$B = \frac{\bar{p}(\xi)}{2(\lambda+2\mu)\eta|\xi|}e^{-|\xi|h}\left\{\lambda+3\mu+(\lambda+\mu)(\Lambda+2h)|\xi|-\frac{\tau^*}{2\mu}|\xi|\left[\lambda+2\mu+\frac{(\lambda+\mu)(\lambda+3\mu)}{\lambda+2\mu}\Lambda|\xi|+\frac{2(\lambda+\mu)^2}{\lambda+2\mu}\Lambda h\xi^2\right]\right\} \tag{43}$$

$$C = -\frac{\bar{p}(\xi)e^{-|\xi|h}}{2\xi^2}\left[1+\frac{\lambda+\mu}{\lambda+2\mu}h|\xi|\right] \tag{44}$$

$$D = \frac{\bar{p}(\xi)e^{-|\xi|h}(\lambda+\mu)}{2|\xi|(\lambda+2\mu)} \tag{45}$$

$$E = \frac{\bar{p}(\xi)}{2\eta\xi^2}\left\{\begin{array}{l} e^{|\xi|h}\left\{(1+\Lambda|\xi|)\left(1-\frac{\lambda+\mu}{\lambda+2\mu}h|\xi|\right)+\frac{\tau^*}{2\mu}|\xi|\left[\frac{\lambda+2\mu}{\lambda+\mu}-h|\xi|+\frac{\lambda+3\mu}{\lambda+2\mu}\Lambda|\xi|-\frac{(\lambda+\mu)(\lambda+3\mu)}{(\lambda+2\mu)^2}\Lambda h\xi^2\right]\right\} \\ +e^{-|\xi|h}\left\{(1+\Lambda|\xi|)\left(1+\frac{\lambda+\mu}{\lambda+2\mu}h|\xi|\right)-\frac{\tau^*}{2\mu}|\xi|\left[\frac{\lambda+2\mu}{\lambda+\mu}+h|\xi|+\frac{\lambda+3\mu}{\lambda+2\mu}\Lambda|\xi|+\frac{(\lambda+\mu)^2}{(\lambda+2\mu)^2}\Lambda h\xi^2\right]\right\} \end{array}\right\} \tag{46}$$

$$F = \frac{\bar{p}(\xi)}{2(\lambda+2\mu)\eta|\xi|}\left\{\begin{array}{l} e^{|\xi|h}\left\{(\lambda+\mu)(1+\Lambda|\xi|)+\frac{\tau'}{2\mu}|\xi|\left[\lambda+2\mu+\frac{(\lambda+\mu)(\lambda+3\mu)}{\lambda+2\mu}\Lambda|\xi|\right]\right\} \\ +e^{-|\xi|h}\left\{\lambda+3\mu+(\lambda+\mu)(\Lambda+2h)|\xi|-\frac{\tau'}{2\mu}|\xi|\left[\lambda+2\mu+\frac{(\lambda+\mu)(\lambda+3\mu)}{\lambda+2\mu}\Lambda|\xi|+\frac{2(\lambda+\mu)^2}{\lambda+2\mu}\Lambda h\xi^2\right]\right\} \end{array}\right\} \tag{47}$$

3.2.2 Arbitrary functions for internal horizontal loading

$$A = \frac{i\bar{q}(\xi)}{2(\lambda+2\mu)\eta|\xi|\xi}e^{|\xi|h}\left\{[\mu-(\lambda+\mu)h|\xi|](1+\Lambda|\xi|)-\tau'|\xi|\left[\frac{\lambda+2\mu}{2(\lambda+\mu)}-\frac{\lambda+2\mu}{2\mu}h|\xi|-\frac{\lambda+3\mu}{2(\lambda+2\mu)}\Lambda|\xi|-\frac{(\lambda+\mu)^2}{2\mu(\lambda+2\mu)}\Lambda h\xi^2\right]\right\} \tag{48}$$

$$B = \frac{i\bar{q}(\xi)}{2(\lambda+2\mu)\eta\xi}e^{|\xi|h}\left\{\lambda+3\mu-(\lambda+\mu)(\Lambda+2h)|\xi|+\frac{\tau'}{2\mu}|\xi|\left[\lambda+2\mu-\frac{(\lambda+\mu)(\lambda+3\mu)}{\lambda+2\mu}\Lambda|\xi|+\frac{2(\lambda+\mu)^2}{\lambda+2\mu}\Lambda h\xi^2\right]\right\} \tag{49}$$

$$C = -\frac{i\bar{q}(\xi)e^{-|\xi|h}[\mu-(\lambda+\mu)h|\xi|]}{2|\xi|\xi(\lambda+2\mu)} \tag{50}$$

$$D = -\frac{i\bar{q}(\xi)e^{-|\xi|h}(\lambda+\mu)}{2\xi(\lambda+2\mu)} \tag{51}$$

$$E = -\frac{i\bar{q}(\xi)}{2(\lambda+2\mu)\eta|\xi|\xi}\left\{\begin{array}{l} e^{|\xi|h}\left\{[\mu+(\lambda+\mu)h|\xi|](1+\Lambda|\xi|)+\tau'|\xi|\left[\frac{\lambda+2\mu}{2(\lambda+\mu)}+\frac{\lambda+2\mu}{2\mu}h|\xi|+\frac{\lambda+3\mu}{2(\lambda+2\mu)}\Lambda|\xi|+\frac{(\lambda+\mu)(\lambda+3\mu)}{2\mu(\lambda+2\mu)}\Lambda h\xi^2\right]\right\} \\ -e^{-|\xi|h}\left\{[\mu-(\lambda+\mu)h|\xi|](1+\Lambda|\xi|)-\tau'|\xi|\left[\frac{\lambda+2\mu}{2(\lambda+\mu)}-\frac{\lambda+2\mu}{2\mu}h|\xi|-\frac{\lambda+3\mu}{2(\lambda+2\mu)}\Lambda|\xi|-\frac{(\lambda+\mu)^2}{2\mu(\lambda+2\mu)}\Lambda h\xi^2\right]\right\} \end{array}\right\} \tag{52}$$

$$F = \frac{i\bar{q}(\xi)}{2(\lambda+2\mu)\eta\xi}\left\{\begin{array}{l} e^{|\xi|h}\left\{(\lambda+\mu)(1+\Lambda|\xi|)+\frac{\tau'}{2\mu}|\xi|\left[\lambda+2\mu+\frac{(\lambda+\mu)(\lambda+3\mu)}{\lambda+2\mu}\Lambda|\xi|\right]\right\} \\ +e^{-|\xi|h}\left\{\lambda+3\mu-(\lambda+\mu)(\Lambda+2h)|\xi|+\frac{\tau'}{2\mu}|\xi|\left[\lambda+2\mu-\frac{(\lambda+\mu)(\lambda+3\mu)}{\lambda+2\mu}\Lambda|\xi|+\frac{2(\lambda+\mu)^2}{\lambda+2\mu}\Lambda h\xi^2\right]\right\} \end{array}\right\} \tag{53}$$

4. Numerical results and discussion

It is noted that the solutions for displacements and stresses given by Eqs. (7) - (11) are expressed in terms of semi-infinite integrals. A closed-form solution cannot be obtained due to the complexity of the integrands. Therefore, it is proposed to employ an accurate numerical scheme to evaluate these integrals. In this study, the integrals are evaluated by using globally adaptive numerical quadrature scheme based on 21-point Gauss-Kronrod rule (Piessens 1983). The surface elastic constants can be obtained by using atomistic simulations (Miller and Shenoy 2000, Shenoy 2005, Dingreville and Qu 2007). It is convenient to introduce the non-dimensional coordinates, $x_0 = x/\Lambda$ and $z_0 = z/\Lambda$, in the numerical study. The numerical results in the present study correspond to the case of an elastic layer subjected to a uniformly distributed load applied over a strip $-a \le x \le a$. In the numerical study, a hypothetical material with $\lambda/\mu = 2.226$ and $\Lambda = 1$ *nm* are used. In addition

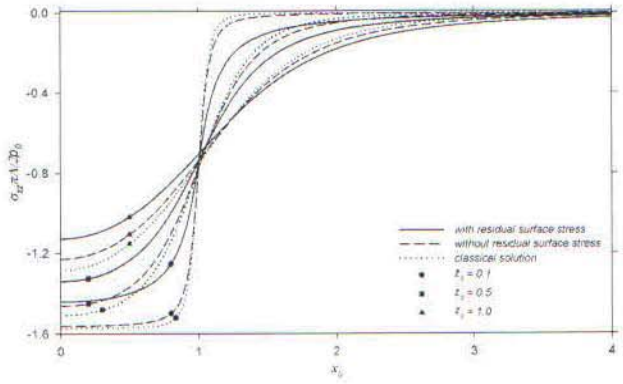

(a)

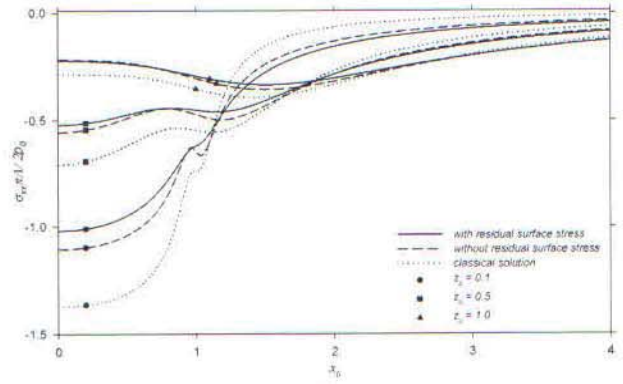

(b)

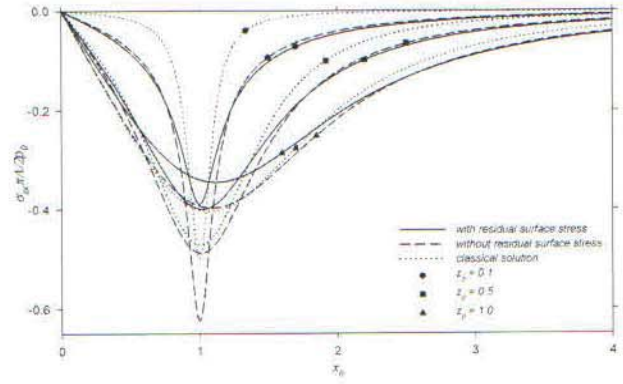

(c)

Fig. 2 Non-dimensional stress profiles of a half-plane under vertical surface load: (a) Vertical stress, (b) Horizontal stress, (c) Shear stress

$\tau^s = 5\ N/m$ is used to demonstrate the influence of residual surface stress.

Figs. 2 to 7 demonstrate the influence of surface elasticity and residual surface stress on the stress

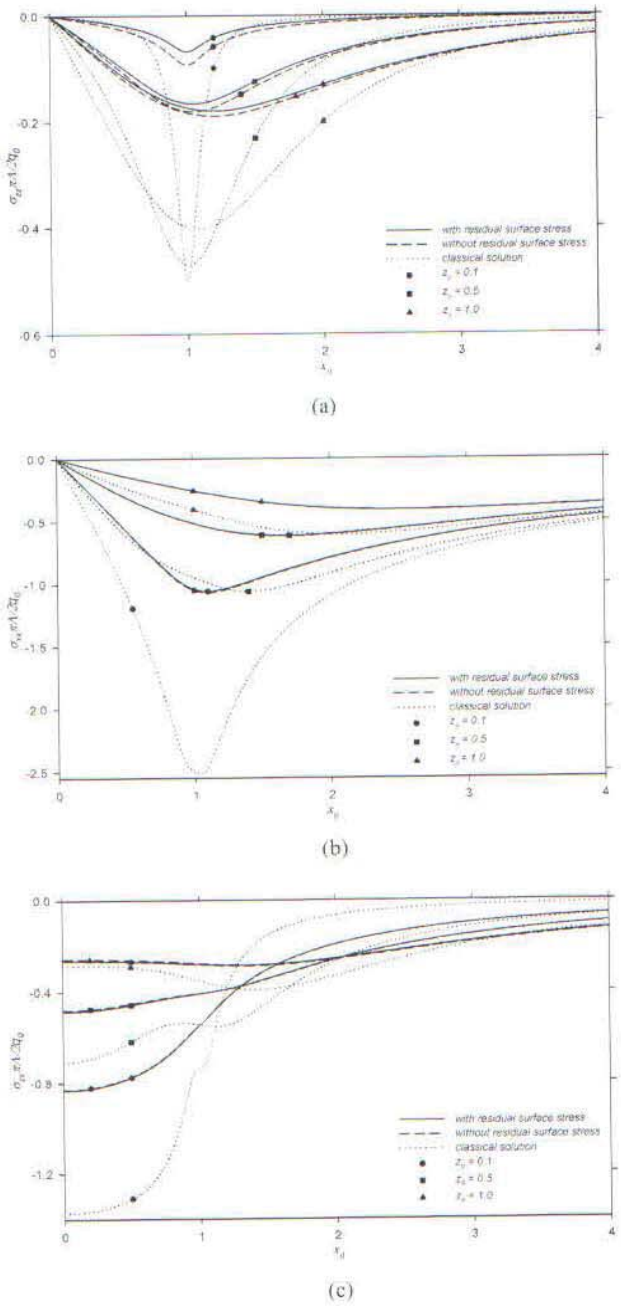

Fig. 3 Non-dimensional stress profiles of a half-plane under horizontal surface load: (a) Vertical stress, (b) Horizontal stress, (c) Shear stress

field of an elastic layer with very large value of t (a half-plane) under different loading cases. Figs. 2 and 3 show the variation of non-dimensional stresses along the x-direction of a half-plane at

various depths under a uniform vertical strip load of magnitude p_0 and a horizontal strip load of magnitude q_0 respectively applied at the surface. A non-dimensional load width, $a_0 = a / \Lambda = 1$, is used in the numerical study. Only the solutions along the positive x-axis are presented due to the symmetry or anti-symmetry of the solutions about the z-axis.

The influence of surface elasticity on an identical problem was previously examined by Zhao and Rajapakse (2009) by ignoring the out-of-plane component of surface stresses. The dotted lines denote the classical elasticity solutions corresponding to zero surface stress (i.e. $\kappa^s = \tau^s = 0$) and the dash lines denote the solutions that neglect the out-of-plane component of surface stresses (Zhao and Rajapakse 2009), which also disregard the influence of residual surface stress (τ^s) as previously discussed. It is evident from the figures that the influence of residual surface stress is more significant in the case of vertical strip load when compared to the horizontal strip load case. On the contrary, the influence of surface elasticity is more evident in the case of horizontal loading. It is also found that for the horizontal loading the influence of residual surface stress is negligible on horizontal normal and shear stresses but more evident on vertical normal stress, whereas in the case of vertical strip load all stress components depend significantly on the residual surface stress. This behavior can be described from the fact that the residual surface stress appears in the equilibrium equation of the vertical normal stress, Eq. (13), but apparently vanishes in the shear stress equation, Eq. (14), due to the assumption that the residual surface stress is constant. As expected, the influence of residual surface stress becomes significant only in a local region near the surface (i.e. $z_0 < 2.0$ for the vertical loading and $z_0 < 1.0$ for the horizontal loading) and would diminish with the distance from the free surface. In addition, the influence of the residual surface stress becomes negligible when $x_0 / a_0 > 4$.

To investigate the influence of the surface material parameter Λ and the residual surface stress τ^s, the non-dimensional stress profiles along the x-direction of a half-plane due to a uniform vertical strip load p_0 are shown in Fig. 4 for different values of Λ and in Fig. 5 for different values of τ^s respectively. Note that in Figs. 4 and 5 stresses are calculated at $z_0 = 0.1$. In Fig. 4, the non-dimensional stresses are presented for a hypothetical material with the surface material parameter Λ_1 being varied from 0 to 100Λ, whereas the residual surface stress parameter (τ^s) is unchanged. It can be seen from the figure that the free surface is stiffer with increasing values of Λ_1 resulting in the reduction of the stresses in the layer. The influence of the residual surface stress in Fig. 5 shows a similar trend to Fig. 4. It can be seen from Fig. 5 that all bulk stress components decrease when residual surface stress (τ^s) increases from 0 to 100 *N/m*.

Figs. 6 and 7 show the variation of non-dimensional stresses along the z-axis of an elastic half-plane subjected to an internal vertical strip load p_0 and an internal horizontal strip load q_0 over a region $2a$ (with $a_0 = 1$) at various depths. A non-dimensional quantity, $h_0 = h / \Lambda$, is used in the numerical analysis. The influence of surface elasticity of an identical problem was recently considered by Intarit *et al.* (2010) without the out-of-plane component of surface stresses and the influence of residual surface stress (τ^s). Numerical results shown in Figs. 6 and 7 indicate that the stresses increase when approaching the plane of applied loading. A discontinuity in both vertical and horizontal stresses is observed at the level where the vertical strip load is applied, whereas for the case of a horizontal strip load the shear stress is discontinuous at the loading plane. It is found that the residual surface stress shows more significant influence on the stress field in the case of a vertical strip loading, especially at points closer to the free surface ($z_0 < 2$) when compared to the case of a horizontal strip loading. It should be noted that σ_{zz} in Fig. 6 is no longer zero at the surface due to the presence of the residual surface stress τ^s.

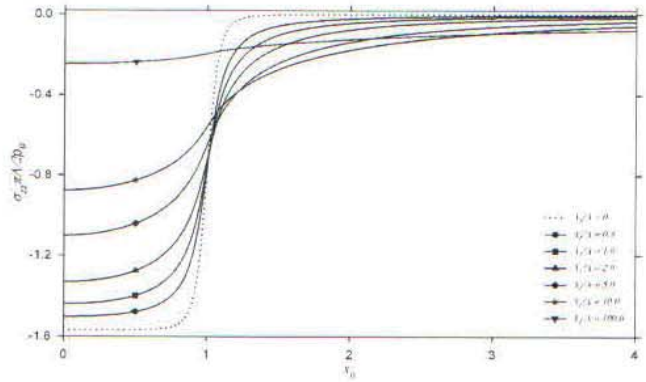

(a)

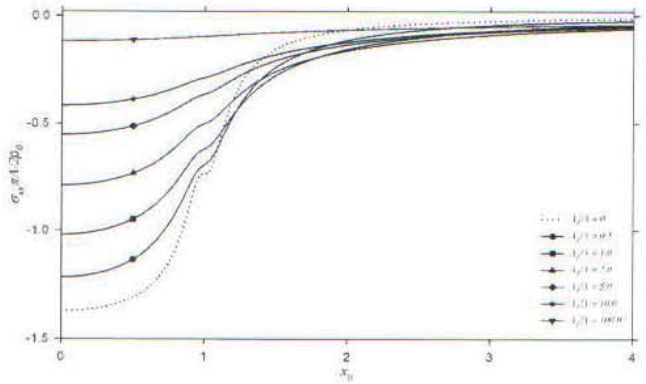

(b)

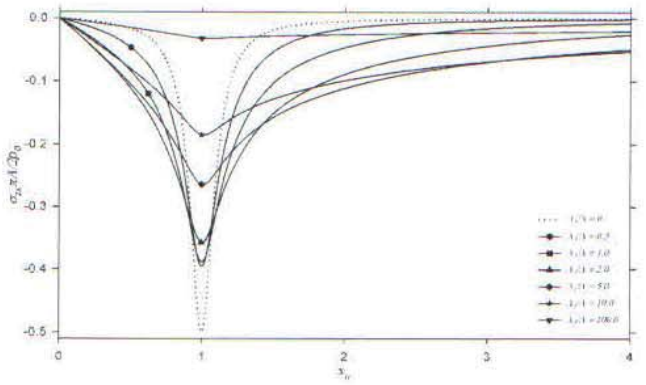

(c)

Fig. 4 Non-dimensional stress profiles at $z_0 = 0.1$ under vertical surface load for different material constants: (a) Vertical stress, (b) Horizontal stress, (c) Shear stress

To investigate the influence of layer thickness, the profiles of non-dimensional stresses in elastic layers of different thicknesses bonded to a rigid base and subjected to a uniformly distributed